Doctoral Thesis

Design and Synthesize Small Molecular Self-Assembling Peptides for Biomedical Applications

Shijin Zhang

November, 2020

Supervisor: Dr. Ye Zhang

Declaration of Original and Sole Authorship

I, Shijin Zhang, declare that this thesis entitled “Design and Synthesize Small Molecular Self-Assembling Peptides for Biomedical Applications” and the data presented in it are original and my own work. I confirm that:

- This work was done solely while a candidate for the research degree at the Okinawa Institute of Science and Technology Graduate University, Japan.
- No part of this work has previously been submitted for a degree at this or any other university.
- References to the work of others have been clearly attributed. Quotations from the work of others have been clearly indicated, and attributed to them.
- In cases where others have contributed to part of this work, such contribution has been clearly acknowledged and distinguished from my own work.
- None of this work has been previously published elsewhere, with the exception of the following:

1. Shijin Zhang[+], William Cortes[+], Toshio Sasaki, Shunsuke Asahina, Asano Natsuko, Qizheng Zhang, and Ye Zhang.* "Mechanoresponsive Alignment of Molecular Self-assembled Negatively Charged Nanofibrils" *ACS Applied Bio Materials.* **2020**, 3, 1698-1704. (+*These authors contribute equally to this work*)
2. Wei Ji, Shijin Zhang, Gerogy A. Filonenko, Guanying Li, Toshio Sasaki, Chuanliang Feng* and Ye Zhang.* "Co-Organizing Synthesis of Heterogeneous Nanostructure through Photo-Cleavage of Pre-Stabilized Self-Assemblies" *Chem. Commun.* **2017**, 53, 4702-4705.
3. Wei Ji, Shijin Zhang, Sachie Yukawa, Shogo Onomura, Toshio Sasaki, Kun'ichi Miyazawa, and Ye Zhang.* "Regulate Higher-order Organization through the Synergy of Two Self-sorted Assemblies" *Angew. Chem. Int. Ed.* **2018**, 57, 3636-3640.
4. Shijin Zhang, William Cortes, Ye Zhang* “Constructing Cross-linked Nanofibrous Network via Enzyme-instructed Hierarchical Assembly*” Langmuir.* **2020***,* 36, 6261-6267.
5. Shijin Zhang, Xunwu Hu, Dingze Mang, Toshio Sasaki, and Ye Zhang.* "Self-Delivery

of N-hydroxylethyl Peptide Assemblies to the Cytosol Inducing Endoplasmic Reticulum Dilation in Cancer Cells " *Chem. Commun.* **2019**, 55, 7474-7477.

6. Shijin Zhang and Ye Zhang.* "Promote Dual-subcellular-targeting Anticancer Efficacy by Regulating the Intracellular Self-assembly Dynamics" *ACS Appl. Mater. Inter.,* **2020***, 12,* 41105-41112.

Signature: 

Date: November, 2020

Abstract

Molecular self-assembly is a spontaneous process of molecular association through non-covalent bond interaction. Imitating molecular self-assembly and creating novel functional molecular assemblies through synthetic chemistry are important issues in nanotechnology development. Small peptidic molecules are ideal candidates for imitating molecular self-assembly in biological system because of their biocompatibility and easy functionalization for bio-related applications including drug delivery, anti-cancer treatment and biosensors. In the first part (Chapter I), we address the essential role of nanotechnology in daily life, and a brief summarization on nanomaterial species, interaction mode, representative examples from biological system, available characterization methods, classes of artificial nanomaterials and their bio-related applications are outlined. In the second part (Chapter III), we have fabricated well-orientated nanofibrous structure through conjugation of easily deprotonated functional group to self-assembly building block. *Via* pH adjustment to manipulate molecular charge status, and further mechanical force guiding orientation of the nanofibrous structure. Large scale nanomaterial fabrication is achieved through evaporation casting capillary confinement. In the third part (Chapter IV), higher-order nanomaterial is approached by combination of co-assembly and self-sorting in multiple components. Stimulus such as light is applied on pre-stabilized template to obtain unconventional nanostructures. Two self-sorting components interact with each other at a nanoscale *via* both ALP and light regulation to reach a higher-order hierarchical assembly. Through ALP and CES - catalysed molecular self-assembly, two self-sorting components interact with each other to deliver a more robust nano-scaffold with potential in cell culture. In the fourth part (Chapter V), precisely subcellular organelle molecular self-assembly is realized by incorporation of the enzyme responsive motif with self-assembly building block. Introducing CES responsive motif to self-assembly peptide enhance cellular uptake of the self-assembly building block, intracellular recovery of the self-assembly peptide enriches on endoplasmic reticulum and thus leading to cancer cell apoptosis. Dual-subcellular-targeting anticancer therapy is reached by conjugating endoplasmic reticulum (ER)-targeted coumarin-functionalized short peptides and DNA alkylating agent (chlorambucil). After being uptaken and hydrolysis by intracellular CES, the coumarin-functionalized peptides self-assemble on ER to introduce ER stress while the chlorambucil targeting the nucleus to show synergistic effect on cancer cells.

ACKNOLOWEDGEMENTS

This work would not have been possible without the following collaborations:

- Dr. Ye Zhang for the professional suggestions on all the projects and manuscript preparation;
- Dr. Guanying Li for the help in confocal microscope imaging and flowcytometry experiments;
- Dr. Wei Ji for the help in coumarin derivatives synthesis and the basic characterization method for nanomaterial;
- Dr. Dingze Mang for the help in western blotting assay;
- Dr. Sona Rani Roy for the help in protein extraction experiments;
- Mr. Xunwu Hu for the help in cell culture and cell lysis experiments;
- Ms. Sachie Yukawa for the help in TEM imaging;
- Mr. William Cortes for help in evaporation casting capillary film fabrication and nanomaterial characterization through rheology and TEM;
- Mr. Sasaki Toshio for the technical support in TEM and SEM imaging experiments;
- Dr. Roy Michael for the technical support in NMR and MS measurements;
- Financial support from Okinawa Institute of Science and Technology Graduate University;

Abbreviations

F: Phenylalanine
K: lysine
V: Valine
P: Proline
T: Threonine
E: Glutamic acid
D: Aspartic acid
A: Alanine
I: Isoleucine
G: Glysine
L: Leucine
R: Arginine
N: Asparagine
Q: Glutamine
Y: Tyrosine
S: Serine
W: Tryptophan
H: Histidine
Yp: O-phospho-L-tyrosine
Fmoc: Fluorenylmethyloxycarbonyl protecting group
Nap: 2-Naphthaleneacetic acid
SA: Self-assembly
CA: Co-assembly
ALP: Alkaline phosphatase
CES: Carboxylesterase
XRD: X-ray powder diffraction
CD: Circular dichroism
FTIR: Fourier transform infrared
TEM: Transmission electron microscopy
AFM: Atomic force microscopy
SEM: Scanning electron microscopy
PLM: Polarized light microscope
PA: Peptide amphiphile
ELP: Elastin-like polypeptide
ER: Endoplasmic reticulum
HBTU: 2-(1H-benzotriazol-1-yl)-1,1,3,3-tetramethyluronium hexafluorophosphate
TFA: Trifluoroacetic acid
TFE: 2,2,2-Trifluoroethanol
DMF: Dimethylformamide
DCM: Dichloromethane
MeOH: Methanol
DIEA: N, N-Diisopropylethylamine
DIC: N, N’-Diisopropylcarbodiimide
NHS: N-Hydroxysuccinimide
EDCI: N-(3-dimethylaminopropyl)-N'-ethylcarbodiimide hydrochloride
DMAP: 4-Dimethylaminopyridine
EA: Ethyl acetate

THF: Tetrahydrofuran
UA: uranyl acetate

Table of Contents

List of Figures

List of Tables

I. General Introduction

Nanostructure is an intermediate state between molecular and microscopic structures with dimensions ranging from 1 to 100 nanometers.[1] Although such structures are beyond our direct visual observation and easily to be ignored, they are inescapable part in our daily life (shown in Figure 1). For example, solar cells fabricated at nanoscale, sun creams with nano-size zinc oxide, airborne nanoparticles in the smoke from fire and nano-size antibacterial silver particles.

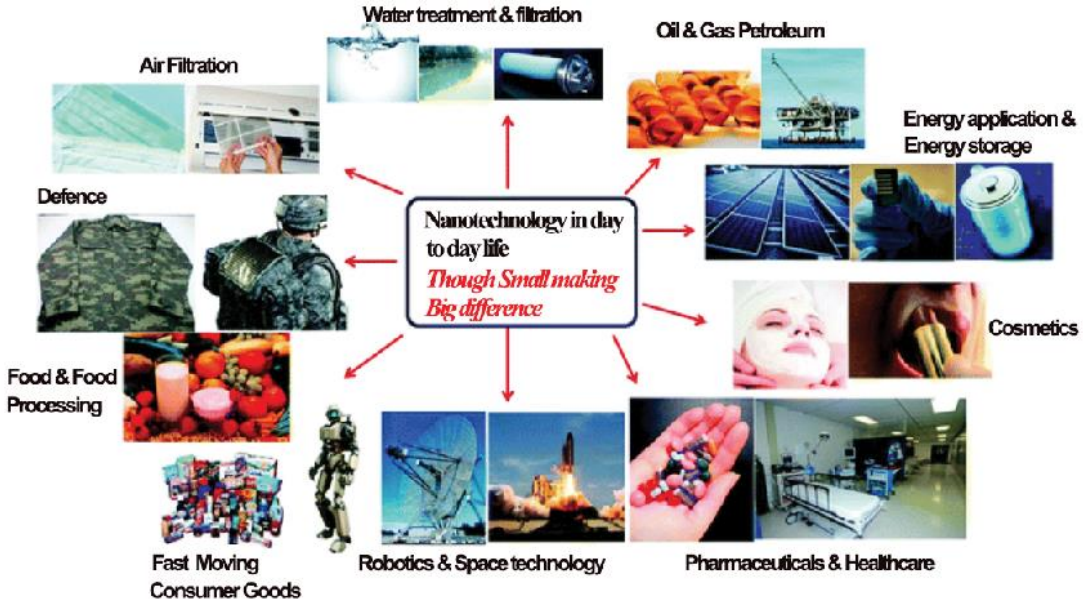

Figure 1. Nanotechnology in our daily life: various areas, industries.[3]

In addition, nanostructures are universally existing in biological science, such as proteins (e.g. haemoglobin (oxygen-transportation protein) is 5.5 nm in diameter), virus (e.g. tobacco mosaic virus is 18 nm in width), and sub-cellular organelle (e.g. ribosome is around 30 nm in diameter). To chemist (especially organic chemist), nanostructures are a kind of molecule assemblies with the number of atoms from 10^3 to 10^9, bearing a molecular weight of 10^4 to 10^{10} Daltons.[2]

I. 1. Types of Artificial Nanomaterials by Chemical Bonds

In pursuing artificial functional nanostructures, chemists have exploited their efforts to reach well-defined shape and size structures with specific molecules either through co-valent bond connection or non-covalent bond interaction. Since the seminal work from Gilbert N. Lewis on chemical bonding "The Atom and the Molecule",[4] organic synthesis progresses hugely both at the synthetic craft and approaching varieties of molecules. Covalently linking molecules is feasible to generate functional nanostructures such as polymer nanocapsules,[5] two dimensional polymer films,[6] polymer microrings.[7] Covalent linking molecules to fabricate functional nanostructures has its advantage in producing robust structures, but it is

still limited in enriching nanostructures due to its compromise between chain building and secondary structure manipulation. Fabricating nanostructures through non-covalent interaction provides more choices to reach various functional nanostructures. For example, nanotubes,[8] nanovesicles,[9] nanofibers[10] and nanocoils.[11] Nanostructures fabrication through non-covalent interaction is usually consisted by small molecular building blocks. The conformation of small molecular building blocks is easy to control. Additionally, synthesis of the building unit is not a laborious

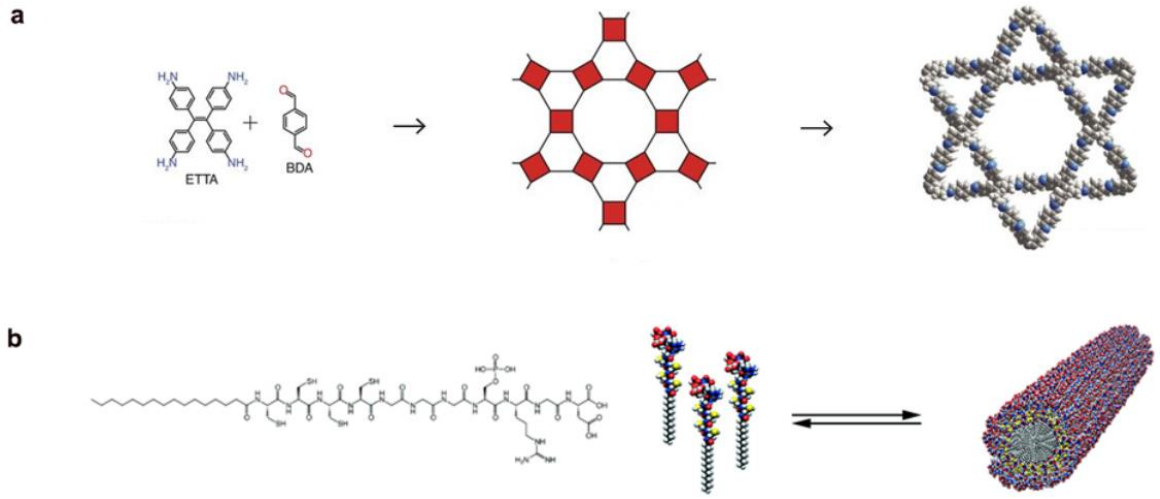

Figure 2. (a) Chemical structure of co-valent bond forming molecules and schematic showing covalent organic nanostructure;[12] (b) chemical structure of amphiphile peptide and schematic showing self-assembly of molecules into cylindrical micelle.[13]

work, secondary structure manipulation could be achieved by carefully molecular design. Typical nanomaterials fabricated through covalent bond and non-covalent interactions are illustrated in Figure 2.

Molecular self-assembly is a spontaneous process to generate ordered molecular aggregates through non-covalent interaction at equilibrium state. It happens not only at a simple molecule level, but also in the more complexed motif, such as polymer. Formation of large, complexed, functional nanostructures usually involves hydrogen bonds, π-π interaction, hydrophobic interaction, van der Waals interaction, and ionic interaction. The strength and distance of these non-covalent interaction is summarized in Table 1.[14] The key for this kind of nanostructure fabrication lies in thoroughly understanding and controlling of non-covalent interaction between building blocks.

Force	Strength (kJ/mol)	Distance (nm)
Van der Waals	0.4 - 4.0	0.3 – 0.6
π-π Interactions	8 - 12	0.5
Hydrogen Bonds	12 – 30	0.3
Ionic Interaction	20	0.25
Hydrophobic Interactions	< 40	Varies

Table 1. Comparation of different non-covalent interaction forces in strength and distance.

I. 2. Non-covalent Interaction

The driving forces to build flexible nanomaterials are non-covalent interactions. However, this kind of interaction is weak (0.4 – 40 kJ/mol, table 1) compared to co-valent bonds (100 – 500 kJ/mol).[15] To reach a stable and well-shape nanostructure, the strength of non-covalent interactions should overcome the single molecular thermodynamics in the solvent to favour molecular assemblies. Normally, within nanostructures, there exist several kinds of non-covalent interactions and sufficient numbers of non-covalent bonds. These non-covalent interactions work collectively to generate well-defined nanostructures.

I. 2. 1. Van der Waals Interaction

When two atoms are in a distance of 0.3 – 0.6 nm, there will be a weak and nonspecific attractive force caused by transient dipoles that named van der Waals interaction (Figure 4a). Transient dipole is a result of fluctuated distribution of electrons of the atom. If any of non-bonded atoms are close to each other, the transient dipole of one atom will perturb the electron distribution of the other. Thus, causing transient dipole in the second atom, and these two dipoles will attract each other. Van der Waals interactions exist in both polar and nonpolar molecules. Distance plays a key role in van der Waals interaction, when the two atoms get too close (< 0.3 nm), they will repel each other due to the negative charged electrons in the outer shell of the atoms; when the distance increases beyond 0.6 nm, van der Waals interaction decreases rapidly.

I. 2. 2. π-π Interaction

In aromatic molecules, the specific attractive non-covalent interaction among the aromatic rings is named π-π interaction. Though it is a weak attractive force within aromatic molecules, it not only requires specific distance at around 0.5 nm, but also has stringent request on geometric configuration. Preferred geometric configuration in aromatic rings packing for π-π interaction are sandwich, T-shaped, and parallel-displaced (shown in Figure 3).[16] This kind of non-covalent interactions extensively exist in biological system, such as nucleobase stacking within RNA and DNA molecules, tertiary structures of proteins, and intercalation of aromatic molecules into DNA.

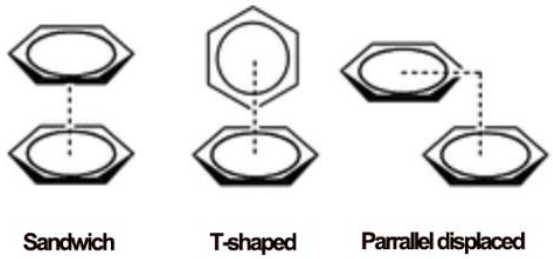

Figure 3. Three types of typical p-p aromatic interactions at varied geometries.

I. 2. 3. Hydrogen Bonding

Hydrogen atom has only one electron surrounding its nucleus. It often forms one covalent bond with another atom, thus creating a deficient electron environment around hydrogen nucleus. Upon approaching another atom with at least one non-bonding pair of electrons at

its outer shell, hydrogen bond forms (Figure 4b). Hydrogen bonds are widely existing in molecules with amino (-NH_2) and hydroxyl (-OH) groups, both intramolecular and intermolecular. In biological system, there is a huge amount of hydrogen bonds due to the abundance of amino and hydroxyl groups in proteins, DNA, RNA and its aqueous environment. The collectively hydrogen bonding interaction contributes to guarantee the stable nanostructures in biological system to fulfill their functions.

I. 2. 4. Ionic Interaction

Some atoms (e.g. Na), their outer shell electrons are weakly constrained by the nucleus, while the other atoms (e.g. Cl) have a strong attractive force even for the outer shell electrons. When these two kinds of atoms come close to each other, for example, Na and Cl, Na is apt to lose its outer shell to produce Na^+ and Cl is going to accept the escaping electron to become Cl^-. Ionic interaction occurs between Na^+ and Cl^- (Figure 4c). In liquid state, ionic interaction does not require specific geometric orientation, it occurs at all directions between cationic and anionic ions within the ideal distance around 0.25 nm. It is indispensable to maintain proper configuration nanostructures in biological system.

I. 2. 5. Hydrophobic Interaction

Nonpolar molecules are not likely to interact with water molecules in the way of neither hydrogen bonding nor ionic interaction, only van der Waals interaction happens between them. Such weak interaction force does not guarantee them enough access to freely distributed within water molecules. They are apt to aggregate together, and it is called hydrophobic interaction (Figure 4d). In the aqueous environment, different nonpolar molecules can bond together through van der Waals interaction. Once they come close to each other, the collective of hydrophobic and van der Waals interactions are powerful enough to generate stable nanostructures within the aqueous environment.

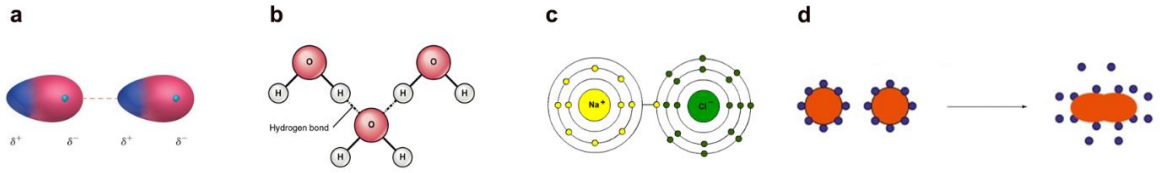

Figure 4. Typical illustration of Van der Waals Interaction (a), hydrogen bonding (b), ionic interaction (c), and hydrophobic interaction (d).

I. 3. Nanomaterials from Biological System

A variety of precise nanoscale structures extensively exist in the biological system which are formed through molecular self-assembly. For instance, cell contains an astonishing of complex and functional nanostructures ranging from folded proteins and double helix DNA structure to phospholipid bilayer membrane. These well-organized nanostructures derived from non-covalent interactions at the molecule scale by the basic molecular motif. Their precise shape and size guarantee the distribution and bio functionalities to fulfill the requirement of energy and exchange of information and substance for the cells.

I. 3. 1. Protein folding

It is an omnipresent biological process involving abundant non-covalent interactions of molecular self-assembly in aqueous environment. The primary structure of peptide sequence is consisted by 20 natural amino acids, it is stringently controlled through translation of messenger RNA sequence. To reach a functional protein, the primary structure should undergo maturation process to its secondary, tertiary and quaternary structure. Secondary structure is normally consisted by α-helix, β-sheet, and β-strand. These structures are achieved by the intramolecular hydrogen bonds, which are formed between the carbonyl oxygen atoms (C=O) and the hydrogen atoms in the amide groups (NH). Collectively hydrogen bonds provide a powerful force to stabilize the secondary structure. Further interaction among α-helix, β-sheet, and β-strand will generate tertiary structure. The folding process to tertiary structure is driven by the non-specific hydrophobic, ionic interactions, hydrogen bonds and disulfide bonds among the secondary structures. Tertiary structures are of critical important owing to its formation of functional regions such as binding pockets or catalytic points. Non-covalent interactions or disulfide bonds among the tertiary structure will lead to quaternary structure, which serves as a single functional unit. The assembly process of protein is illustrated in Figure 5.

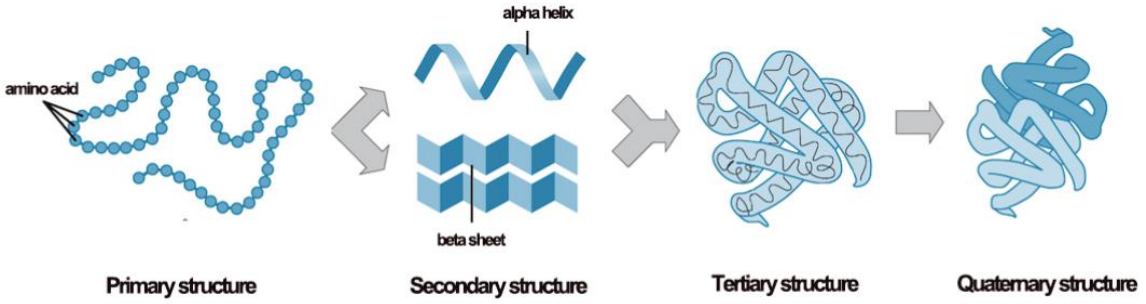

Figure 5. Assembly process of protein from its chain structure to higher order structure.

I. 3. 2. Nucleic Acid Double Helix

Illustrated by James Watson and Francis Crick - double helix model of DNA - is a well-known molecular self-assembly and it is central in hereditary information transmitting. The basic unit involves in double helix structure for molecular self-assembly are nucleotides: adenine (A), cytosine (C), guanine (G) and thymine (T). Nucleotide is a combination of 5-carbon sugar, phosphate group and nitrogenous base. In single stranded DNA, sugar-phosphate sequence serves as the backbone and nitrogenous bases extend from the chain. Hydrogen bonds forms between A-T and C-G, intermolecular hydrogen bonding makes the complementary single stranded DNA together (Figure 6a). Further enhanced by π-π stacking interactions between A and G, C and T, double helix structure forms. The synergistic effect of hydrogen bond and π-π interaction produce robust double helix DNA structure (Figure 6b). Thus, guarantee correct hereditary information transmitting. The double helix DNA is around 2 nm in width, and about 50 nm in length.

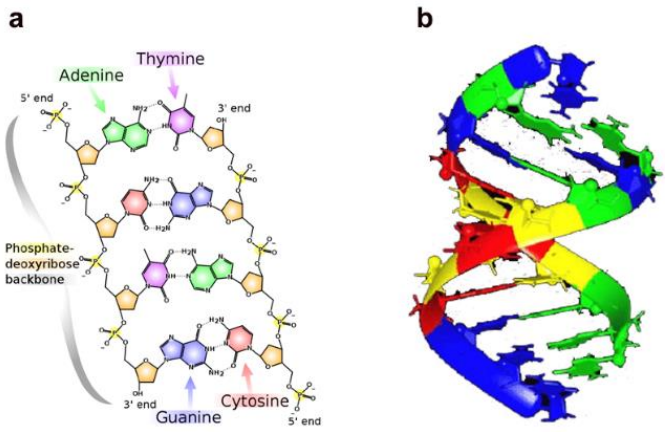

Figure 6. (a) Two single DNA strands and the hydrogen bonding between the complementary bases; (b) models of DNA double helix structure.

I. 3. 3. Phospholipid Bilayer

The cytoplasmic membrane is consisted by phospholipid bilayer to make the cell as an isolated identity in the aqueous environment. Phospholipid monomer includes hydrophilic group (phosphate and glycerol portion) and hydrophobic group (fatty acid). In the aqueous environment, hydrophobic interaction among the fatty acids and hydrogen bonding between the hydrophilic group and water leading to the self-assembly of these monomers to form phospholipid bilayer (Figure 7). The collective non-covalent interactions are strong enough to make the bilayer maintain at a dynamic equilibrium state for substance exchange between the cell and its environment, such as K^+, Na^+ ions, O_2, and so on.

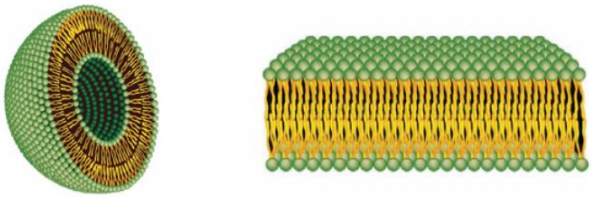

Figure 7. Typical lipid bilayer structure found in biological system, liposome (left) and membrane structure (right)[17].

I. 3. 4. Virus

Viruses infect all kind of life forms from plants and animals to microorganisms, the infectious agent starts to work after entering into the living cells. They are generally composed of a protective protein coat and nucleic acid core, and their sizes range from 20 to 300 nm in diameter. Take the tobacco mosaic virus (TMV) for example, it appears as a rod-like morphology with 18 nm in width and 300 nm in length (Figure 8). Its core is a single strand RNA with 6400 bases, and the protective protein coat is made up by 2130 protein monomers. The monomer is consisted by 158 amino acids. The single strand RNA works as a template for the protein monomers to strictly self-assemble around it to make an integrated virus. It has been proved that TMV can be disassembled into its component parts, and these component parts can be reconstituted to form an intact, fully infectious virus. The reversible

molecular self-assembly process can be explained by the non-covalent interactions between the proteins and RNA.

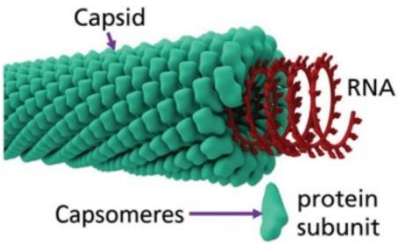

Figure 8. Structure of tobacco mosaic virus, capsid proteins assemble around RNA core.

There are still plenties of precise-organize nanostructures in biological system generated in a molecular self-assembly pathway which cannot be thoroughly discussed in current thesis. Through above mentioned examples, we still can learn some basic principles for the molecular self-assembly in biological system:

1): Non-covalent interactions play a key role in guiding molecular self-assembly; though single non-covalent interaction is weak, collective non-covalent interactions deliver a powerful force to stabilize self-assembly structures;

2): Complementary interaction (A-T, C-G in DNA; A-U, C-G in RNA) not only plays a fundamental basis for association between different components, but also controls the size and shape for the final self-assembly nanostructures;

3): Most of the components involve in non-covalent interactions containing functional groups such as carbonyl (C=O), amide (NH), hydroxyl (OH), and aromatic rings.

I. 4. Manipulate Molecular Self-assembly in Artificial System

As mentioned above, nanostructures from biological system always form in an aqueous environment. To reach a better biomimetic nanomaterial design, most of the current research on molecular assembly are carried out in solution. In the solution state, the self-assembly motif not only interact with each other, but also interact with other solutes and the solvent. In addition, in solution state, molecular level of self-assembly motif distribution would be able to achieve, and the thermal motion will bring them together to form assembly nanostructures. A strong orthogonal interaction force to reach a final molecular self-assembly nanomaterial is highly preferred. To obtain stable nanostructures, the association of the self-assembly motif should be strong enough to overwhelm the interaction between the self-assembly motif with its environment.

I. 4. 1. Molecular Self-assembly in Solution

Molecular environment greatly affects its self-assembly behaviour, such as pH, temperature, ionic strength. Additionally, self-assembly could also be triggered by external stimuli, such as light and enzyme. The presence form of the self-assembly molecule can be changed due to interactions from other ions, pH value, the solvent species and so on (Figure 9). For

example, if there is carboxyl group in the self-assembly molecule, presence of Ca^{2+} in the solution will chelate with the carboxyl group, thus changing molecule form of the self-assembly molecule, leading to transition in its self-assembly behaviour. Ca^{2+} has been shown to trigger the self-assembly of FmocFF, and further regulate co-assembly with alginate.[18] If the self-assembly molecule contains pH sensitive groups, for example, amine, amide, carboxyl, and hydroxyl group, protonation or deprotonation would occurs in different pH environment. Such difference

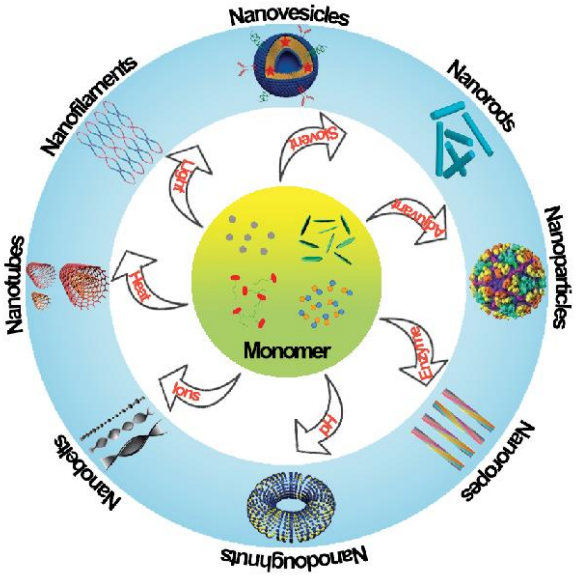

Figure 9. Schematic showing monomer under various triggers to self-assemble into different nanostructures.

would have a significant effect on the molecular self-assembly. Prof. Gao's group has designed an ultra-pH sensitive block copolymer, and when pH < pKa, it will stay as monomer in the solution, upon increasing the pH value in the solution until pH > pKa, it will self-assemble into micelles.[19] The solvent effect on molecular self-assembly is studied by Prof. Yan. In their study, a simple dipeptide FF form crystal in dichloromethane; upon adding a trace amount of hydrogen-bond-forming solvents (ethanol, acetone, and N, N-dimethylformamide), it starts to form fibrous structure.[20] Most of the aromatic peptide sequence show thermal-trigger self-assembly behaviour. In Prof. Ulijn's study, they show a simple tripeptide (KYpF) heated to 60 ^{o}C, and then cooled down to room temperature, it formed gel.[21]

To reach dynamic molecular self-assembly, chemists have taken the advantage of smart molecules. Among them, light-sensitive and enzyme-responsive molecules are widely explored. Generally, before exposing to external stimuli, the precursor will not self-assemble; upon external stimuli, the precursor will transform into a self-assembly building block, triggering molecular self-assembly. Light-trigger instant gelation is demonstrated by Prof. Zhu's group. They introduce a photo-sensitive group into HA-NB, upon photo-radiation, it will generate aldehyde groups. The aldehyde groups will cross-link with the amino groups in GelMA, instantly forming gel at the photo-radiation spot. The forming gel effectively stops high-pressure bleeding from pig carotid.[22] To instruct molecular self-assembly in biological system, enzyme is extensively utilized. Prof. Xu's group has demonstrated that alkaline phosphatase and esterase can trigger formation of supramolecular assemblies in cell

milieu. In their molecular design, phosphotyrosine containing peptide will undergo dephosphorylation upon approaching cancer cells which highly express alkaline phosphatase (ALP). Dephosphorylated product will self-assemble to form nanofibers around the cancer cells, leading to cell death.[23] Ester bond containing dipeptide will be hydrolysed after entering into cancer cells (e.g. HeLa), the hydrolysed product will self-assemble into nanofibers inside the cancer cells, thus killing cancer cells.[24]

I. 4. 2. Characterization Method for the Self-assembly Nanomaterial

The structure properties of nanostructures play a key role in their functions. Proper characterization method could provide structure details and further reveal the mechanism in its application. Various technics have been well applied in nanomaterial characterization from angstrom level to centimetre level (shown in Figure 10). In the molecular level, NMR is effective in probing molecular self-assembly. In Prof. Karasawa's research, they show that upon molecular self-assembly, chemical shift of H_A and H_B in quinoline will shift to high

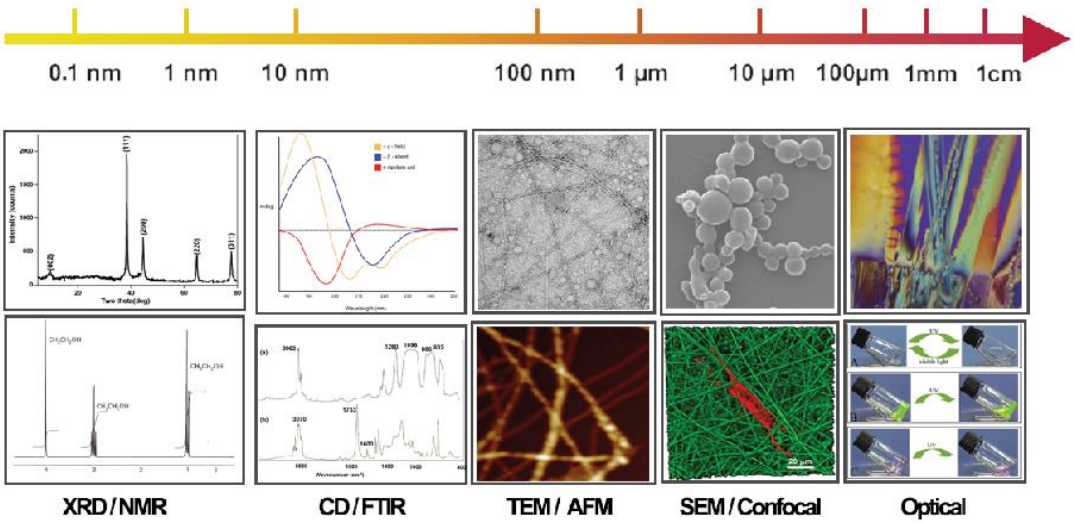

Figure 10. Nanomaterial characterization method from angstrom level to centimetre scale.

fields with broaden peaks, H_E and H_F in benzene ring will shift to low fields with broaden peaks. In the further 2D-HNMR (NOE) measurement, strong correlation is observed between H_A and H_D in quinoline and H_E in benzene, indicating space interactions between quinoline and benzene ring.[25] To gain a clear understanding of the structure of nanomaterials, X-ray powder diffraction (XRD) is often employed in the study. The wavelengths of X-ray are at the range of 0.01 to 10 nanometers, it is feasible to probe structure for nanomaterials. Phase identification can be achieved by XRD measurement when comparing with the reference pattern. From XRD spectrum, we can easily distinguish amorphous with nanocrystalline products. Nanocrystal products show clear diffraction patterns with discernible peaks, while amorphous products show some significant broaden peaks. To those highly crystalline nanomaterials, lattice constants can be obtained from XRD measurements.[26] Circular dichroism (CD) spectroscopy is widely applied in proteins to determine their secondary structure. Proteins are consisted by peptide assemblies, and the two most common secondary structures are α-helix and β-sheets, though random coil occurs as well. CD spectroscopy can be used to distinguish those secondary structure from the characteristic peaks in the obtained spectrum. For β-sheets, a positive peak around 195nm

and negative maximum at 218nm; in α-helix, it is characterized by a positive peak at 193nm and two negative peak at both 208nm and 222nm; random coil show a negative peak at 195nm and low ellipticity above 210nm.[27] Besides CD, Fourier transform infrared (FTIR) is one of the well-established technique used in analysing secondary structure of polypeptides. In the amide I region (1700 – 1600 cm^{-1}), different types of secondary structure bring somewhat change in C=O stretching, thus providing useful information on analysing protein secondary structure. One issue of FTIR in protein secondary structure prediction is the solvent, H_2O has strong IR absorbance at 1645 cm^{-1} (H-O-H bending). Some researchers choose the alternate solvent – D_2O, which doesn't have any absorbance at amide I region. However, replace H_2O with D_2O still brings an issue: is the secondary structure obtained in D_2O consistent with that in H_2O? There is no ideal way to solve the problem, both solvents are still used in FTIR to estimate the secondary protein structure, and the characteristic peaks are shown in Table 2.[28]

H_2O		D_2O	
Mean frequencies	Assignment	Mean frequencies	Assignment
1624 ±1.0	β-sheet	1624 ±4.0	β-sheet
1627 ±2.0	β-sheet		
1633 ±2.0	β-sheet	1631 ±3.0	β-sheet
1638 ±2.0	β-sheet	1637 ±3.0	β-sheet
1642 ±1.0	β-sheet	1641 ±2.0	3_{10} Helix
1648 ±2.0	Random	1645 ±4.0	Random
1656 ±2.0	α-Helix	1653 ±4.0	α-Helix
1663 ±3.0	3_{10} Helix	1663 ±4.0	β-Turn
1667 ±1.0	β-Turn	1671 ±3.0	β-Turn
1675 ±1.0	β-Turn	1675 ±5.0	β-sheet
1680 ±2.0	β-Turn	1683 ±2.0	β-Turn
1685 ±2.0	β-Turn	1689 ±2.0	β-Turn
1691 ±2.0	β-sheet	1694 ±2.0	β-Turn
1696 ±2.0	β-sheet		

Table 2: Assignments of secondary protein structure in H_2O and D_2O media.

To gain a visual sense of biological nanomaterials, we can use electron microscope to observe those nanostructures. Transmission electron microscopy (TEM) and atomic force microscopy (AFM) are good at probing nanoscale details, scanning electron microscopy (SEM) can be used in revealing microscale structures. For TEM, general sample preparation includes the dehydration step, it may bring artefacts in the morphology or size of the secondary structure. Progress in cryo-TEM has solved the problem and deliver a more convincible observation on the nanostructure.[29] AFM allows the experiment to carry out in aqueous condition, it can provide live imagination of the biological samples.[30] SEM sample preparation starts with fast fixation of the biological specimen at the beginning either in -80 ^{o}C freezer or liquid nitrogen, then follow with lyophilization step to maximize preserving the native structure and deliver a robust observation on the nanostructure.[31] To some biological nanomaterials, their specific characteristic enables direct observation at mili-scale or centi-scale. Such as liquid crystal-like biomaterials, their well-structure arrangement and orientation make it possible to observe by polarized light microscope (PLM). Strong birefringence phenomenon from PLM indicates well-orientation of the nanomaterials.[32]

I. 1. 5. Classes of Synthetic Self-assembly Peptides

In pursuing artificial biological materials, scientists have designed and synthesized various peptide sequences with self-assembly ability to generate functional nanomaterials. We would like to summarize the widely discussed literature in field.

I. 1. 5. 1. β-Hairpin Peptides

The basic characteristic of β-hairpin peptide is intramolecular folding propensity, and it is originated from the two proline residues, intramolecular hydrogen bond is formed to deliver a robust β-hairpin structure.

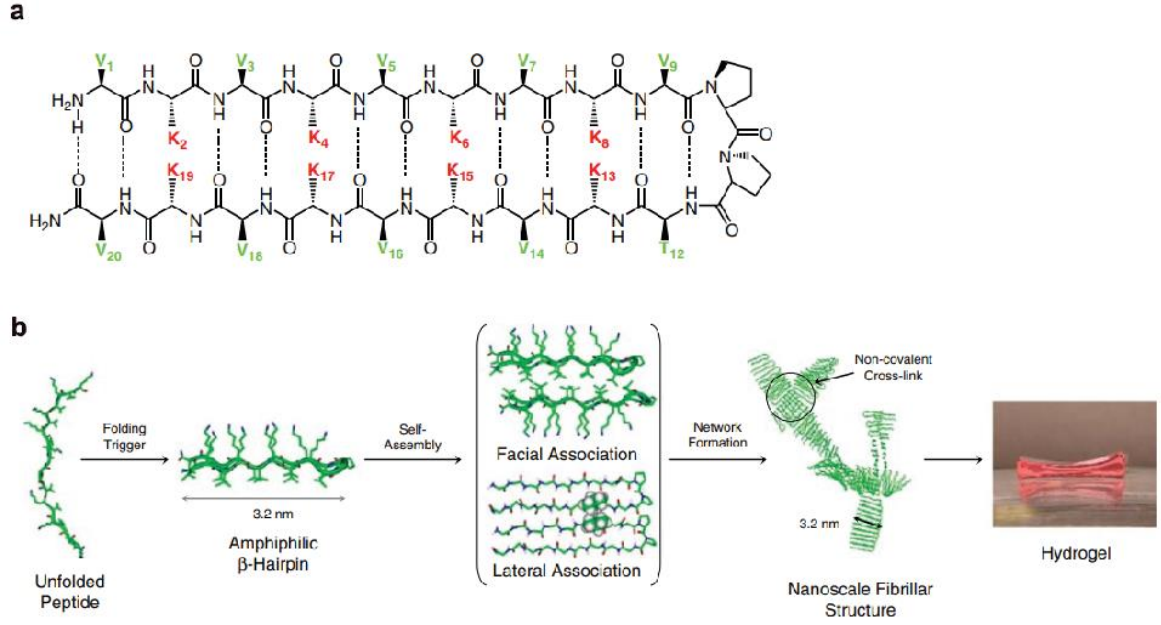

Figure 11. Chemical structure of MAX1 (a) and its proposed self-assembly mechanism (b).[33]

This kind of peptides is widely explored by Prof. Schneider's and Prof. Pochan's groups. They design such kind of peptides with a turn unit of tetra-peptide sequence (-V^{D}PPT-), the two neighbouring peptide sequences are consisted by alternating hydrophobic amino acid (V) and hydrophilic amino acid (K), such as MAX1 sequence which represents [(VK)$_4$-V^{D}PPT-(KV)$_4$] (Figure 11). Due to its rich in lysine, in acid condition, it will be protonated and disrupt intramolecular hydrogen bonding. Upon increasing pH or addition of counterions, self-assembly is triggered and form a rigid hydrogel.[34] To further modify the peptide sequence, a simply change of lysine at position 15 with glutamic acid – [(VK)$_4$V^{D}PPT-K(VE)(VK)$_2$V] will bring significant increase in gelation process in cell culture condition. It has been proved that the β-hairpin peptides can be used in cell encapsulation, enhance drug uptake to increase its efficiency.[33]

I. 1. 5. 2. Surfactant-like Peptides

In aqueous environment, surfactant is able to form aggregates such as spherical or cylindrical micelles, lipid bilayers. A bit dug into the molecule structure, surfactant is consisted by a hydrophobic tail and a hydrophilic head. Inspired by surfactant, Prof. Zhang's group at MIT has designed and synthesized a series of surfactant-like peptides. In these peptide sequence, hydrophilic head is made up by charged amino acids (D, K) and hydrophobic tail consists by six hydrophobic amino acids (G, A, V, I, L, and F). The hydrophilic residue makes it possible to dissolve in water, and the hydrophobic part endows self-assembly behaviour in aqueous environment.

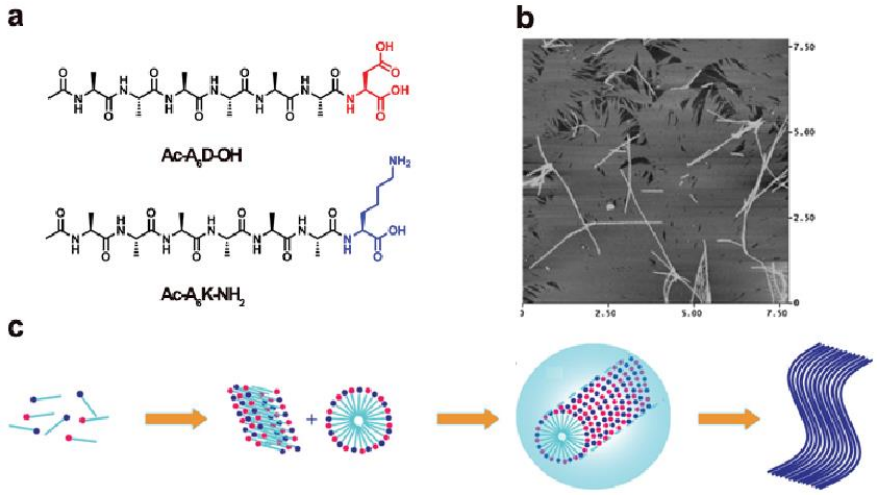

Figure 12. (a) Chemical structure of Ac-A$_6$D-OH and Ac-A$_6$K-NH$_2$; (b) AFM image of 1:1 ratio of Ac-A$_6$D-OH/Ac-A$_6$K-NH$_2$; (c) Proposed mechanism for the assembly process of nanorope structure.[35]

Examples of such peptide sequence are: Ac-A$_6$K-NH$_2$, Ac-A$_6$D-OH, DA$_6$-NH$_2$, KA$_6$-NH$_2$, Ac-A$_6$K-OH, Ac-V$_6$K$_2$-NH$_2$, Ac-I$_6$K$_2$-NH$_2$, Ac-A$_6$D$_2$-OH, and Ac-V$_6$R$_2$-NH$_2$.[35] Normally, this kind of peptide sequence is consisted by one or two charged amino acids and four or more consecutive hydrophobic amino acids. Their self-assembly behaviour is observed in water at neutral pH, and they form nanotubes or nanovesicles (Figure 12).

I. 1. 5. 3. Self-complementary peptides

Design of self-complementary peptides is inspired by the ionic peptide – $(RERERKRK)_2$ which is found in the Z-DNA binding protein zuotin. In Prof. Zhang's group at MIT, they design and synthesize a class of self-complementary ionic peptides, RAD16-I ($(RADA)_4$), EAK16-II ($(AE)_2(AK)_2(AE)_2(AK)_2$) and KLD-12 ($(LKLD)_3$). Representative example was shown in Figure 13. These synthetic peptides share the same design principle: in one basic unit, it contains a positive and a negative charged amino acid, and they are separated by a non-charged spacer. The synthetic peptides are found to self-assemble in aqueous environment to form β-sheet configuration, they can further form hydrogel *via* pH adjustment or salt addition.[36]

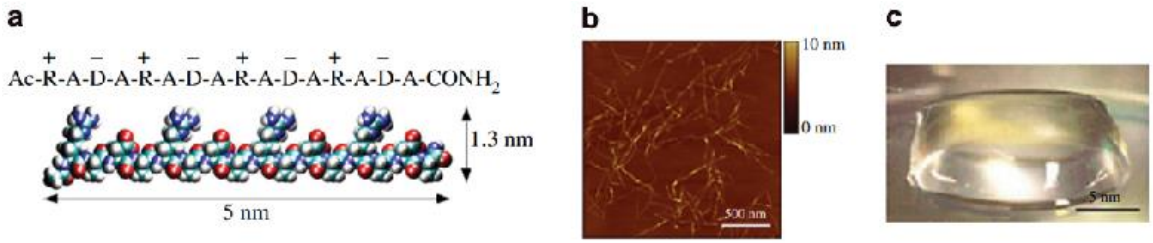

Figure 13. (a) Peptide sequence of RADA16-I; (b) AFM image of RADA16-I nanofiber scaffold; (c) Optical hydrogel image from RADA16-I.[37]

I. 1. 5. 4. Peptide Amphiphiles (PAs)

Design of this kind of peptide sequence is also inspired by surfactant. Compared to surfactant-like peptide, its hydrophobic tail is conjugated with alkyl chain which is found in lipid molecules. The introduction of lipid alkyl chain make PAs tend to self-assemble with hydrophilic head towards the periphery and hydrophobic tail in the core. Prof. Stupp's group contributes a lot of exploration to understand this kind of PAs. In the molecular level, they reveal that PAs can be divided into two or three segments. Hydrophobic part includes alkyl chain and hydrophobic amino acids, hydrophilic residues are charged amino acids. The hydrophobic sequence is designed to promote forming β-sheet and further self-assemble into cylindrical nanostructures. The hydrophilic head not only increases molecular solubility in aqueous environment, but also suppress their self-assembly behaviour due to charge repulsion. Upon interacting with the environment, charge repulsion can be relieved by counterions or pH adjustment, thus endowing PAs response to its environment to form cylindrical nanofibers. Incorporation of other functional peptide sequence can make the forming nanofibers be recognized by cell. For example, conjugation of RGD motif will help cells attach to these nanofibers (shown in Figure 14).[38]

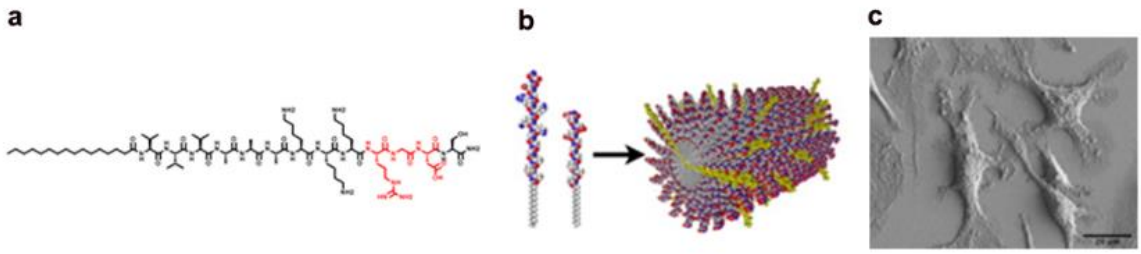

Figure 14. (a) Chemical structure of RGD peptide amphiphile (PA); (b) Model of binary PA fibers; (c) BMNCs cultured on the surfaces coated with 10% RGD PA.[38]

Take the advantage of CS protein from malaria parasite, Prof. Hest's group focus on structure modification on $GANPNA_2G$ sequence with different length of alkyl chains (C_n-$GANPNA_2G$; n=6, 10, 12, 14, 16, 18). In their molecular self-assembly study, they find that conjugating with short alkyl chains (≤12C), no aggregate formed; with longer tails (≥16C), the modified sequences self-assemble into stable nanostructure.[39]

In Prof. Hamley's group, they carry out a lot of original research work to understand the pentapeptide from procollagen I. Upon conjugating with hexadecyl lipid chain (C_{16}-KT_2KS), it self-assembles into extended nanotapes in aqueous environment,[40] and they successfully make it as a commercial PA.[41]

To further explore PAs in pharmaceutical development, Prof. Cui's group start to conjugate drug molecule (hydrophobic) with peptide sequence (hydrophilic). They have successfully modified VQIVYK sequence (originate from Tau protein) with camptothecin, and it self-assembles into filamentous nanostructures. These nanostructures can work as a carrier to transport quantitative drug.[42]

I. 1. 5. 5. Aromatic Peptide Derivatives

Consisted by two phenylalanine amino acids, FF has been proved as the shortest peptide sequence that could self-assemble into robust nanofibrous structure. The representative self-assembly of this kind of peptide (FmocFF) was shown in Figure 15. Various sequence modifications have been carried out to study its self-assembly, either by conjugating with bulky aromatic groups (fluorenylmethoxycarbonyl (Fmoc), naphthalene (Nap), etc.) or enzyme responsive motif (Tyr-(PO_3H_2)-OH). Prof. Gazit and Prof. Ulijn's group have done a lot of fundamental research work on Fmoc-peptides. For example, by varying amino acids on the dipeptide (Fmoc-FF-OH, Fmoc-FG-OH, Fmoc-GF-OH, Fmoc-LG-OH, Fmoc-GG-OH, Fmoc-AA-OH, Fmoc-AG-OH), Prof Ulijn's group successfully illustrates necessary residues for molecular self-assembly on the simple dipeptide.[43] Prof Xu's group have explored a lot on understanding Nap-peptide (enzyme responsive). In their research, they have successfully designed and synthesized alkaline phosphatase responsive peptide sequence.[44] And they have also successfully developed imaging agents either for intracellular observation[45] or membrane dynamic imaging.[46] In anticancer research, they have developed molecular self-assembly either on the membrane[23] or inside[47] the cell to trigger cancer cell apoptosis.

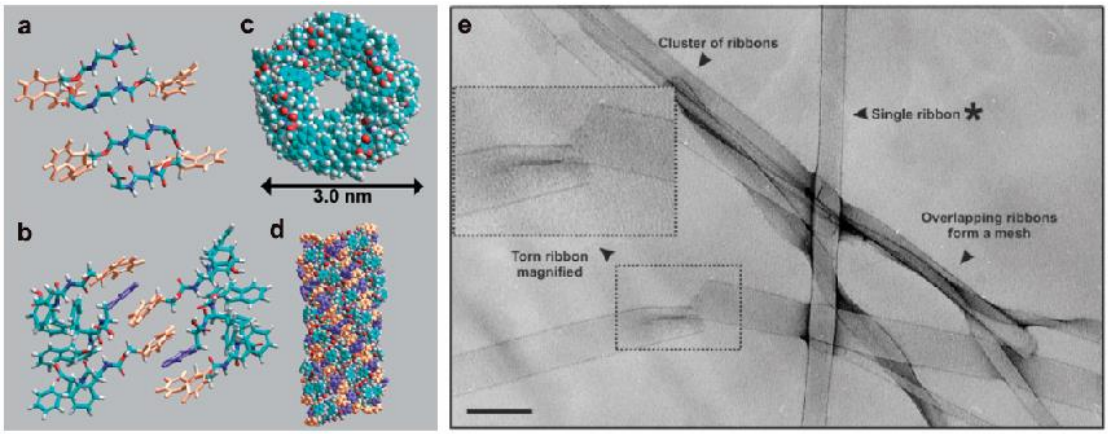

Figure 15. A model structure of Fmoc-FF arranged in an anti-parallel b-sheet pattern (a), interlocking of Fmoc groups from alternate b-sheets to create p-stacked pairs with interleaved phenyl rings (b), top view (c) of the creating cylindrical structure and its side view (d), TEM image of Fmoc-FF (e).[48]

I. 1. 5. 6. Multi-Domain Peptides

Prof Hartgerink's group have developed a new design of peptide sequence, term as ABA block motif. B is consisted by alternating hydrophilic and hydrophobic amino acids, A is charged amino acids (E, K). For example, $K_2(QL)_6K_2$, $K_2(SL)_6K_2$, $E(QL)_6E$, $E(SL)_6E$ are representatives of such peptide sequences. They have been proved that the introduction of alternating hydrophilic (Q, S) and hydrophobic (L) amino acids facilitate self-assembling into nanofibers in aqueous environment (Figure 16).[49]

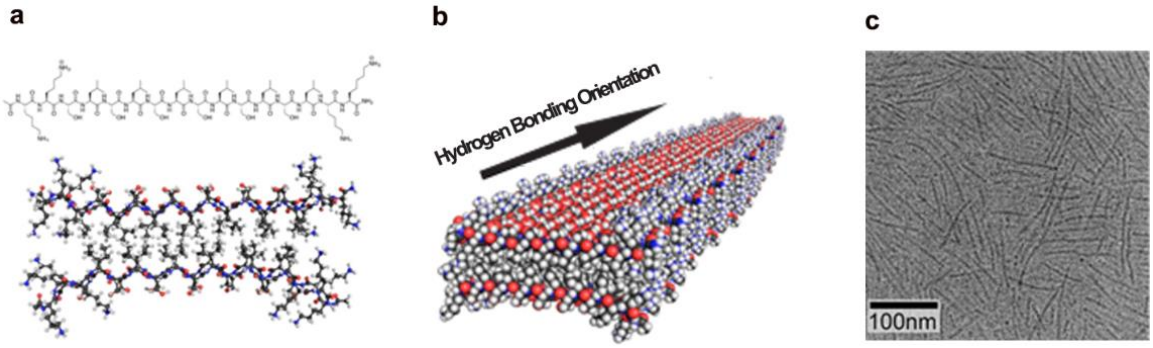

Figure 16. (a) Chemical structure of $K_2(SL)_6K_2$ (up), and repeating unit of the self-assembly motif (bottom); (b) Model of the self-assembly nanofiber; (c) Cryo-TEM image of the self-assembled $K_2(QL)_6K_2$.[49]

I. 1. 6. Applications of Self-Assembly Peptides

I. 1. 6. 1. 3D Cell Culture

Traditionally, cell culture is carried out on 2D plastic dishes, and we cannot monitor cell growth in a 3D environment, which is the normal growth condition for cells in biological system. Observation on cell-cell or cell-extracellular matrix interaction from 3D cell culture

model would be more likely to reveal the real cell behaviour in biological system. To recreate a 3D biomimetic cell culture model, we should pay attention to cell adhesion sites, matrix viscoelasticity, cell mobility and cell encapsulation ability of the 3D culture material. Self-assembly peptides are composed by biocompatible amino acids, cells could be able to keep in a healthy condition when growing in these biomaterials. The development in 3D peptide hydrogel makes it possible to culture cells in a 3D model. Zhan and co-workers have developed a 3D hybrid peptide hydrogel matrix for HeLa cell and human mesenchymal stem cells culture. In their molecular design, they have included cellular binding peptide sequence (RGDS), thus promoting cellular attachment and encapsulation ability (Figure 17).[50] Hainline and co-workers describe a novel self-assembly peptide (bQ13) for 3D culture of prostate cancer spheroids. bQ13 self-assembles into nanofibers and shows significant cytocompatibility. In the meantime, the mechanical property of the hydrogel can be carefully tuned by adjustment of the bQ13 concentration.[51]

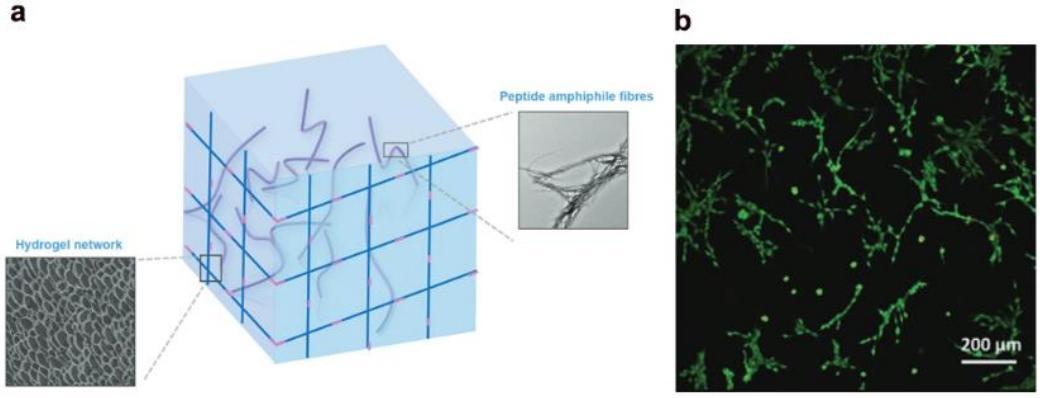

Figure 17. (a) Schematic representation of peptide amphiphile fibers encapsulated in a polymer hydrogel matrix; (b) HeLa cells incubated in PEG-based hydrogel.[50]

I. 1. 6. 2. Antimicrobial Investigation

Antimicrobial resistance is becoming one of the most serious threats worldwide, developing novel and nonconventional antimicrobial agents is in great demand. Synthetic cationic short peptides are one of the promising agents to treat microbes. Their positive charged feature helps them easily to interact with microbe and disrupting bacterial membranes, exerting antimicrobial activity. To reach effective bacterial membrane interaction, a combination with hydrophobic tail would enhance antimicrobial activity of cationic short peptides. Generally, the cationic peptide sequence is consisted by lysine (K) and arginine (R), and the hydrophobic moiety is a combination of hydrophobic amino acids (A, V, I, L, F, W and F). The peptide sequence chain length ranges from 6 to 15 amino acids, and hydrophobic amino acids is greater than the positive charged amino acids. Lam and co-workers report an effective peptide polymer towards multidrug-resistant Gram-negative bacteria. In their molecular design, lysine and valine are chosen as cationic and hydrophobic amino acids. The obtained polymer exhibits strong Gram-negative bacteria at sub-μM, and with low toxicity towards red blood cells (Figure 18).[52] In Prof. Demizu's group, they carry out peptide sequence modification based on a well-known antimicrobial peptide (Magainin 2) originating from skin of frogs. In their optimized peptide 11, which has more cationic lysine amino acids in the sequence, it self-assembles into helical structure in solution and exhibits antimicrobial activities against both Gram-positive and Gram-negative bacteria.[53]

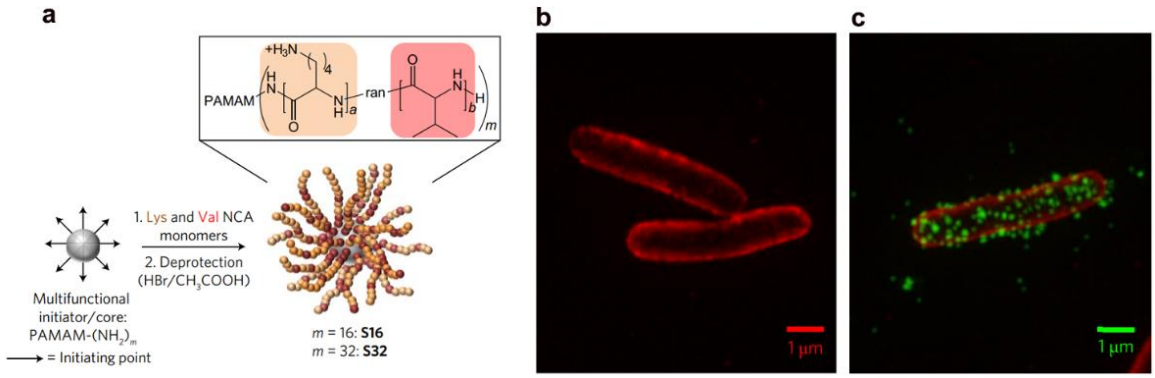

Figure 18. (a) Synthesis of target compound; E. coli before treatment (b) and after treatment (c), green represents tag-S16.[52]

I. 1. 6. 3. Anticancer research

Cancer is a major threat to the public health worldwide. Genomic instability causes the main challenge in chemotherapy drug resistance. Developing new strategy base on peptide self-assembly has been promising in anticancer research. Prof. Xu's group has explored a lot on enzyme responsive molecular self-assembly. Alkaline phosphatase (ALP) triggering peptide self-assembly is the representative example. ALP is highly express in cancer cells, such as HeLa cell. Molecular design base on ALP can reach cancer cell selectively targeting self-assembly. Kuang and co-workers design and synthesize NapFFYp sequence, it selectively self-assembles on the membrane of cancer cells, blocking mass exchange and disrupting cell communication, leading to anticancer cell growth.[23] Considering esterase is highly expressed in cancer cells, Yang et. al. design an esterase responsive peptide sequence. Upon esterase catalysis, the resulting peptide sequence will self-assemble into nanofibers inside cancer cells, leading to cancer cell death.[24] Prof. Maruyama's group designed a matrix metalloproteinase-7 responsive precursor, it specifically self-assembly in cancer cells upon enzyme cleavage and leading to cancer cell death (shown in Figure 19).[47]

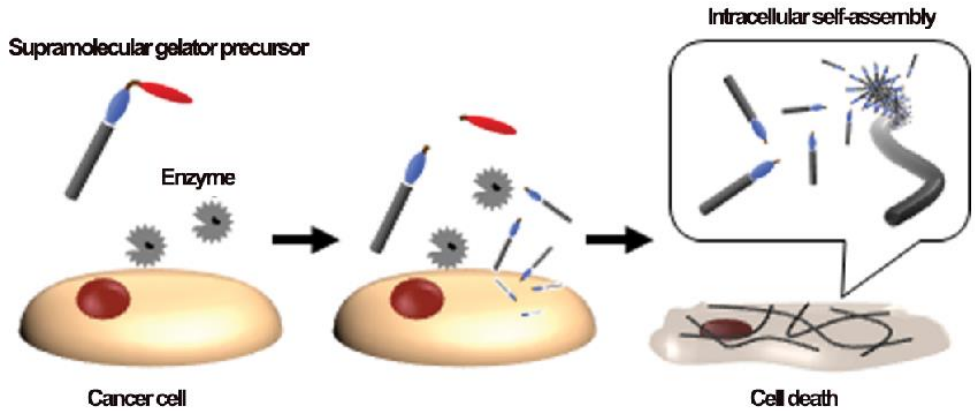

Figure 19. Schematic showing of intracellar self-assembly leading to cancer cell death.[47]

I. 1. 6. 4. Nanofabrication and Biomineralization

By conjugation of functional groups on the self-assembly peptide sequence, after obtaining robust nanostructures, guided nucleation or biomineralization can be achieved through interacting with the functional groups on the nanostructure. Sahoo and co-workers develop a pathway-dependent gold nanoparticle by tuning nanofiber formation process. In their study, they introduce an ALP responsive motif – phosphorylated tyrosine into the self-assembly peptide sequence. Upon ALP catalysis, nanofiber forms, in the meantime, phenol is recovered and thus guiding reductive synthesis of gold nanoparticles (shown in Figure 20).[54] Inspired by biomineralization in nature, Hartgerink and co-workers introduce phosphorylated serine to self-assembly peptide amphiphiles. After molecular self-assemble into nanofibers, direct mineralization of hydroxyapatite are guiding to form along the nanofiber axes.[13]

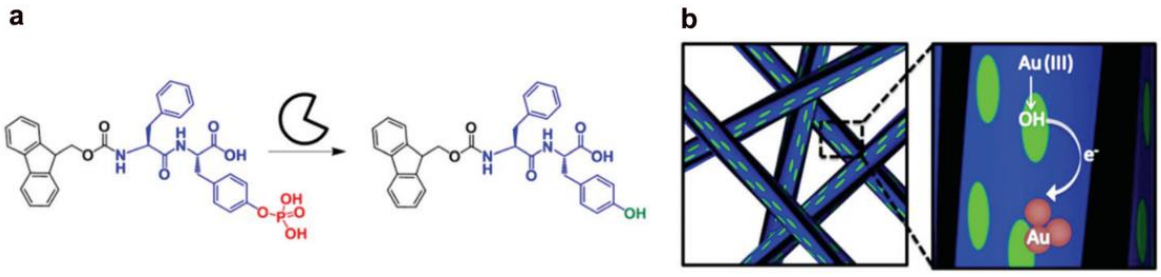

Figure 20. (a) Biocatalytic hydrolysis to form self-assembling motif; (b) Reduction of Au(III) to gold nanoparticle Au(0).[54]

I. 1. 6. 5. Therapeutic Agents Delivery

Self-assembly nanomaterials are promising candidates for therapeutic agent delivery due to their excellent trans-membrane capability either through active or passive cellular uptake pathway. By interacting with nanomaterials, no matter through electrostatic or hydrophobic interaction, therapeutic agents can be encapsulated in nanomaterials, and enhance cellular uptake by these nanomaterials. Gene therapeutic agents such as DNA or RNA, they are well-known for negative charged nature, combining with cationic peptide sequence is a promising way to enhance delivery efficiency of gene therapeutic agents. Mazza and co-workers make use of electrostatic interaction and design a peptide sequence with three positively charged amino acids (KRK) to endow cationic nature of the sequence. They have successfully proved the designed peptide self-assembling into nanofibers and significantly enhance delivery of siRNA (shown in Figure 21).[55] Luginbuhl and co-workers design a biohybrid molecule by combination of lipid and polypeptide. They use elastin-like polypeptide (ELP), it serves as a hydrophilic head. The hybrid material forms micelles in aqueous environment, with the lipid tail in the core. They prove the lipid core can successfully encapsulate hydrophobic drugs such as doxorubicin and paclitaxel, enhancing their efficacy.[56]

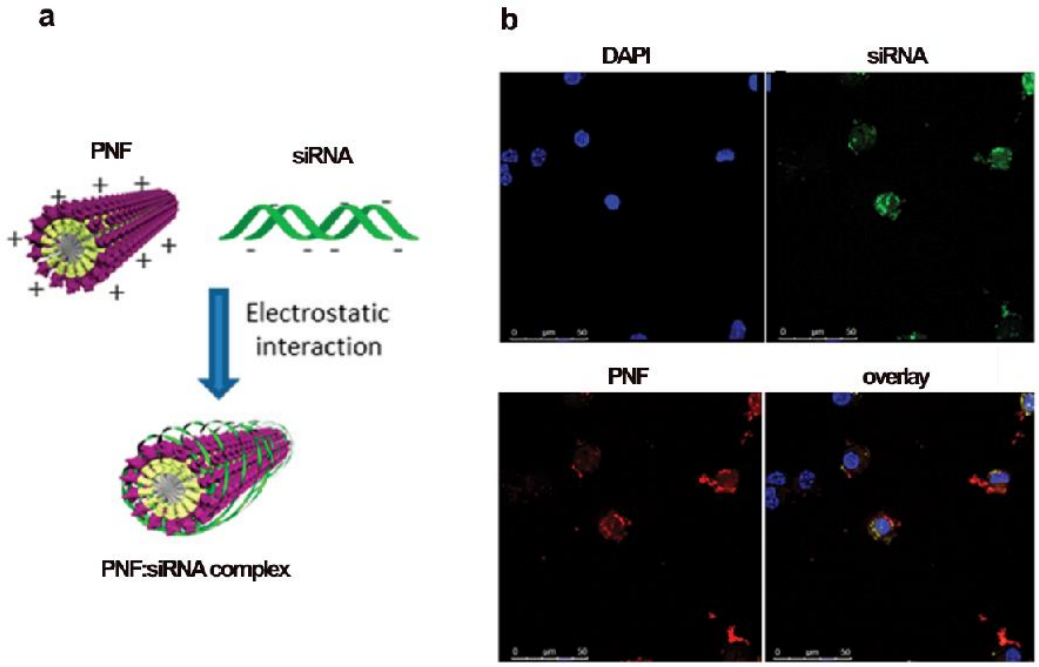

Figure 21. (a) Schematic representation of the PNF:siRNA complex formation; (b) Cellular internalization of PNF:siRNA complex.[55]

I. 1. 6. 6. Skin Care and Cosmetics

Surfactants such as sodium dodecyl sulfate and sodium myreth sulfate are widely used in daily care products, for example, shampoos and cosmetics. They work as cleaning and foaming agents. Surfactant-like peptides can not only serve as surfactant, but also exhibit more functions such as anti-wrinkle, anti-microbial when applying in skin care products. Compared to conventional surfactants, surfactant-like peptides would be more effective in cosmetics application. One of the well explored peptide sequences in cosmetics is GHK (glycyl-histidyl-lysine), it originates from human plasma and declines with age. GHK is proposed chelating with copper, which accelerates wound healing and skin repair. In cosmetics, GHK has been found effective in tighten loose skin and enhance elasticity, skin density, and firmness.[57] Collagen type I derived peptide KTTKS has been proved stimulating synthesis of collagen, elastin and glucosaminoglycans. Conjugating with C_{16} acyl chain, it will enhance oil solubility and skin penetration, making KTTKS as an effective cosmetic against wrinkles.[58]

MAIN OBJECTIVES

The main objective of this thesis is to study molecular self-assembly and co-assembly based on small peptidic molecules and explore their bio-related applications through precisely delivering molecular assemblies into subcellular organelles.

Towards this end, the well-established building block naphthalene-phenylalanine-phenylalanine is selected for molecular engineering owing to its strong π-π interaction and hydrogen bonding oriented self-assembly. By conjugating with light- or enzyme-responsive motifs, the peptidic molecules can reach controllable self-assembly upon external stimuli. Novel nanostructures in higher order can be reached either by multi-component co-assembly, or stage-by-stage assembly triggering by multiple external stimuli. Delivery of molecular assemblies into specific subcellular organelle can be guided by overexpress enzyme on the organelle.

In the first part of this thesis (Chapter III), we focused on study single component self-assembly behaviour. Inspired by the mechanoresponsive orientation of actin filaments in cytoplasm, we developed an artificial mechanoresponsive system based on synthetic negatively charged peptidic molecule. The obtained molecule self-assembling into randomly orientated nanofibrils; guided by external force in one direction, highly ordered uniaxial aligned nanofibers can be achieved; through evaporation casting, the self-assembling nanofibrils transform into scalable lamellar domains.

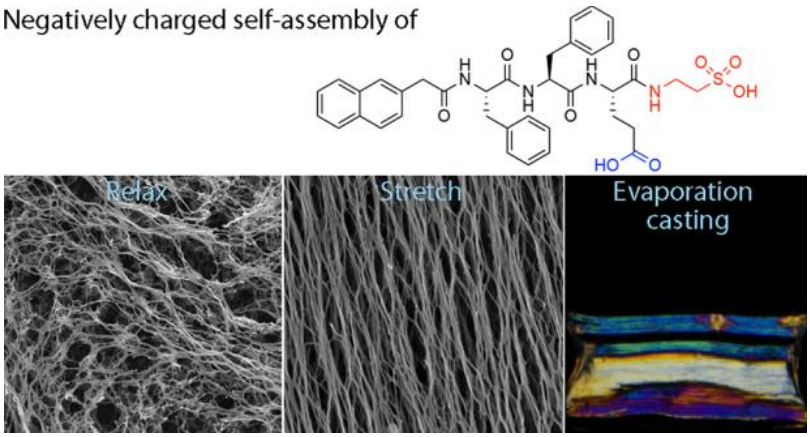

In the second part of this thesis (Chapter IV), we focused on multicomponent assembly based on co-assembly and self-sorting to generate novel nanostructures triggering by UV light or enzyme. Conjugating with photo-cleavable motif, we are able to generate metastable nanostructures through UV radiation on pre-stabilized self-assembled nanostructures and successfully obtained exotic nanostructures that are away from thermodynamic minima through molecular co-assembly process.

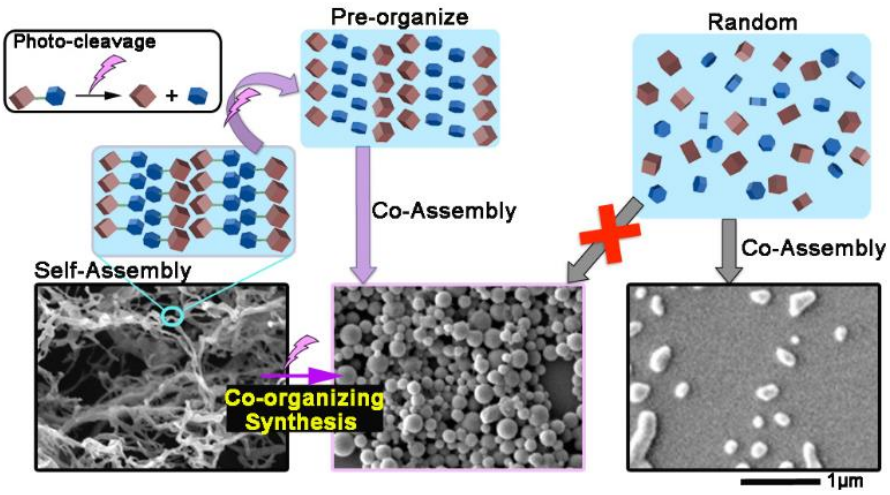

To mimic the dynamic and reciprocal interactions of fibrous scaffold in extracellular matrix on cell behaviours, we chose two self-sorting coumarin-based gelators endowed with enzyme and light responsive properties. Upon triggering by enzyme, the growth of one gelator will regulate growth of the other gelator through surface interaction on the nanostructures. And this behaviour can be further controlled by UV light. Through combination of enzyme and light, we can achieve spatial-temporal growth of the scaffold, and this dynamic behaviour will affect the growth of the other component.

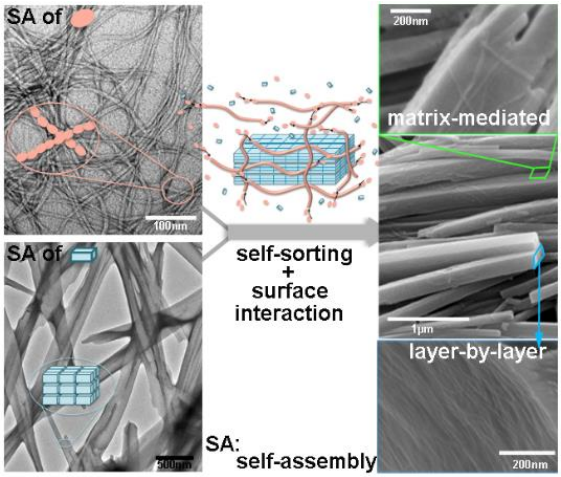

To regulate higher order nanostructure in a biological way, we select two synthetic molecules responsive to alkaline phosphatase and carboxyl esterase, respectively. The enzyme catalysed kinetics of these two molecules are dramatically different. Treated in a specific stage-by-stage order, we are able to reach a physically knotted nanofibrous scaffold that is potentially applicable in cell culture.

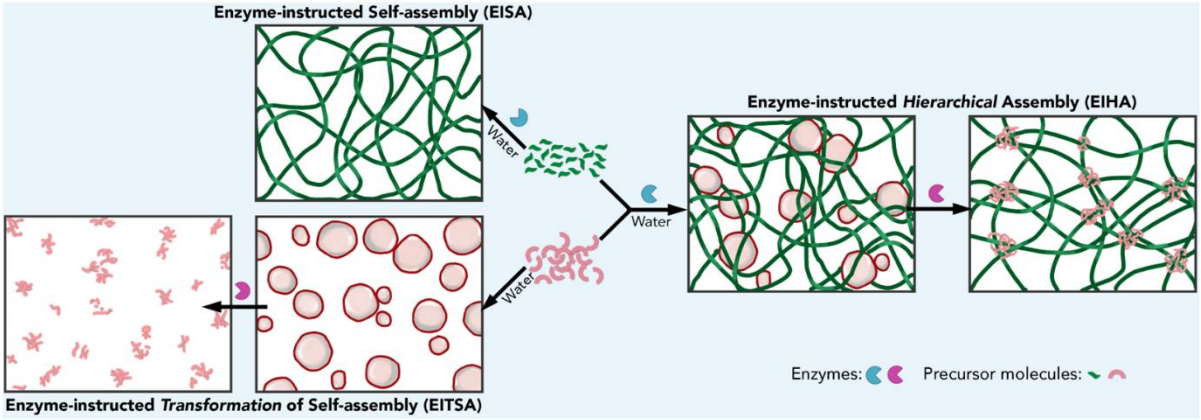

In the third part of this thesis (Chapter V), we focused on delivering molecular assemblies into subcellular organelle and investigating their bio-related application. Take the advantages of overexpressing enzyme in cancer cells, we designed and synthesized enzyme-responsive molecules. Mediated by carboxyl esterase, we are able to deliver a N-hydroxylethyl peptide assembly to endoplasmic reticulum (ER). The assemblies upregulated ER stress in cancer cells, and triggered ER-specific apoptosis, thus leading to cancer cell death.

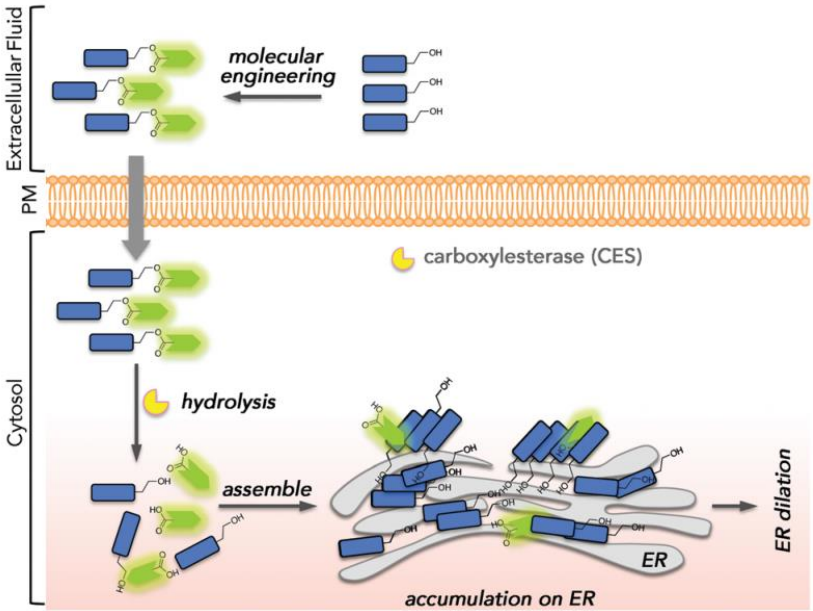

To reach dual-subcellular-targeting, we conjugated ER-targeted coumarin-functionalized peptides with DNA alkylating agent through ester bond. After being uptaken and intracellular hydrolysis, the coumarin-functionalized peptide self-assembled on ER to induce ER stress and the alkylating agent worked towards nucleus. Upon action on both subcellular organelles, cancer cells are effectively inhibited.

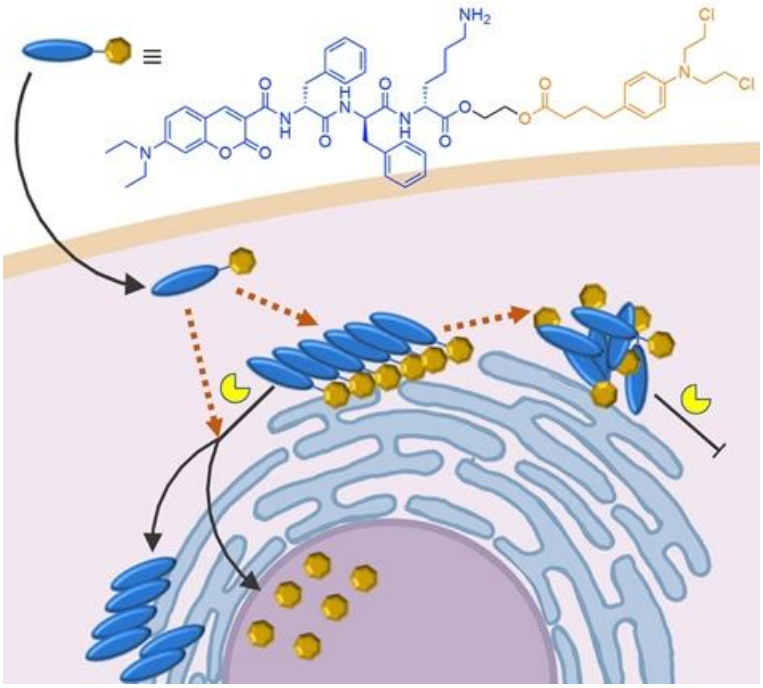
NH2
Cl
Cl
N
N
H
O

III. 1. Mechano-responsive alignment of molecular self-assembled negative charged peptide nanofilaments

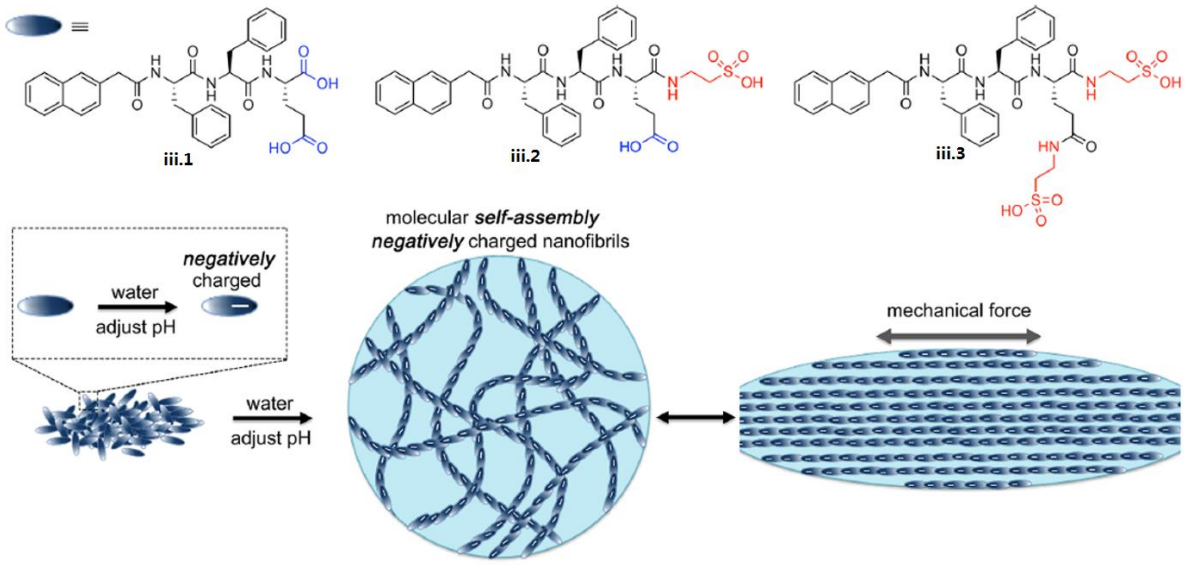

This chapter corresponding to the following publication:

Shijin Zhang[+], William Cortes[+], Toshio Sasaki, Shunsuke Asahina, Asano Natsuko, Qizheng Zhang, and Ye Zhang.* "Mechanoresponsive Alignment of Molecular Self-assembled Negatively Charged Nanofibrils" *ACS Applied Bio Materials*. **2020**, 3, 1698-1704 (+*These authors contribute equally to this work*).

III.1. 1. Introduction

In biological system, the long and moderately flexible actin filaments originate from the self-assembly of G-actin protein monomers.[1] Upon suitable external force stimulation to the cell, actin filaments will collectively self-organize in both position and orientation within the cytoplasm, determining the cellular shape and its motility. Creating a biomimetic material adopting mechano-responsive active filament property in a synthetic chemistry way is one of the ultimate goals in new material development. Mechanical force responsive polymer-based filamentary network at both micro- and nano-fibril alignment has been successfully in fabricating functional materials.[2] But in supramolecular research, few researches on constructing macroscopic self-assembly filaments through mechanical force have been reported.[3] The driving force for the alignment of polymer-based filaments is the interfilament interactions, while the molecular self-assembly filaments depends both interfilament and intermolecular interactions. The diverse driving force for the self-assembly filament make it possible reach various morphologies for different functions,[4] but it also limits long-range order over scales to these uses.[5] Therefore, in the mechanical force responsive self-assembly system, hierarchical regulation is critical in controlling the macroscopic filament alignment.[3a,6] Considering the biomimetic capabilities for small molecular self-assembly,[7] we come with a new design on artificial system that is hierarchically controllable by mechanical force for higher order alignment fabrication. In the molecular design, we chose naphthalene-phenylalanine-phenylalanine (NapFF) as the basic building block for molecular self-assembly through π-π interaction and hydrogen bonding.[8] Inspired by the negative charge of actin filament that guiding the long-range ordering through electrostatic interaction,[9] we introduced the building block with protonatable functional groups – glutamic acid or taurine – to adopt electrostatic interaction. C-terminal of NapFF is modified with glutamic acid to obtain molecule iii.1, it contains two protonatable carboxylic groups (α-COOH and φ-COOH). Molecule iii.2 is achieved by modifying the α-COOH of molecule iii.1 with taurine; molecule iii.3 is the conjugation of both carboxylic group in molecule iii.1 with taurine (Figure 1, top).

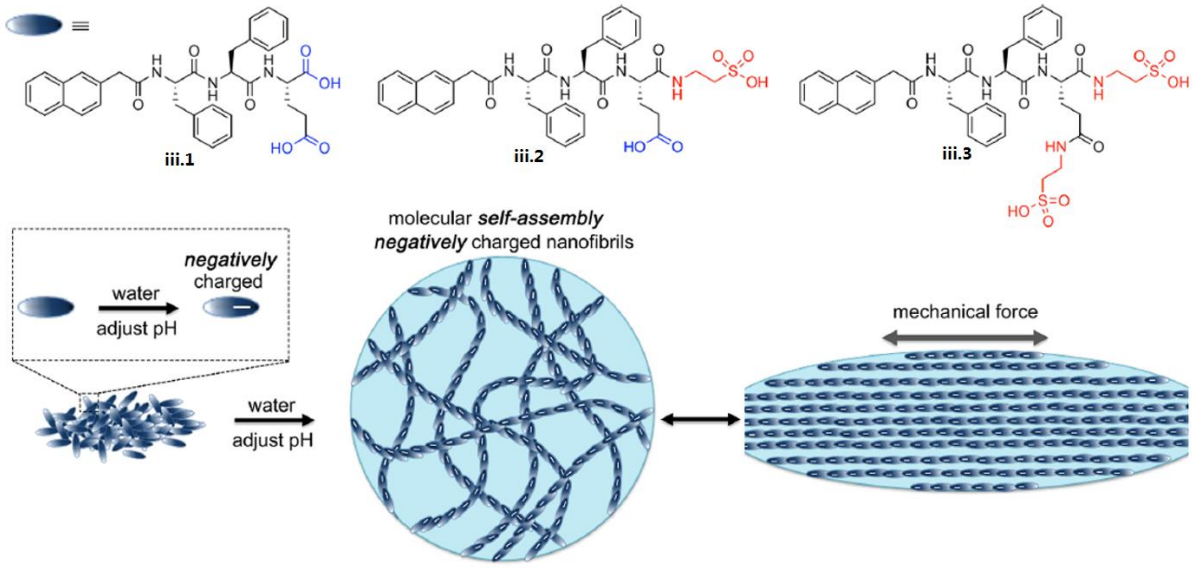

Figure 1. Chemical structures of molecule iii.1, iii.2, and iii.3 for self-assembling filaments (top), schematic illustration of mechano-responsive alignment of self-assembled nanofibrils (bottom).

All the designed molecules bare anisotropic electron distribution. Deprotonated of all the molecules is achieved by adjusting the pH value of the solution, further intermolecular electrostatic interaction regulation can be approached by carefully controlling the pH value of the system. Combination of π-π interaction, hydrogen bonding, and electrostatic interaction, and all these molecular interaction forces guide molecular self-assembly behaviour of the three designed molecules. Upon external mechanical force stimulation, the negatived charge self-assembly nanofibers will adopt uniaxial orientation to reach highly-order domains (Figure 1, bottom).

III. 1. 2. Experiment Section

III. 1. 2. 1. Materials

Chemical reagents	Grade	Manufacturer
Fmoc-Amino acid	98.0%	GL Biochem (Shanghai, China)
2-(1*H*-benzotriazol-1-yl)-1,1,3,3-tetramethyluronium hexafluorophosphate (HBTU)	98.5%	Matrix Scientific
Trifluoroacetic acid (TFA)	98.0%	Nacalai Tesque
2,2,2-Trifluoroethanol (TFE)	99.0%	Nacalai Tesque
Dimethylformamide (DMF)	99.5%	Nacalai Tesque
Dichloromethane (DCM)	99.5%	Nacalai Tesque
Piperidine	99.0%	Nacalai Tesque
Hexane	95.0%	Nacalai Tesque
Taurine	98.5%	Nacalai Tesque
Methanol (MeOH)	99.0%	Nacalai Tesque
Acetonitrile	HPLC grade	Nacalai Tesque
N, N-Diisopropylethylamine (DIEA)	98.0%	Nacalai Tesque
N, N'-Diisopropylcarbodiimide (DIC)	99.0%	FUJIFILM Wako
N-Hydroxysuccinimide (NHS)	98.0%	Tokyo Chemistry Industry

All organic solvents were dehydrated before experiment by a solvent purification system.

III. 1. 2. 2. Instruments

Agilent 1260 Infinity Preparation HPLC (Column: 19 mm×150 mm XBridge® Peptide BEH C18 column), Thermo LTQ-ETD mass spectrometer (ESI-MS), NMR equipment: Bruker Advance 400 MHz spectrometer, Thermo Nanodrop 2000C spectrophotometer, Transmission Electron Microscope (JEM-1230R), Milli-Q® Integral 3/5/10/15 System, Scanning Electron Microscope (FEI Quanta 250 FEG), Polarized Optical Microscope (SMZ18, Nikon).

III. 1. 2. 3. Synthesis

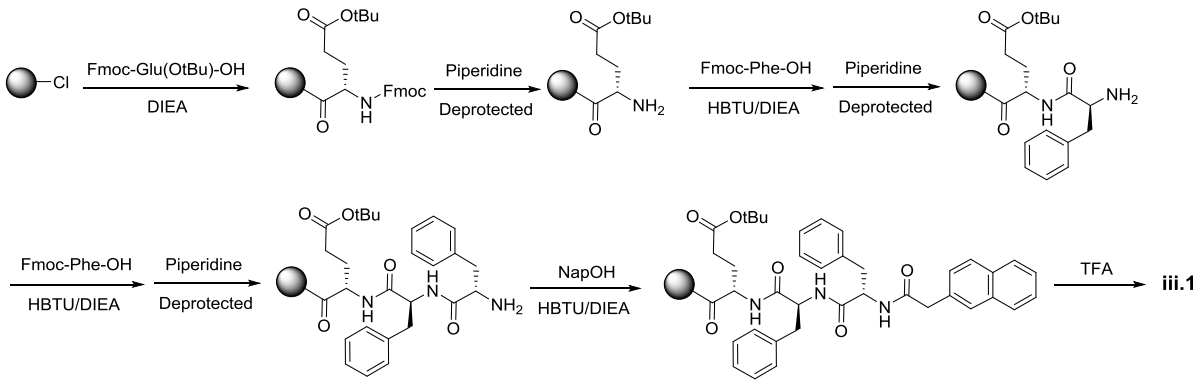

Scheme 1. Synthesis of compound iii.1.

Preparation of **compound iii.1**: Compound iii.1 were prepared from solid phase peptide synthesis (SPPS) using 2-chlorotrityl chloride resin. 2-Chlorotrityl chloride resin (2.0 g, 2 mmol) was swelled in anhydrous DCM for 20 min, Fmoc-Glu(OtBu)-OH (2.13 g, 5 mmol) dissolved in anhydrous DMF was conjugated to resin in the presence of DIEA (1.29 g, 10 mmol) for 30 min. Then washed the resin with dehydrated DMF for 3 times, unreacted sites in the resin were blocked with DCM/MeOH/DIEA (80:15:5) for 20 min and washed the resin by dehydrated DMF for 5 times. Then 20% piperidine solution (in DMF) was added to react for 30 min to remove the protecting group in the amino acid. We carried out the peptide elongation according to standard SPPS protocol to get the desired compound[10]. Compound iii.1 was cleaved off the resin by TFA in 2 h. The yield is 82.1%.

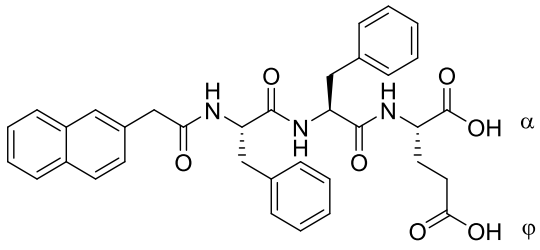

iii.1

Compound iii.1: ^{1}H NMR (400 MHz, DMSO-*d6*) δ = 8.28 (ddd, *J*=34.8, 17.2, 5.7, 3H), 7.78 (ddd, *J*=18.2, 12.0, 5.3, 4H), 7.59 (d, *J*=4.9, 1H), 7.51 – 7.44 (m, 2H), 7.28 – 7.06 (m, 10H), 4.65 – 4.49 (m, 2H), 4.31 – 4.16 (m, 1H), 3.12 – 2.92 (m, 2H), 2.87 – 2.62 (m, 2H), 2.29 (dd, *J*=9.3, 6.2, 2H), 2.11 – 1.94 (m, 2H), 1.80 (dd, *J*=13.9, 8.7, 2H) ppm.

^{13}C NMR (101 MHz, DMSO-*d6*) δ = 174.21, 173.53, 172.27, 171.97, 170.31, 156.25, 144.17, 141.12, 138.63, 138.26, 138.03, 134.42, 133.37, 132.17, 129.70, 128.55, 128.50, 128.08, 127.89, 127.81, 127.69, 127.52, 126.72, 126.43, 125.81, 120.53, 66.09, 54.12, 51.69, 47.01, 42.68, 37.85, 30.45, 26.87 ppm.

MS: calculated for $C_{35}H_{35}N_3O_7$ is 609.25, found 610.18, $[M + H]^+$.

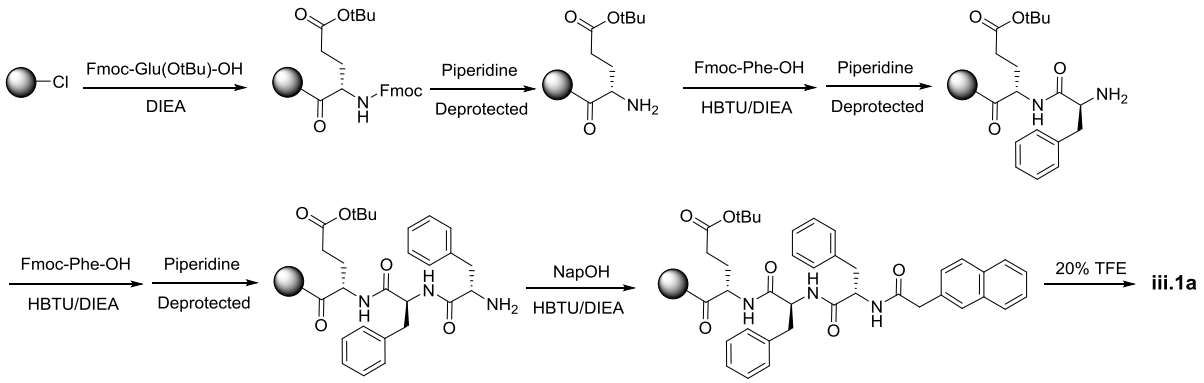

Scheme 2. Synthesis of compound iii.1a.

Preparation of compound iii.1a: The synthesis process is the same as compound iii.1, only cleavage solvent was changed to 20% TFE (in DCM). The yield is 78.3%.

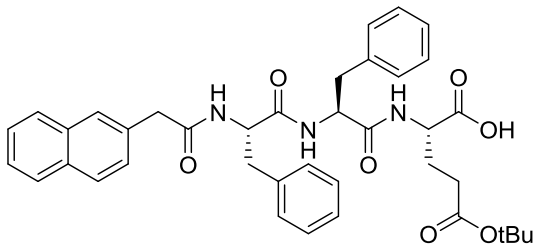

iii.1a

Compound **iii.1a**: ^{1}H NMR (400 MHz, DMSO-*d6*) δ = 8.28 – 8.15 (m, 3H), 7.80 (ddd, *J*=21.5, 11.7, 7.8, 4H), 7.59 (s, 1H), 7.46 (ddd, *J*=7.2, 5.2, 1.6, 2H), 7.27 – 7.11 (m, 10H), 4.62 – 4.48 (m, 2H), 4.29 – 4.23 (m, 1H), 3.53 (dd, *J*=39.7, 14.1, 2H), 3.00 (ddd, *J*=29.4, 14.0, 4.3, 2H), 2.84 – 2.67 (m, 2H), 2.33 – 2.19 (m, 2H), 2.09 – 1.90 (m, 2H), 1.87 – 1.68 (m, 2H), 1.38 (s, 9H) ppm.

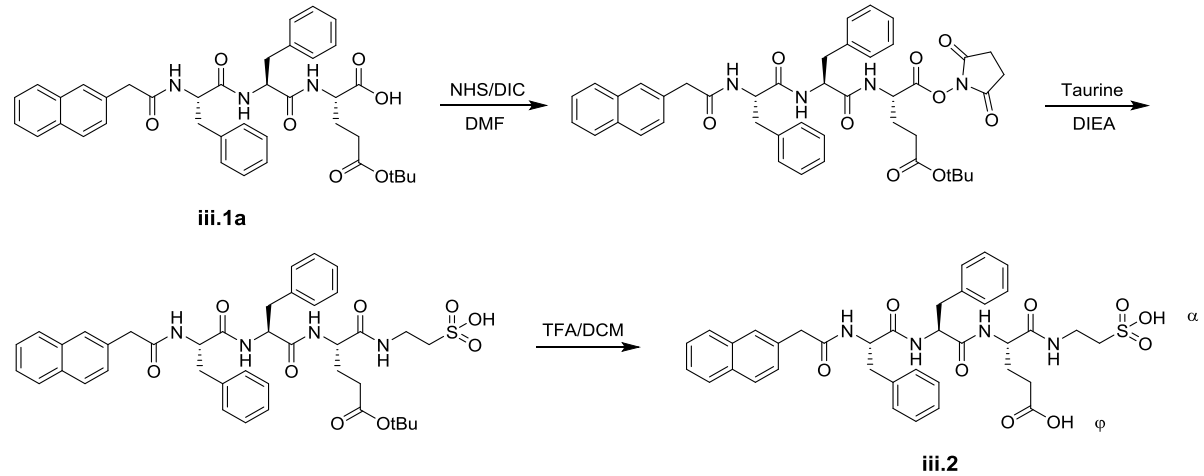

Scheme 3. Synthesis of compound iii.2.

Compound **iii.2**: 0.15 mmol (100.0 mg) of compound iii.1a was dissolved in 5 ml of DMF, cooling down to 0 ºC, 0.23 mmol (25.8 mg) of NHS and 0.20 mmol (24.6 mg) of DIC were added into the solution, the mixture was stirred for 8 h. Filtered and added 0.23 mmol (28.8

mg) of taurine and 0.30 mmol (38.8 mg) of DIEA into the filtrate, after stirring at room temperature overnight, the solvent was removed in reduced pressure rotary evaporator.[11] 10 mL of 20% TFA in DCM was added into the flask, stirring at room temperature for 4 h to remove the protecting group. Further purified by preparation HPLC, the yield was 70.2%.

^{1}H NMR (400 MHz, DMSO-*d6*) δ = 8.48 – 8.17 (m, 3H), 7.92 (t, J=9.5, 2H), 7.82 (dd, J=16.0, 8.5, 2H), 7.66 (d, J=16.1, 1H), 7.56 – 7.48 (m, 2H), 7.35 – 7.15 (m, 10H), 4.63 – 4.50 (m, 2H), 4.25 (td, J=8.4, 5.4, 1H), 3.54 (d, J=14.0, 1H), 3.46 – 3.33 (m, 2H), 3.17 (dd, J=14.0, 4.5, 1H), 3.09 – 2.70 (m, 4H), 2.68 – 2.57 (m, 2H), 2.40 – 2.10(m, 2H), 2.05 – 1.70 (m, 2H) ppm.

^{13}C NMR (101 MHz, DMSO-*d6*) δ = 174.28, 173.15, 171.94, 170.78, 170.23, 138.26, 137.97, 134.38, 133.37, 132.16, 129.71, 129.67, 128.54, 128.37, 128.16, 127.88, 127.83, 126.59, 126.38, 125.86, 54.64, 54.06, 52.67, 50.89, 42.63, 36.05, 30.42, 27.11 ppm.

MS: calculated for $C_{37}H_{40}N_4O_9S$ is 716.25, found 717.18, $[M + H]^+$.

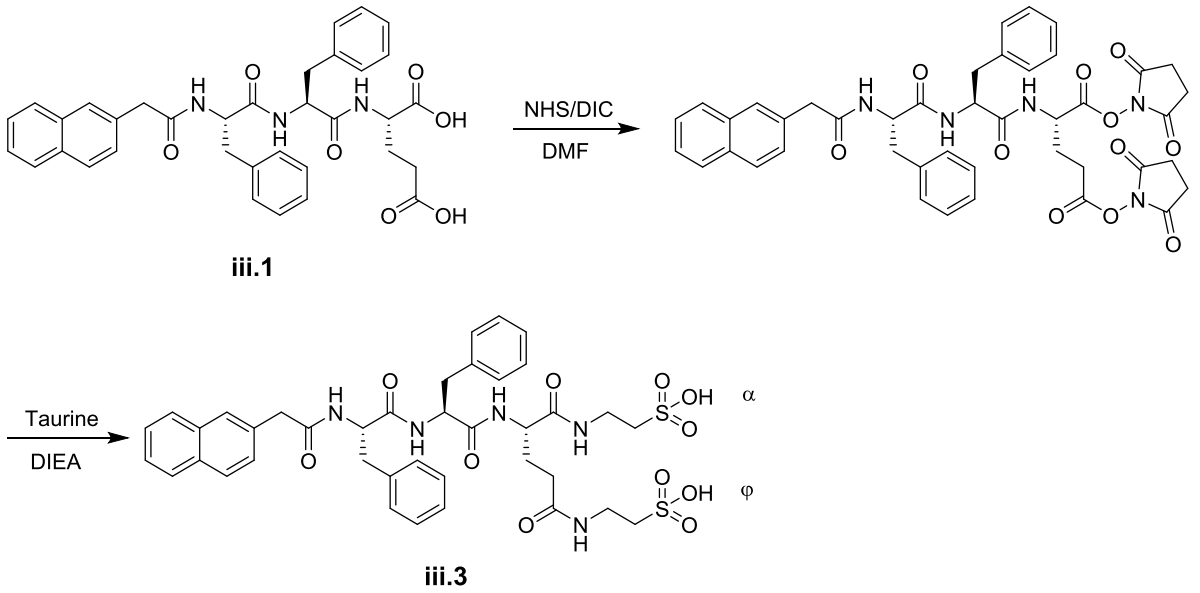

Scheme 4. Synthesis of compound iii.3.

Compound **iii.3**: 0.16 mmol (100.0 mg) of compound iii.1 was dissolved in 5 ml of DMF, cooling down to 0 ºC, 0.48 mmol (55.2 mg) of NHS and 0.42 mmol (53.0 mg) of DIC were added into the solution, the mixture was stirred for 8 h. Filter and add 0.48 mmol (60.0 mg) of taurine and 0.96 mmol (124.1 mg) of DIEA into the filtrate, after stirring at room temperature overnight, the reaction mixture was concentrated in reduced pressure rotary evaporator, and further purified through HPLC, finally got 62.2% yield.

^{1}H NMR (400 MHz, DMSO-*d6*) δ = 8.47 – 8.12 (m, 3H), 7.93 – 7.78 (m, 3H), 7.66 – 7.49 (m, 3H), 7.40 (d, J=7.2, 1H), 7.32 – 7.18 (m, 10H), 5.89 – 5.64 (m, 1H), 4.76 – 4.54 (m, 2H), 3.67 – 3.33 (m, 5H), 3.26 – 2.90 (m, 3H), 2.86 – 2.62 (m, 6H), 2.44 – 1.77 (m, 4H) ppm.

^{13}C NMR (101 MHz, DMSO-*d6*) δ = 176.22, 172.90, 171.95, 170.63, 170.08, 138.18, 138.00, 137.53, 134.36, 134.29, 133.35, 132.16, 129.79, 129.73, 129.66, 128.55, 128.37, 128.03,

127.89, 127.81, 127.68, 126.41, 125.88, 59.46, 59.17, 54.31, 54.01, 50.93, 42.65, 38.05, 37.78, 36.50, 36.12, 32.30, 22.39 ppm.

MS: calculated for $C_{39}H_{45}N_5O_{11}S_2$ is 823.26, found 824.18, $[M + H]^+$.

III. 1. 2. 4. Specimen solution preparation

Compound iii.1, iii.2, and iii.3 were dissolved with DI water to make a concentration of 5.0 mg/mL. We prepared different pH value solutions at 2.0, 4.0 and 7.0, pH was carefully adjusted by 1 mM HCl or 1 mM NaOH solution.

For specimen solution with metal ions, stock solution with 20 mM KCl and 10mM $CaCl_2$ were prepared individually. Then the prepared KCl and $CaCl_2$ solution were used to prepare a concentration of 5 mg/mL of compound iii.2, the system pH value was adjusted with 1 mM HCl to make pH=4 solution.

For all the dynamic experiments, after sample solution was prepared, the solution was quickly transferred to a quartz cuvette and start imaging accordingly.

III. 1. 2. 5. Optical birefringence measurement

The experiment setup for optical birefringence imaging was shown in Figure 2. Briefly, a white light source was put at the backside of the polarizer, and two perpendicular crossed polarizers were setup in the middle, then a camera was put at the front side to record the birefringence image. The prepared sample solution in quartz cuvette (49 mm in length, 12 mm in width and thickness at 1 mm) was put between the two perpendicular crossed polarizers.

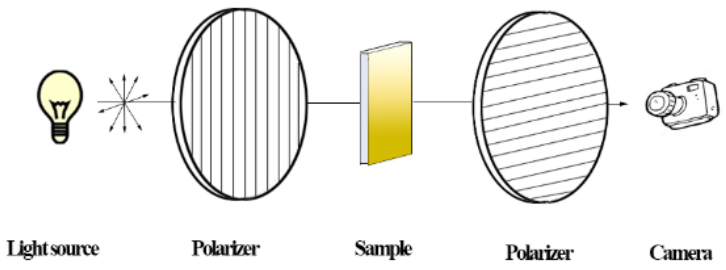

Figure 2. Experiment setup for birefringence imaging.

III. 1. 2. 6. TEM specimen preparation and observation

TEM specimen with shear force in one direction was prepared according to the following steps, for the specimen in the relaxed state, it was not necessary to carry out step ③. Transmission electron microscopy (TEM) images were obtained using JEM-1230R (100 KV).

① Carbon-coated copper grids were pre-treated to enhance hydrophilicity;

② Then 5 μL of specimen solution was dropped onto the grid, left the specimen solution on the grid for about 60s;
③ Used the pipette to shear the sample solution in one direction;
④ Removed the excess solution with filter paper in the direction of shear force;
⑤ 5 μL of 1% uranyl acetate was placed on the grid for negative staining for 20s;
⑥ Excess stain solution was removed by filter paper;
⑦ Washed the grid with 5 μL of water, left the water solution on the grid for 30s;
⑧ Removed the excess solution with filter paper, dried the grid at room temperature before observation.

III. 1. 2. 7. SEM specimen preparation and observation

SEM specimen with shear force in one direction was prepared according to the following steps, for the specimen in the relaxed state, it was not necessary to carry out step ③. Scanning electron microscopy (SEM) images were obtained using FEI Quanta 250 with accelerated voltage at 5 KV.

① Silicon wafer (0.5 cm x 0.5 cm) was cleaned with ethanol and dried before use;
② 5 μL of specimen solution was placed on the corner of clean silicon wafer;
③ Used the pipette to draw and pull the sample and align it on the silicon wafer, and move the wafer to the top of dry ice immediately
④ The silicon wafer with sample was lyophilized for 3h; the lyophilized specimen was coated with Pt-Pd using sputter coater to enhance conductivity before SEM measurement.

III. 1. 3. Results

III. 1. 3. 1. Charged state on molecular self-assembly study

In the molecule structure of iii.1, iii.2 and iii.3, they are either ended with glutamic acid or taurine group at the C-terminal. They will adopt varied charged state at different pH environment due to protonated of glutamic acid or taurine group. For glutamic acid, the pKa values for α-COOH and φ-COOH are 2.10, 4.07, respectively. The pKa value of -SO_3H in taurine is 1.5.[12] The predicted charged value at different pH environment is calculated according to the following formula and the results are shown in Table 1:

$$HA \rightleftharpoons A^- + H^+$$

$$pKa = pH + \log_{10}\frac{[A^-]}{[HA]}$$

Molecule charged value (deprotonated ratio): $e^- = \frac{[A^-]}{[A^-]+[HA]}$

		Compound iii.1		Compound iii.2		Compound iii.3	
			$-e^-$		$-e^-$		$-e^-$
pH value of the solution	**pH=1.0**	α-COOH	-0.074	α-SO_3H	-0.240	α-SO_3H	-0.240
		φ-COOH	-0.001	φ-COOH	-0.001	φ-SO_3H	-0.240
		total charged	**-0.075**	**total charged**	**-0.241**	**total charged**	**-0.481**
	pH=2.0	α-COOH	-0.443	α-SO_3H	-0.760	α-SO_3H	-0.760
		φ-COOH	-0.008	φ-COOH	-0.008	φ-SO_3H	-0.760
		total charged	**-0.451**	**total charged**	**-0.768**	**total charged**	**-1.520**
	pH=3.0	α-COOH	-0.888	α-SO_3H	-0.969	α-SO_3H	-0.969
		φ-COOH	-0.074	φ-COOH	-0.074	φ-SO_3H	-0.969
		total charged	**-0.962**	**total charged**	**-1.043**	**total charged**	**-1.938**
	pH=4.0	α-COOH	-0.988	α-SO_3H	-0.997	α-SO_3H	-0.997
		φ-COOH	-0.443	φ-COOH	-0.443	φ-SO_3H	-0.997
		total charged	**-1.431**	**total charged**	**-1.440**	**total charged**	**-1.994**
	pH=5.0	α-COOH	-0.999	α-SO_3H	-1.000	α-SO_3H	-1.000
		φ-COOH	-0.888	φ-COOH	-0.888	φ-SO_3H	-1.000
		total charged	**-1.887**	**total charged**	**-1.888**	**total charged**	**-1.999**
	pH=6.0	α-COOH	-1.000	α-SO_3H	-1.000	α-SO_3H	-1.000
		φ-COOH	-0.988	φ-COOH	-0.988	φ-SO_3H	-1.000
		total charged	**-1.988**	**total charged**	**-1.988**	**total charged**	**-2.000**
	pH=7.0	α-COOH	-1.000	α-SO_3H	-1.000	α-SO_3H	-1.000
		φ-COOH	-0.999	φ-COOH	-0.999	φ-SO_3H	-1.000
		total charged	**-1.999**	**total charged**	**-1.999**	**total charged**	**-2.000**

Table 1. Calculated molecular charged state at different pH environment.

We chose three pH levels, 2.0, 4.0, 7.0 to reach different negative charged state of molecules. At pH 2.0, the charged state of molecule iii.1, iii.2, and iii.3 is -0.45, -0.77 and -1.52, respectively. At pH 4.0, molecule iii.1, iii.2 and iii.3 bare -1.43, -1.44, and -1.99, respectively. At pH 7.0, all three molecules are at the charge state of -2.0. The charged state of molecules plays an important role in their conformation and interaction with adjacent molecules.[13] The self-assembly nanostructures at different pH environments were examined by transmission electron microscope (TEM). We can observe in Figure 3a, at pH 2.0, molecule iii.1 self-assembled into uniformed nanofibers with a width at 13 nm, twisted nanoribbons with a width

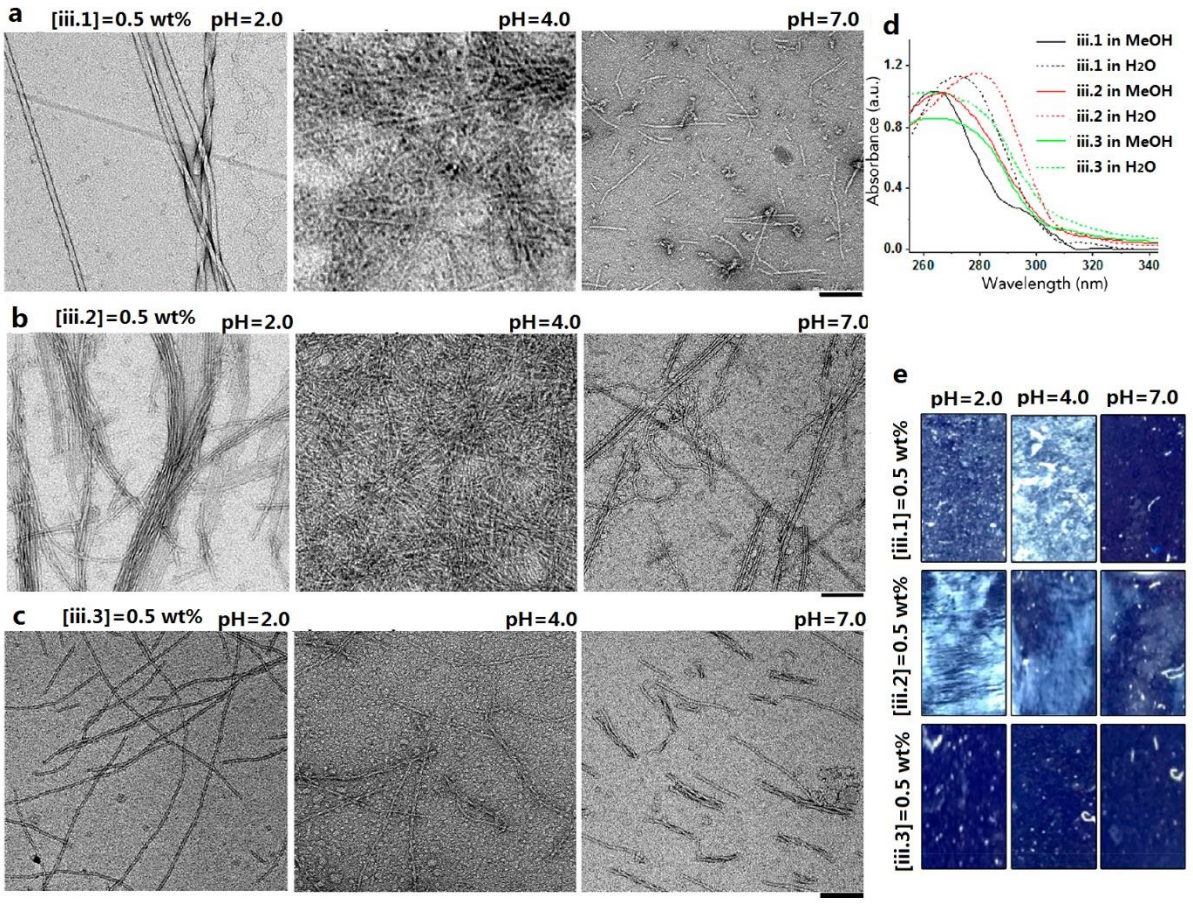

Figure 3. TEM images of nanofilaments formed by self-assembly of molecule iii.1 (a), iii.2 (b), or iii.**3** (c) in water (0.5 wt%) at pH 2.0, 4.0, and 7.0. Scale bars represent 100 nm. (d) UV-vis absorption of molecules iii.1, iii.2, and iii.3 in MeOH (solid lines) *vs.* in water (dash lines) at the same concentration (0.5 wt%). (e) Optical birefringence of molecules iii.1, iii.2, and iii.3 in water (0.5 wt%) at pH 2.0, 4.0, and 7.0. The solutions are contained in a standard 1mm quartz cuvette, viewed between perpendicularly crossed polarizers.

of 21nm and a twist length of 120 nm. At pH 4.0, it self-assembled into uniformed nanofibers with a width of 8 nm. At pH 7.0, only some short nanostrands with a width of 8 nm was found. In the case of molecule iii.2 (Figure 3b), at pH 2.0, bundles of aligned nanofibers with a width of 8 nm were observed. At pH 4.0, dense nanofibers with a similar width (8 nm) were formed. At pH 7.0, it started to self-assemble into a mixture of nanofibers (8 nm in width) and nanotubes (10 nm in width). For molecule iii.3 (Figure 3c), its self-assembly ability was highly reduced due to the two taurine groups, we can observe some nanofibers (~ 8 nm in width) in a very low density at pH 2.0, as we increased the pH to 4.0, only some short nanostrands can be observed, and in pH 7.0, even shorter nanostrands were formed. To fulfill long-range mechanical force transduction, fibrous structure is required.[14] Self-assembly structure from molecule iii.1 at pH 4.0, and molecule iii.2 at pH 2.0 or 4.0 is more likely to respond to external mechanical force. UV-Vis absorbance was applied to study the self-assembly state and monomer state. As shown in Figure 3d, the assembly state of molecule iii.1 and iii.2 (in water) exhibited obvious redshifts comparing with the monomer state (in methanol). It suggested the assembly state of molecule iii.1 and iii.2 adopt J-aggregation,[15] and the aromatic domain packed in a nematic-like stacking mode.[16] Molecule iii.3 didn't show obviously redshift between its assembly state and monomer

state. The birefringence results were consistent with the absorbance spectra, both molecules iii.1 and iii.2 showed birefringent effect at their assembly state, while molecule iii.3 showed little birefringence (Figure 3e). Specifically, molecule iii.1 showed obvious birefringence effect at pH 2.0 and pH 4.0. In the meantime, sol-gel transition was observed, it suggested spatial nanofibril alignment may originate from poor mobility.[17] Molecule iii.2 showed birefringence phenomenon at all pH levels, but birefringence intensity decreased as increasing pH values. Comparing the results from these three molecules, we could find that nematic-like stacking of the aromatic domains led to uniformed nanofibers and baring a negative charge between -0.77 and -1.44 will facilitate the alignment of the nanofibers to exhibit strong birefringence.

III. 1. 3. 2. Metal ions effect on molecular self-assembly

To gain a clear understanding on the electrostatic interaction on the molecular self-assembly behaviour, we chose molecule iii.2 solution at pH 4.0 which proved to be good self-assembly and showed relative strong birefringence for further study. Upon addition of salts of K^+ and Ca^{2+} before initiation of molecular self-assembly, we observed its effect on birefringence through polarized optical microscope and TEM. As is shown in Figure 4a, without addition any salts in the solution, molecule iii.2 solution exhibited steadily enhancing birefringence intensity during the 36 hours observation; when K^+ was introduced into the solution, it showed a similar birefringence effect comparing to the solution without any salts, indicating no disturbance in the molecule self-assembly. Further TEM imaging also confirmed little disturbance on molecular self-assembly by adding K^+ salts (Figure 4b). However, when Ca^{2+} was adding into the solution, we couldn't observe any enhance in birefringence effect during the 36 hours incubation, it suggested interruption in the molecule self-assembly behaviour.

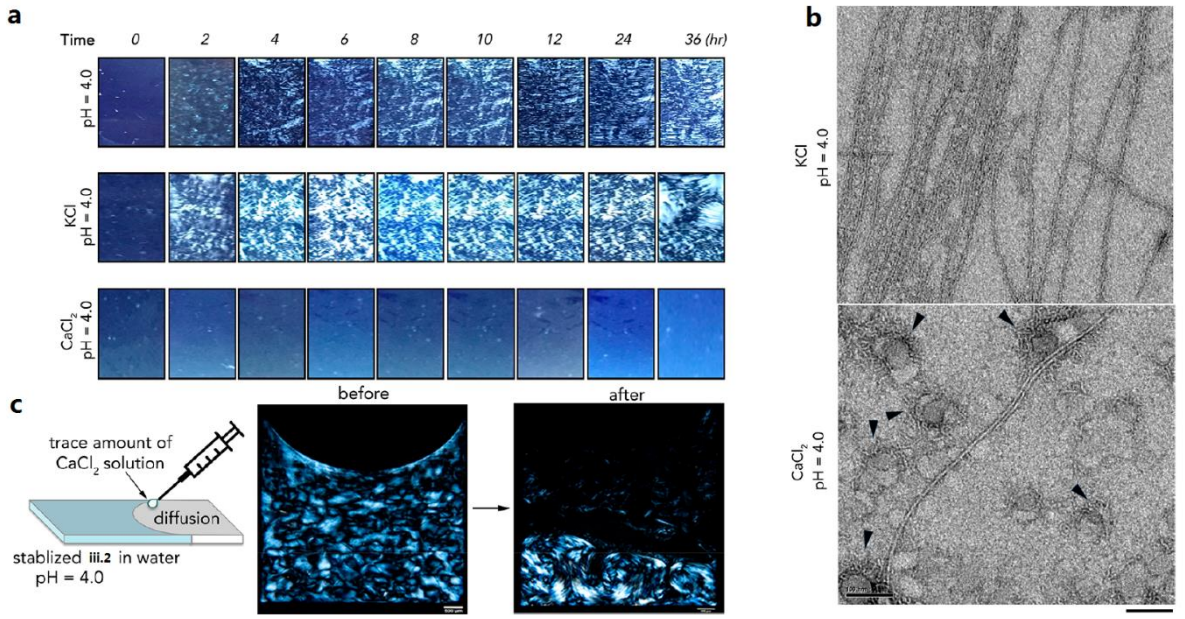

Figure 4. (a) Time-dependent optical birefringence images of molecule iii.2 (0.5 wt%) in water, in KCl (20 mM) solution, and $CaCl_2$ (10mM) solution at pH 4.0. (b) TEM images of molecule iii.2 (0.5 wt%) in KCl (20 mM) solution, and $CaCl_2$ (10mM) solution at pH 4.0. Scale bar represents 100 nm. (c) Schematic illustration of how to introduce trace amount $CaCl_2$ solution (pH 4.0) to the surface of self-assembled molecule iii.2 (0.5 wt%) in water at pH 4.0 (left); optical birefringence images of molecule iii.2 (0.5 wt%) in water at pH 4.0 before and after the addition of trace amount $CaCl_2$ solution (right).

Nanostructure observation by TEM only showed some aggregates of nanostrands (Figure 4b), it confirmed the self-assembly behaviour of molecule iii.2 was prevented by the divalent Ca^{2+} ions. For molecule iii.2 solution at pH 4.0, it beared 1.44 negative charge, divalent cations may work as ion bridges and affected the intermolecular interaction.[18]

To further investigate the effect of electrostatic interaction on fiber alignment, we introduced Ca^{2+} salts into a well stabilized self-assembly molecule iii.2 solution. Before adding the Ca^{2+} salts, we could observe the well stabilized molecule iii.2 solution exhibited obvious birefringence phenomenon, it indicated the formation of spatially oriented nanofibers in the solution. As Ca^{2+} salts solution was introduced into the solution, we could find that the birefringence phenomenon was slowly vanished together with the diffusion of Ca^{2+} salts in the solution (Figure 4c). And further nanostructure observation by TEM also showed the disassembly of the nanofibers after addition of Ca^{2+} salts. Possible explanation of the phenomenon could be the counterion condensation theory, the addition of the divalent counterions will reduce the interaction between the negative charged nanofibers, and further interrupt the interaction among self-assembly molecules, thus leading to the vanish of birefringence and molecule disassembly.

III. 1. 3. 3. Mechanical study on fiber alignment

Self-assembly specimen of molecule iii.2 at a concentration of 0.5 wt%, pH 4.0 still maintained optimal fluidity, it was suitable for further mechano-response characterization. We first check the solution by rheometer, as is shown in Figure 5a, in the frequency sweep at a strain below the critical strain, the elastic modulus G' remained at the same level between 0 rad/s and 200 rad/s. In the quartz cell filled with molecule iii.2 solution exhibiting birefringence, we slowly

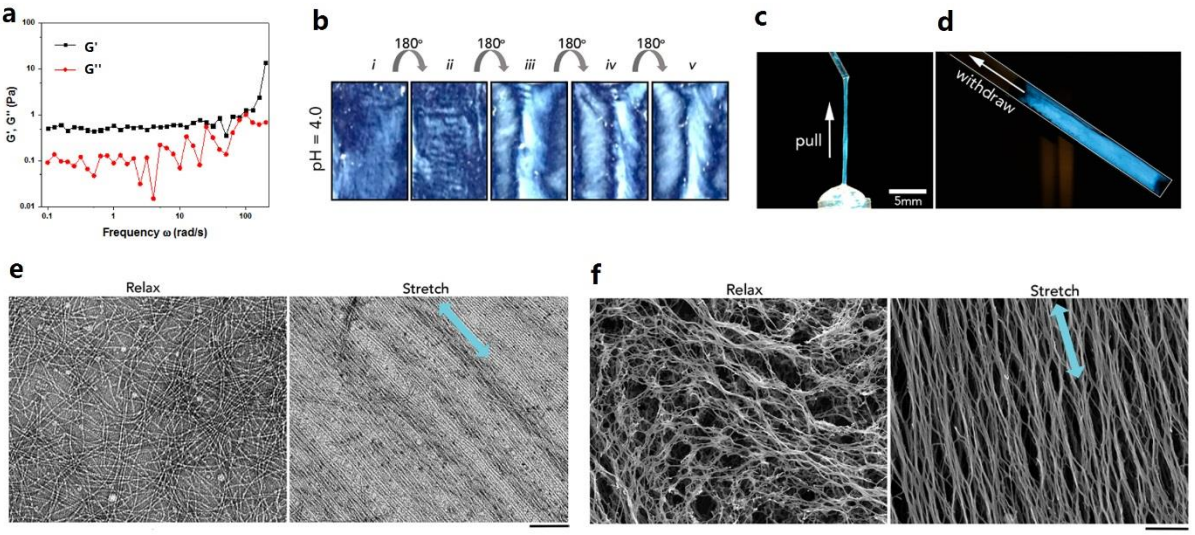

Figure 5. (a) Storage (G') and Loss (G'') moduli versus frequency of molecule iii.2 (0.5 wt%) at pH 4.0; (b) Birefringence images of stabilized molecule iii.2 (0.5 wt%) solution after sequential vertical rotation at pH 4.0; Birefringence image of stabilized self-assembly of molecule iii.2 (0.5 wt%) stretched by a glass rod (c) or withdrawn into quartz capillary (d). (e) TEM images of molecule iii.2 (0.5 wt%) solution at relaxed status (left) and after stretch at one direction (right), scale bar is 100 nm; (f) SEM image of of molecule iii.2 (0.5 wt%) solution at relaxed status (left) and after stretch at one direction (right), scale bar is 20 mm.

rotated the cell vertically. In the second round of rotation, we can observe dramatically enhanced birefringence effect. It indicated the rotation process guiding the orientation of the nanofibers in the solution, reaching a high-order nanofiber alignment state. Further rotating the quartz cell didn't bring much change in the birefringence pattern, suggesting a relatively stable fiber alignment (Figure 5b). To confirm the self-assembly solution of molecule iii.2 responsive to external force, we used a glass rod to stretch the solution or withdrew the solution by a quartz capillary. In both experiments, we observed an enhanced birefringence phenomenon through cross polarizer, it indicated stretch force or shear force enhancing nanofiber alignment (Figure 5c/d). In the further investigation of the nanostructure, we used electron microscope to identify the fiber alignment. In the TEM observation, we could observe tangling random coiled nanofiber at the relax state; after a shear force at one direction, we could observe parallelly aligned nanofibers in the direction of the shear force (Figure 5e). At the microscale observation by SEM, we also observed isotropic nanofiber alignment, and anisotropic nanofiber alignment after a shear force at one direction (Figure 5f). Both TEM and SEM results were in consistent with the birefringence effect, self-assembly nanofibers of molecule iii.2 can be guided by external force to reach higher-order fiber alignment.

III. 1. 3. 4. Large-scale aligned domain fabrication

To reach large scale hierarchical assemblies is still a big challenge in bottom-up materials fabrication.[19] Tsukruk's group has reported uniformly oriented cellulose nanocrystal fabrication through capillary confinement,[20] in our current study, we tried to fabricate highly ordered peptide film in thin capillaries under confined drying conditions. The fabrication scheme is shown in Figure 6a, briefly, self-assembly solution of molecule iii.2 was introduced into a thin-walled rectangular capillary (50 μm height, 1 mm width) *via* wetting-induced upward flow. Due to the presence of saturated vapor at the top meniscus, the evaporation rate was slow; while the solvent evaporation at the bottom was fast, asymmetric drying of nanofibers made it flow to the pinned interface after pulling the capillary out. The time-dependent orientation of the nanofibers was monitored by polarized light microscope (PLM) by putting the capillary in a horizontal position. The results were shown in Figure 6b, within the micro-capillary, alignment of self-assembly nanofibers was reached by the differential evaporation rate of the solvent. Steadily growth of uniform highly ordered birefringent domains was observed in the first 9 hours, it indicated the condensation of the ordered nanofibers. As the solvent evaporation continuing, shrinkage of the birefringent area was observed at the edge of the capillary, exhibiting white interface color. The solidification process completed in 10 hours of evaporation, and densely packing of the birefringent area was initiated. Morphology mismatched between the twisted structures leading to the formation of cracks parallel to the drying edge of the capillary, these cracks divided the lamellar domains into 4 sections. By the end of the drying process, the shrinkage of the lamellar domains was reflected by the color shifts from white to yellow, orange, purple, blue or green, indicating a densely packing of the highly oriented nanofibers.

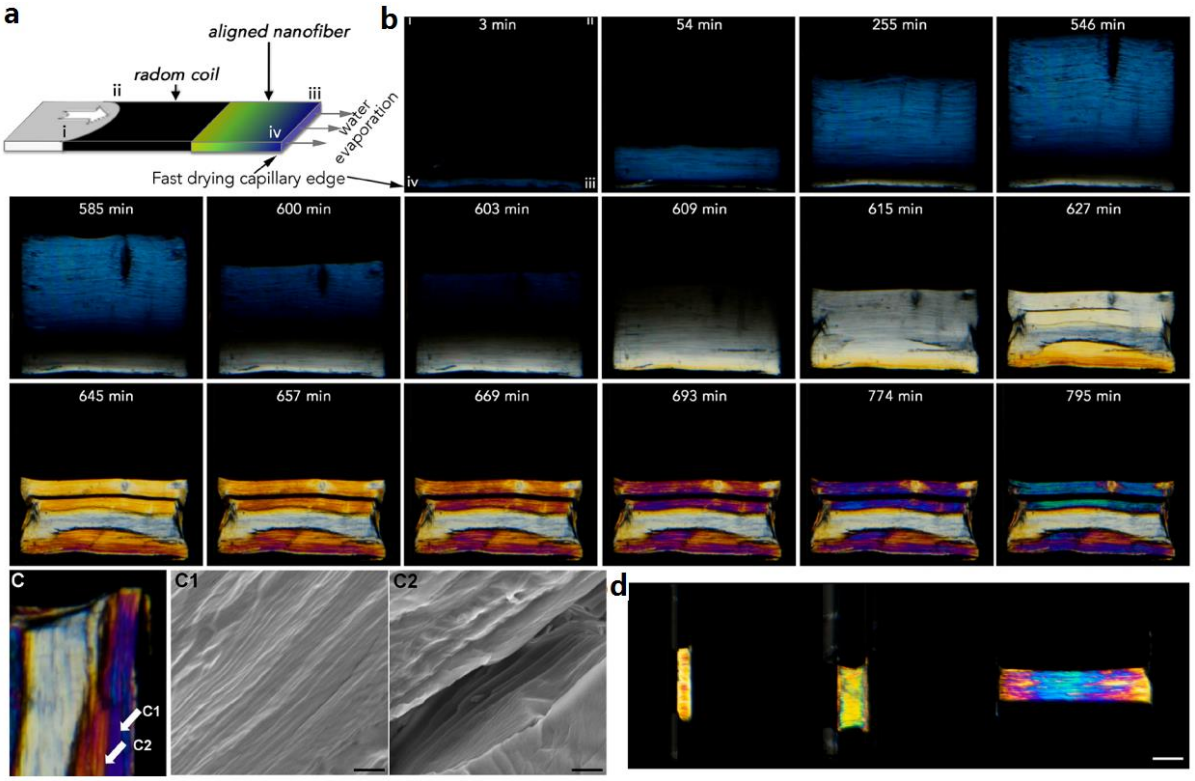

Figure 6. (a)Schematic diagram of evaporation casting in a rectangular capillary. (i-iv) indicate capillary orientation in subsequent sub-figures. (b) Polarized light microscopy (PLM) time-lapse of evaporation casting of molecule iii.2 (0.5 wt%) in pure water at pH 4.0 in rectangular capillary (50 µm height, width 1 mm). (c) Zoomed in PLM image of the last image in panel B with two indicated positions for SEM imaging. c1 represents the surface of the evaporation-induced film. c2 is SEM image of wall-to-wall crack parallel to the drying edge. Scale bars in panel c1 and c2 represent 1 µm. (d) POM images of evaporation casting of molecule iii.2 (0.5 wt%) in pure water at pH 4.0 under varying capillary dimensions. From left to right, the dimension of the capillary is 0.05 x 0.05 mm, 0.1 x 0.1 mm, and 0.05 x 0.5 mm. Images were selected from times when qualitative changes in birefringent domains were no longer observed. Scale bar represents 100 µm.

Microstructure observation on the dried densely packing nanofibers was conducted in SEM, it exhibited uniaxially alignment of nanofibers (Figure 6c/c1). A further SEM imaging on the crack between two sections was shown in Figure 6c2, layer-by-layer stack of the nanofiber's structures preserved from the core to surface. In addition, varied birefringence domains with different intensity and interface color were observed across the capillary and in different capillaries. Within one capillary, it was more birefringent in the center than the edge part. It was in good agreement with evaporation direction of the solvent, and the nanofiber alignment was confirmed to be force responsive. By further adjustment of the capillary geometry and control on the drying procedures, it would be able to generate various mesoscale peptide nanofiber alignment patterns.

III. 1. 4. Conclusion

We were able to reach self-assembly nanostructures adopted liquid crystal properties without using the traditional rigid molecular functional group.[21] Self-assembly peptide building block was modified by easily protonated function groups at the asymmetric sites, by adjusting the pH

value of the environment, negative charged self-assembly motifs were obtained and they self-assembled into nanofibrils. Guiding by uniaxial external mechanical force, the nanofibrils would orientate in the same direction, showing enhanced birefringence. Large scale well-orientated nanofibrils structure can be approached by evaporation casting in capillary confinement. Solvated negative charged specimen solution was transferred into highly ordered peptide film, exhibiting varied interference colors at different domains. Current mechanical force guiding hierarchical nanostructure fabrication through introducing easily protonated groups into self-assembly peptide building block was promising in obtaining artificial bio-optic materials,[22] tissue scaffold.[23] And it also provided structure-function characterization clues for large scale biomaterials fabrication.

IV. 1. Co-organizing synthesis of heterogeneous nanostructures through the photo-cleavage of pre-stabilized self-assemblies.

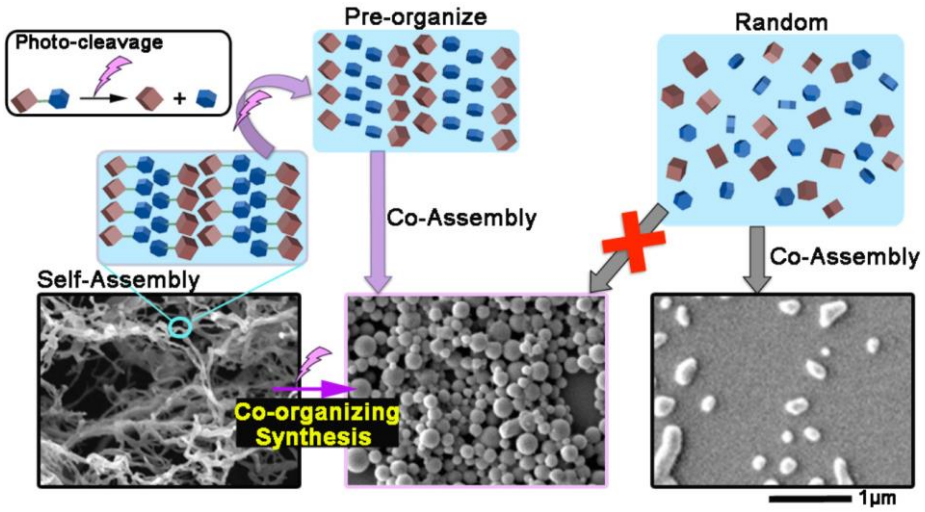

This chapter corresponding to the following publication:

Wei Ji, Shijin Zhang, Gerogy A. Filonenko, Guanying Li, Toshio Sasaki, Chuanliang Feng* and Ye Zhang.* "Co-Organizing Synthesis of Heterogeneous Nanostructure through Photo-Cleavage of Pre-Stabilized Self-Assemblies" *Chem. Commun.* **2017**, 53, 4702-4705.

IV.1. 1 Introduction

In biological system, size and shape play an important role on the function of the biomaterials. To reach biomaterials with a size up to micrometers, molecular assembly through non-covalent interaction is an effective pathway.[1] For traditional chemical synthesizers, to fabricate well-defined macroscale structures through covalent bonds is still hard to approach. It limits the material scientists to fabricate functional nanomaterials from biomimetic way. Several decades ago, chemists found molecular self-assembly is an effective approach to generate non-biological nanomaterials that staying in the ground state with intrinsic morphologies.[2] In biological system, functional nanomaterials were often fabricated in a synergistic way of several components due to their co-assembly. The stable functional nanomaterials usually adopt the ground state,[3] while the transitional state often stay away from the thermodynamic minima state. To fabricate nanomaterials at the ground state, material scientists have started applying multi-components assembly. Basic building units are often coated or composed by DNA,[4] the specific interaction between nitrogenous bases will avoid non-specific interaction to reach desired nanomaterials.[5] To date, most of the report based on self-assembly or co-assembly to build nanostructures are relying on creating nanostructures in their thermodynamic minima state. Though the principle based on ground state has generate a lot of robust structure, there is still a big gap in understanding the transitional state structure and limited fabrication of such nanomaterials.

To fabricate co-assembly transitional state (undesired) structures is often competed with the formation of ground state co-assembly structures. Though the undesired structures are hard to reach in a traditional way,[3] such a competition can be taken as the opportunities to generate new heterogeneous nanostructures. In the process of co-assembly, the series of kinetic traps far away from the ground state could provide possibilities to generate various nanostructures. Take the advantage of kinetic traps, we developed a way to reach metastable nanostructures from a co-organizing synthesis. It is illustrated in Figure 1,[6] the conventional way for co-assemble nanostructures from different components depend on the entropy-driven assembly to reach to thermodynamic minima state. In order to increase the probabilities of keeping nanostructures in the kinetic trap state, we started with pre-organized nanostructures, and applied the photo-cleavage process to generate different components. The physically close distance between the generated components facilitating their in-situ co-assembly, enabling the nanostructures to maintain in the kinetic trap states that are far away from the ground state. Thus, enriched the pathway to achieve exotic heterogenous nanostructures that are hard to reach in the conventional synthetic pathways.

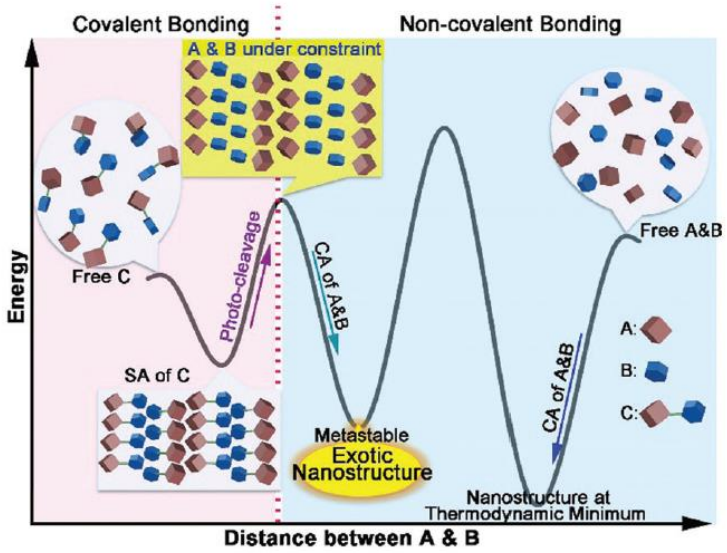

Figure 1. Energy profile of a co-organizing synthetic pathway that targets metastable CAs for exotic heterogeneous nanostructures. SA is short for self-assembly, and CA is short for co-assembly.

To reach this end, we designed and synthesized two self-assembly molecule iv.1.1 and iv.1.2, the self-assembly motifs were consisted by (FmocFF)[7] and coumarin derivatives[8] through a photo-cleavable bond (Figure 2).[9] All the basic unit (iv.1.3, iv.1.4, iv.1.5) underwent π-π and hydrogen bond interactions to form nanostructures. Thus, we may assume that molecule iv.1.1 and iv.1.2 also adopted same mechanism to self-assemble into nanostructures. Upon UV-light initiation, molecule iv.1.1 and iv.1.2 would be converted to the corresponding basic unit iv.1.3/1.4 and iv.1.4/1.5, respectively. Comparing molecule iv.1.3 and iv.1.5, only a small change from the ester bond in iv.1.3 to ether bond in iv.1.5, it fundamentally affected the coumarin derivatives' intermolecular hydrogen bonding manners and strength, thus leading to a quite different co-assembled nanostructures after UV-light cleavage. The aim of current study was to illustrate how molecular design would shed a light on the co-organizing synthesis of nanostructures, and evaluated the systematic efficiency and sensitivity.

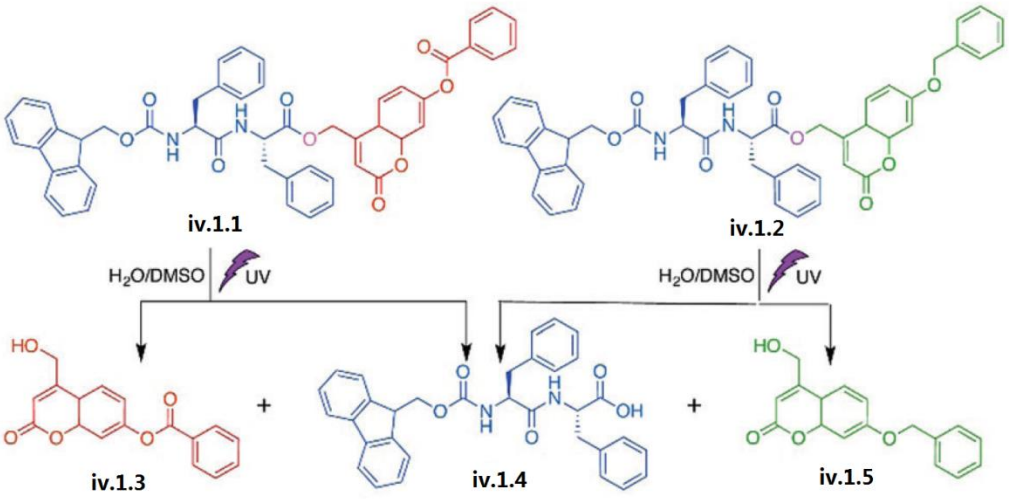

Figure 2. Chemical structure of molecule iv.1.1, iv.1.2 and their responding hydrolysis products upon UV light treatment.

IV. 1. 2. Experiment Section

IV. 1. 2. 1. Materials

Chemical reagents	Grade	Manufacturer
Fmoc-Amino acid	98.0%	GL Biochem (Shanghai, China)
2-(1*H*-benzotriazol-1-yl)-1,1,3,3-tetramethyluronium hexafluorophosphate (HBTU)	98.5%	Sigma Aldrich
Trifluoroacetic acid (TFA)	98.0%	Sigma Aldrich
Ethyl 4-chloroacetoacetate	95.0%	Sigma Aldrich
Resorcinol	99.0%	Sigma Aldrich
Potassium carbonate	99.0%	Sigma Aldrich
N-(3-dimethylaminopropyl)-*N*'-ethylcarbodiimide hydrochloride (EDCI)	98.0%	Sigma Aldrich
4-Dimethylaminopyridine (DMAP)	98.0%	Sigma Aldrich
Sulfuric acid (H_2SO_4)	95.0%	Nacalai Tesque
Methanol (MeOH)	99.0%	Nacalai Tesque
Benzoic acid	99.5%	Nacalai Tesque
Ethyl acetate (EA)	99.0%	Nacalai Tesque
Tetrahydrofuran (THF)	98.0%	Nacalai Tesque
N, N-Diisopropylethylamine (DIEA)	98.0%	Nacalai Tesque
Acetone	99.0%	Nacalai Tesque
Benzyl bromide	97.0%	Nacalai Tesque

All organic solvents were dehydrated before experiment by a solvent purification system.

IV. 1. 2. 2. Instruments

Agilent 1260 Infinity Analysis HPLC (Column: 2.1 mm ×150 mm XBridge® Peptide BEH C18 column), Thermo LTQ-ETD mass spectrometer (ESI-MS), NMR equipment: Bruker Advance 400 MHz spectrometer, UV-Vis spectrophotometer (Cary 60 UV-Vis, Agilent), Transmission Electron Microscope (JEM-1230R), Milli-Q® Integral 3/5/10/15 System, Scanning Electron Microscope (FEI Quanta 250 FEG), Circular dichroism spectroscopy (JASCO J-820), Rigaku XtaLab PRO instrument.

IV. 1. 2. 3. Synthesis

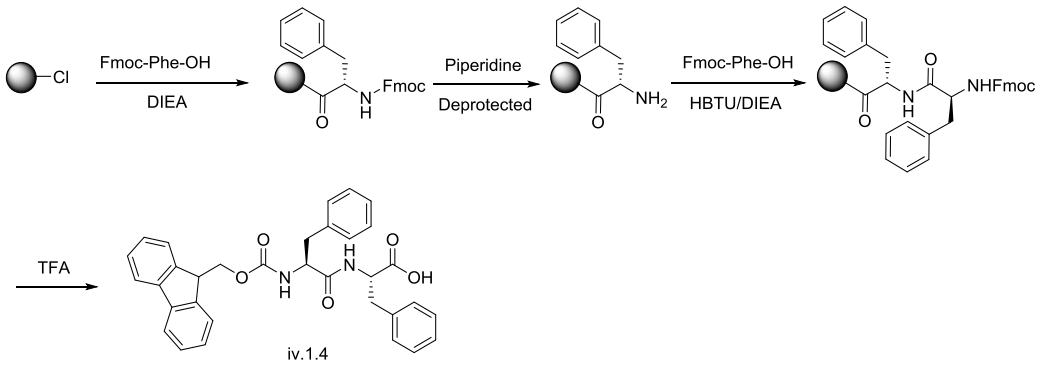

Scheme 1. Synthesis of compound iv.1.4.

Compound **iv.1.4**: Compound iv.1.4 was obtained via solid phase peptide synthesis (SPPS). 2-Chlorotrityl chloride resin (2.0 g, 2 mmol) was swelled in anhydrous DCM for 20 min, L-Fmoc-Phe-OH (1.94 g, 5 mmol) dissolved in anhydrous DMF was conjugated to resin with DIEA in 30 min. Then washed with anhydrous DMF for 3 times, unreacted sites in the resin were blocked with DCM/MeOH/DIEA (80:15:5) for 20 min and washed by anhydrous DMF for 5 times. Then piperidine solution (20% in DMF) was added into reaction for 30 min to remove the Fmoc protecting group on the amino acid. Elongation was conducted in the presence of conjugation reagents HBTU (2.28 g, 6 mmol) and DIEA (2.08 mL, 12 mmol), they were dissolved in 5 mL anhydrous DMF together with L-Fmoc-Phe-OH (2.32 g, 6 mmol), the mixture was added into the resin and kept reaction for 30 min. The resin was washed by anhydrous DMF, MeOH, DCM and hexane for 5 times, the iv.1.4 was cleaved off the resin using TFA for 2 h. After removing the solvent, anhydrous ether was added into the concentrated product and white precipitation of iv.1.4.

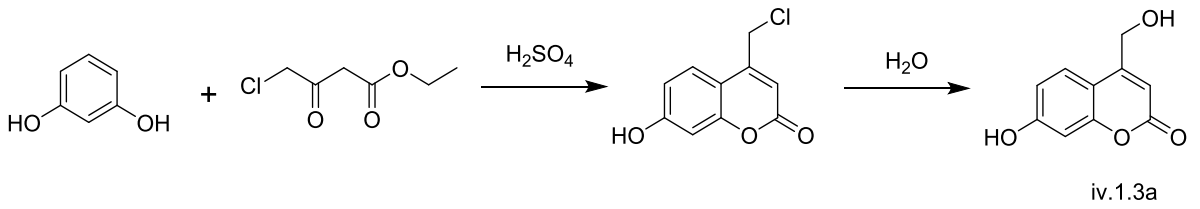

Scheme 2. Synthesis of compound iv.1.3a.

Compound **iv.1.3a**: Resorcinol (5.50 g, 50 mmol) was carefully adding into the cooled down (0 ^{o}C) concentrated 40mL H_2SO_4 solution. Then ethyl 4-chloroactoacetate (9.10 g, 55 mmol) was adding into the reaction mixture and kept stirring at room temperature overnight. The reaction mixture was slowly pouring into 500 mL ice/water mixture, the precipitates was filtered and washed by 100mL water for 3 times. The resulting white precipitates was transferred to a 500mL round bottom flask and 200 mL water was added into the flask, refluxed for 3 days. The hot reaction mixture solution was filtered, the filtrated was cooled down to room temperature for 12 hours. The pale needle crystal formed in the solution was filtered and washed by 50mL water for 3 times. The obtained crystal was dried in a 60 ^{o}C oven to give iv.1.3a. The yield is 70.1%.

^{1}HNMR (400 MHz, DMSO-*d6*) δ = 10.49 (d, *J*=13.1, 1H), 7.50 (dd, *J*=13.3, 8.7, 1H), 6.85 – 6.63 (m, 2H), 6.21 (d, *J*=13.2, 1H), 5.74 – 5.35 (m, 1H), 4.68 (d, *J*=13.2, 2H).

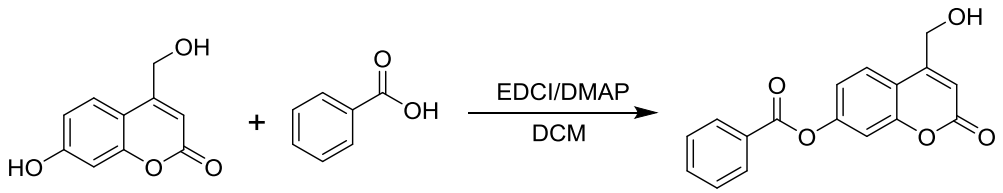

iv.1.3a iv.1.3

Scheme 3. Synthesis of compound iv.1.3.

Compound **iv.1.3**: Benzoic acid (0.24 g, 2 mmol) was dissolved in 20mL anhydrous DCM, then EDCI (0.38 g, 2 mmol), DMAP (24 mg, 0.2 mmol) and iv.1.3a (0.39 g, 2 mmol) were added into the reaction mixture, stirring at room temperature overnight. The reaction mixture was washed by 5mL water for 3 times, the organic layer was dehydrated with anhydrous Na_2SO_4 for 4 hours. It was further purified by silica column chromatography to give compound iv.1.3. The yield was 48.1%.

^{1}HNMR (400MHz, DMSO-*d6*) δ = 8.17 (d, *J* = 0.8 Hz, 2H), 7.77-7.83 (m, 2H), 7.64 (t, *J* = 0.8 Hz, 2H), 7.50 (d, *J* = 0.4 Hz, 1H), 7.33-7.36 (dd, J_1 = 0.4 Hz J_2 = 0.4 Hz, 1H), 6.49 (s, 1H), 5.71 (t, *J* = 0.8 Hz, 1H), 4.81 (d, *J* = 0.4 Hz, 2H).

^{13}CNMR (101MHz, $CDCl_3$) δ = 164.72, 160.50, 156.80, 154.16, 153.48, 135.07, 134.88, 130.51, 129.58, 129.04, 125.99, 119.09, 115.90, 111.04, 110.69, 59.64.

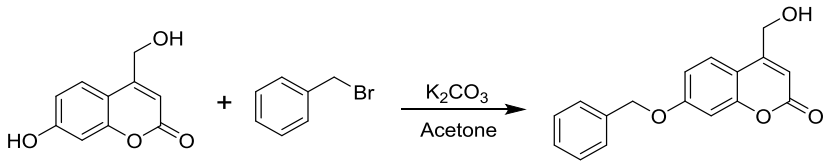

iv.1.3a iv.1.5

Scheme 4. Synthesis of compound iv.1.5.

Compound **iv.1.5**: Compound iv.1.3a (1 g, 5 mmol) was dissolved by 100 mL acetone in a 250 mL round-bottom flask, benzyl bromide (1.06 g, 6.25 mmol) and potassium carbonate (1.0 g, 7.2 mmol) were added into the solution. Refluxed overnight, the hot solution was filtered. The obtained filtrate was subjected to reduced pressure rotary evaporator to remove the solvent, DCM was used to wash the precipitates and dried to give compound iv.1.5. The yield is 70.1%.

^{1}HNMR (400 MHz, DMSO-*d6*) δ = 7.60 – 7.56 (m, 1H), 7.46 – 7.41 (m, 2H), 7.39 – 7.28 (m, 3H), 7.05 (d, *J*=2.5, 1H), 6.99 – 6.94 (m, 1H), 6.28 – 6.25 (m, 1H), 5.18 (s, 2H), 4.71 – 4.65 (m, 2H).

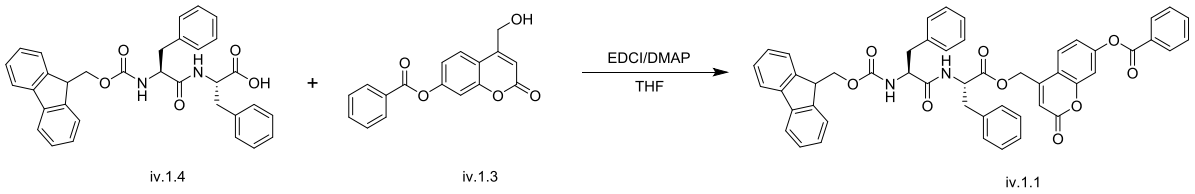

iv.1.4 iv.1.3 iv.1.1

Scheme 5. Synthesis of compound iv.1.1.

Compound **iv.1.1**: A THF solution (20ml) of iv.1.3 (0.29 g, 1 mmol), iv.1.4 (0.80 g, 1.5 mmol), 1-Ethyl-3-(3-dimethylaminopropyl) carbodiimide hydrochloride (EDCI) (0.29 g, 1.5 mmol) and 4-dimethylaminopyridine (DMAP) (12 mg, 0.1 mmol) was stirred at room temperature for 48 hours. The resulting solution was washed with deionized water (3 x 5 ml) and then the organic layer was collected. The solvent was removed, and the resulting precipitate was purified by silica gel chromatography (DCM/EA = 10/1) yielding iv.1.1 as a white solid (0.35 g, 43%).

^{1}HNMR (400MHz, DMSO-*d6*) δ = 8.63 (d, *J* = 0.8 Hz, 1H), 8.09 (d, *J* = 0.8 Hz, 2H), 7.79 (t, *J* = 0.8 Hz, 2H), 7.71 (t, *J* = 0.8 Hz, 2H), 7.53-7.58 (m, 5H), 7.44 (t, *J* = 0.4 Hz, 1H), 6.95-7.40 (m, 14H), 6.39 (d, *J* = 1.6 Hz, 1H), 5.26-5.42 (m, 2H), 4.59-4.66 (m, 1H), 4.19-4.26 (m, S10 1H), 4.00-4.11 (m, 4H), 2.98-3.12 (m, 2H), 2.84-2.88 (m, 1H), 2.61-2.70 (m, 1H).

^{13}CNMR (101MHz, $CDCl_3$) δ = 172.57, 172.35, 171.40, 164.67, 159.88, 156.26, 156.22, 154.24, 153.71, 149.83, 144.31, 144.22, 141.16, 138.57, 137.45, 137.36, 134.89, 130.51, 129.81, 129.74, 129.64, 129.58, 129.00, 128.82, 128.76, 128.53, 128.13, 127.57, 127.20, 126.76, 126.46, 125.89, 125.81, 120.61, 119.25, 115.39, 112.75, 111.15, 66.20, 62.26, 56.33, 55.45, 54.37, 47.03.

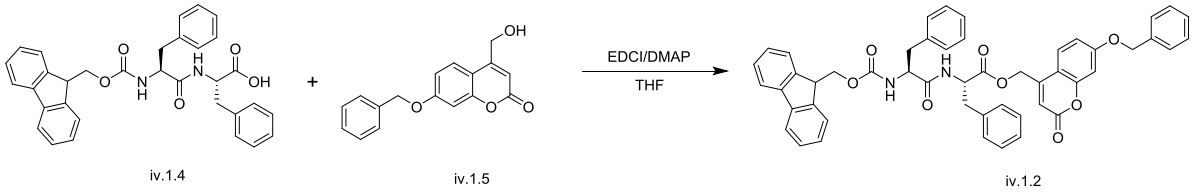

iv.1.4 iv.1.5 iv.1.2

Scheme 6. Synthesis of compound iv.1.2.

Compound **iv.1.2**: Compound iv.1.2 was synthesized according to the same way of preparing compound iv.1.1.

^{1}HNMR (400MHz, DMSO-*d6*) δ = 8.60 (dd, J_1 = 0.4 Hz J_2 = 0.8 Hz, 1H), 7.80 (dd, J_1 = 0.4 Hz, J_2 = 0.8 Hz, 2H), 7.46-7.57 (m, 3H), 6.92-7.40 (m, 22H), 6.20 (d, *J* = 1.6 Hz, 1H), 5.14-5.31 (m, 4H), 4.59 (t, *J* = 0.8 Hz, 1H), 3.95-4.22 (m, 4H), 2.95-3.10 (m, 2H), 2.80-2.89 (m, 1H), 2.59-2.65 (m, 1H).

^{13}CNMR (101MHz, $CDCl_3$) δ = 172.72, 171.54, 171.14, 167.39, 161.95, 161.19, 160.37, 159.16, 158.34, 155.29, 153.34, 152.93, 144.48, 144.32, 144.21, 142.21, 141.11, 136.77, 129.79, 129.72, 129.64, 129.04, 128.64, 128.52, 128.40, 128.12, 127.56, 127.16, 126.75, 126.44, 126.36, 120.58, 115.59, 113.42, 111.45, 110.88, 73.36, 70.42, 69.46, 66.12, 51.93, 46.95.

IV. 1. 2. 4. Transmission electron microscope (TEM) imaging

Aliquots (10 µL) of sample solution were added into a glow discharge copper grid (400 mesh) coated with thin carbon film and incubated for 30 s at room temperature. After removing excess solution, the grid was washed with deionized water three times and then stained with 2.0% (w/v) uranyl acetate (UA) by exposing the grid in three drops of UA solution for 30 s. TEM images were captured at high vacuum on transmission electron microscope JEM-1230R (JEOL, Japan).

IV. 1. 2. 5. Scanning electron microscope (SEM) imaging

Aliquots (10 µL) of sample solution were added into on silicon wafer, freeze dried overnight, and sprayed with a thin gold layer. SEM images were taken on a scanning electron microscope FEI Quanta 250 FEG.

IV. 1. 2. 6. Photo-cleavage monitoring by HPLC

The Photo-cleavage monitoring of molecules iv.1.1 and iv.1.2 (2×10^{-4} mol/L) under different photo irradiation time was tested by using a Agilent 1260 Infinity HPLC and UV-Vis spectrophotometer (Cary 60 UV-Vis, Agilent), respectively.

IV. 1. 2. 7. Circular dichroism (CD) measurement

CD spectra of all the samples were collected on a spectrometer JASCO J-820 CD with bandwidth of 1.0 nm in the ultraviolet (UV) region (190 - 400 nm) using a 1 mm quartz cuvette.

IV. 1. 2. 8. Single crystal X-ray diffraction

Single crystal structures of molecules iv.1.4 and iv.1.5 were used according to the reported literatures, respectively. Single crystal of molecule iv.1.3 suitable for X-ray diffraction was obtained by slow evaporation of n-hexane / dichloromethane (v/v 1:2) solution at room temperature. The X-ray diffraction data for the single crystals were collected on a Rigaku XtaLab PRO instrument (ω-scan mode) using graphite monochromated MoKα radiation (0.71073 Å). The diffractometer was equipped with a Rigaku GN2 low temperature system (air cooling type) and data were collected at 93 K. The performance mode of the microfocus sealed X-ray tube was 50 kV, 0.60 mA. Suitable crystals of appropriate dimensions were mounted on loops in random orientations. Preliminary unit cell parameters were determined with three sets of total 30 narrow frame scans. Data collection: images were indexed and integrated using CrysAlisPro data reduction package (version 1.171.39.7b, Rigaku Oxford Diffraction, 2015). Final cell constants were determined by global refinement of reflections from the complete data set. Data were corrected for systematic errors and absorption using the ABSPACK module. The structures were solved by the intrinsic phasing method using SHELXT-2014/5 and refined by the full matrix least-squares on F2 using SHELXL-2014/7.

IV. 1. 3. Results

IV. 1. 3. 1 Single Component Study

Molecule iv.1.1, iv.1.2 and their corresponding photo-cleavage products iv.1.3, iv.1.4, iv.1.5 (Figure 3a) were dissolved in H_2O/DMSO mixed solution, and their self-assembly (SA) nanostructures were observed by transmission electron microscope (TEM). Both molecule iv.1.1 and iv.1.2 formed thick nanofibers with a width at 10 – 20 nm; molecule iv.1.4 self-assemble into similar nanofibers, but with a narrower width at around 7 nm; in the case of molecule iv.1.3 and iv.1.5, though a minor difference in their molecule structure, the self-assembly nanostructures were quite different, molecule iv.1.3 self-assemble into nanoribbons with a width at 70 – 80 nm, molecule iv.1.5 just formed some linear aggregates with irregular shapes (Figure 3b).

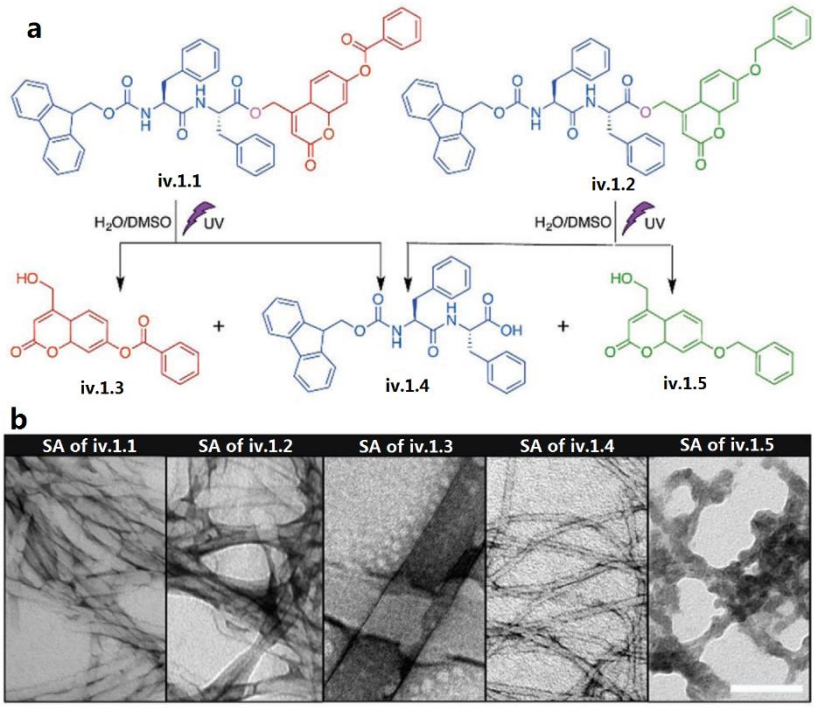

Figure 3. (a) Chemical structures of iv.1.1, iv.1.2 and their photo-cleavage products iv.1.3 and iv.1.4, and iv.1.4 and iv.1.5, respectively. (b) TEM images show self-assemblies of iv.1.1, iv.1.2, iv.1.3, iv.1.4 and iv.1.5 in appropriate aqueous solutions. The scale bar is 100 nm.

IV. 1. 3. 2. Kinetic Study Introduced by Photo-cleavage

As is shown in Figure 3a, when suitable light was applied on both molecule iv.1.1 and iv.1.2, they would go through photo-cleavage to produce molecule iv.1.3 and iv.1.4, iv.1.4 and iv.1.5, respectively. The optimal light source to ensure the photo-cleavage for molecule iv.1.1 and iv.1.2 is 320 nm (100 mW cm^{-2}), and the photo-cleavage process was monitored by HPLC (Figure 4a). The chemical conversion of both molecule iv.1.1 and iv.1.2 adopted a single exponential profile, and 90% of them were cleaved in the 60 min radiation.

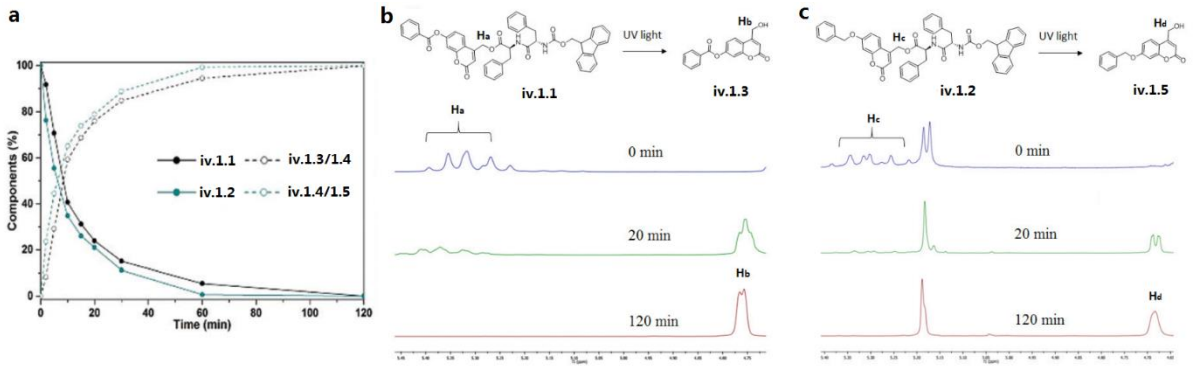

Figure 4. (a) Concentration-time profiles for photocleavage process of iv.1.1 (500 μM) and iv.1.2 (500 μM) under the irradiation of 320 nm. ^{1}HNMR spectra comparisons before and after photo-cleavage of iv.1.1 (b) and iv.1.2 (c).

And the reaction was extended another hour, both molecules iv.1.1 and iv.1.2 were totally transformed to iv.1.3 and iv.1.4, iv.1.4 and iv.1.5, respectively. In the meantime, we have also used ^{1}HNMR to monitor the process. As is shown in Figure 4b, the chemical shift for "Ha" hydrogen in molecule iv.1.1 was around 5.3, as the photo-cleavage process went on, it slowly disappeared and the new peak around 4.7 appeared ("Hb" hydrogen for molecule iv.1.3). Molecule iv.1.2 showed a similar phenomenon for the photo-cleavage process (Figure 4c).

IV. 1. 3. 3. Nanostructure characterization during the photo-cleavage process

Before photo-cleavage, the self-assembly solution of both molecules iv.1.1 and iv.1.2 were emulsions. At the end of photo-cleavage, precipitates and phase separation were formed in both emulsions, suggesting a change in the self-assembly nanostructures (Figure 5a). In the circular dichroism (CD) measurement experiment, we can observe the disappearance of β-sheet for molecule iv.1.1 after photo-cleavage (Figure 5b); random coil formation was observed after the photo-irradiation of molecule iv.1.2 (Figure 5c). The change in CD spectra confirmed the transition of secondary structure induced by the photo-cleavage. In a control experiment, the photo-cleavage products iv.1.3, iv.1.4, and iv.1.5 at the same concentration were irradiated by the UV light for 2 hours, but no precipitates or phase separation were observed. Further mixing iv.1.3 and iv.1.4 or iv.1.4 and iv.1.5, no phase separation was observed (Figure 5a). Comparing the CD spectra of the mixture of iv.1.3 and iv.1.4 or iv.1.4 and iv.1.5 with the simple sum (theoretical) of single component's CD spectra, they were different, indicating the existence of the driving force for the co-assembly of iv.1.3 and iv.1.4, or iv.1.4 and iv.1.5 (Figure 5d/e).[12] The CD spectra obtained from the photo-cleavage of molecule iv.1.1 and iv.1.2 were quite different from the simply mixed of iv.1.3 and iv.1.4, iv.1.4 and iv.1.5, it meant that the self-assembly nanostructures from the photo-cleavage process were distinct from the regular entropy driven process.

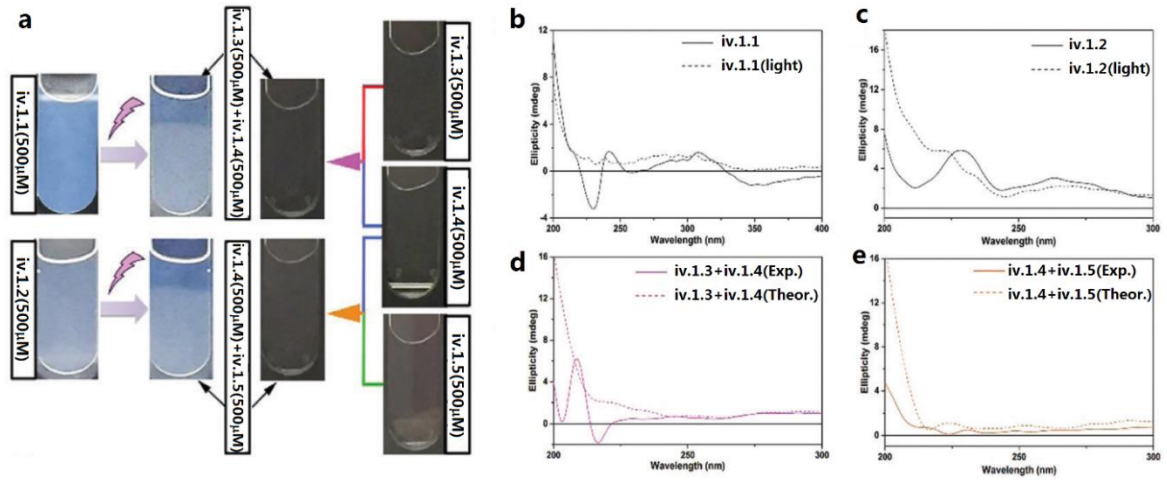

Figure 5. (a) Optical images taken in front of a black background (from left to right) of iv.1.1 (500 μM) and iv.1.2 (500 μM) in H_2O/DMSO (v/v = 3 : 2) before and after photo-cleavage; iv.1.3 plus iv.1.4, iv.1.4 plus iv.1.5, with each component concentration at 500 mM in H_2O/DMSO (v/v = 3 : 2); iv.1.3 (500 μM), iv.1.4 (500 μM), iv.1.5 (500 μM) in H_2O/DMSO (v/v = 3 : 2). CD spectra of iv.1.1 (b) and iv.1.2 (c) at 500 μM in H_2O/DMSO (v/v = 3 : 2) before and after photo irradiation (320 nm). CD spectra of iv.1.3 / 1.4 mixture (d) and iv.1.4 /1.5 mixture (e) at 500 μM each in H_2O/DMSO (v/v = 3 : 2).

The nanostructure observation was conducted by scanning electron microscope (SEM) and transmission electron microscope (TEM). The nanostructure of molecule iv.1.1 was shown in Figure 6, before photo-cleavage, it formed nanofibers with a width around 20 nm. Upon photo radiation, the nanofibers merged into big bundles (Figure 6a/b, transition), suggesting an enhanced fiber-fiber interaction. Until the end of photo-cleavage, the fibers transformed into large irregular aggregates (Figure 6a/b, final). In the case of mixture of iv.1.3 and iv.1.4, after photo radiation for 2 hours, they formed some cluster of nanorods (Figure 6c).

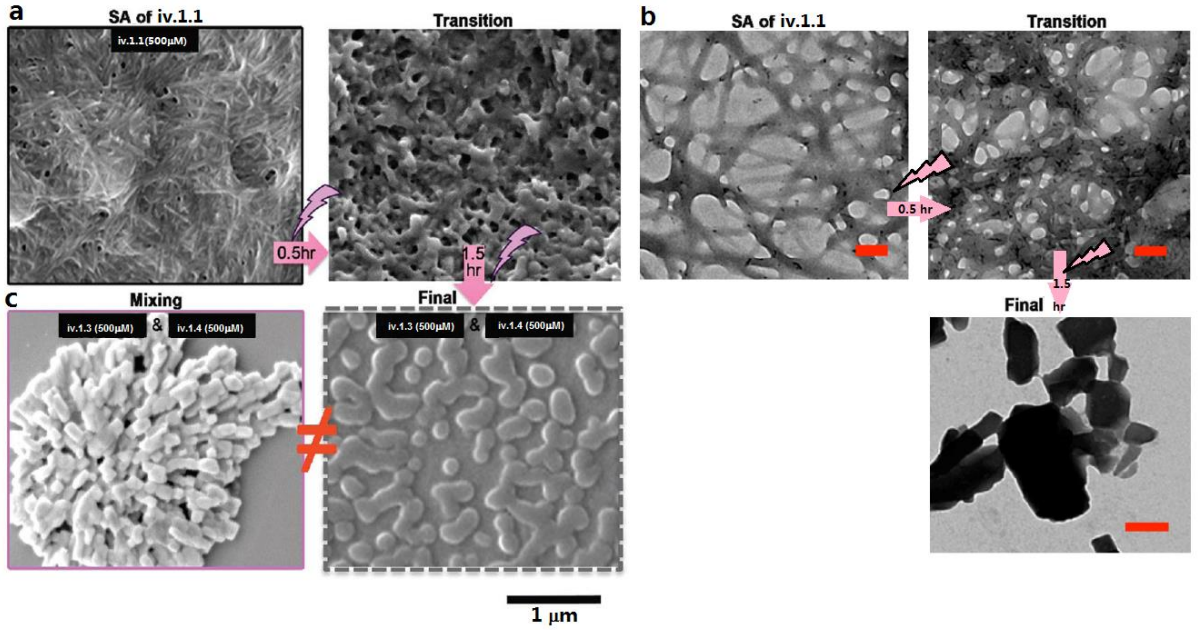

Figure 6. SEM (a) and TEM (b) images of self-assemblies of iv.1.1, at 500 μM in H_2O/DMSO (v/v = 3 : 2), and the transition, final state of photo-cleavage of SA of iv.1.1, scale bar for b is 100 nm. (c) SEM images of iv.1.3/iv.1.4 mixture at 500 μM each in H_2O/DMSO (v/v = 3 : 2).

Upon photo radiation, molecule iv.1.2 slowly transformed into nanoparticles with a wide range of sizes (70 - 380 nm) (Figure 7a/b, transition), the co-localization of nanofibers with nanoparticles indicating the stronger fiber-fiber interaction facilitating the formation of nanoparticles. Until the end of photo-cleavage process, only nanoparticles could be observed (Figure 7a/b, final). The mixture of iv.1.4 and iv.1.5 only formed some irregular aggregates (Figure 7c), which was quite different from the nanoparticles formed in the photo-cleavage pathway. Molecule iv.1.2 formed some thicker nanofibers, indicating the stronger fiber-fiber interaction.

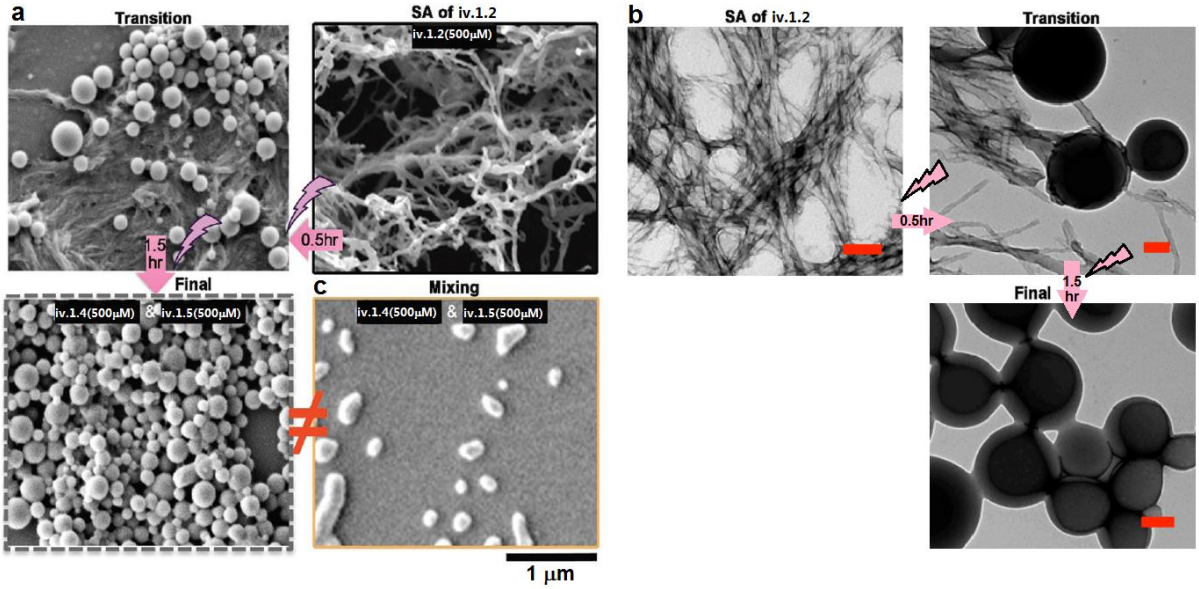

Figure 7. SEM (a) and TEM (b) images of self-assemblies of iv.1.2, at 500 μM in H_2O/DMSO (v/v = 3 : 2), and the transition, final state of photo-cleavage of SA of iv.1.2, scale bar for b is 100nm. (c) SEM images of iv.1.4/1.5 mixture at 500 μM each in H_2O/DMSO (v/v = 3 : 2).

From above results, we could find that even with the same components, if the nanostructures were generated from a pre-stable system through photo-cleavage process, we could achieve some nanostructures that were different from the ground state morphology. Reports from other groups suggested fiber-nanoparticle transformation only lead to nanoparticles with a size smaller than the width of nanofibers.[13] Our current photo-cleavage process provided a new pathway to generate more exotic heterogeneous nanostructures for the nanomaterial fabrication.

IV. 1. 3. 4. Crystal structure

The crystal data of molecule iv.1.3 was collected and structure refinement details are summarized in Table 1, 2 and Figure 8, 9. Crystal data of molecule iv.1.4[10] and iv.1.5[11] were adopted from published results. Crystallographic data for the investigated molecule 6 have been deposited in the Cambridge Crystallographic Data Centre as supplementary publication number CCDC 1531717.

Identification code	shelx
Empirical formula	C17 H12 O5
Formula weight	296.27
Temperature	93(2) K
Wavelength	0.71073 Å
Crystal system	Triclinic
Space group	P -1
Unit cell dimensions	a = 7.1640(4) Å a= 85.162(4) °.
	b = 9.2165(5) Å b= 82.217(4) °.
	c = 10.1606(5) Å g = 81.222(5) °.
Volume	655.52(6) Å3
Z	2
Density (calculated)	1.501 Mg/m3
Absorption coefficient	0.112 mm-1
F(000)	308
Crystal size	0.217 x 0.065 x 0.046 mm3
Theta range for data collection	2.900 to 28.000 °.
Index ranges	-9<=h<=8, -10<=k<=12, -13<=l<=12
Reflections collected	8284
Independent reflections	2901 [R(int) = 0.0696]
Completeness to theta = 25.242 °	99.8 %
Refinement method	Full-matrix least-squares on F2
Data / restraints / parameters	2901 / 0 / 203
Goodness-of-fit on F2	1.037

Final R indices [I>2sigma(I)]	R1 = 0.0504, wR2 = 0.1359
R indices (all data)	R1 = 0.0613, wR2 = 0.1434
Extinction coefficient	n/a
Largest diff. peak and hole	0.463 and -0.319 e.Å-3

Table 1. Crystal data and structure refinement for molecule iv.1.3.

D-H...A	d(D-H)	d(H...A)	d(D...A)	<(DHA)
O(3)-H(3)...O(5)#1	0.87(2)	1.98(2)	2.7561(16)	148(2)

Table 2. Hydrogen bonds for molecule iv.1.3 [Å and °]

Symmetry transformations used to generate equivalent atoms:

#1 -x+2, -y+1, -z+1

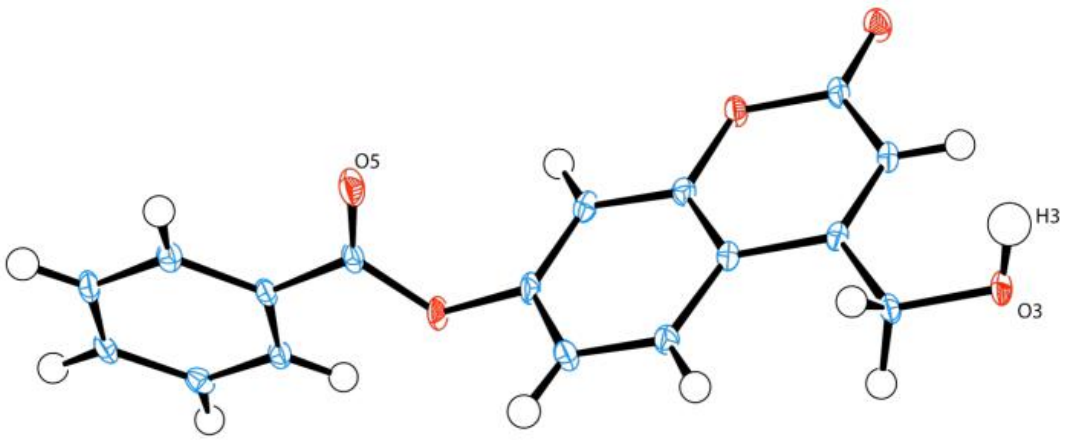

Figure 8. ORTEP diagram showing 50% probability anisotropic displacement ellipsoids for non-hydrogen atoms for molecule iv.1.3.

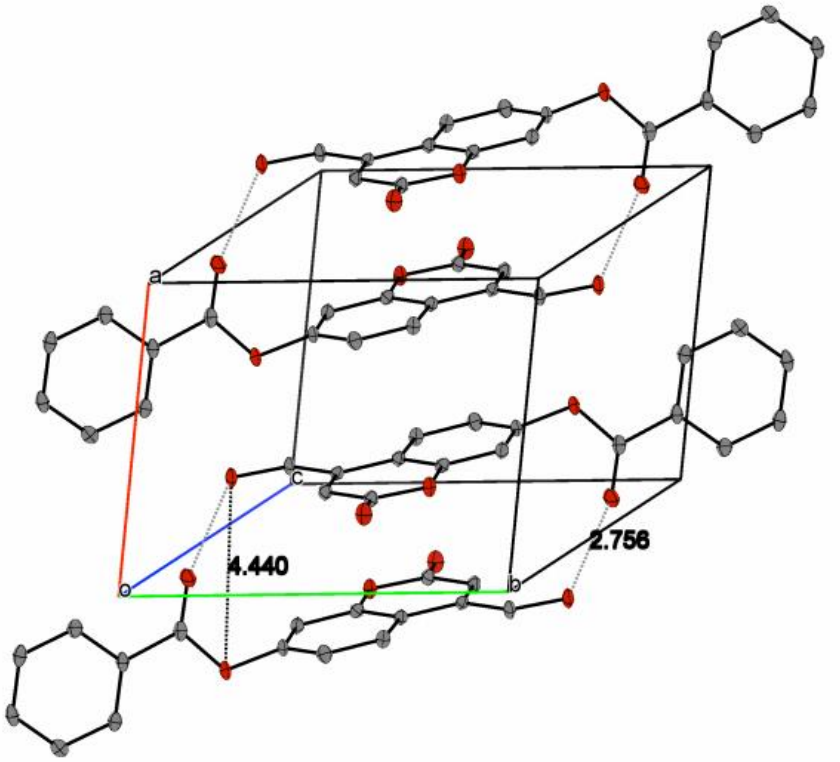

Figure 9. Illustration of the intermolecular packing in molecule iv.1.3.

IV. 1. 3. 5. Potential theoretical explanation on the nanostructure formation

Considering the crystal structure of molecule iv.1.3, iv.1.4 and iv.1.5, we built molecule packing model for self-assembly of molecule iv.1.1 and iv.1.2 through Material Studio (Figure 10). For both molecules iv.1.1 and iv.1.2, strong pi-pi interaction is the main driving force for the fiber formation, and no hydrogen bonding was found in the molecular calculation. After molecular degradation by UV light, we could find that π-π interaction was still retained. Apart from the π-π interaction, intermolecular hydrogen bonding was also formed between the degradation components (green dot line, Figure 10).

The hydrogen bonding between the pre-organized iv.1.4 and iv.1.5 present a larger extent than iv.1.3 and iv.1.4. It may be the possible reason for the formation of very different co-assembly nanostructures. The molecular modelling data suggested that with enhanced non-covalent intermolecular interaction, co-assembly process could produce distinct nanostructures far away from the ground state morphology.

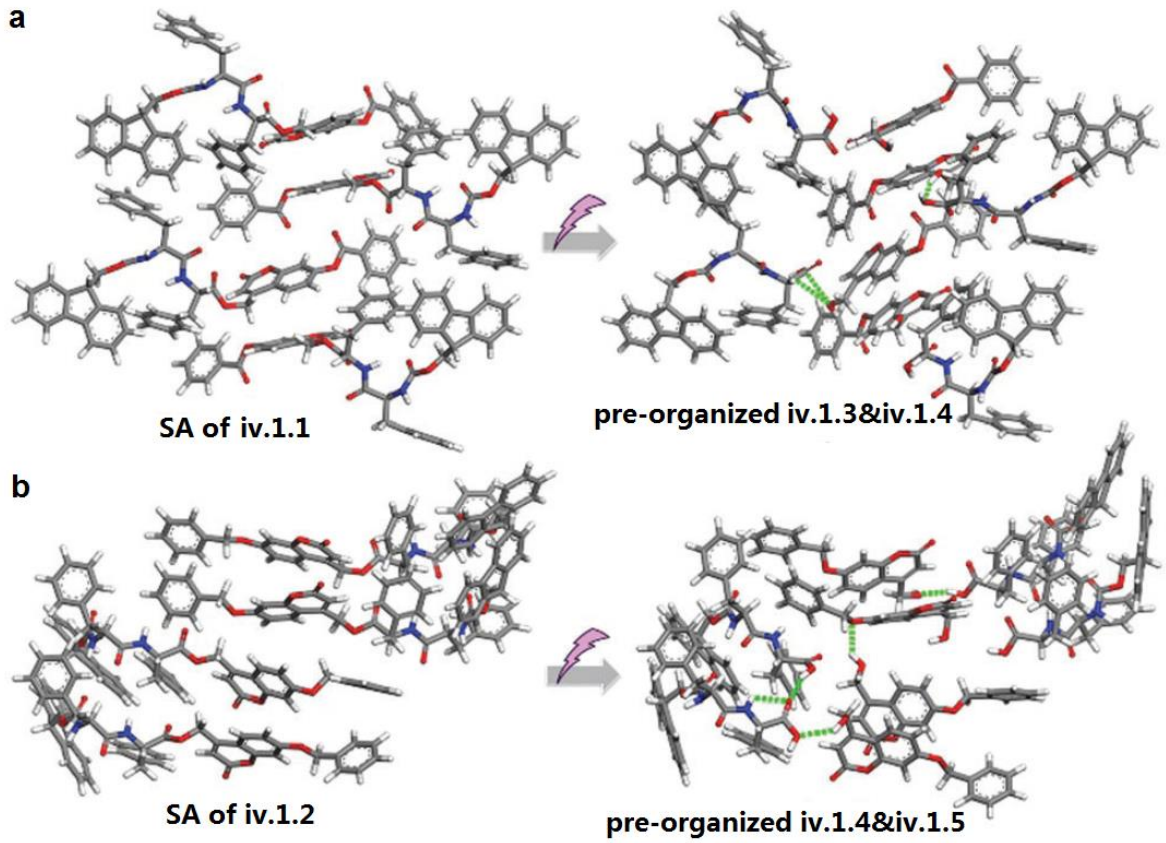

Figure 10. (a) The model structure transitions from SA of iv.1.1 to the preorganized iv.1.3 & iv.1.4 after photo-cleavage. (b) The model structure transitions from SA of iv.1.2 to the pre-organized iv.1.4 & iv.1.5 after photo-cleavage. The green dotted lines represent intermolecular hydrogen bonding.

IV. 1. 4. Conclusion

To synthesize diverse nanostructures from new technologies was still a big challenge for material scientists. Current approach in our study exploited a pre-stabilized self-assembled nanostructure, upon UV-light initiating the degradation of the molecules to their basic building units, the obtained multiple components underwent co-assembly to generate new nanostructures. This co-organizing process provided more choices to diversify the nanostructures fabrication from the same components. Surprisingly, current strategy deliver unconventional nanostructures[14] that were inaccessible through the normal fabrication method due to their favour for lower thermodynamic stability. Our current strategy still faces the challenge in fabricating homogeneous nanostructures, but we successfully provided a new way to fabricate unconventional nanostructures. In addition, the current metastable materials were fabricated through the light stimulus[15], which was clean, non-invasive and good for spatial-temporal control on nanostructure generation. Current work provided an opening for nanomaterial fabrication through delicately controlling on intermolecular distance and precisely light-initiated hydrolysis, it would diversify our strategies to reach various nanomaterial synthesis.

IV. 2. Regulating Higher-Order Organization through the Synergy of Two Self-Sorted Assemblies

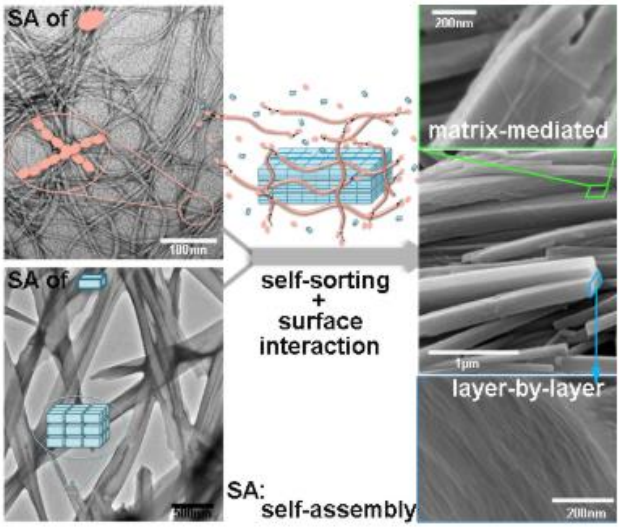

This chapter corresponding to the following publication:

Wei Ji, Shijin Zhang, Sachie Yukawa, Shogo Onomura, Toshio Sasaki, Kun'ichi Miyazawa, and Ye Zhang.* "Regulate Higher-order Organization through the Synergy of Two Self-sorted Assemblies" *Angew. Chem. Int. Ed.* **2018**, 57, 3636-3640

IV. 2. 1. Introduction

In pursuing new method to fabricate functional nanomaterials, molecular self-assembly in chemical synthesis has been proved as an effective bottom-up fabrication pathway.[1] Material scientists have also made much progress in fabricating nanomaterial through mimicking living system, but there is still a huge gap between synthetic self-assembly and biological design. One of the major challenges is to fabricate higher-order organization based on an extended length scale. To develop higher-order organization material,[2] mesoscale self-assembly (MESA)[3] through interactive components is one of the well-developed pathways, especially in the field of fabricating inorganic-organic system. It is well recognized that in living organisms, the higher-order substance with advance functions are fabricated through basic unit self-assembly.[4] However, construction of higher-order and functional materials through a bottom-up process is still a main topic for chemical synthesis self-assembly.

Inspired by the interaction of extracellular matrix (ECM) and cells,[5] cells are constantly reconstructed the model of ECM around them either through their physical movement or excretes; and reciprocally, ECM guides the group behaviour of the cells. We developed a system that the growth of the building block was constructed by the dynamic change of the scaffold (shown in Figure 1).

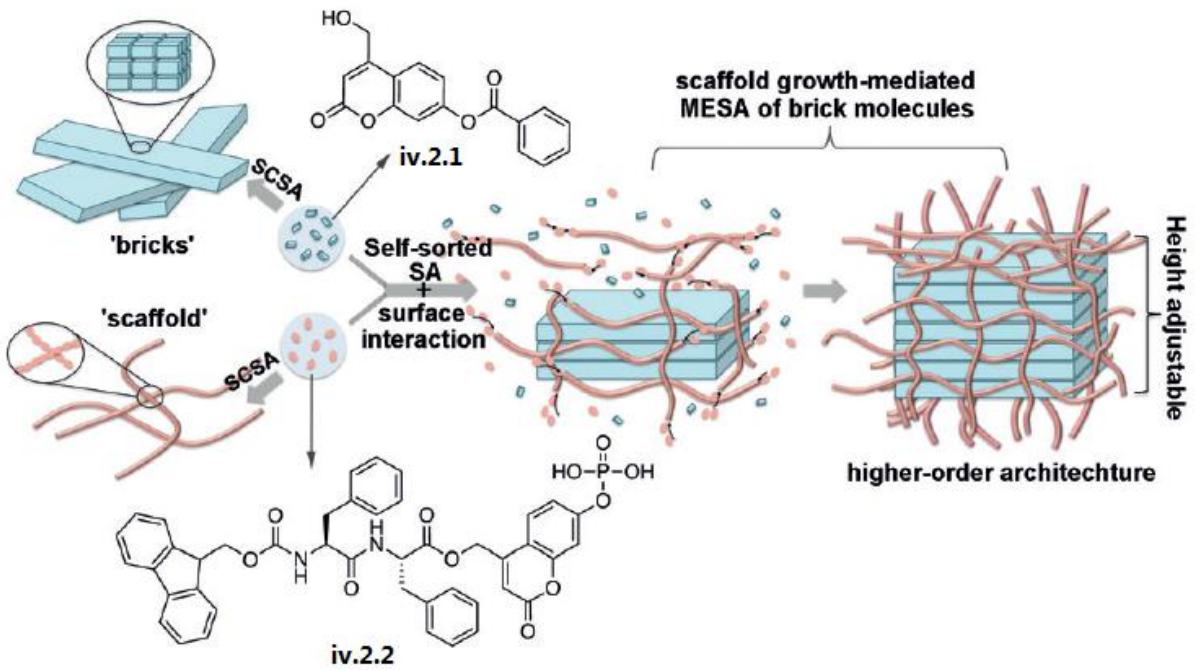

Figure 1. Illustration of higher-order organization through the synergy of two types of self-sorted assembly with molecular structures of molecule iv.2.1 and iv.2.2.

In our molecular design, molecule iv.2.1 self-assembles into brick-like structure, it serves as the building block; molecule iv.2.2 self-assembles into fibrous structure, it serves as the scaffold. And in the mixture system, molecule iv.2.1 and iv.2.2 will adopt the self-sorting behaviour for their orthogonal self-assembly.[6] They work synergistically in a system, with the growing of scaffold, the surface interaction will guide the fabrication of the brick structure into

a higher-order architecture. In a spatial-temporal modification way, dynamic regulating the scaffold growth will further lead to a height regulating in the brick structure.

In exploring the molecules suitable for the higher-order regulation, several key points should keep in mind. First, at the nanoscale level, the driving force for molecule self-assembly should be different, thus they won't adopt co-assembly behaviour in a system; in addition, at the mesoscale level, there should be some surface interaction between the two distinct nanostructure,[3d] thus some extent of similar in the two molecules is required. Secondly, the two self-assembly nanostructures should be distinguishable in the electron microscope observation, thus facilitating morphology confirmation by electron microscope. Third, the scaffold molecule should be responsive to external stimuli, thus dynamic regulating of the scaffold structure could be reached, further regulating on the building block can be controlled. To fulfil all the requirements, we chose coumarin-derived gelators[7] that were responsive to light,[8] designed and synthesized molecule iv.2.1 and iv.2.2 in our study.

IV. 2. 2. Experiment Section

IV. 2. 2. 1. Materials

Chemical reagents	Grade	Manufacturer
Fmoc-Amino acid	98.0%	GL Biochem (Shanghai, China)
2-(1*H*-benzotriazol-1-yl)-1,1,3,3-tetramethyluronium hexafluorophosphate (HBTU)	98.5%	Sigma Aldrich
Trifluoroacetic acid (TFA)	98.0%	Sigma Aldrich
Ethyl 4-chloroacetoacetate	95.0%	Sigma Aldrich
Resorcinol	99.0%	Sigma Aldrich
N-(3-dimethylaminopropyl)-*N*'-ethylcarbodiimide hydrochloride (EDCI)	98.0%	Sigma Aldrich
4-Dimethylaminopyridine (DMAP)	98.0%	Sigma Aldrich
Dibenzyl phosphite	95.0%	Tokyo Chemistry Industry
Sulfuric acid (H_2SO_4)	95.0%	Nacalai Tesque
Methanol (MeOH)	99.0%	Nacalai Tesque
Benzoic acid	99.5%	Nacalai Tesque
Ethyl acetate (EA)	99.0%	Nacalai Tesque
Tetrahydrofuran (THF)	98.0%	Nacalai Tesque
Carbon tetrachloride	99.5%	FUJIFILM Wako Pure Chemical

All organic solvents were dehydrated before experiment by a solvent purification system.

IV. 2. 2. 2. Instruments

Agilent 1260 Infinity Preparation HPLC (Column: 19 mm×150 mm XBridge® Peptide BEH C18 column), Agilent 1260 Infinity Analysis HPLC (Column: 2.1 mm×150 mm XBridge® Peptide BEH C18 column), Thermo LTQ-ETD mass spectrometer (ESI-MS), NMR equipment: Bruker Advance 400 MHz spectrometer, Thermo Nanodrop 2000C spectrophotometer, Transmission Electron Microscope (JEM-1230R), Milli-Q® Integral 3/5/10/15 System, Scanning Electron Microscope (FEI Quanta 250 FEG), Circular dichroism spectroscopy (JASCO J-820), Atomic force microscope (SHIMADZU Scanning Prob Microscope SPM-9700HT), Rotary Rheometer (Anton-Paar MCR302), FTIR (Bruker ALPHA II).

IV. 2. 2. 3. Synthesis

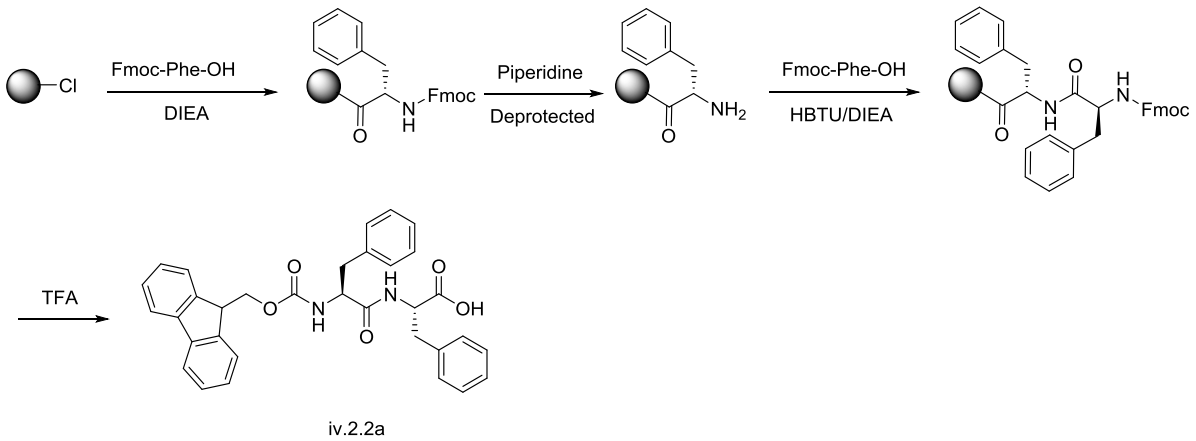

 iv.2.2a

Scheme 1. Synthesis of compound iv.2.2a.

Compound **iv.2.2a**: Compound iv.2.2a was obtained via solid phase peptide synthesis (SPPS). 2-Chlorotrityl chloride resin (2.0 g, 2 mmol) was swelled in anhydrous DCM for 20 min, L-Fmoc-Phe-OH (1.94 g, 5 mmol) dissolved in anhydrous DMF was conjugated to resin with DIEA in 30 min. Then washed with anhydrous DMF for 3 times, unreacted sites in the resin were blocked with DCM/MeOH/DIEA (80:15:5) for 20 min and washed by anhydrous DMF for 5 times. Then piperidine solution (20% in DMF) was added into reaction for 30 min to remove the Fmoc protecting group on the amino acid. Elongation was conducted in the presence of conjugation reagents HBTU (2.28 g, 6 mmol) and DIEA (2.08 mL, 12 mmol), they were dissolved in 5 mL anhydrous DMF together with L-Fmoc-Phe-OH (2.32 g, 6 mmol), the mixture was added into the resin and kept reaction for 30 min. The resin was washed by anhydrous DMF, MeOH, DCM and hexane for 5 times, the iv.2.2a was cleaved off the resin using TFA for 2 h. After removing the solvent, anhydrous ether was added into the concentrated product and white precipitation of iv.2.2a.

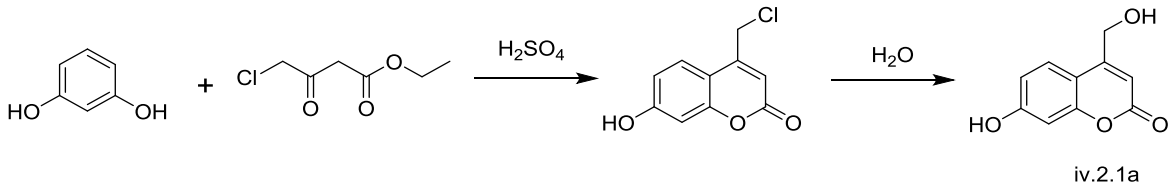

iv.2.1a

Scheme 2. Synthesis of compound iv.2.1a.

Compound **iv.2.1a**: Resorcinol (5.50 g, 50 mmol) was carefully adding into the cooled down (0 ^{o}C) concentrated 40mL H_2SO_4 solution. Then ethyl 4-chloroactoacetate (9.10 g, 55 mmol) was adding into the reaction mixture and kept stirring at room temperature overnight. The reaction mixture was slowly pouring into 500mL ice/water mixture, the precipitates was filtered and washed by 100mL water for 3 times. The resulting white precipitates was transferred to a 500mL round bottom flask and 200mL water was added into the flask, refluxed for 3 days. The hot reaction mixture solution was filtered, the filtrated was cooled down to room temperature for 12 hours. The pale needle crystal formed in the solution was filtered and washed by 50mL water for 3 times. The obtained crystal was dried in a 60 ^{o}C oven to give iv.2.1a. The yield is 70.1%.

[1]HNMR (400 MHz, DMSO-*d6*) δ = 10.49 (d, *J*=13.1, 1H), 7.50 (dd, *J*=13.3, 8.7, 1H), 6.85 – 6.63 (m, 2H), 6.21 (d, *J*=13.2, 1H), 5.74 – 5.35 (m, 1H), 4.68 (d, *J*=13.2, 2H).

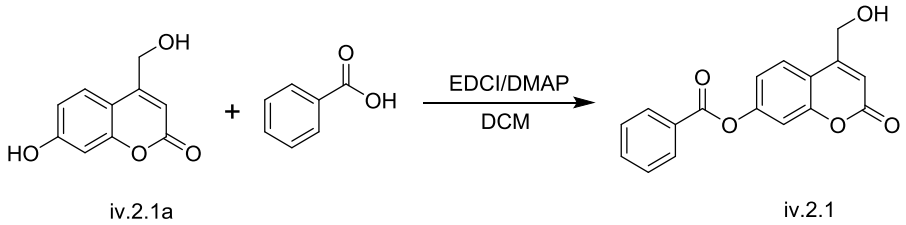

iv.2.1a iv.2.1

Scheme 3. Synthesis of compound iv.2.1.

Compound **iv.2.1**: Benzoic acid (0.24 g, 2 mmol) was dissolved in 20mL anhydrous DCM, then EDCI (0.38 g, 2 mmol), DMAP (24 mg, 0.2 mmol) and iv.2.1a (0.39 g, 2 mmol) were added into the reaction mixture, stirring at room temperature overnight. The reaction mixture was washed by 5mL water for 3 times, the organic layer was dehydrated with anhydrous Na_2SO_4 for 4 hours. It was further purified by silica column chromatography to give compound iv.2.1. The yield was 48.1%.

[1]HNMR (400MHz, DMSO-*d6*) δ = 8.17 (d, *J* = 0.8 Hz, 2H), 7.77-7.83 (m, 2H), 7.64 (t, *J* = 0.8 Hz, 2H), 7.50 (d, *J* = 0.4 Hz, 1H), 7.33-7.36 (dd, J_1 = 0.4 Hz J_2 = 0.4 Hz, 1H), 6.49 (s, 1H), 5.71 (t, *J* = 0.8 Hz, 1H), 4.81 (d, *J* = 0.4 Hz, 2H).

[13]CNMR (101MHz, $CDCl_3$) δ = 164.72, 160.50, 156.80, 154.16, 153.48, 135.07, 134.88, 130.51, 129.58, 129.04, 125.99, 119.09, 115.90, 111.04, 110.69, 59.64.

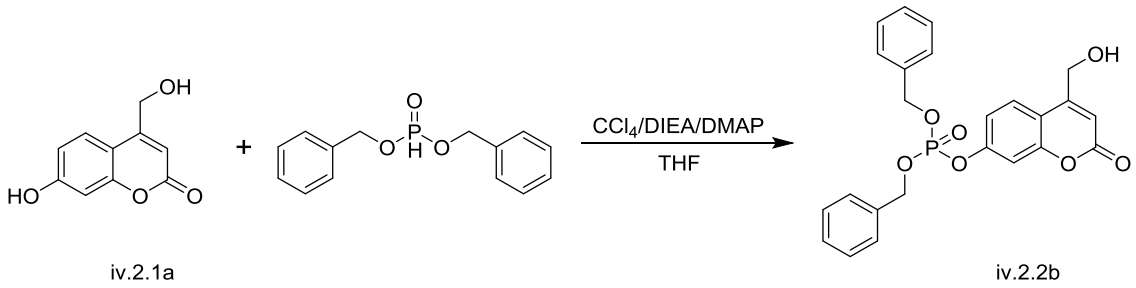

iv.2.1a iv.2.2b

Scheme 4. Synthesis of compound iv.2.2b.

Compound **iv.2.2b**: A solution of iv.2.1a (0.95 g, 5 mmol) in THF (25 mL) was cooled to -10 ℃, then carbon tetrachloride (CCl_4) (7.5 g, 50 mmol), N,N-diisopropylethylamine (DIEA) (1.3 g, 10 mmol), 4-dimethylaminopyridine (DMAP) (0.05 g, 0.5 mmol) and dibenzyl phosphite (1.3 g, 5 mmol) were added into THF solution in sequence, respectively. The whole mixture was stirred for overnight at room temperature. The resulting solution was concentrated, and the resulting precipitate was purified by silica column chromatography (DCM/EA = 5/1) yielding iv.2.2b as a white solid (1.50 g, 68%).

[1]HNMR (400 MHz, DMSO-*d6*) δ: 7.71 (d, *J* = 8.0 Hz, 1H), 7.37 (s, 10H), 7.16-7.21 (m, 2H), 6.44 (s, 1H), 5.69 (s, 1H), 5.21 (d, *J* = 8.0 Hz, 4H), 4.75 (s, 2H).

^{13}CNMR (101 MHz, DMSO-*d6*) δ: 160.31, 156.57, 154.21, 152.73, 135.94, 135.88, 129.07, 128.98, 126.39, 116.82, 115.17, 110.34, 108.69, 70.27, 70.22, 59.53.

HRMS (ESI) calculated for $C_{24}H_{21}O_7P$ $[M+H]^+$, 453.1025; found, 453.4546

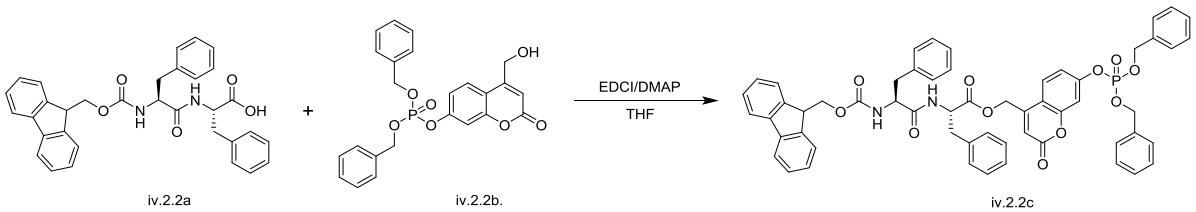

iv.2.2a iv.2.2b. iv.2.2c

Scheme 5. Synthesis of compound iv.2.2c.

Compound **iv.2.2c**: A THF solution (20 mL) of iv.2.2a (0.50 g, 1.1 mmol), iv.2.2b (0.70 g, 1.32 mmol), 1-Ethyl-3-(3-dimethylaminopropyl) carbodiimide hydrochloride (EDCI) (0.25 g, 1.32 mmol) and 4-dimethylaminopyridine (DMAP) (14 mg, 0.11 mmol) was stirred at room temperature for 24 hours. The resulting solution was concentrated and dissolved in DCM (20 mL). The solution was washed with deionized water (3 x 5 mL) and then the organic layer was collected. The solvent was removed, and the resulting precipitate was purified by column chromatography (DCM/EA = 5/1), yielding iv.2.2c as a white solid (0.68 g, 63%).

^{1}HNMR (400 MHz, DMSO-*d6*) δ: 8.67 (d, *J* = 8.0 Hz, 1H), 7.80-7.84 (m, 2H), 7.53-7.60 (m, 4H), 7.11-7.33 (m, 26H), 6.37 (d, *J* = 16.0 Hz, 1H), 5.32-5.36 (m, 2H), 5.15-5.18 (d, *J* = 12.0 Hz, 4H), 4.60-4.68 (m, 1H), 4.22-4.26 (m, 1H), 3.96-4.11 (m, 3H), 2.51-3.09 (m, 4H).

^{13}CNMR (101 MHz, DMSO-*d6*) δ: 172.53, 171.33, 159.72, 156.24, 154.29, 153.00, 152.90, 149.56, 144.24, 144.13, 141.10, 138.46, 137.34, 137.26, 135.88, 135.81, 129.69, 129.55, 129.08, 128.99, 128.74, 128.59, 128.47, 128.08, 127.51, 127.12, 126.74, 125.79, 125.73, 120.50, 117.01, 114.63, 112.33, 108.73, 70.36, 70.30, 66.19, 62.09, 56.34, 54.32, 47.00, 37.89, 36.95.

HRMS (ESI) calculated for $C_{57}H_{49}N_2O_{11}P$ $[M+H]^+$, 969.3074; found, 969.2728.

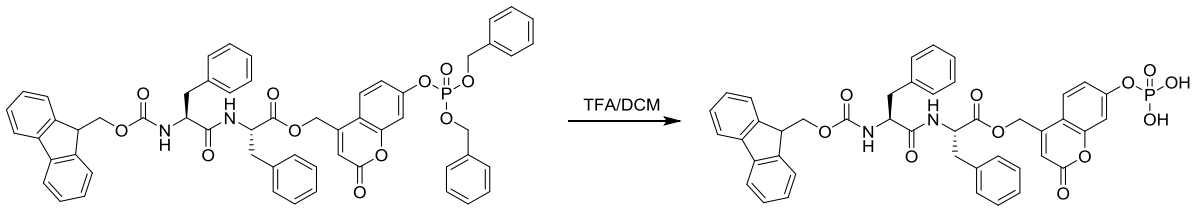

iv.2.2c iv.2.2

Scheme 6. Synthesis of compound iv.2.2.

Compound **iv.2.2**: A DCM solution (5 mL) of iv.2.2c (0.10 g, 1.1 mmol) and trifluoroacetic acid (TFA) (5 mL) was stirred at room temperature for overnight. The resulting solution was

concentrated, and the crude product was purified by column chromatography (DCM/MeOH = 20/1) yielding iv.2.2 as a white solid (0.06 g, 76%).

^{1}HNMR (400 MHz, DMSO-*d6*) δ: 8.67 (d, *J* = 8.0 Hz, 1H), 7.81-7.84 (m, 2H), 7.38-7.57 (m, 4H), 7.22-7.35 (m, 4H), 7.11-7.17 (m, 12H), 6.32 (d, *J* = 16.0 Hz, 1H), 5.28-5.39 (m, 2H), 4.62-4.66 (m, 1H), 4.24-4.26 (m, 1H), 3.94-4.06 (m, 3H), 2.55-3.03 (m, 4H).

^{13}CNMR (101 MHz, DMSO-*d6*) δ: 172.47, 171.33, 159.94, 158.52, 154.94, 154.41, 149.87, 144.26, 144.16, 141.11, 137.28, 134.16, 129.66, 129.55, 129.49, 129.27, 129.16, 128.89, 128.74, 128.68, 128.46, 128.08, 127.50, 127.12, 126.68, 126.42, 125.82, 125.75, 120.53, 117.10, 111.43, 108.16, 70.22, 66.14, 62.12, 56.25, 54.27, 46.98, 37.82, 36.91.

HRMS (ESI) calculated for $C_{43}H_{37}N_2O_{11}P$ $[M+H]^+$, 789.2135; found, 789.2727.

IV. 2. 2. 4. Gel preparation.

To avoid nanostructure change induced by solvent effect, we applied same solvent combinations to all the gel preparations. 20 μL dimethyl sulfoxide (DMSO) solution of the iv.2.1, iv.2.2, or mixture iv.2.1/2.2 were added to 180 μL water with a final adjustment of DMSO concentration to 10%. Gel formation was judged by the "invert-vial" method. For scaffold modifications, the UV light irradiation and enzyme addition were applied right after the final adjustment of DMSO concentration.

IV. 2. 2. 5. Circular dichroism (CD) spectroscopy

CD spectra of all the samples were collected on a spectrometer JASCO J-820 CD with bandwidth of 1.0 nm in the ultraviolet (UV) region (190-400 nm) using a 1 mm quartz cuvette.

IV. 2. 2. 6. Scanning electron microscopy (SEM)

SEM samples were prepared by adding a drop of sample on a silicon wafer. The silicon wafer was allowed to freeze at -80 ℃ for 30 min and then lyophilized. Samples were coated with platinum before imaging. SEM images were taken on a scanning electron microscope FEI Quanta 250 FEG.

IV. 2. 2. 7. Transmission electron microscopy (TEM)

Aliquots (10 μL) of sample solution were added into a glow discharge copper grid (400 mesh) coated with thin carbon film and then remove the excess solution, the grid was washed with deionized water three times and then stained with 2.0% (w/v) uranyl acetate (UA) by exposing the grid in one drop of UA solution for 10 s. TEM images were captured at high vacuum on transmission electron microscope JEM-1230R (JEOL, Japan).

IV. 2. 2. 8. Atomic force microscope (AFM)

AFM samples were prepared by depositing dilute solution (30-fold) of gels on mica substrates. Images were taken by using SHIMADZU Scanning Probe Microscope SPM-9700HT.

IV. 2. 2. 9. Rheology measurements.

The rheological properties of gels iv.2.1, iv.2.2, or mixture iv.2.1/2.2 were measured with a Rotary Rheometer (Anton-Paar MCR302). The dynamic frequency sweep measurements were performed using a sinusoidal shear strain of constant peak amplitude (0.1%) over a range of frequencies (0.1-100 $rads^{-1}$) at 25℃.

IV. 2. 2. 10. Kinetics of time-dependent photo-cleavage and enzyme hydrolysis of iv.2.2.

Both UV-light irradiation (320nm, 100 mW/cm^2) and enzyme addition were applied right after the compound was dissolved. At certain reaction time, 40 μL of sample was taken out and mixed with 160 μL MeOH, then injected into HPLC (Agilent 1260 Infinity) to analyse and quantify the hydrolysis rate of iv.2.2. The compositions were confirmed by LC-MS (Thermo, Finniqan LTQ).

IV. 2. 3. Results

IV. 2. 3. 1. Single Component Self-assembly Study

Fully investigation on single component will help us to get a clearer understanding of each component, it will definitely help us to figure out whether these two components are suitable for further combination study. We firstly carried out gelation study.

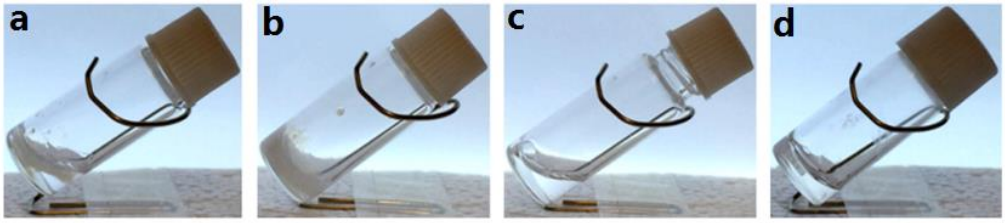

Figure 2. Investigation of critical gelation concentration (CGC) of iv.2.1 and iv.2.2. Gel test of iv.2.1 below (a) and over (b) the concentration of 0.12 wt% in H_2O/DMSO (v/v = 9:1). Gel test of iv.2.2 below (c) and over (d) the concentration of 0.25 wt% in H_2O/DMSO (v/v = 9:1).

As is shown in Figure 2, both molecules iv.2.1 and iv.2.2 could form self-supported hydrogels when their concentrations are over the critical gelation concentration. For molecule iv.2.1, it immediately formed opaque gel (Figure 2b); and molecule iv.2.2 showed a relatively slow rate to form transparent gel after 48 s (Figure 2d). The gel from molecule iv.2.1 and iv.2.2 is visually different, we further use electron microscope to figure out whether there is any difference in their nanostructure.

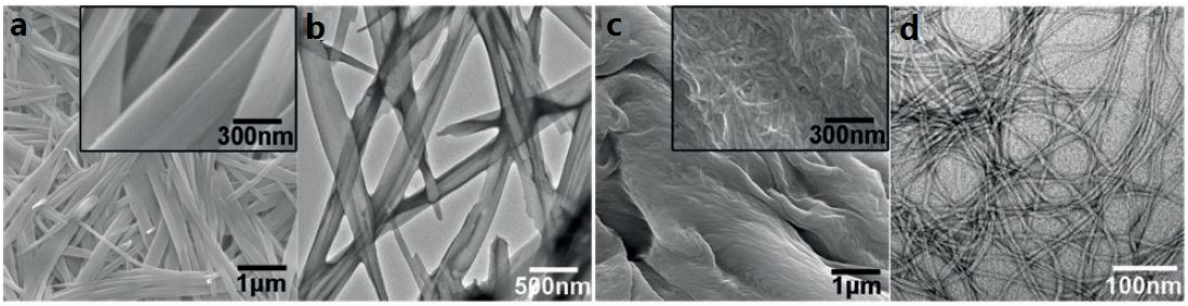

Figure 3. (a) SEM and (b) TEM images of nanostructure of iv.2.1 in H_2O/DMSO (v/v=9:1) at concentration of 0.8 wt%. (c) SEM and (d) TEM images of nanostructure of iv.2.2 in H_2O/DMSO (v/v=9:1) at concentration of 0.8 wt%.

Under the electron microscope (SEM, TEM), we can observe some rigid nanobelts formed by molecule iv.2.1, they ranged from 150 nm to 250 nm in width (Figure 3a/b). In the meantime, we can observe molecule iv.2.2 self-assembling into flexible nanofibers with a width from 7 nm to 8 nm (Figure 3c/d). The totally different nanostructures from molecule iv.2.1 and iv.2.2 make them possible to be distinguished when they were mixed in a system. In the mixed system, molecule iv.2.1 could work as the building block due to its large and rigid structure, while molecule iv.2.2 could work as the scaffold due to its flexible nature. When we dug a bit further into their molecule structure, we found that the driving forces for molecule iv.2.1 to self-assemble were π-π interaction between coumarins and O—H ··O

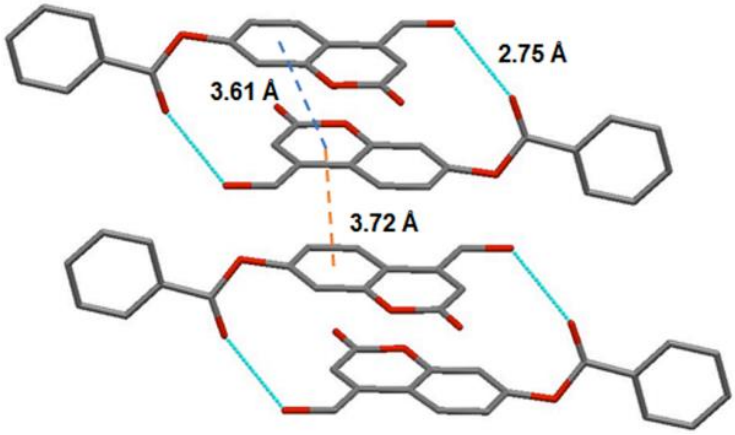

Figure 4. Packing mode of iv.2.1 in the single crystal framework.

hydrogen bonding. It was confirmed by the single-crystal packing mode from molecule iv.2.1 (Figure 4).[7b] In the case of molecule iv.2.2, the driving forces for molecule self-assembly were a different π-π interaction and N—H ··O hydrogen bonding.[9] The difference in the driving forces for molecule self-assembly will make it possible to support a self-sorting behaviour when they were mixed in a system.

To confirm the orthogonality of molecule iv.2.1 and iv.2.2, we checked their circular dichroism (CD) spectra by studying the self-assembly induced Cotton effect.[6e] The results were shown in Figure 5, it was obvious that the CD spectrum of molecule iv.2.1 is quite different from molecule iv.2.2. The CD spectrum of molecule iv.2.2 showed a positive peak at 231nm, which was originated from the peptide subunit; the positive peak at 255nm was caused by the exciton

effect induced by the J-aggregation of fluorenyl group and coumarin subunit (Figure 5b/c).[9c, 9f]

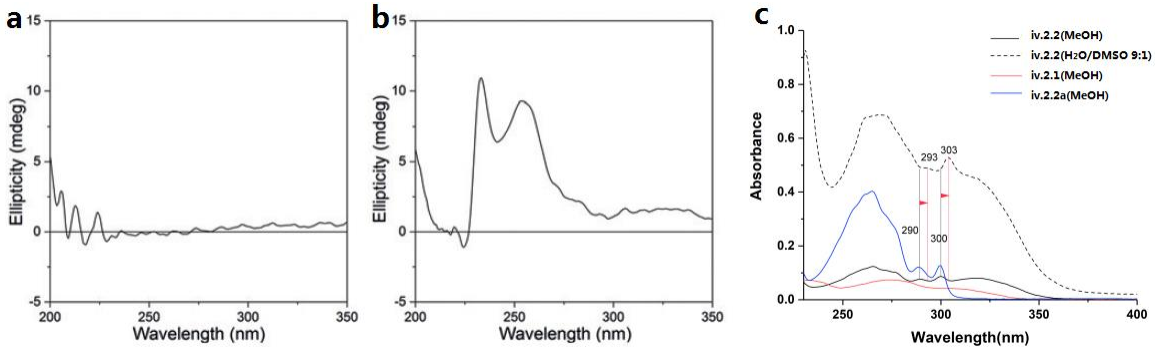

Figure 5. CD spectra of (a) iv.2.1 (0.05 wt%), (b) iv.2.2 (0.05 wt%) in H_2O/DMSO (v/v=9:1); (c) UV-Vis spectra of iv.2.2 in MeOH (monomer) and in H_2O/DMSO (9:1) (self-assembly), iv.2.1 in MeOH (monomer), and iv.2.2a in MeOH (monomer). Through the comparison between the spectra before and after self-assembly, the red shifts are indicated by lines and arrows.

IV. 2. 3. 2. Self-sorting Behaviour Study in a System

CD spectroscopy has been widely used in distinguish two components whether they adopt co-assembly or self-sorting behaviour in a system. Briefly, if the spectrum from the simply sum of the two components (Theor.) is equal to the result obtained from the measurement of the two components in a solution (Exp.), it indicates the two components adopt self-sorting behaviour in the solution. If the Theor. result is not equal to Exp. result, it means the two components have some interaction in the solution, they adopt co-assembly behaviour. We started with 1 : 1 ratio of molecule iv.2.1 and iv.2.2. As is shown in Figure 6a, the experiment result is almost identical to the theoretical result, it indicates that molecule iv.2.1 and iv.2.2 adopt self-sorting behaviour in the solution. To further confirm the two components adopting self-sorting behaviour in a system, we varied the ratio of molecule iv.2.1 and iv.2.2 in the solution and checked the CD spectra. We chose to vary the ratio of molecule iv.2.1/iv.2.2 from 4 : 1 to 1 : 4, specifically, the concentration of molecule iv.2.1 changed from 0.08 wt% to 0.02 wt%; and the concentration of molecule iv.2.2 started with 0.02 wt% and ended with 0.08 wt%. The CD spectra for the single component were shown in Figure 6b (molecule iv.2.1) and Figure 6c (molecule iv.2.2), and the experiments results for varied ratios of mixture were shown in Figure 6d. In the quantitative results (Figure 6e), we can find that the peaks at both 231nm and 255nm rose linearly by increasing the ratio of molecule iv.2.2. And the experiment results were consistent with the theoretical sum of both components, it suggested even we varied the ratio of molecule iv.2.1 and iv.2.2 in a system, they were not likely to interact with each other.
To make our assumption more convinced, we carried out FTIR experiments based on single components and the mixture. The results were shown in Figure 7, the theoretical FTIR spectrum from molecule iv.2.1 and iv.2.2 was almost identical to the experiment spectrum from the mixture, it suggested molecule iv.2.1 and iv.2.2 adopting self-sorting behaviour in the solution.

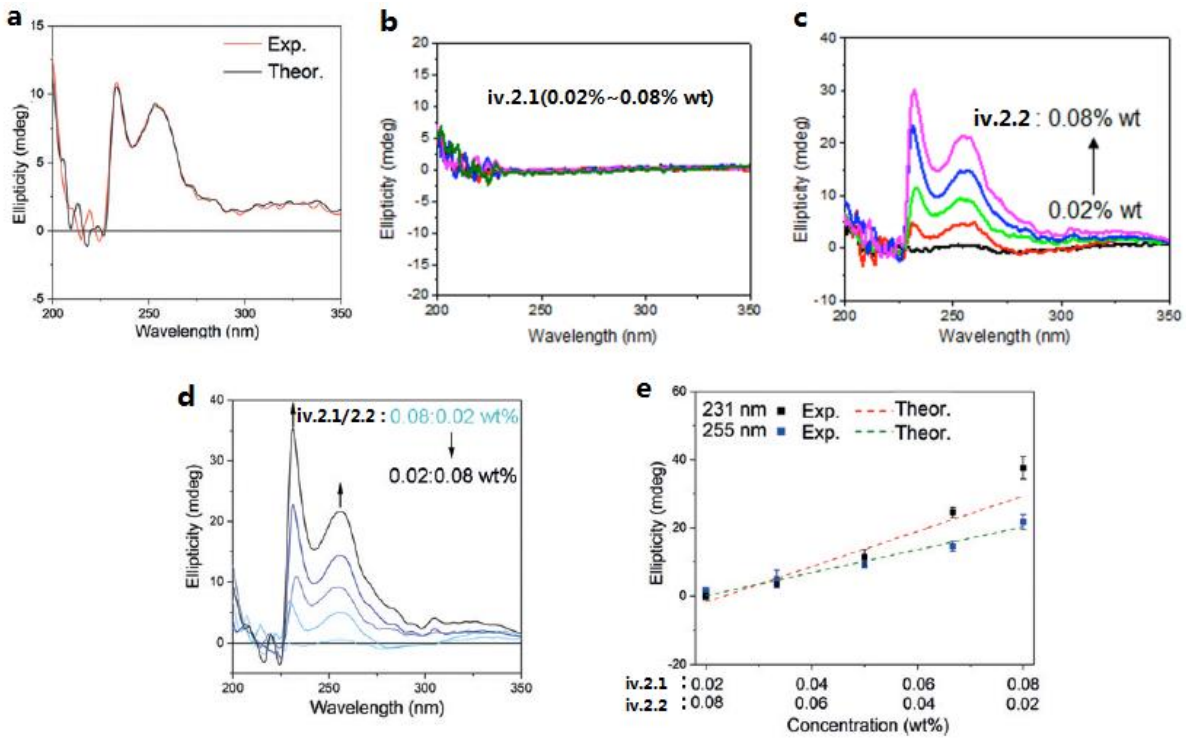

Figure 6. CD spectra (a) a iv.2.1/ iv.2.2 mixture ([iv.2.1]=0.05 wt%, [iv.2.2]=0.05 wt%) in H_2O/DMSO (v/v=9:1); concentration-dependent changes of CD spectra (b: iv.2.1, c: iv.2.2); (d) CD spectra of a iv.2.1/iv.2.2 mixture at various ratios in H_2O/DMSO (v/v=9:1). (e) Plots of CD intensities of the iv.2.1/iv.2.2 mixture at 231 nm and 255 nm versus mixing ratios from (d). Theoretical lines were calculated from the CD intensities of each component at various concentrations. Data represent mean ±standard deviation of the mean (n=3).

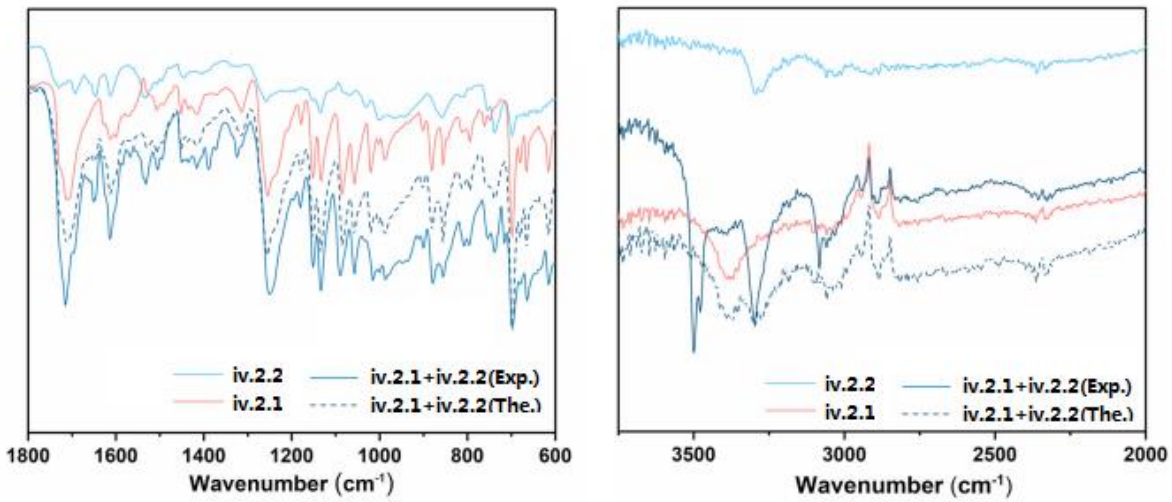

Figure 7. FTIR spectra of iv.2.1 (0.8 wt%), iv.2.2 (0.8 wt%), and iv.2.1 + iv.2.2 mixture (0.8 wt% of each) in H_2O/DMSO (v/v = 9:1). Exp. and The. Represent experimental and theoretical FTIR spectra, respectively.

IV. 2. 3. 3. Evaluate the Influence of Scaffold (Molecule iv.2.2) on Higher Order of Building Block (Molecule iv.2.1)

In order to study the influence of molecule iv.2.2 on the growth of molecule iv.2.1, we varied the ratio of molecule iv.2.2 when mixed with molecule iv.2.1 in a system. The nanostructures were observed by SEM and AFM, and results were shown in Figure 8. In the absence of molecule iv.2.2, we can observe nanobelts from the self-assembly of molecule iv.2.1 (Figure 8a). When molecule iv.2.1 was added into the system, we can find two distinct nanostructures from SEM, one was nanobelt from molecule iv.2.1 and the other was nanofibers from molecule iv.2.2 (Figure 8b-f). We further measured the height of the nanobelts through AFM.

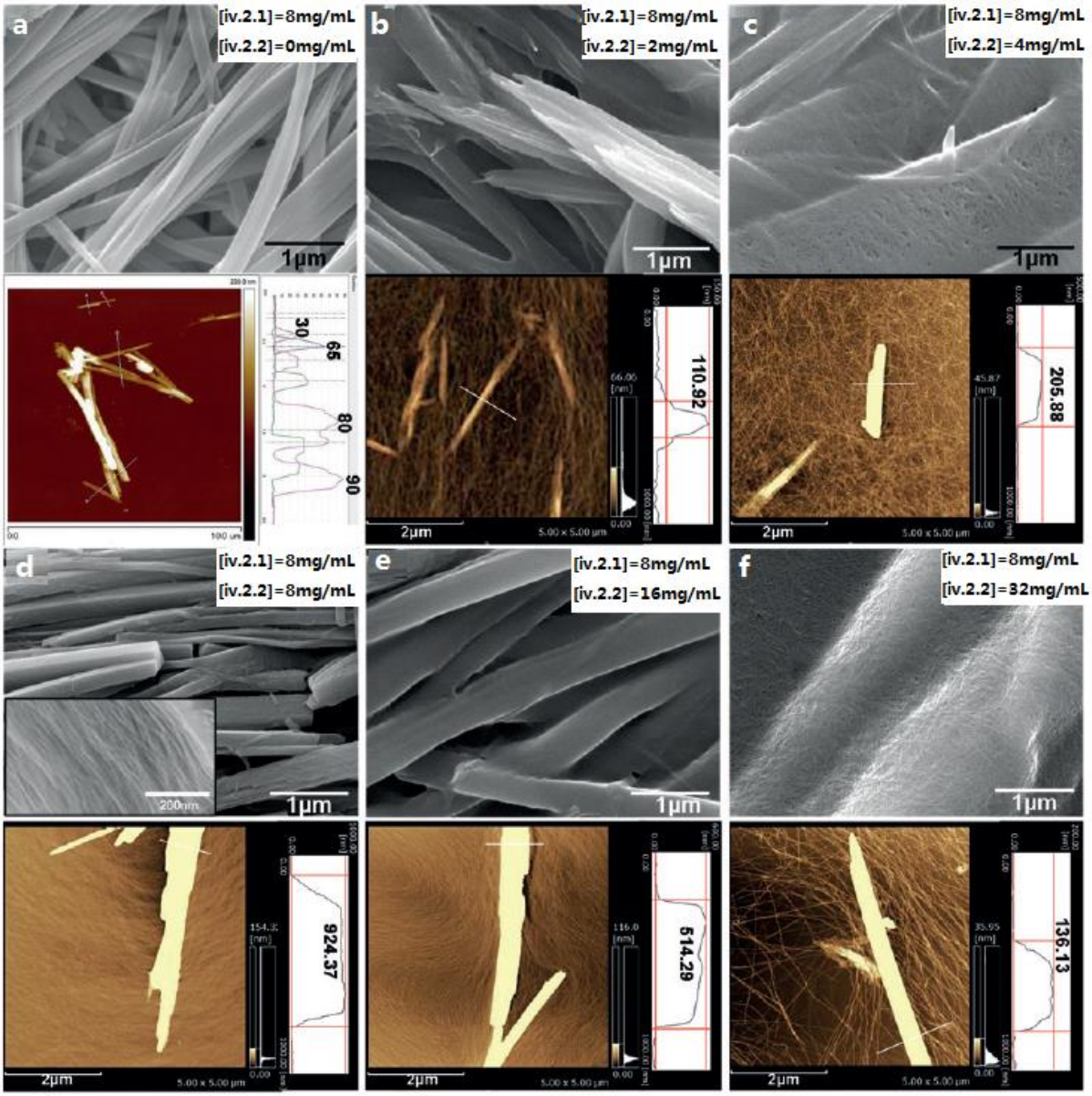

Figure 8. SEM images and the correlated AFM images with height profiles of (a) self-assembly nanostructure of iv.2.1 and (b-f) a mixture of iv.2.1 (8 mg mL^{-1}) with iv.2.2 at various concentrations, from (b) 2 mg mL^{-1}, (c) 4 mg mL^{-1}, (d) 8 mg mL^{-1}, (e) 16 mg mL^{-1}, to (f) 32 mg mL^{-1} in H_2O/DMSO (v/v=9:1). The inset SEM image in (d) is the section structure of layer-by-layer nanosheet.

In the absence of molecule iv.2.2, the height of the nanobelts were around 50 nm. Upon increasing the concentration of molecule iv.2.2 to 2 mg mL^{-1}, we found the height of the nanobelts increased to 110 nm. When the concentration of molecule iv.2.2 was 4 mg mL^{-1}, the height of the nanobelts was 205 nm. Once the concentration of molecule iv.2.2 was 8 mg mL^{-1}, the height of the nanobelts reached 920 nm. We further look into the way for the nanobelts growth. Through the section observation of the nanobelts (Figure 8d, inset), we found layer-by-layer architecture, it suggested that a mesoscale self-assembly pathway to reach a higher organization of the nanobelts. Over-increasing the concentration of molecule iv.2.2 will result in a decreased height of the nanobelts. Molecule iv.2.2 at a concentration of 16 mg mL^{-1}, the height of the nanobelts was 514 nm, further increase the concentration to 32 mg mL^{-1}, the height of the nanobelts was 136 nm. The quantitative results were shown in Figure 9.

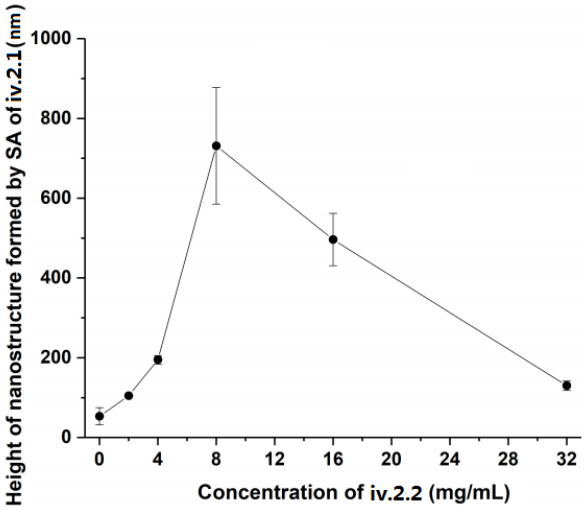

Figure 9. The graph shows the heights of nanobelts formed by self-assembly (SA) of iv.2.1 (8mg/mL) of iv.2.1/2.2 mixture in H_2O/DMSO (v/v = 9:1) versus concentrations of iv.2.2 in the mixture measured by AFM. The error bars represent the standard deviation.

To gain a clear understanding of the influence of molecule iv.2.2 on molecule iv.2.1 in a mixed solution, we carried out the kinetic process study of both single component and the mixture.[10] The phase transition results based on visual observation was shown in Figure 10. We can easily find phase transition from transparent to opaque in high concentration (16 mg mL^{-1}) of molecule iv.2.2 or in the mixture solution during the self-assembly process.

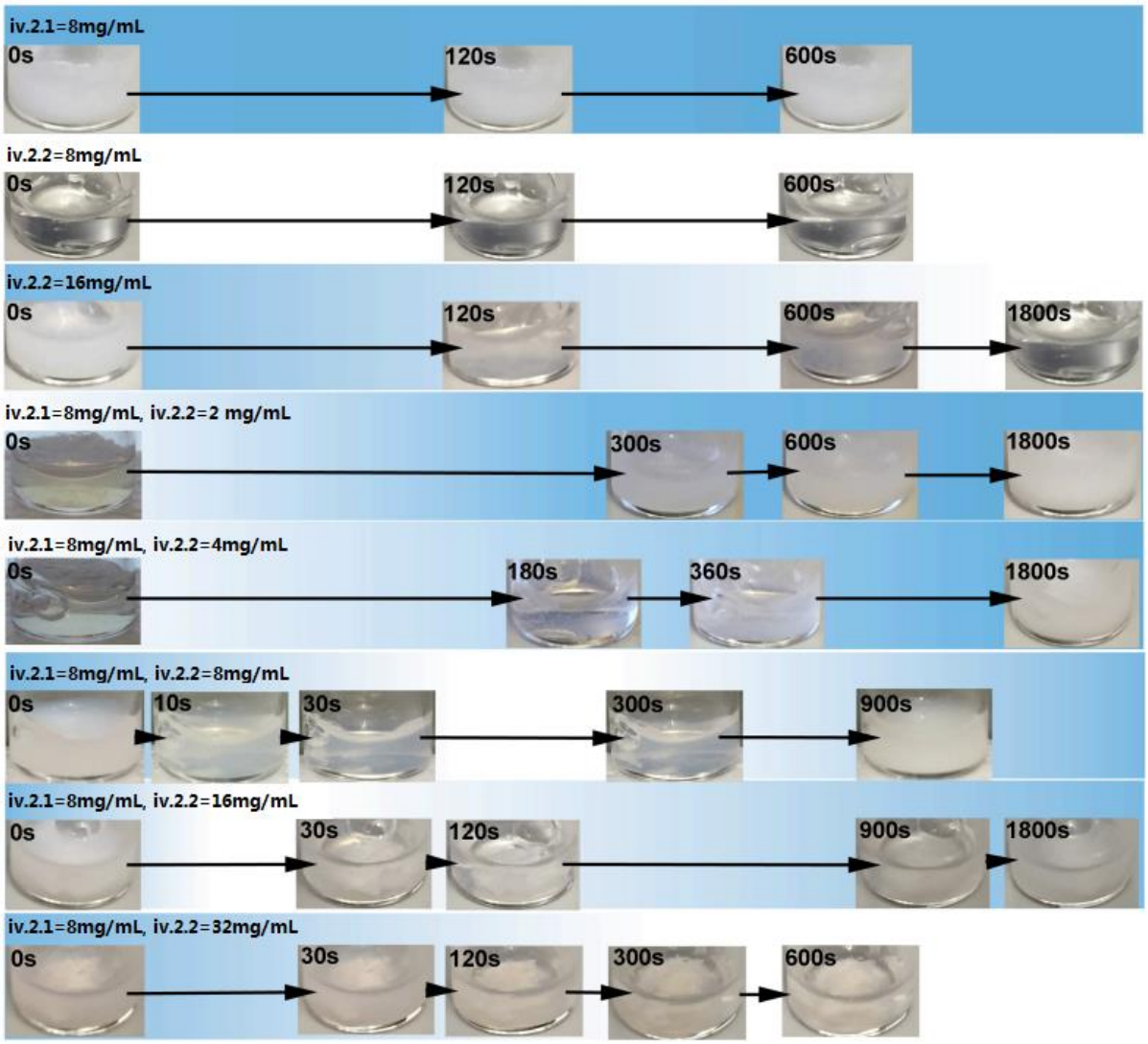

Figure 10. Time lapse optical images of iv.2.1 (8 mg/mL), iv.2.2 (8 mg/mL, 16 mg/mL) and iv.2.1/iv.2.2 at various ratios in H_2O/DMSO (v/v = 9:1) applied for estimation of time-dependent transparency profiles.

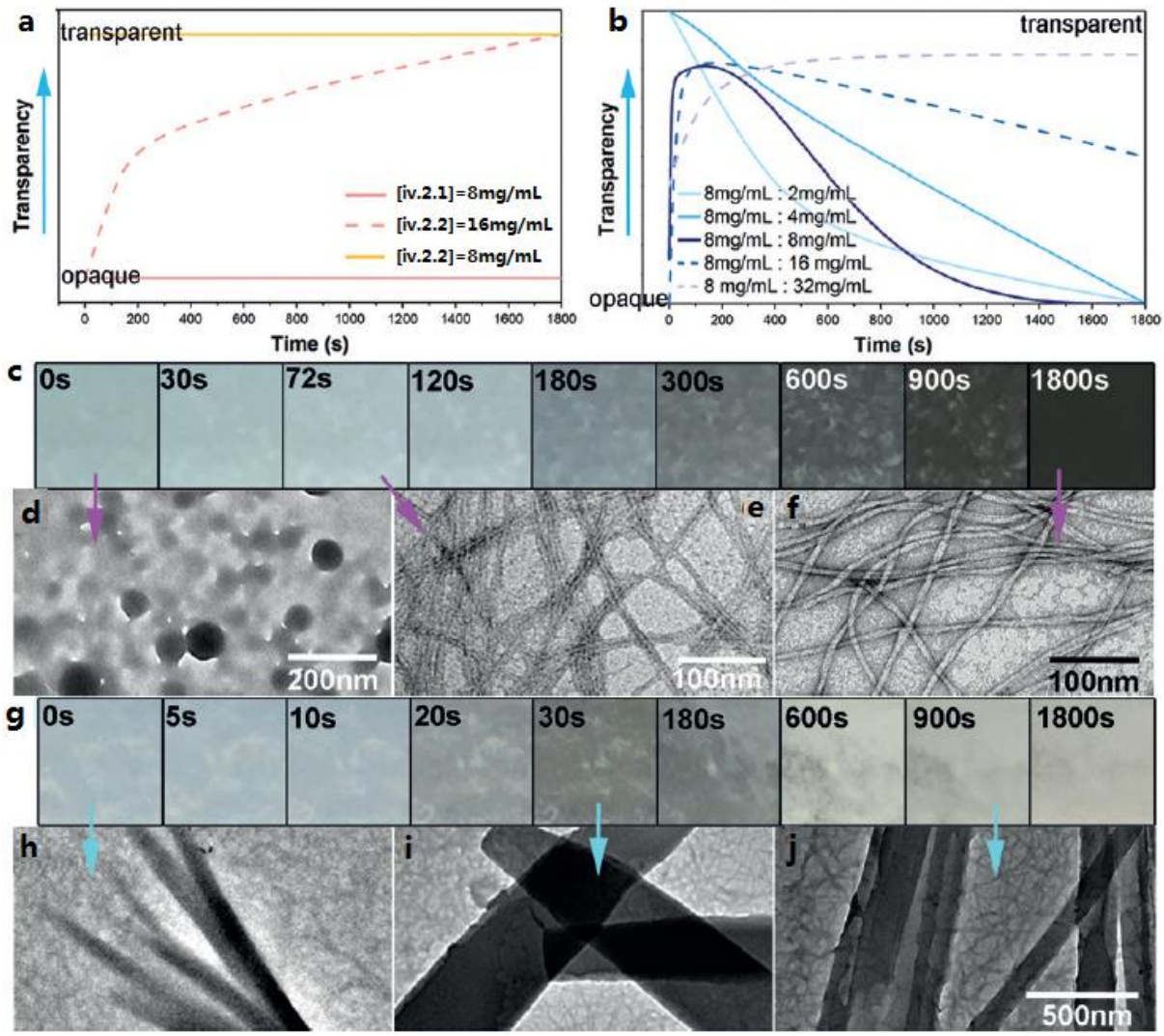

Figure 11. Estimated time-dependent transparency profiles of (a) single component self-assembly and (b) self-assembly of a iv.2.1/2.2 mixture. (c) Time-lapse optical images of iv.2.2 in H_2O/DMSO (v/v=9:1) at a concentration of 16 mg mL^{-1}, and (d-f) the correlated TEM images at (d) 0 s, (e) 72 s, and (f) 1800 s. (g) Time-lapse optical images of a iv.2.1/ iv.2.2 mixture in H_2O/DMSO (v/v=9:1) at a concentration of 8 mg mL^{-1} of each, and (h-j) the correlated TEM images at (h) 0 s, (i) 30 s, and (j) 1800 s.

Quantify opaque and transparency was achieved by measure the UV-Vis absorption of the solution, and the results for single component and mixture solution were shown in Figure 11a/b. At the concentration of 8 mg mL^{-1}, molecule iv.2.1 formed an opaque gel with nanobelt structure; and molecule iv.2.2 form a transparent gel with fibrous nanostructure. When increasing the concentration of molecule iv.2.2 to 16 mg mL^{-1}, we can observe a phase transition from opaque to transparent in 30 min. The detailed observation process was shown in Figure 11c-f, at 0 s, only some irregular aggregates can be found, as time increase to 72 s, some nanofibers with width at 4 nm formed, and it would finally stabilize at 7 – 8 nm width nanofibers. The increase concentration of molecule iv.2.2 helped to deliver a detailed study on the kinetic self-assembly process. In the mixed solution with 2 mg mL^{-1} of molecule iv.2.2 and 8 mg mL^{-1} of molecule iv.2.1, the solution changed from clear to opaque. Upon increasing the concentration of molecule iv.2.2 to 4 mg mL^{-1}, the transition process slight postponed. Further increased molecule iv.2.2's concentration to 8 mg mL^{-1}, we could observe a full cycle of opaque-transparent-opaque phases transition, leading to the highest layer-by-layer nanobelts

among all the combinations. In the time-dependent TEM experiment, we could observe the nanostructures changed from irregular nanofibers/nanobelts to uniformed nanofibers/nanobelts, and ended with uniformed nanofibers/layered nanobelts (Figure 11h-j). Besides the regulation on the self-assembly of molecule iv.2.1 by molecule iv.2.2, molecule iv.2.1 also played a reciprocal role on molecule iv.2.2. When further increased the concentration of molecule iv.2.2 to 16 mg mL^{-1} or 32 mg mL^{-1} in the mixture system, we could observe an incompletely phase transition cycle. The mixture solution ended in a translucent gel with some unevenly distributed white aggregates on the bottom, and in the meantime, reduced height nanobelts were produced. Above results suggested that the coexistence of molecule iv.2.1 and molecule iv.2.2 showed some effects on their own self-assembly behaviour reciprocally. The presence of different density and morphology of the scaffold from molecule iv.2.2 kinetically regulated the height of the nanobelts from molecule iv.2.2 in a collective fashion.

IV. 2. 3. 3. Further Spatially Regulated Nanostructure by Enzyme and UV Light

In the molecular design, molecule iv.2.2 is responsive to both enzyme and UV light, we assumed the change in molecule iv.2.2 at molecular scale would play a role in regulating the nanostructure from molecule iv.2.1.

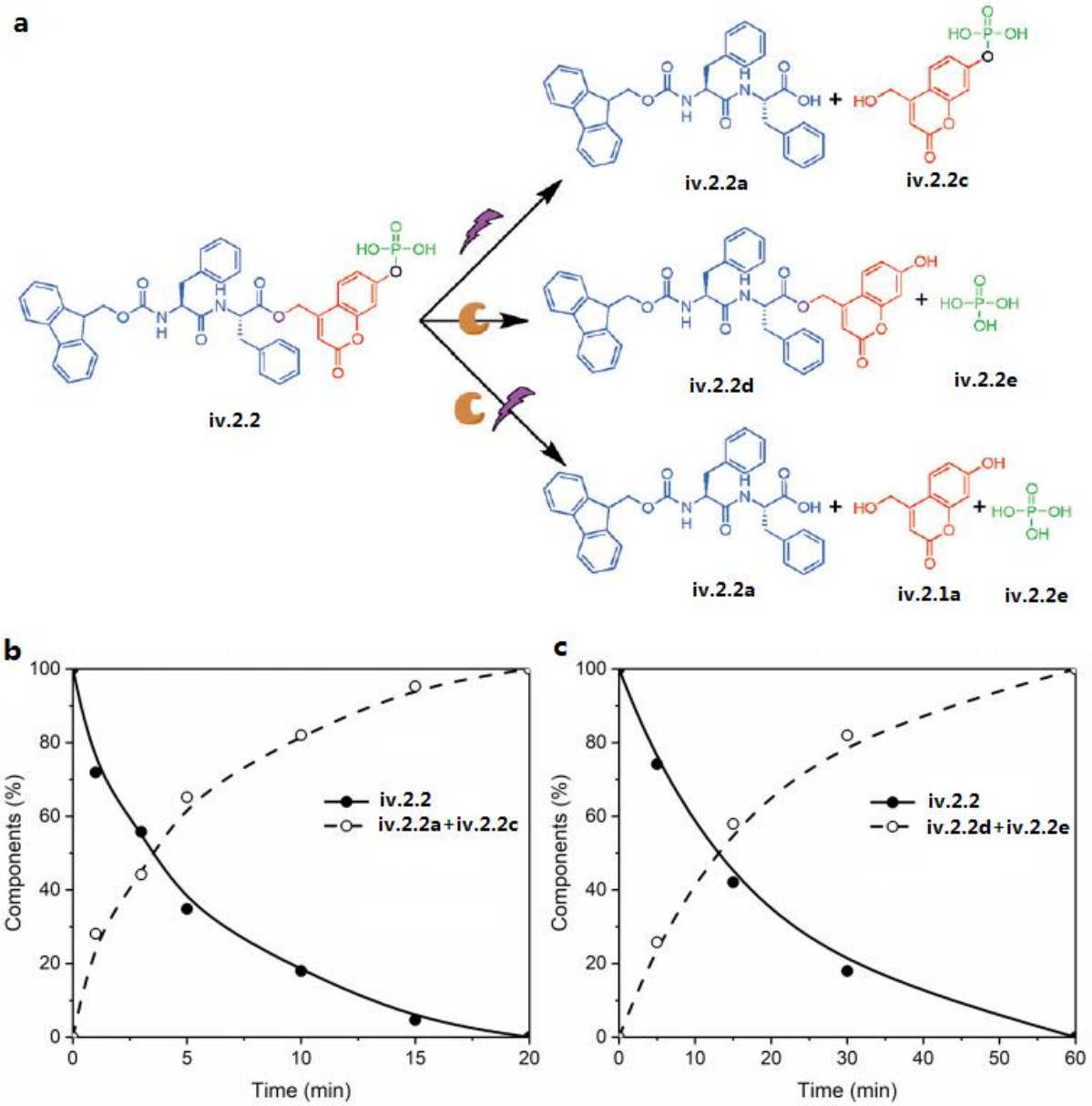

Figure 12. (a) UV light and/or enzyme triggered degradations of iv.2.2; Concentration-time profiles for (b) photochemical and (c) enzymatic chemical conversion of iv.2.2 (100 μM) under the irradiation of 320 nm and alkaline phosphatase (1 u/μL).

As is shown in Figure 12a, under UV treatment, molecule iv.2.2 was cleaved into iv.2.2a and iv.2.2c; under enzyme (ALP) treatment,[11] molecule iv.2.2 cleaved into iv.2.2d and iv.2.2e. The kinetic conversion process was monitored by LC-MS, UV cleavage ended in 20 min (Figure 12b), and enzyme cleavage completed in 60 min (Figure 12c).

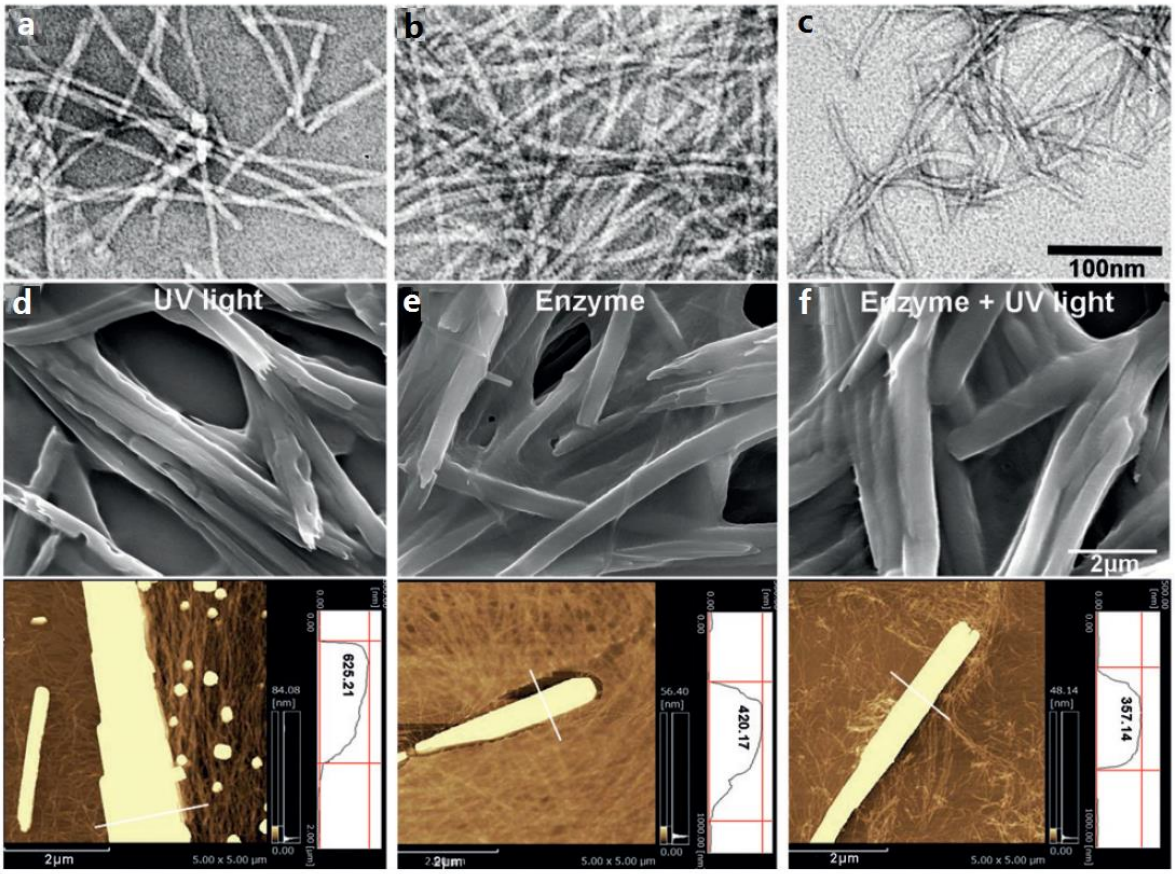

Figure 13. The TEM images of iv.2.2 (100 M) in H_2O/DMSO (v/v=9:1) under (a) UV light, (b) enzyme treatment, and (c) both UV light/enzyme treatment for 30 min. SEM images and correlated AFM images with height profiles of a iv.2.1/iv.2.2 mixture in H_2O/DMSO (v/v=9:1) at a concentration of 8 mg mL^{-1} of each under (d) UV light, (e) enzyme treatment, and (f) UV light/enzyme treatment.

We used TEM to check the nanostructure of molecule after UV treatment, it showed shorter but similar width nanofibers after UV cleavage (Figure 13a); in the case of enzyme treatment, it also showed similar nanofibers compared to those without treatment (Figure 13b); if both UV and enzyme treatment were applied on molecule iv.2.2, we could only observe some even shorter nanofibers (Figure 13c). Molecular structure changes will definitely have some difference in driving force for self-assembly, and in the mixture system it will further lead to some difference for the surface interactions in regulating the growth of molecule iv.2.1. To study the effect of UV and enzyme treatment on the growth on self-assembly of molecule iv.2.1, we chose 1 : 1 ratio of molecule iv.2.1 and iv.2.2 at a concentration of 8 mg mL^{-1}, nanostructure was examined by SEM and AFM. For example, treated by UV, we can obtain nanobelts from molecule iv.2.1 with a height of 625nm (Figure 13d); treated by enzyme, the height of the nanobelts was 420nm (Figure 13e); in the case of both stimuli, the height of the nanobelts was reduced to 354nm (Figure 13f). Quantitative results and the control study of molecule iv.2.1 were shown in Figure 14.

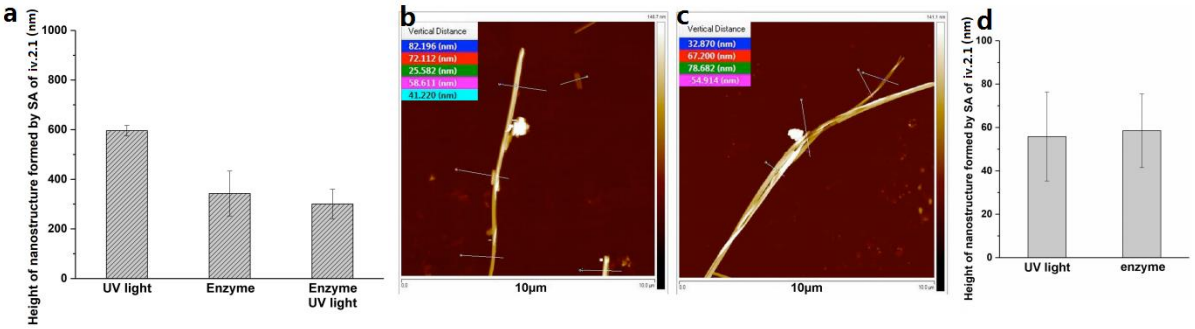

Figure 14. (a) The column plot shows the heights of nanostructures formed by self-assembly (SA) of iv.2.1 from iv.2.1/ iv.2.2 mixture (8mg/mL of iv.2.1 and 8mg/mL of iv.2.2) in H_2O/DMSO (v/v = 9:1) under the treatment of UV light irradiation, enzyme, and UV light irradiation with enzyme measured by AFM; AFM images with height profiles of nanostructures formed by SA of iv.2.1 (8mg/mL) in H_2O/DMSO (v/v = 9:1) under the irradiation of UV light (b) or with the addition of enzyme (c); (d) The column plot of the heights of the nanostructures in Figure b and c. The error bars represent the standard deviation.

In the control study of molecule iv.2.1, we applied UV and enzyme treatment on it, and the AFM results did not show much change on the height of self-assembly nanobelts, indicating in the mixture system, the different height of the nanobelts was caused by the change in the scaffold.

IV. 2. 4. Conclusion

ECM is a dynamic system composed by various ingredients. Every single cell interacts specifically with its surrounding ECM, ECM plays a crucial role in affecting biological properties and behaviour of the cell. Material scientists have worked a lot in developing material adopting property and activity of the ECM through mimicking their complexed network, however, most of the previous focused in the static state of the ECM. The most fascinating part of ECM should be its dynamic interaction with the cell, and which is still rarely reported in the artificial material fabrication. Inspired by the nanoarchitectonics,[12] we selected two molecules which adopted self-sorting behaviour, and we found the dynamic molecular self-assemble nanofibrous nanostructure could work as scaffold to control the hierarchical assembly of the other molecule into a higher-order architecture. Our study opened a way to generate biomimetic materials via two components hierarchical assembly.

IV. 3. Constructing Cross-linked Nanofibirous Scaffold via Dual-Enzyme-Instructed Hierarchical Assembly

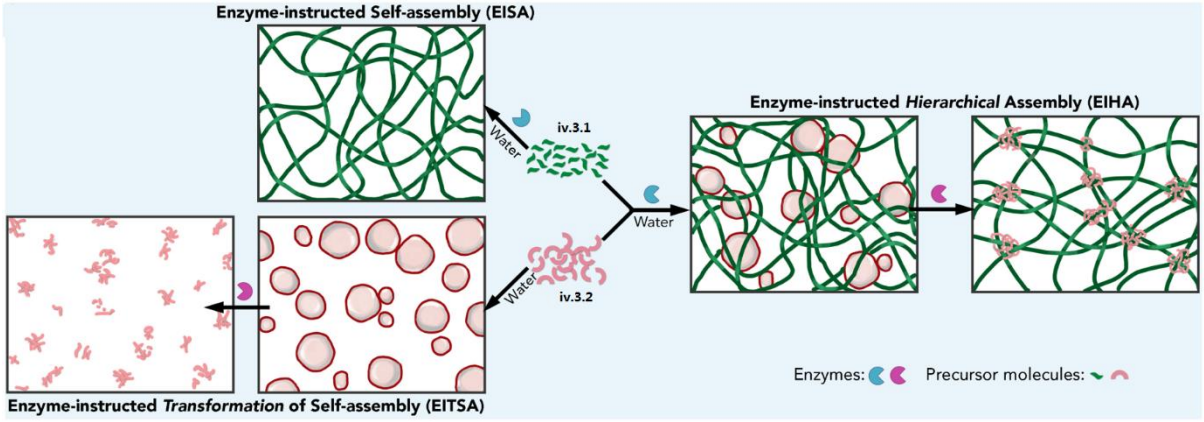

This chapter corresponding to the following manuscript:

Shijin Zhang, William Cortes, Ye Zhang* "Constructing Cross-linked Nanofibrous Network via Enzyme-instructed Hierarchical Assembly" *Langmuir*, **2020**, 36, 6261-6267.

IV. 3. 1. Introduction

In biological system, advanced enzyme catalytic activities largely rely on high-level structural complexity.[1] To pursue such advanced structures in an artificial way, organic chemists have developed a promising bottom-up approach (hierarchical assembly)[2] to reach such sophisticated structures.[3] A lot of studies focused in special morphology construction through coordination chemistry,[4] which emphasized in fluorescence transition.[5] Though the fabrication of advanced nanostructures has progressed greatly, it is still challenging in bridging the gap in hierarchical assembly at multiple length- and time-scales. To reach stable nanostructures, we should pay attention to the energetics and kinetics of fabrication process.[6] In our current study, we are able to reach synergistic structural energetic stability and kinetic accessibility[2b] in a hierarchical assembly through step-by-step fabrication method.

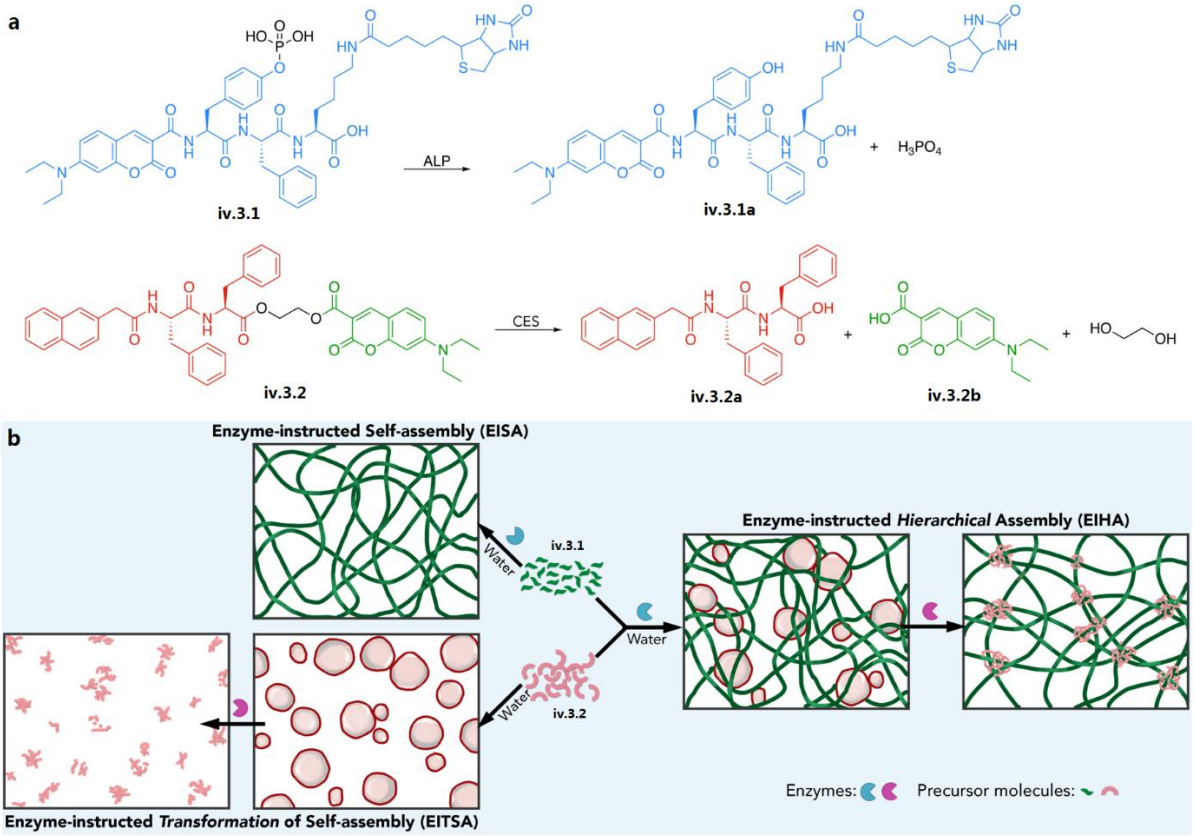

Figure 1. (a) Chemical structures of peptidic molecule iv.3.1 and iv.3.2, and their enzymatic catalysis reactions, ALP catalysed dephosphorylation of iv.3.1 and CES catalysed hydrolysis of iv.3.2. (b) Schematic illustration of constructing physically cross-linked scaffold using enzyme-instructed hierarchical assembly (EIHA).

To reach a controllable molecular self-assembly system, chemists have investigated various stimuli to initiate self-assembly behaviour.[7] They can be divided into two groups, one is chemical stimuli – gases, solvents, metal ions, acid/base signals, redox signals and biomacromolecules, the other is physical stimuli – light, magnetic fields and temperature. Among them, biomacromolecules (e.g. enzyme) are ideal choices to trigger molecular self-assembly and fabricate biomaterial due to their optimal activity in a physiological condition. Enzyme-instructed self-assembly (EISA)[8] and enzyme-instructed transformation of self-assembly (EITSA)[9] are the representative examples utilizing enzyme to fabricate biomaterial nanostructures.[10] Carboxyl esterase (CES) and alkaline phosphatase (ALP) are widely applied

in EISA and EITSA process, due to their broad substrate specificity. In addition, these two enzymes are highly expressed in cancer cells, and they have been applied in nanomedicine development for cancer treatment.[11] To maximize the potential of hierarchical assembly nanostructures for bio-related application, we chose these two enzymes as external stimuli in our study to reach a step-by-step molecular assembly. In our molecular design, we chose aromatic amino acids as our building block,[12] by conjugating with 7-(diethylamino)-coumarin-3-carboxylic acid which served as an indicator for the self-assembly behaviour.[13] Considering the designed molecule can be potentially applied as biomaterial, we conjugated cell interaction functional group – biotin into molecule iv.3.1.[14] The chemical structures of molecule iv.3.1, iv.3.2 and their enzyme catalysed reaction were shown in Figure 1a. Their self-assembly behaviour and enzyme assisted morphology transformation were shown in Figure 1b. For molecule iv.3.1, ALP guided molecular self-assembly formed nanofibrils; in the case of molecule iv.3.2, CES transformed the self-assembled nanovesicles into nanoaggregates. When they were mixed in an aqueous solution, step-by-step administration of the two enzymes could reach a more robust nanostructure. Specifically, the mixture was firstly treated by ALP to form nanofibrils, and then CES was applied to transform the nano vesicles into nanoaggregates to cross-link the nanofibrils tightly due to its close contact with the nanofibrils before nanostructure transformation.

IV. 3. 2. Experiment Section

IV. 3. 2. 1. Materials

Chemical reagents	Grade	Manufacturer
Fmoc-Amino acid	98.0%	GL Biochem (Shanghai, China)
2-(1*H*-benzotriazol-1-yl)-1,1,3,3-tetramethyluronium hexafluorophosphate (HBTU)	97.0%	Matrix Scientific
Trifluoroacetic acid (TFA)	98.0%	Sigma Aldrich
Dimethylformamide (DMF)	99.5%	Nacalai Tesque
Dichloromethane (DCM)	98.0%	Nacalai Tesque
N-(3-dimethylaminopropyl)-*N*'-ethylcarbodiimide hydrochloride (EDCI)	98.0%	Nacalai Tesque
4-Dimethylaminopyridine (DMAP)	98.0%	Sigma Aldrich
Piperidine	99.0%	Nacalai Tesque
N,N-diisopropylethylamine (DIEA)	99.0%	Nacalai Tesque
Methanol (MeOH)	99.0%	Nacalai Tesque
Ethanol (EtOH)	99.5%	Nacalai Tesque
Hexane	95.0%	Nacalai Tesque
Ethyl acetate (EA)	99.0%	Nacalai Tesque
Tetrahydrofuran (THF)	98.0%	Nacalai Tesque
N,N'-diisopropylcarbodiimide (DIC)	99.0%	FUJIFILM Wako Pure Chemical
Ethylene glycol	99.8%	Sigma Aldrich
Piperidinium acetate	98.0%	Tokyo Chemistry Industry
N-hydroxysuccinimide (NHS)	98.0%	Tokyo Chemistry Industry
Biotin	98.0%	Tokyo Chemistry Industry
4-(diethylamino)salicylaldehyde	98.0%	BLD Pharmatech Ltd.
2-Naphthylacetic acid (NapOH)	98.0%	Combi-Blocks

All organic solvents were dehydrated before experiment by a solvent purification system.

IV. 3. 2. 2. Instruments

Agilent 1260 Infinity Preparation HPLC (Column: 19 mm×150 mm XBridge® Peptide BEH C18 column), Agilent 1260 Infinity Analysis HPLC (Column: 2.1 mm×150 mm XBridge® Peptide BEH C18 column) (Eluent: Acetonitrile and water (0.1% TFA)), Thermo LTQ-ETD mass spectrometer (ESI-MS), ^{1}HNMR and ^{13}CNMR spectra were recorded on a JEOL 400 (400MHz and 100MHz, respectively) spectrometer, Mass spectra were recorded by Thermo LTQ-ETD mass spectrometer (ESI-MS), Thermo Nanodrop 2000C spectrophotometer, Transmission Electron Microscope (JEM-1230R), Milli-Q® Integral 3/5/10/15 System, Circular dichroism spectroscopy (JASCO J-820), Rotary Rheometer (Anton-Paar MCR302).

IV. 3. 2. 3. Synthesis

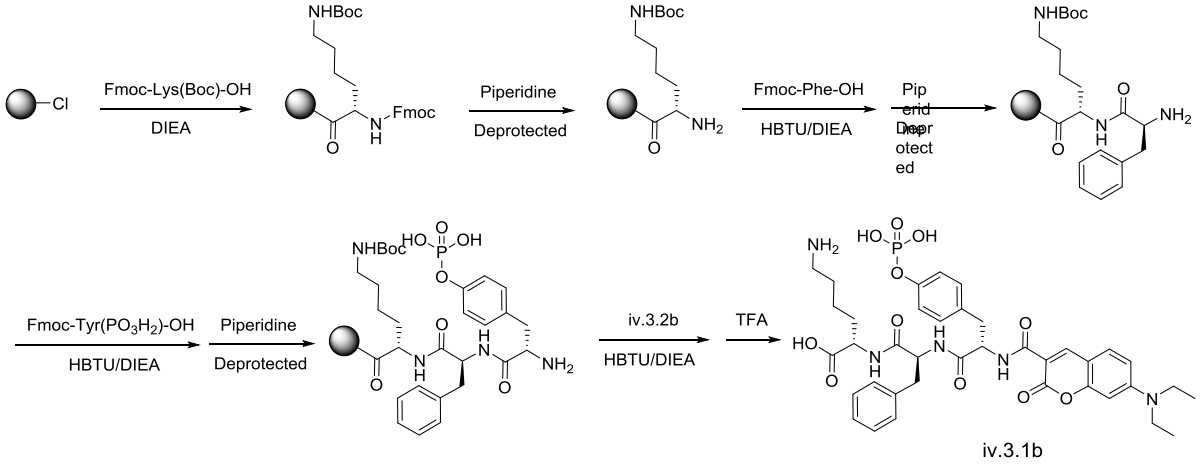

Scheme 1. Synthesis of compound iv.3.1b.

Compound **iv.3.1b**: Compound iv.3.1b was obtained via solid phase peptide synthesis (SPPS). 2-Chlorotrityl chloride resin (2.0 g, 2 mmol) was swelled in anhydrous DCM for 20 min, L-Fmoc-Lys(Boc)-OH (2.34 g, 5 mmol) dissolved in anhydrous DMF was conjugated to resin with DIEA in 30 min. Then washed with anhydrous DMF for 3 times, unreacted sites in the resin were blocked with DCM/MeOH/DIEA (80:15:5) for 20 min and washed by anhydrous DMF for 5 times. Then piperidine solution (20% in DMF) was added into reaction for 30 min to remove the Fmoc protecting group on the amino acid. We carried out the peptide elongation according to standard SPPS protocol to get the desired compound. iv.3.1b was cleaved off the resin using TFA for 2 h. After removing the solvent, anhydrous ether was added into the concentrated product and white precipitation of iv.3.1b was obtained, the yield is 82.1%.

^{1}HNMR (400 MHz, DMSO-*d6*) δ = 8.89 (d, J=7.5 Hz, 1H), 8.64 (s, 1H), 8.50 (d, J=8.3 Hz, 1H), 8.42 (d, J=7.8 Hz, 1H), 7.68 (d, J=9.1 Hz, 1H), 7.33 – 7.21 (m, 5H), 7.18 – 7.12 (m, 1H), 7.03 – 6.91 (m, 4H), 6.84 – 6.78 (m, 1H), 6.60 (s, 1H), 4.82 – 4.49 (m, 2H), 4.30 – 4.26 (m, 1H), 3.07 – 2.94 (m, 4H), 2.85 – 2.67 (m, 6H), 1.82 – 1.72 (m, 2H), 1.67 – 1.51 (m, 4H), 1.44 – 1.36 (m, 2H), 1.14 (t, J=7.0 Hz, 6H) ppm.

MS: calculated for $C_{38}H_{46}N5O_{11}P$ is 779.2931, found 780.2991, $[M + H]^{+}$.

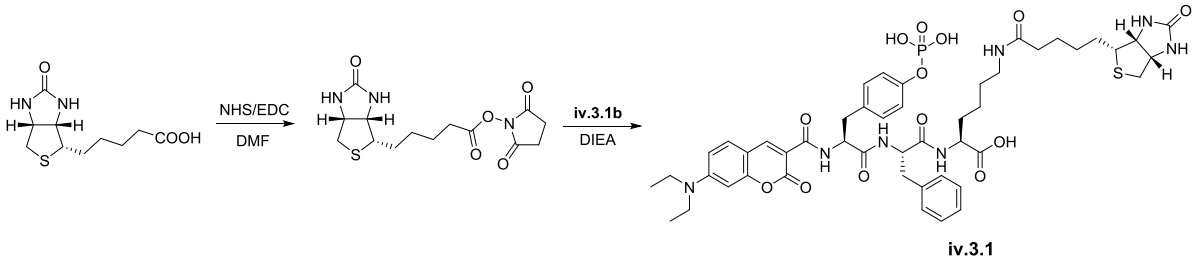

Scheme 2. Synthesis of compound iv.3.1.

Compound **iv.3.1**: Biotin (0.41 mmol, 100 mg), NHS (0.45 mmol, 51.8 mg) and EDC (0.45 mmol, 86.3 mg) were transferred into a 25mL round bottom flask, then dissolved in 5 mL anhydrous DMF. Stirred at room temperature for overnight. TLC was applied to confirm the generation of activated ester, then iv.3.1b (0.38 mmol, 300 mg) was adding into the reaction mixture, DIEA (155.8 mg, 1.2 mmol) was slowly dropping into the solution, stirring at room temperature for 24h. Preparation HPLC was applied to purify the target compound. The yield is 62.3%.

^{1}HNMR (400 MHz, DMSO-*d6*) δ 8.82 (d, *J* = 7.7 Hz, 1H), 8.55 (s, 1H), 8.38 (d, *J* = 8.3 Hz, 1H), 8.26 (d, *J* = 7.6 Hz, 1H), 7.75 (t, *J* = 5.4 Hz, 1H), 7.62 (d, *J* = 8.7 Hz, 1H), 7.27 – 6.92 (m, 9H), 6.75 (dd, *J* = 9.1, 1.6 Hz, 1H), 6.56 (d, *J* = 1.4 Hz, 1H), 6.38 (d, *J* = 28.5 Hz, 2H), 4.70 – 4.50 (m, 2H), 4.30 – 4.04 (m, 5H), 3.43 (dd, *J* = 13.8, 6.8 Hz, 5H), 3.08 – 2.88 (m, 5H), 2.88 – 2.66 (m, 3H), 2.00 (t, *J* = 7.3 Hz, 2H), 1.75 – 1.19 (m, 12H), 1.09 (t, *J* = 7.0 Hz, 6H) ppm.

^{13}CNMR (101 MHz, DMSO-*d6*) δ = 174.01, 172.50, 171.70, 170.74, 163.30, 162.23, 157.81, 153.08, 150.58, 150.52, 148.43, 138.26, 133.07, 132.21, 130.86, 129.76, 129.69, 128.54, 126.77, 120.09, 110.71, 109.21, 108.11, 96.37, 61.56, 59.72, 55.94, 54.09, 52.51, 44.87, 35.73, 28.74, 28.52, 25.84, 23.38, 18.59, 17.24, 12.84 ppm.

MS: calculated for $C_{48}H_{60}N_7O_{13}PS$ is 1005.3707, found 1006.3771, $[M + H]^+$.

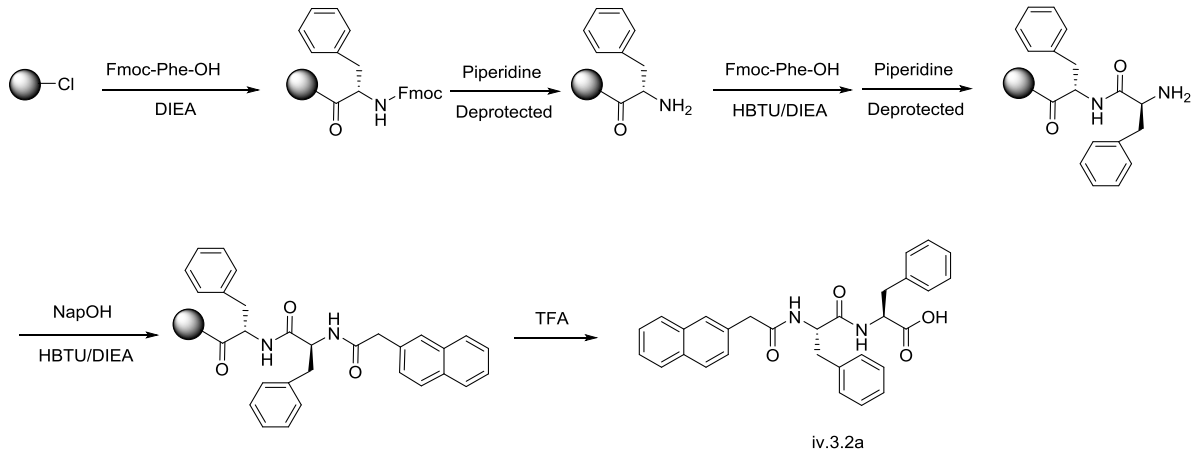

Scheme 3. Synthesis of compound iv.3.2a.

Compound **iv.3.2a**: Synthesis was completed according to SPPS.

^{1}HNMR (400 MHz, DMSO-*d6*) δ = 8.28 (dd, J=25.7, 8.2 Hz, 2H), 7.87 – 7.76 (m, 1H), 7.75 – 7.64 (m, 2H), 7.53 (s, 1H), 7.46 – 7.38 (m, 2H), 7.23 – 7.08 (m, 11H), 4.55 – 4.48 (m, 1H), 4.45 – 4.35 (m, 1H), 3.04 – 2.63 (m, 6H) ppm.

MS: calculated for $C_{30}H_{28}N2O_4$ is 480.2049, found 503.1931, $[M + Na]^+$.

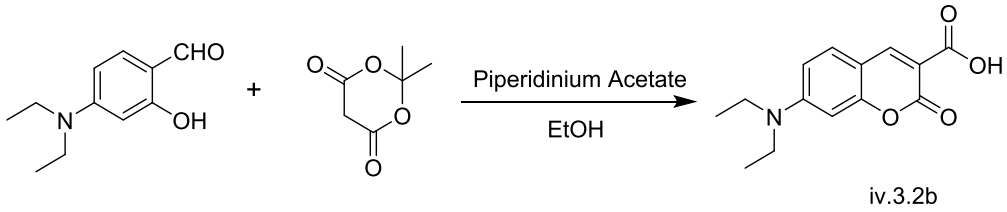

Scheme 4. Synthesis of compound iv.3.2b.

Compound **iv.3.2b** was synthesized by following the published method.[15]

^{1}HNMR (400 MHz, $CDCl_3$) δ = 8.63 (d, J=0.6 Hz, 1H), 7.44 (d, J=9.1 Hz, 1H), 6.71 (dd, J=9.1, 2.5 Hz, 1H), 6.53 (dd, J=2.4, 0.4 Hz, 1H), 3.48 (q, J=7.2 Hz, 4H), 1.25 (t, J=7.2 Hz, 6H) ppm.
MS: calculated for $C_{14}H_{15}NO_4$ is 261.1001, found 284.0886, $[M + Na]^+$.

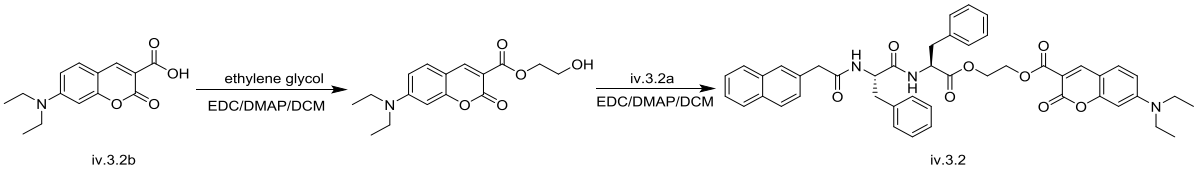

Scheme 5. Synthesis of compound iv.3.2.

Compound **iv.3.2**: Synthesis was completed according to the published method.

^{1}HNMR (400 MHz, DMSO-*d6*) δ = 8.57 (dd, J=27.6, 7.7 Hz, 1H), 8.47 (d, J=15.0 Hz, 1H), 8.30 – 8.18 (m, 1H), 7.82 – 7.77 (m, 1H), 7.74 – 7.65 (m, 2H), 7.51 (dd, J=14.9, 9.2 Hz, 2H), 7.46 – 7.36 (m, 2H), 7.20 – 7.05 (m, 10H), 6.75 – 6.60 (m, 1H), 6.51 – 6.41 (m, 1H), 4.60 – 4.43 (m, 2H), 4.40 – 4.22 (m, 4H), 3.57 – 3.49 (m, 1H), 3.41 (q, J=7.2 Hz, 4H), 3.30 (s, 2H), 3.09 – 2.99 (m, 1H), 2.96 – 2.83 (m, 1H), 2.70 – 2.59 (m, 1H), 1.08 (t, J=7.0 Hz, 6H) ppm.

^{13}CNMR (101 MHz, DMSO-*d6*) δ = 171.89, 170.24, 163.54, 163.53, 158.63, 157.47, 153.45, 153.44, 150.05, 138.19, 138.12, 137.64, 137.51, 134.44, 133.40, 132.20, 129.76, 129.66, 129.58, 128.75, 128.34, 128.08, 127.93, 127.83, 127.73, 126.47, 125.94, 110.31, 107.50, 107.16, 96.35, 63.20, 62.70, 54.06, 44.89, 42.67, 38.36, 37.00, 12.84 ppm.

MS: calculated for $C_{46}H_{45}N_3O_8$ is 767.3207, found 790.3104, $[M + Na]^+$.

IV. 3. 2. 4. Stage-by-stage treatment with enzyme

In the mixture of compound iv.3.1 and iv.3.2 in borate buffer, regulated hydrolysis process was achieved by adding ALP and CES in different order, thus resulting in different nanostructures.

Firstly, both ALP and CES can be added in a time to trigger hydrolysis of the mixture at the same time; secondly, ALP was added to hydrolyse compound iv.3.1, and added CES into the mixture after completely hydrolysis of iv.3.1; thirdly, CES was added to hydrolyse compound iv.3.2, and not added ALP into the mixture until completely hydrolysis of iv.3.2.

IV. 3. 2. 5. Transmission electron microscopy (TEM)

Carbon-coated copper grids were glow discharged to enhance hydrophilicity; then 5 μL of sample solution was placed on the grid, leave the sample on the grid around 60 s, removed the excess fluid with a filter paper; washed the grid with 5 μL of distilled water for 3 times, removed the excess water with filter paper; 5 μL of 1% uranyl acetate was placed on the grid, after 20 s, removed the excess solution by touching the edge of grid using a filter paper; dried the grid at room temperature. Observation was carried on JEM-1230R with acceleration voltage at 100 kV.

IV. 3. 2. 6. Circular dichroism (CD) spectroscopy

CD spectra measurements were carried out on spectrometer JASCO J-820. The bandwidth was set at 1.0 nm and the measurement range was 190 – 400 nm. All measurements were carried out in a 1 mm quartz cuvette at room temperature. Theoretical curve was obtained by a simple sum of every single components.

IV. 3. 2. 7. UV-Vis absorption and emission spectroscopy

UV-Vis absorption measurements of specimen solutions are carried out on Thermo Nanodrop 2000C spectrophotometer. The detection path length of the cuvette is 1 cm. The detection range was set to 250 – 700 nm with a spectral resolution at 1.0 nm. Emission spectra were collected on a home-made Hamamatsu fluorescence spectrometer. The excitation wavelength was set to 405 nm and emission collection length was between 415 and 750 nm.

IV. 3. 2. 8. Rheology measurement

Rheology tests were conducted on Anton-Paar MCR302, parallel-plate geometry with an upper plate at the diameter of 25 mm was used during the experiment, and the gap was 0.1 mm. Throughout the experiment, the stage temperature was maintained at 25 ^{o}C. The specimen was transferred to the stage by spatula, dynamic strain (0.1 – 100%) was performed at 6.28 rad/s, maximum storage moduli in the linear range of the strain sweep test was selected for frequency sweep test (0.1 – 200 rad/s).

IV. 3. 2. 9. Kinetic profiling of ALP-catalysed dephosphorylation of iv.3.1

Alkaline phosphatase (ALP) from calf intestinal was purchased from Invitrogen (Cat no. 18009-019). Following the instruction, ALP stock solution (1u/μL) was prepared with the dilution buffer. Stock solutions of compound iv.3.1 or mixture of compound iv.3.1 and iv.3.2 (40 mM in DMSO) were diluted in borate buffer to the desired concentration. Proper volume of ALP stock solution was added into 200 μL of compound solution reaching final

concentration of 1u. LCMS were applied to identify the reaction products and monitor the progress of hydrolysis at room temperature.

IV. 3. 2. 10. Kinetic profiling of CES-catalysed hydrolysis of iv.3.2

Carboxylesterase (CES) from rabbit liver lyophilized powder was purchased from Sigma-Aldrich (E0887-500UN). Following the instruction, CES stock solution (1u/5μL) was prepared in borate buffer (pH 8.0). Stock solutions of compound iv.3.2 or mixture of compound iv.3.1 and iv.3.2 (40 mM in DMSO) were diluted in borate buffer to the desired concentration. Proper volume of CES stock solution was added into 200 μL of compound solution reaching final concentration of 1u. LCMS were applied to identify the reaction products and monitor the progress of hydrolysis at room temperature.

IV. 3. 2. 11. Cell viability assay

HeLa cells in exponential growth phase were seeded in a 96 well plate at a concentration of 8000 cells/well for all cell lines. The cells were allowed to attach to the wells for 12 h at 37 ℃, 5% CO_2. The culture medium was removed followed by addition of 100 μL culture medium containing different concentrations (50, 100, 200, and 500 μM) of compound iv.3.1 and iv.3.2. After the desired time of incubation, 10 μL MTT solution (5 mg/mL) was added to each well and incubated at 37°C for another 4 h, and then 100 μL of SDS solution (10% in Milli-Q water) was added to stop the reduction reaction and dissolved the purple formazan. The absorbance at 570 nm was measured using Nivo3 microplate reader (PerkinElmer). All experiments were performed in triplicate and repeated three times.

IV. 3. 3. Results

IV. 3. 3. 1. Self-assembly of molecule iv.3.1 and iv.3.2 upon enzyme treatment

Molecule iv.3.1 was easily dissolved in aqueous solution, and once treated by ALP, dephosphorylation of iv.3.1 would trigger the molecular self-assembly to form nanofibrils at the critical concentration. In details, when molecule iv.3.1 was dissolved in borate buffer at the concentration of 0.5 mM, and treated by ALP, we can only observe irregular nanoaggregates through TEM imaging (Figure 2a). Upon increasing the concentration to 1 mM, ALP hydrolysis assisted the formation of uniform nanofibrils (Figure 2b). In the case of molecule iv.3.2, it self-assembled into varied size nanovesicles in borate buffer, further treatment by CES would result in clusters of nanoaggregates in irregular shapes (Figure 2c).

Enzyme catalytic hydrolysis kinetic profile for molecule iv.3.1 and iv.3.2 was shown in Figure 3. At room temperature, molecule iv.3.1 was completely converted to iv.3.1a under the treatment of ALP with 30 minutes (Figure 3a), the hydrolysis process was confirmed by HPLC (Figure 3b) and the molecular weight of new peak was further measured by MS (Figure 3c) ; the CES catalytic hydrolysis of molecule iv.3.2 to iv.3.2a took about 12 hours (Figure 3d) which was much slower than the hydrolysis of molecule iv.3.1, and the molecular weight of new peak confirmed by MS (Figure 3f).

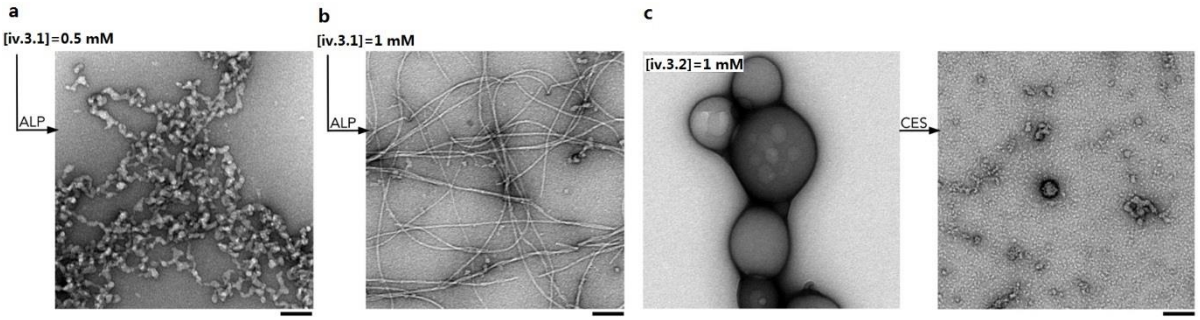

Figure 2. TEM images of ALP-catalyzed dephosphorylation of molecule iv.3.1 at 0.5 mM (a) and 1 mM (b) induced self-assembly. (c) TEM images of CES-catalyzed hydrolysis of molecule iv.3.2 at 1 mM induced transformation of self-assembly. Scale bars: 100nm.

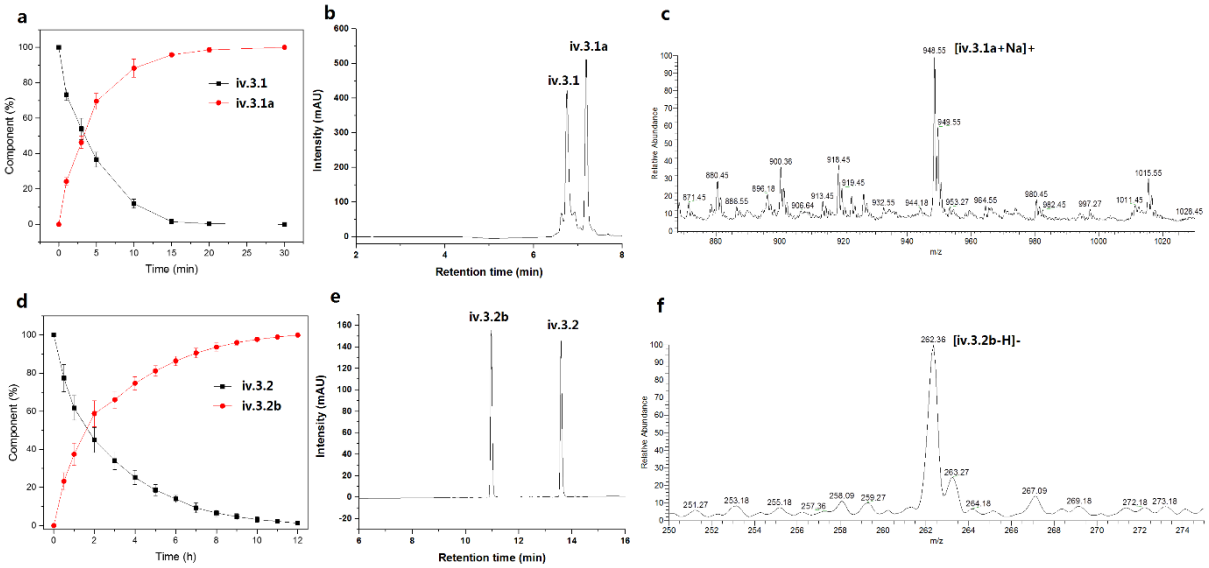

Figure 3. (a) Kinetic profiles of ALP catalysed hydrolysis of compound iv.3.1 (0.2 mM) in borate buffer at room temperature; (b) HPLC spectrum of hydrolysis of iv.3.1 at 3 min; (c) MS spectrum obtained from the fraction of peak iv.3.1a in (b); (d) Kinetic profiles of CES catalysed hydrolysis of compound iv.3.2 (0.2 mM) in borate buffer at room temperature; (e) HPLC spectrum of hydrolysis of iv.3.2 at 2h; (f) MS spectrum obtained from the fraction of peak iv.3.2b in (e).

Therefore, the self-assembly process of molecule iv.3.1 to form nanofibrils was much faster than the disassembly process of molecule iv.3.2 to form nanoaggregates. The molecular self-assembly behavior was also confirmed by UV-Vis absorbance and emission fluorescence measurement. For molecule iv.3.1 in borate buffer, the maximum absorption (434 nm) and emission (484 nm) peak remained the same, but there was obvious decrease in absorbance and emission intensity (Figure 4a), which suggested chemical environment of the aromatic building was affected by molecular self-assembly.[16] For molecule iv.3.2, before enzyme treatment, the maximum absorption peak was at 421 nm, and the maximum emission peak was 546 nm. After CES treatment, both showed blue shift with maximum absorption peak at 412 nm and maximum emission peak at 468 nm (Figure 4b). Comparing to the maximum absorption (424 nm) and emission (472 nm) peak of molecule iv.3.2b (Figure 4c), it suggested blue shifted caused by CES for molecule iv.3.2 via component and morphological change.

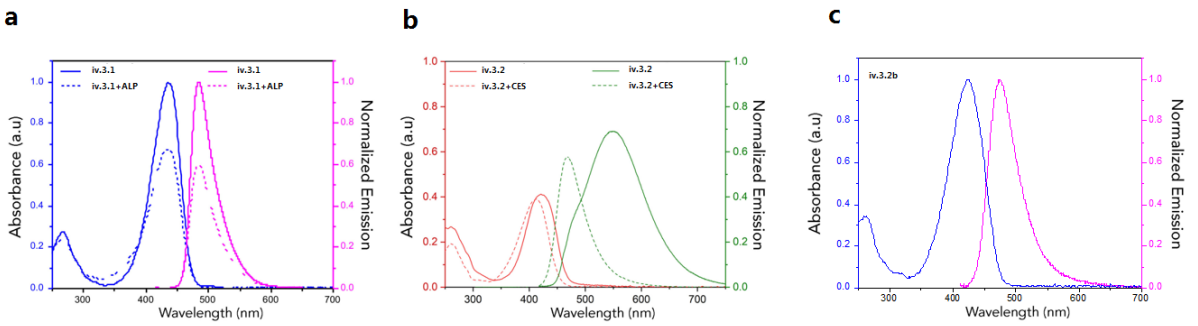

Figure 4. (a) UV-vis absorption spectra and emission spectra (excited at 405 nm) of molecule iv.3.1 (0.2 mM) in borate buffer at 25 °C before and after treatment with ALP (1u/mL) for 12 hours; (b) UV-vis absorption spectra and emission spectra (excited at 405 nm) of molecule iv.3.2 (0.2 mM) in borate buffer at 25 °C before and after treatment with CES (0.2 u/mL) for 12 hours; (c) UV-vis absorption spectra and emission spectra (excited at 405 nm) of molecule iv.3.2b (0.2 mM) in borate buffer at 25 °C.

IV. 3. 3. 2. Stage-by-stage administration of enzymes leads to EIHA

In the mixture of molecule iv.3.1 and iv.3.2 (ratio = 1:1) in borate buffer, we can only observe some nanovesicles by TEM (Figure 5a), which was the same as single component of molecule iv.3.2. In the CD measurements, the spectrum from the mixture was similar to the simply sum of both components, it suggested that addition of molecule iv.3.1 didn't interfere the self-assembly behavior of molecule iv.3.2 (Figure 5c). Upon treatment by enzyme in the mixture, different orders of enzyme catalytic reactions led to various combination of nanostructures. For example, when ALP and CES were added into the mixture at the same time, we could only observe some scattered nanofibrils (Figure 5b), and CD results confirmed they adopted co-assembly behavior in the solution (Figure 5c). If the mixture was treated by ALP first to generate nanofibrils (Figure 5d) from molecule iv.3.1 and further treated by CES, we could observe dense nanofibrous scaffold (Figure 5e). They adopted molecular co-assembly behavior, which was confirmed by the CD measurements (Figure 5f). While we added CES firstly, then nanovesicles disassembled to form some irregular nanoaggregates (Figure 5g); and further treated by ALP, we can observe the nanofibrils tangling with the nanoaggregates via co-assembly (Figure 5h/i). These results indicated that co-assembly of the same components can lead to different nanostructures through a step-by-step assembly.

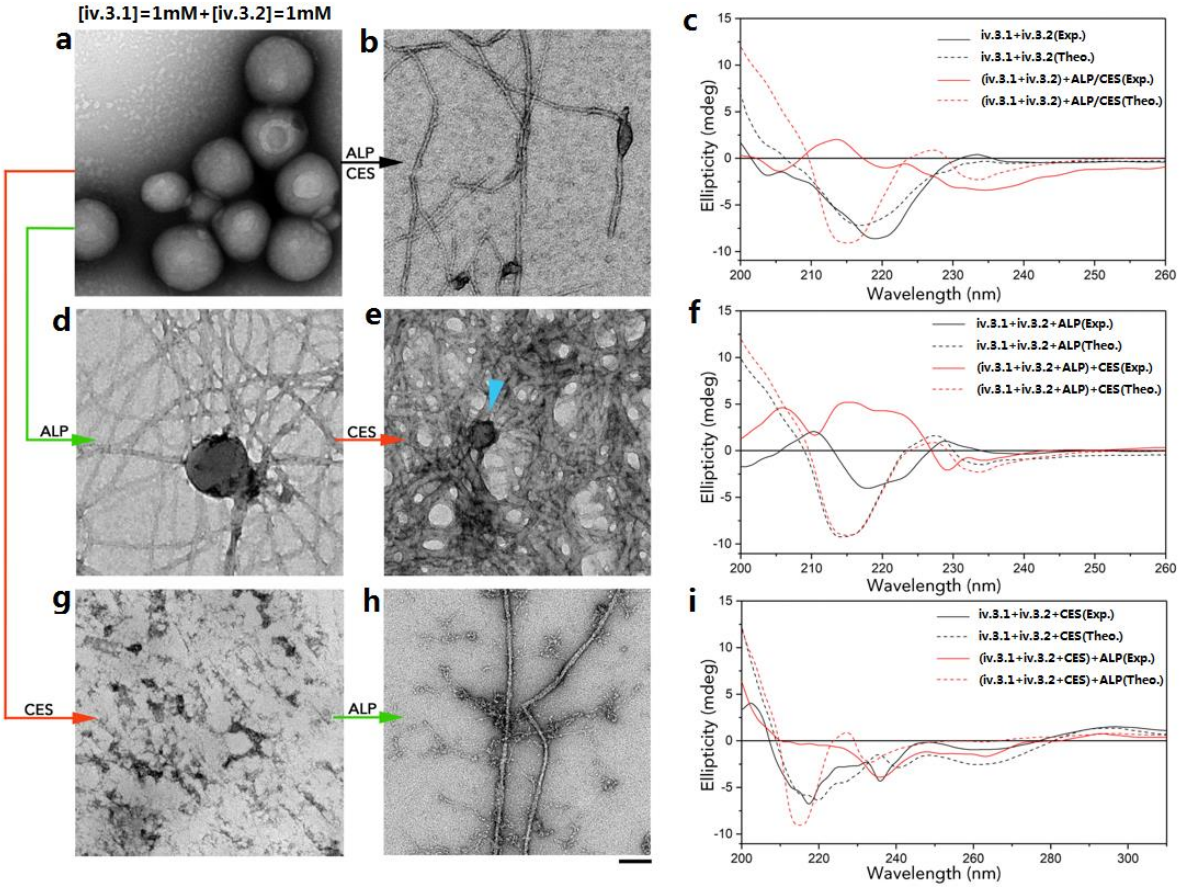

Figure 5. TEM images of molecule iv.3.1 (1 mM) and molecule iv.3.1 (1 mM) mixture in borate buffer at 25 °C before (a) and after (b) treatment with ALP can CES simultaneously for 16 hours; treated with ALP for 30 minutes (d) first, and then with CES for 14 hours (e); treated first with CES for 12 hours (g) and then with ALP for 40 mins (h). (c) CD spectra of molecule iv.3.1 and molecule iv.3.2 mixture in borate buffer at 25 °C before and after treated by ALP and CES simultaneously. (f) CD spectra of molecule iv.3.1 and molecule iv.3.2 mixture in borate buffer at 25 °C treated by ALP for 30 minutes, and after the second stage treatment with CES. (i) CD spectra of molecule iv.3.1 and molecule iv.3.2 mixture in borate buffer at 25 °C treated by CES for 12 hours, and after the second stage treatment with ALP. Solid and dash lines in panels c, f, and i represent experimental (Exp.) and theoretical (Theo.) CD spectra, respectively.

To figure out the underline mechanism for molecular co-assembly in the step-by-step hierarchical assembly process, we studied the enzyme-catalytic kinetics of ALP dephosphorylation of molecule iv.3.1 and CES-guided hydrolysis of molecule iv.3.2 in three different manners together with their respective TEM characterization of the molecular assembly at transition stages. When both ALP and CES were administrated simultaneous in the mixture of molecule iv.3.1 and iv.3.2 solution, ALP-catalytic dephosphorylation rate was the same as the single component solution of molecule iv.3.1. While CES-catalytic hydrolysis process of molecule iv.3.2 took another 4 more hours compared with the single component solution (Figure 6a). In the middle of the enzyme catalytic reaction, we could observe that the nanovesicles were trapped by the nanofibrils (Figure 6b). Varied size of nanovesicles and they're tightly binding with nanofibrils resulted in the formation of scattered beaded nanofibrils at the end of the reactions. When ALP and CES were added in a stage-by-stage manner, for instance, ALP was firstly added to trigger the dephosphorylation of molecule iv.3.1 and not added CES until the completement of dephosphorylation process. The stage-by-stage enzyme-catalytic reaction rates were similar to the single component treated by the enzyme in borate

solution (Figure 6c). In the middle of dephosphorylation process, we could observe short nanofibrils surrounded by the nanovesicles. One hour after the administration of CES, TEM image showed dense nanofibrils tangling with the reduced size nanovesicles (Figure 6d). In the stage-by-stage treatment of enzyme at an order of CES and ALP, the CES-guided hydrolysis of molecule iv.3.2 completed in 10 hours, which was 2 hours less than the single component hydrolysis in borate buffer; and the ALP-catalyzed dephosphorylation rate of molecule iv.3.1 was similar to the single component (Figure 6e). 15 minutes after administration of CES, we could observe the rough edges and disrupted shape of nanovesicles, which indicated the disassembly of nanovesicles. 15 minutes after the administration of ALP, we could observe some short nanofibrils surrounding by irregular nanoaggregates, and it eventually grew into elongated nanofibrils with surrounding nanoaggregates (Figure 6f).

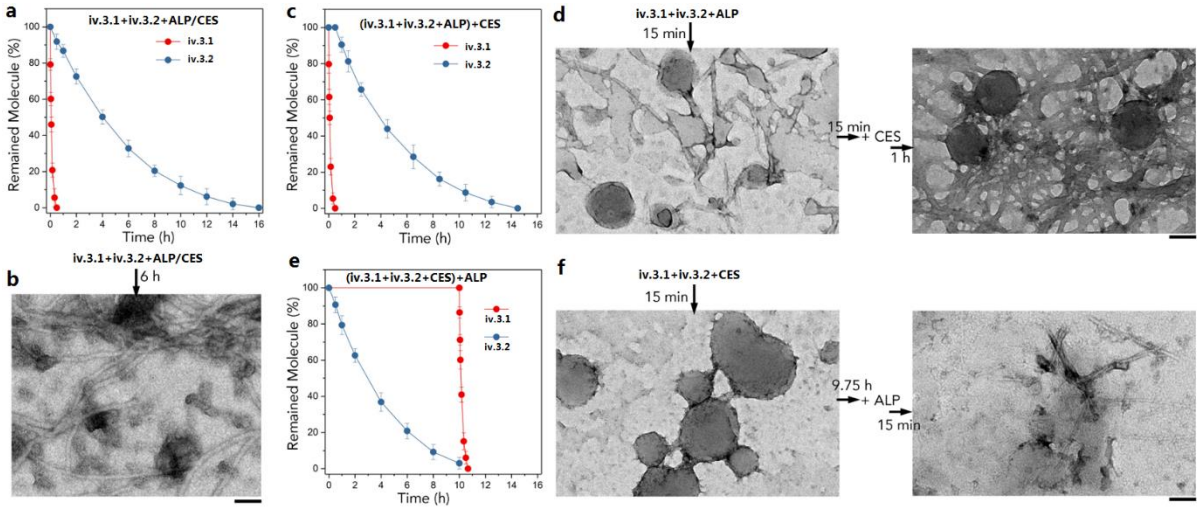

Figure 6. (a) Kinetic profiles of ALP-catalyzed hydrolysis of iv.3.1 and CES-catalyzed hydrolysis of iv.3.2 when iv.3.1, iv.3.2, ALP and CES are mixed together simultaneously. TEM image of iv.3.1 and iv.3.2 mixture reacts with ALP and CES simultaneously for 6 hours. (b) TEM image of iv.3.1 and iv.3.2 mixture reacts with ALP for 6 hours, and TEM image of iv.3.1 and iv.3.2 mixture first reacts with ALP for 12 hours, then with CES for 1 hour. (c) Kinetic profiles of ALP-catalyzed hydrolysis of iv.3.1 and CES-catalyzed hydrolysis of iv.3.2 when iv.3.1 and iv.3.2 mixture react with ALP first, then CES. (d) TEM image of iv.3.1 and iv.3.2 mixture reacts with ALP for 15 minutes, and TEM image of iv.3.1 and iv.3.2 mixture first reacts with ALP for 15 minutes, then with CES for 1h. (e) Kinetic profiles of ALP-catalyzed hydrolysis of iv.3.1 and CES-catalyzed hydrolysis of iv.3.2 when iv.3.1 and iv.3.2 mixture react with CES first, then ALP. (f) TEM image of iv.3.1 and iv.3.2 mixture reacts with CES for 15 minutes, and TEM image of iv.3.1 and iv.3.2 mixture first reacts with CES for 9.75 hours, then with ALP for 15 min.

IV. 3. 3. 3. Multicellular spheroid culture in stage-by-stage assembled nanostructures

The mechanical property of the nanostructures obtained through three pathways were evaluated by rheological tests. In the oscillatory strain sweep test, we could find that the stage-by-stage treatment manner in the order of ALP and CES showed most stable scaffolds. In the oscillatory frequency sweep measurements (Figure 7a), we could also draw the conclusion that the nanostructures obtained through stage-by-stage treatment of molecule iv.3.1 and iv.3.2 mixture in the order of ALP and CES delivered most stable scaffold, and it was consistent with cross-linked nanofibrous scaffold by TEM. In a further biocompatible evaluation, we found both molecules iv.3.1 and iv.3.2 were innocuous HeLa cells (Figure 7b/c). The obtained

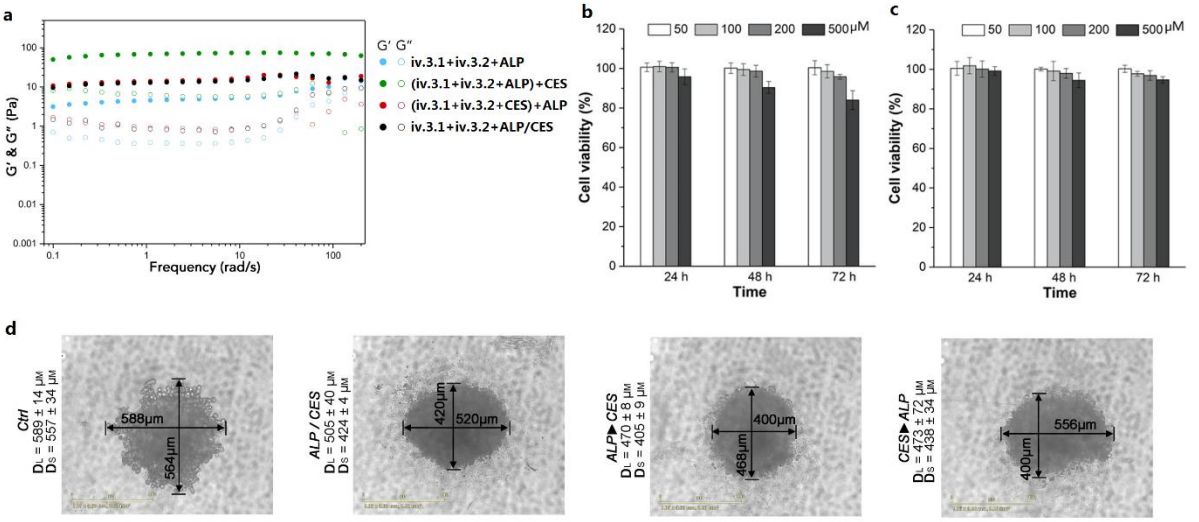

Figure 7. (a) The frequency sweep tests of co-assembled nanostructures obtained by administration of two enzymes in three different orders; HeLa cell viability assay upon the treatment of molecule iv.3.1 (b) and molecule iv.3.2 (c); (d) Optical images of HeLa cell spheroids cultured under various conditions exhibiting the influence of nanostructures obtained by stage-by-stage assembly.

nanostructure via EIHA could be potentially applied as biomaterials. We prepared HeLa spheroids in culture with different nanostructures. By measuring the diameter of the obtained spheroids, we found that tightly packing spheroids were achieved when culturing in the medium with nanostructures due to the interaction between nanostructures and cells via biotin-avidin binding (Figure 7d). By comparing the detail in diameters, the most stable nanostructure obtaining from stage-by-stage treatment of ALP and CES delivered the most tightly packed spheroids with less variations in all directions.

IV. 3. 4. Conclusion

In our current study, we introduced nanostructure fabrication guiding by two enzymes, ALP and CES. A change in the order of enzyme administration lead to distinctly different nanostructures. Stage-by-stage treatment by ALP and CES delivered a more robust nanostructures in which the nanofibrils was crossed by small aggregates, and it potentially controlled 3D cell-cell interaction in multicellular spheroid culture. Detailed study in the assembly process revealed that ALP-guided dephosphorylation was barely affected by its surrounding environment; while the CES-catalyzed hydrolysis was effectively affected by their surrounding molecules and nanostructures. Employing the kinetics difference and regulating enzyme administration will provide more choices to reach functional hierarchical nanostructure assembly.

V. 1. Carboxylesterase Trigger Intra-Cellular Molecular Self-assembly for Anti-cancer Therapy

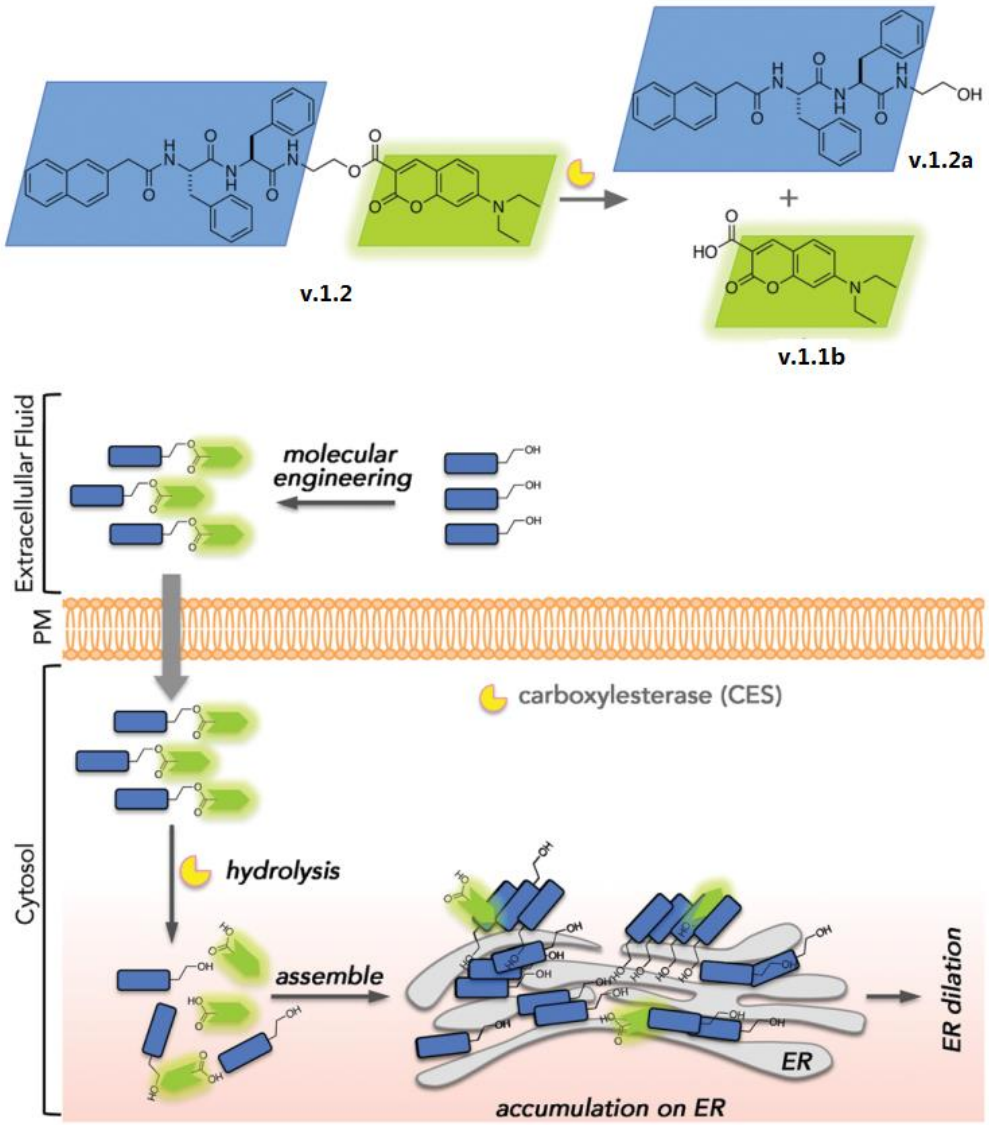

This chapter corresponding to the following publication:

Shijin Zhang, Xunwu Hu, Dingze Mang, Toshio Sasaki, and Ye Zhang*. "Self-delivery of N-hydroxylethyl peptide assemblies to the cytosol inducing endoplasmic reticulum dilation in cancer cells". *Chem. Commun.*, **2019**, 55, 7474

V. 1. 1. Introduction

The homeostasis of every cellular organelle plays an important role in maintaining the survival of cell. Among all the sub-organelles, endoplasmic reticulum (ER) has been shown to be widely interacted with other sub-organelles, such as mitochondria, lipid droplets, endosomes, the Golgi apparatus, and the plasma membrane.[1] Biologists have revealed that ER works on synthesizing, folding, modifying and transporting of proteins. Its function determined that ER will have a close connection with other sub-organelles. Once the ER structure is disrupted, its function would be highly harmed. Thus, leading to a network collapse in the cell, triggering the apoptosis of the cell. Though the detail is not fully disclosed, ER has been recognized as an important sub-organelle in determining the fate of the cell. In pharmaceutical research, regulating the function of ER has been utilized as a target for new drug candidate development. Currently, there are several natural products have been proved in regulating ER stress on various cancer cell lines by monitoring the content of critical proteins in signalling pathway.[2] To get more clues on regulating ER stress in therapeutic application, more investigation on targeting ER is highly demanded.

In clinical studies, upregulated ER stress is widely discovered in alcoholic patients. Upregulated ER stress is a long-term result of alcohol abuse, it leads to the dysfunction multiple organs including liver, heart, brain and pancreas. Typically, detailed study on the alcoholic patient related liver disease, ER dilation (mark of upregulated ER stress in ER structure disruption) is disclosed in hepatocytes.[3] Though the detail in upregulated ER stress leading to multiple organs risk in alcoholic patients is still not fully illustrated, the interesting results have inspired scientists to regulate ER stress by treating cancer cells with ER-targeting molecules. Thus, upregulate ER stress and initiate the cancer cell apoptosis. In our current study, we try to create an acute alcohol abuse effect by combing the strategy of molecular self-assembly and prodrug. Briefly, prodrug design facilitates molecule cellular uptake, molecular self-assembly guarantees enriching alcoholic derivatives around ER, leading to an acute alcohol abuse effect. To reach an acute alcohol abuse effect around ER in cancer cells, we designed and synthesized a N-hydroxylethyl peptide for cytosolic self-assembly. To make an efficient molecular self-assembly intracellular, we adopted the prodrug design.[4] The prodrug design is thought to highly enhance molecule cellular uptake, and enzymatic hydrolysis mediated by carboxylesterse (CES) inside the cell can recover the molecular self-assembly motif.[5]

To reach an efficient molecular self-assembly, we chose a well-recognized molecular self-assembly motif (naphthalene-Phe-Phe) as the building block for molecular design.[6] Conjugating with ethanolamine to create an alcoholic derivative (v.1.2a). By combining with prodrug design, the hydroxyl group was conjugated with a fluorescent motif (coumarin) by an ester linkage to obtain molecule v.1.2. It not only enhances molecule cellular uptake, but also provides fluorescent signal to identify the molecule self-assembly after entering into the cell. To prove the molecular design is rational and effective, we design another two control molecules in the study. Briefly, the building block of molecule v.1.1 does not contain alcoholic group, it can be used to prove the necessary of alcoholic group in the molecular design; for molecule v.1.3, no ester linkage was contained in the molecule, thus prove the CES was necessary to recover the self-assembly motif.

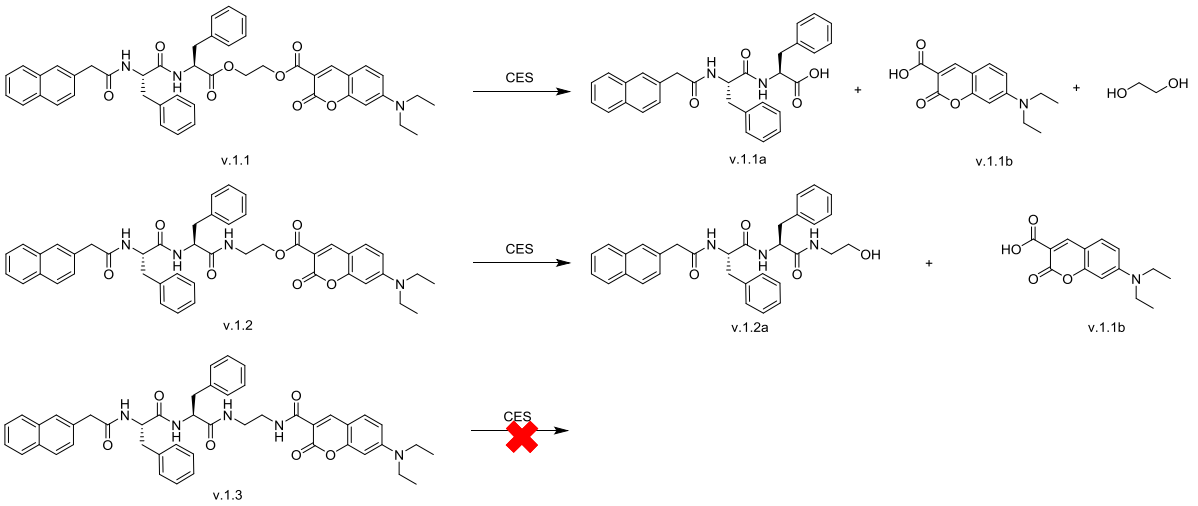

Scheme 1. Carboxyl esterase hydrolysis of molecule v.1.1, v.1.2 and v.1.3.

V. 1. 2 Experimental Section

V. 1. 2. 1. Materials

Chemical reagents	Grade	Manufacturer
Fmoc-Amino acid	98.0%	GL Biochem (Shanghai, China)
2-(1*H*-benzotriazol-1-yl)-1,1,3,3-tetramethyluronium hexafluorophosphate (HBTU)	98.5%	Sigma Aldrich
Trifluoroacetic acid (TFA)	98.0%	Sigma Aldrich
N-Hydroxysuccinimide (NHS)	98.0%	Sigma Aldrich
N,N'-Diisopropylcarbodiimide (DIC)	99.0%	Sigma Aldrich
N-(3-dimethylaminopropyl)-*N*'-ethylcarbodiimide hydrochloride (EDCI)	98.0%	Sigma Aldrich
1-Hydroxybenzotriazole hydrate (HOBT)	97.0%	Sigma Aldrich
4-Dimethylaminopyridine (DMAP)	98.0%	Sigma Aldrich
Ethylene glycol	99.8%	Sigma Aldrich
Ethanolamine	99.0%	Sigma Aldrich
N-Boc-ethylenediamine	98.0%	Sigma Aldrich
Meldrum's acid	98.0%	Sigma Aldrich
Piperidinum acetate	98.0%	Tokyo Chemistry Industry
4-(Diethylamino)salicylaldehyde	98.0%	Tokyo Chemistry Industry
1-Octanol	97.0%	Nacalai Tesque
Boric acid	99.5%	Nacalai Tesque

All organic solvents were obtained from FUJIFILM Wako Pure Chemical Corporation and dehydrated before experiment by a solvent purification system.

Biological reagents: Carboxylesterase (E0887-500UN, Sigma-Aldrich), CelLytic M solution (Sigma-Aldrich), Blocking one-P (Nacalai tesque, Japan), caspase-8 (Abcam, ab32397), caspase-9 (Santa Cruz, sc-56073), DR-5 (Abcam, ab8416), caspase-12 (Santa Cruz, sc-21747), and beta-actin (Abcam, ab8227) antibody, goat anti-mouse IgG (Bio-Rad, Hercules, CA, USA), peroxidase-conjugated goat anti-rabbit IgG (Bio-Rad, Hercules, CA, USA), ECLTM prime Western blotting detection reagent (GE Healthcare, Little Chalfont, UK).

V. 1. 2. 2. Instruments

Agilent 1260 Infinity Preparation HPLC (Column: 19 mm×150 mm XBridge® Peptide BEH C18 column), Agilent 1260 Infinity Analysis HPLC (Column: 2.1 mm × 150 mm XBridge®

Peptide BEH C18 column), Thermo LTQ-ETD mass spectrometer (ESI-MS), NMR equipment: JEOL 400 spectrometer, Eppendorf Centrifuge 5424R, Thermo Nanodrop 2000C spectrophotometer, Hamamatsu fluorescence spectrometer, Transmission Electron Microscope (JEM-1230R), Nivo3 microplate reader (PerkinElmer), flow cytometer (Merck Millipore ImageStream X Mark II), section equipment (Leica EM UC6), Milli-Q® Integral 3/5/10/15 System.

V. 1. 2. 3. Synthesis

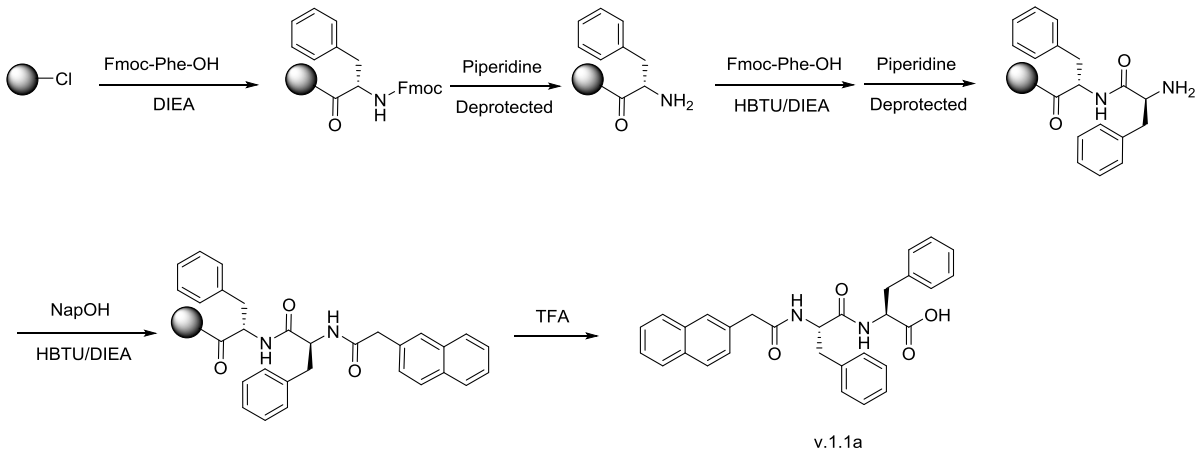

Scheme 2. Synthesis of compound v.1.1a.

Compound **v.1.1a**: Compound v.1.1a was obtained via solid phase peptide synthesis (SPPS). 2-Chlorotrityl chloride resin (2.0 g, 2 mmol) was swelled in anhydrous DCM for 20 min, L-Fmoc-Phe-OH (1.94 g, 5 mmol) dissolved in anhydrous DMF was conjugated to resin with DIEA in 30 min. Then washed with anhydrous DMF for 3 times, unreacted sites in the resin were blocked with DCM/MeOH/DIEA (80:15:5) for 20 min and washed by anhydrous DMF for 5 times. Then piperidine solution (20% in DMF) was added into reaction for 30 min to remove the Fmoc protecting group on the amino acid. We carried out the peptide elongation according to standard SPPS protocol to get the desired compound. v.1.1a was cleaved off the resin using TFA for 2 h. After removing the solvent, anhydrous ether was added into the concentrated product and white precipitation of v.1.1a was obtained.[6]

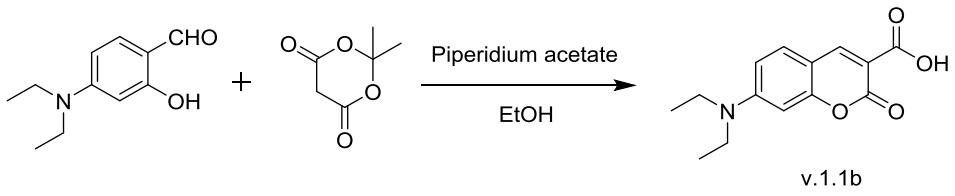

Scheme 3. Synthesis of compound v.1.1b.

Compound v.1.1b was synthesized by following the published method.[7]

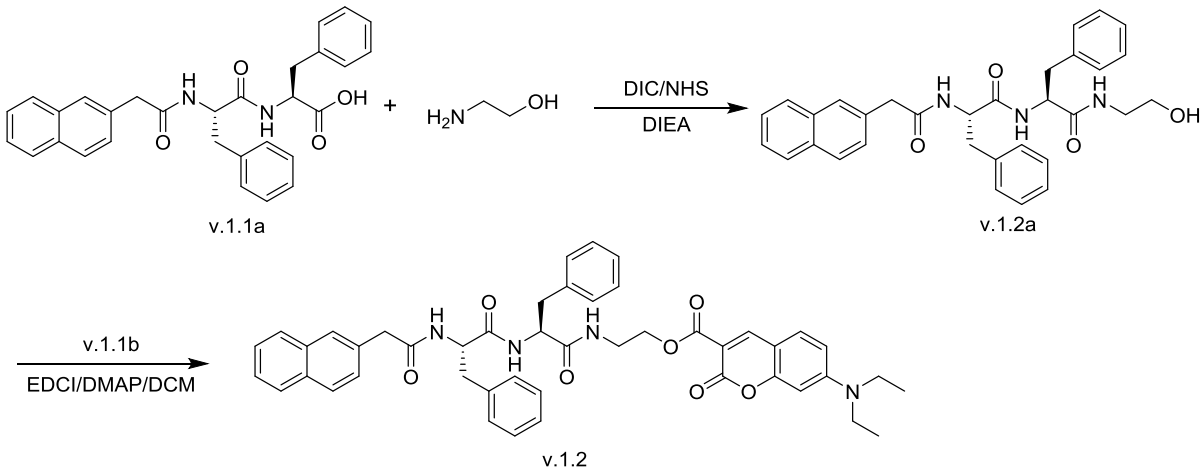

Scheme 4. Synthesis of compound v.1.2.

Compound **v.1.2a**: It was synthesized by following the published method.[8]

^{1}HNMR (400 MHz, DMSO-d_6) δ 7.59 (d, *J* = 6.7 Hz, 1H), 7.49 (d, *J* = 6.6 Hz, 1H), 7.29 (t, *J* = 4.5 Hz, 1H), 7.25 (d, *J* = 6.4 Hz, 1H), 7.20 (d, *J* = 6.3 Hz, 1H), 7.17 (d, *J* = 6.8 Hz, 1H), 7.05 (s, 1H), 6.97 – 6.91 (m, 2H), 6.76 – 6.68 (m, 12H), 4.69 (t, *J* = 4.3 Hz, 1H), 4.60 – 4.53 (m, 2H), 3.83 (dd, *J* = 11.2, 3.4 Hz, 1H), 3.79 – 3.76 (m, 1H), 3.48 – 3.43 (m, 2H), 3.36 – 3.31 (m, 2H), 3.22 (dd, *J* = 11.0, 6.9 Hz, 1H), 3.15 (dd, *J* = 11.0, 7.9 Hz, 1H).

Compound **v.1.2**: In a 100mL round-bottom flask, compound v.1.1b (0.35 g, 1.4 mmol) was dissolved in 30mL anhydrous DCM. After adding EDCI (0.41 g, 2.2 mmol) and DMAP (17 mg, 0.14 mmol) in to the flask, the mixture was kept stirring at room temperature for 5 min. Compound v.1.2a (0.7 g, 1.3 mmol) was transferred into the reaction flask, and kept stirring at room temperature overnight. After removing the solvent, the crude product was purified by silica gel column chromatography to get the target compound (yield: 72%).

^{1}HNMR (400 MHz, DMSO-d_6) δ 7.81 (s, 1H), 7.58 (dd, *J* = 19.9 Hz, 6.5 Hz, 2H), 7.52 – 7.43 (m, 1H), 7.24 (d, *J* = 5.9 Hz, 1H), 7.20 – 7.12 (m, 2H), 7.05 (d, *J* = 4.3 Hz, 1H), 7.01 – 6.89 (m, 3H), 6.78 – 6.63 (m, 11H), 6.36 – 6.28 (m, 1H), 6.16 (d, *J* = 1.3 Hz, 1H), 4.62 – 4.54 (m, 2H), 4.28 – 4.21 (m, 1H), 3.86 – 3.81 (m, 3H), 3.76 – 3.70 (m, 5H), 3.50 – 3.44 (m, 1H), 3.40 – 3.30 (m, 2H), 3.28 – 3.20 (m, 2H), 3.19 – 3.10 (m, 2H), 1.86 (t, *J* = 5.5 Hz, 6H) ppm.

^{13}CNMR(101 MHz, DMSO-d_6) δ 157.25, 156.98, 156.37, 156.31, 150.71, 146.83, 146.04, 142.68, 140.04, 130.57, 130.50, 130.46, 127.52, 126.73, 125.78, 125.74, 123.80, 123.77, 123.73, 122.85, 122.76, 122.71, 122.48, 122.36, 122.29, 122.20, 121.44, 121.35, 121.30, 121.19, 120.77, 108.25, 105.95, 97.08, 70.69, 68.16, 63.58, 55.90, 54.19, 53.58, 50.35, 49.04, 45.03, 30.27 ppm.

MS: calculated for $C_{46}H_{48}N_4O_7$ is 768.91, found 767.18, $[M - H]^-$.

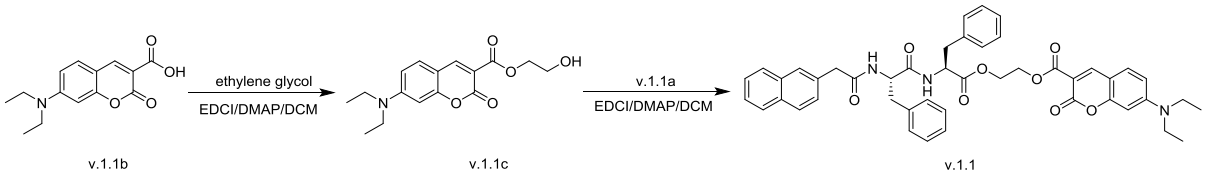

Scheme 5. Synthesis of compound v.1.1.

Compound **v.1.1c**: Compound v.1.1b (1.0 g, 3.8 mmol), EDC (0.81 g, 4.2 mmol), and DMAP (50 mg, 0.4 mmol) were transferred into a 100mL round-bottom flask, dissolved by 30mL anhydrous DCM. Then ethylene glycol (2.36 g, 38 mmol) diluted in 5mL anhydrous DCM was added into the reaction flask. The reaction mixture was stirred at room temperature for 36h. The reaction mixture was diluted by 50mL EtOAc, and washed by 25 mL water twice. The organic layer was collected and dried using anhydrous Na_2SO_4 for 2h. Silica gel column chromatography was applied for purification to obtain the target compound (yield: 71%).

^{1}HNMR (400 MHz, DMSO-d_6) δ 8.55 (s, 1H), 7.58 (d, *J* = 9.0 Hz, 1H), 6.74 (dd, J = 9.0, 2.4 Hz, 1H), 6.51 (d, *J* = 2.3 Hz, 1H), 4.82 (m, 1H), 4.16 – 4.13 (m, 2H), 3.62 (m, 2H), 3.44 (q, *J* = 7.1 Hz, 4H), 1.10 (t, J = 7.1 Hz, 6H) ppm.

Compound v.1.1: In a 100mL round-bottom flask, compound v.1.1a (0.3 g, 1.0 mmol) was dissolved in 30mL anhydrous DCM. After adding EDC (0.21 g, 1.1 mmol) and DMAP (15 mg, 0.1 mmol), the reaction mixture was kept stirring at room temperature for 5 min. Compound v.1.1c (0.57 g, 1.2 mmol) was transferred into the reaction flask, and kept stirring at room temperature overnight. After removing the solvents, the crude product was purified using silica gel column chromatography to get the target compound as yellow solid (yield: 68%).

^{1}HNMR (400 MHz, DMSO-d_6) δ 7.85 (dd, *J* = 22.1 Hz, 6.2, 1H), 7.78 (d, *J* = 12.0 Hz, 1H), 7.59 (dd, *J* = 17.9 Hz, 6.9, 1H), 7.23 (d, *J* = 5.7 Hz, 1H), 7.18 – 7.11 (m, 2H), 7.05 – 6.98 (m, 2H), 6.96 – 6.89 (m, 2H), 6.77 – 6.63 (m, 10H), 6.61 – 6.55 (m, 1H), 6.33 (ddd, *J* =11.7, 7.2, 4.7 Hz, 1H), 6.17 (dd, *J* = 8.4, 1.7 Hz, 1H), 4.65 – 4.55 (m, 2H), 4.51 – 4.39 (m, 4H), 3.80 (dt, *J* = 12.5, 6.2 Hz, 1H), 3.77 (m, 5H), 3.63 (s, 2H), 3.49 – 3.39 (m, 1H), 3.36 – 3.22 (m, 2H), 3.16 – 3.06 (m, 1H), 1.87 (t, *J* = 5.5 Hz, 6H) ppm.

^{13}CNMR (101 MHz, DMSO-d_6) δ 157.69, 157.51, 157.35, 156.18, 150.82, 146.90, 145.97, 142.75, 140.05, 130.55, 130.49, 130.11, 130.00, 127.55, 126.71, 125.90, 125.86, 125.75, 123.80, 123.73, 123.66, 122.99, 122.69, 122.67, 122.46, 122.34, 122.26, 122.17, 121.65, 121.27, 121.17, 120.75, 108.28, 105.98, 97.08, 70.56, 70.16, 63.25, 55.91, 54.13, 50.68, 49.84, 30.28 ppm.

MS: calculated for $C_{46}H_{47}N_3O_8$ is 769.90, found 768.18, $[M - H]^-$.

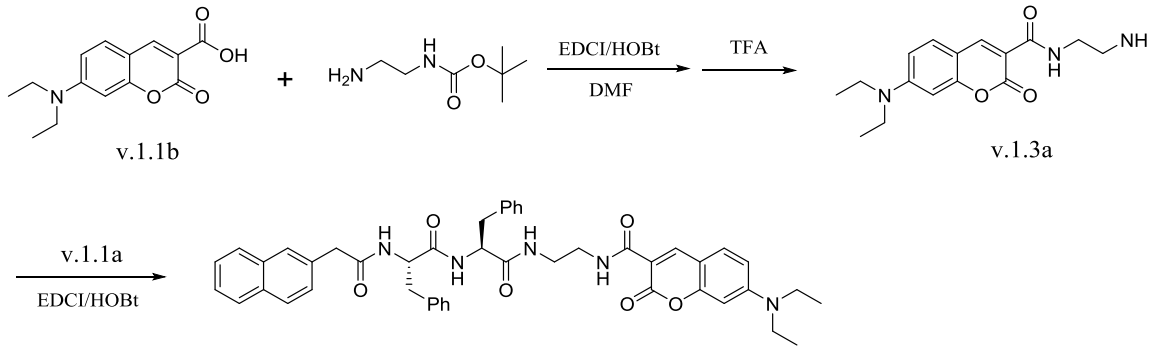

Scheme 6. Synthesis of compound v.1.3.

Compound **v.1.3a** was synthesized by following the published method.[9]

Compound **v.1.3**: In a 100mL round-bottom flask, compound v.1.1a (0.39 g, 0.8 mmol), HOBt (0.14 g, 1.1 mmol) and EDCI (0.2 g, 1.2 mmol) was dissolved in 30mL anhydrous DMF, and kept stirring at room temperature for 5 min. Compound v.1.3a (0.32 g, 1.1 mmol) was transferred into the reaction flask, and kept stirring at room temperature for 24 h. After removing the solvent, the crude product was purified by silica gel column chromatography to get the target compound (yield: 75%).

^{1}HNMR (400 MHz, DMSO-d_6) δ 7.94 (t, J = 4.6 Hz, 1H), 7.88 (s, 1H), 7.59 (d, J = 6.8 Hz, 1H), 7.44 – 7.37 (m, 1H), 7.27 – 7.23 (m, 1H), 7.21 – 7.13 (m, 2H), 7.10 – 7.01 (m, 2H), 6.98 – 6.89 (m, 2H), 6.75 – 6.63 (m, 11H), 6.38 (dd, J = 7.3, 1.8 Hz, 1H), 6.23 (d, J = 1.8 Hz, 1H), 4.64 – 4.48 (m, 2H), 3.81 - 3.75 (m, 5H), 3.66 – 3.60 (m, 3H), 3.59 – 3.54 (m, 2H), 3.54 – 3.47 (m, 2H), 3.35 – 3.29 (m, 2H), 3.26 – 3.06 (m, 2H), 1.87 (t, J = 5.6 Hz, 6H) ppm.

^{13}CNMR(101 MHz, DMSO-d_6) δ 160.00, 157.14, 156.24, 150.48, 149.66, 149.17, 146.20, 142.36, 138.60, 130.63, 130.53, 127.54, 126.73, 125.78, 125.68, 123.79, 123.73, 122.84, 122.71, 122.48, 122.35, 122.30, 122.20, 121.40, 121.29, 121.17, 120.76, 108.49, 107.91, 106.51, 97.09, 63.65, 63.44, 55.87, 54.18, 50.69, 50.35, 30.27 ppm.

MS: calculated for $C_{46}H_{48}N_4O_7$ is 767.93, found 766.18, $[M - H]^-$.

V. 1. 2. 4. Buffer solution preparation

To ensure the best carboxylesterase activity, enzymatic reaction was carried out at the recommended borate buffer solution according to the protocol from Sigma Aldrich. Specifically, 0.62 mg/mL solution in purified water (from MilliQ water purify system) was prepared using boric acid, pH was adjusted to 8.0 with 1N NaOH solution.

V. 1. 2. 5. CES catalysed hydrolysis

V. 1. 2. 5. 1. In buffer solution

Carboxylesterase (CES) from rabbit liver lyophilized powder was purchased from Sigma-Aldrich (E0887-500UN). Following the instruction, CES stock solution (1u/5μL) was prepared

in borate buffer (pH 8.0). Stock solutions of compound v.1.1, v.1.2, or v.1.3 (40 mM in DMSO) were diluted in borate buffer to the desired concentration. Proper volume of CES stock solution was added into 200 μL of compound solution reaching final concentration of 1u. HPLC and LCMS were applied to identify the reaction products and monitor the progress of hydrolysis at 37°C.

V. 1. 2. 5. 2. In cell lysate and extracellular culture medium

HeLa cell was cultured in 10 cm polystyrene culture plate. When cells reached approximately 80% confluence in the log phase growth period, aspirated media and gently washed by PBS buffer. Removed the PBS buffer, 2 mL of Trypsin solution was added and incubated at 37 ℃ with a humidified atmosphere of 5% CO_2 for 3 min to detach the cells. 6 mL of cold PBS buffer was added and transferred to a 15 mL tube, centrifuged at 4 °C to obtain the HeLa cells. Cell lysate was obtained by adding 200μL cold CelLytic M solution (Sigma-Aldrich) to the harvested HeLa cells, incubated for 30 min at 0 °C on a shaker. Then centrifuged the lysed cells for 5 min at 20000 g at 4 °C to collect the supernatant and stored at -20 °C. The obtained cell lysate was applied to v.1.1, v.1.2 within 3 days to ensure the best enzyme activity. Fresh culture medium and post incubated culture medium that collected from HeLa cell culture after 24h incubation were applied as dilution solution without adding extra CES to study the kinetic profile of extracellular CES catalysed hydrolysis at 37°C, no degradation of the original compound was observed, confirmed by HPLC. Treated HeLa cells were collected after time-dependent incubation with three compounds. Sonication (20s × 5 times) was applied to break the cell membrane, centrifuged at 13000 × g for 5 min, and then collected the supernatant. Further analysed using HPLC-MS to study the intracellular CES catalysed hydrolysis.

V. 1. 2. 6. UV-Vis Absorption and emission spectroscopy

UV-vis spectra were collected using Thermo Nanodrop 2000C spectrophotometer. The path length of the cuvette was 1 cm. The detection range was set to 250-700 nm and the spectral resolution was set to 1.0 nm. Emission spectra were collected using Hamamatsu fluorescence spectrometer. The excitation wavelength was set to 405 nm and emission collection wavelength was set between 415 and 700 nm.

V. 1. 2. 7. 1- Octanol/water partition coefficients

Slow-stirring method was applied to determine 1-octanol/water partition coefficients ($P_{Oct/Wat}$). The 1-octanol and Mili-Q water were mutually saturated before using for the experiments. Varied concentrations of v.1.1, v.1.2, and v.1.3 were dissolved in 1-octanol and UV-Vis absorption spectra were measured to obtain the working standard curves. Briefly, $P_{Oct/Wat}$ was obtained by dissolving v.1.1, v.1.2, and v.1.3 in 1-octanol, then mixed with same volume of Mili-Q water. The mixture was vigorously stirred for 24h and left to settle until complete separation of the two phases. UV-Vis absorbance was determined in the 1-octanol layer, and further compared with working standard to obtain $P_{Oct/Wat}$ value.

V. 1. 2. 8. TEM sample preparation

Carbon-coated copper grids were glow discharged to enhance hydrophilicity; then 5 μL of sample solution was placed on the grid, leave the sample on the grid around 60 s, removed the

excess fluid with a filter paper; washed the grid with 5 μL of distilled water 3 times, removed the excess water with filter paper; 5 μL of 1% uranyl acetate was placed on the grid, after 10s, removed the excess solution by touching the edge of grid using a filter paper; dry the grid at room temperature.

V. 1. 2. 9. Circular dichroism (CD) spectroscopy

CD spectra were collected on a spectrometer JASCO J-820 with bandwidth of 1.0 nm in the ultraviolet (UV) region (190-350 nm) using a 1 mm quartz cuvette.

V. 1. 2. 10. Cell culture

HeLa, SKOV3, OVCAR-3, HepG2, PANC-1 cell lines were purchased from American-type Culture Collection (ATCC, USA) and cultured in ATCC recommended media. HeLa and HepG2 cell lines were cultured in DMEM containing 10% FBS, whereas SKOV3 cell line was cultured in McCoy's medium with 10% FBS, OVCAR3 was cultured in RPMI 1640 medium with 20% FBS and PANC1 was cultured in RPMI 1640 with 10% FBS. Incubation was carried out at 37 ℃ with a humidified atmosphere of 5% CO_2. The cells were maintained at 80% confluency and used for the bioassays.

V. 1. 2. 11. Cell viability assay

Cells in exponential growth phase were seeded in a 96 well plate at a concentration of 1×10^4 cells/well for all cell lines. The cells were allowed to attach to the wells for 12 h at 37 ℃, 5% CO_2. The culture medium was removed followed by addition of 100 μL culture medium containing different concentrations (12.5, 25, 50, 100 and 200 μM) of compound v.1.1, v.1.2, v.1.3, v.1.1b, v.1.2a and v.1.3a (immediately diluted from 80 mM stock solution in DMSO). After the desired time of exposure, 10 μL MTT solution (5 mg/mL) was added to each well and incubated at 37°C for another 4 h, and then 100 μL of SDS solution (10% in Milli-Q water) was added to stop the reduction reaction and dissolve the purple formazan. The absorbance at 570 nm was measured using Nivo3 microplate reader (PerkinElmer). All experiments were performed in triplicate and repeated three times.

V. 1. 2. 12. Cellular uptake assay

HeLa cells were seeded in a 35 mm culture dish at a concentration of 2×10^5 cells/dish. The cells were allowed to attach to the dish bottom for 12h at 37 ℃, 5% CO_2. The culture medium was removed followed by addition of 2 mL culture medium containing a concentration of 10 μM of compound v.1.1, v.1.1a, v.1.2, or v.1.2a. The concentrations of the remaining compound in the medium were quantified by HPLC at 0, 1, 3, and 6h.

V. 1. 2. 13. Cellular uptake quantification by flow cytometry

HeLa cells were seeded in a 6 well plate at a concentration of 2×10^5 cells/well. The cells were allowed to attach to the bottom for 12h at 37 ℃, 5% CO_2. The culture medium was removed followed by addition of 2 mL culture medium containing a concentration of 10 μM of compound v.1.1 and v.1.2. After treated certain time (0h (ctrl.), 1h, 3h, 6h, 12h and 24h), all

cells were harvested and washed with ice PBS twice. 50 μL of ice PBS buffer was adding into the obtained cells, and analysis of fluorescence of individual cells were carried out by flow cytometer (Merck Millipore ImageStream X Mark II). 20,000 cells were measured for each experimental condition with excitation wavelength at 405 nm.

V. 1. 2. 14. Section imaging of HeLa cell

HeLa cells were seeded in a 35 mm culture dish at a concentration of 2×10^5 cells/dish. The cells were allowed to attach to the dish bottom for 12h at 37℃, 5% CO_2. The culture medium was removed followed by addition of 2 mL culture medium containing a concentration of 50 μM of compound v.1.1 and v.1.2. After 6h incubation, the medium was removed and washed twice by warm 1 × PBS buffer. Cell resin block preparation followed the published method.[10] The thin cell section (～100 nm) was prepared using Leica EM UC6. Following the staining process using uranyl acetate and lead citrate, the cell section was observed under transmission electron microscope (JEOL JEM-1230R, 100 kV).

V. 1. 2. 15. Western blotting

HeLa cells were cultured in 6-well plate to reach 70% confluency and 20 μM of 13 was added. After treated certain time (0h (ctrl.), 1h, 3h, 6h, 12h and 24h), all cells were harvested and washed with ice PBS twice. 50 μL CelLytic M solution (Sigma-Aldrich) containing protease inhibitors cocktail was added and incubated for 30 min on a shaker. Then centrifuge the lysed cells for 5 min at 20000 g to pellet the cellular debris. The concentrations of lysates were determined using the bicinchoninic acid (BCA) method. Proteins were dissolved in SDS sample buffer containing 2% *β*-mercaptoehtanol. Samples (10 μL of each) were loaded and separated by 10% Laemmli-SDS-PAGE. For Western blot analysis, the proteins were transferred onto a polyvinylidene difluoride (PVDF; Bio-Rad, Her-cules, CA, USA) membrane. After blocking with Blocking one-P (Nacalai tesque, Kyoto, Japan), the membrane was incubated with the antibody. Specifically, incubating with 1:1000 dilution for caspase-8 (Abcam, ab32397), caspase-9 (Santa Cruz, sc-56073) and DR-5 (Abcam, ab8416) antibody, 1:200 dilution for caspase-12 (Santa Cruz, sc-21747), and 1:2000 dilution for beta-actin (Abcam, ab8227) antibody for overnight at 4^{o}C. After washing, the membrane was incubated with 2,000-fold diluted peroxidase-conjugated goat anti-mouse IgG (Bio-Rad, Hercules, CA, USA) or 2,000-fold diluted peroxidase-conjugated goat anti-rabbit IgG (Bio-Rad, Hercules, CA, USA) for 45 min, and then stained using ECLTM prime Western blotting detection reagent (GE Healthcare, Little Chalfont, UK).

V. 1. 3 Results

V. 1. 3. 1. Molecular Self-assembly Study

V. 1. 3. 1. 1. Before enzymatic reaction

Molecular self-assembly was carried out in borate buffer, a series of concentration (62.5 μM, 125 μM, 250 μM and 500 μM) solution were prepared. After overnight aging, imaging sample

was prepared according to the above-mentioned method (TEM sample preparation), images were taken on JEM-1230R at an accelerated voltage of 100 kV.

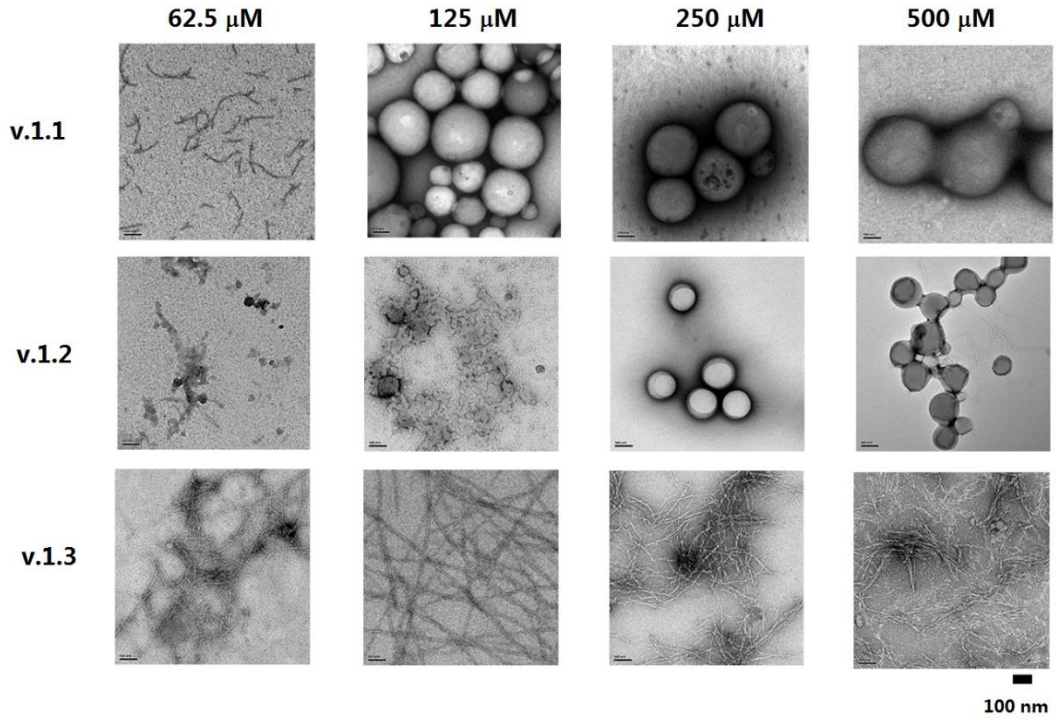

Figure 1. TEM images of concentration-dependent v.1.1, v.1.2 and v.1.3 dissolved in borate buffer/DMSO (v/v = 95:5)

As shown in Figure 1, for the borate buffer of molecule v.1.2, only some irregular aggregates can be observed at a concentration up to 125 μM, it started to form nanovesicles at 250 μM or even higher concentration (e.g. 500 μM). The borate buffer of molecule v.1.1 formed some short nanofibers at a concentration of 62.5 μM, and it started to form nanovesicles from the concentration of 125 μM and even higher concentration (e.g. 250 μM, 500μM). In the case of molecule v.1.3 in borate buffer, it started to form nanofibers at the concentration of 62.5 μM and kept the same nanostructure up to 500 μM. We selected the concentration of 125 μM for further enzymatic hydrolysis, since the morphology of molecule v.1.1, v.1.2 and v.1.3 is different, it would be easier for us to distinguish the nanostructures change visually.

V. 1. 3. 1. 2. After enzymatic hydrolysis

At the molecule scale, CES can work to hydrolyse the ester bond in the molecule as shown in the following scheme 7. In the case of molecule v.1.1 and v.1.2, due to the presence of ester bond in the molecule, they can be hydrolysed by CES, while molecule v.1.3 worked as a control to show CES specifically works on ester bond.

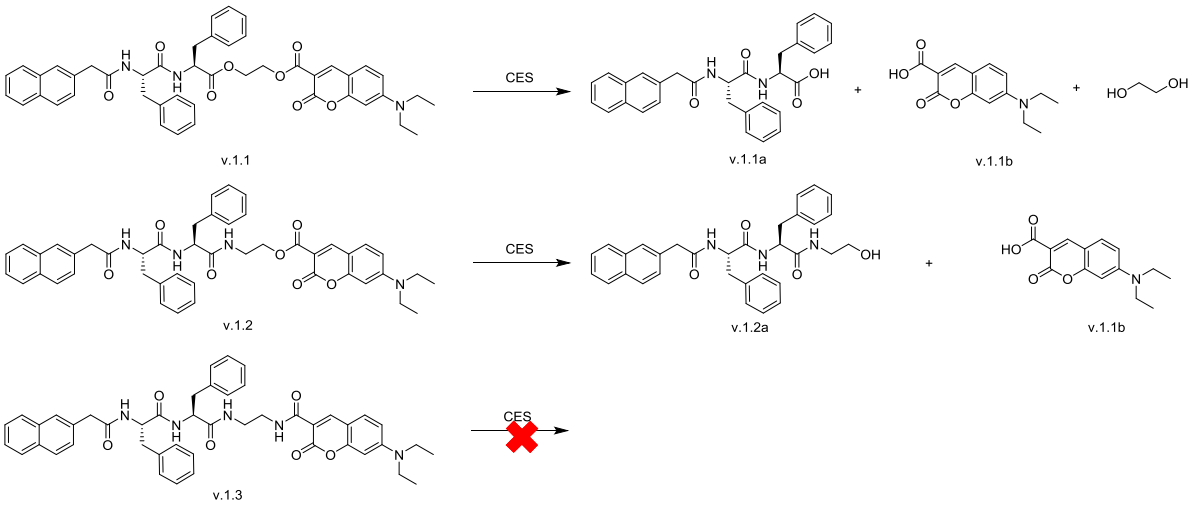

Scheme 7. CES-catalysed hydrolysis of molecule v.1.1, v.1.2 and v.1.3 in borate buffer (pH=8.0, 37°C).

The hydrolysis kinetic process was monitored by analysis HPLC. For molecule v.1.1 and v.1.2, after enzymatic hydrolysis, new peak showed in the HPLC spectrum and the new peak was checked by MS to confirm the hydrolysis of ester bond in the molecule. The hydrolysis was performed on both 20 °C and 37 °C (Shown in Figure 2). For molecule v.1.2, when the CES-catalysed hydrolysis was performed at 20 °C, only about 20% of molecule v.1.2 was hydrolysed (Figure 2b). However, when the hydrolysis temperature was set at 37°C, the hydrolysis process was completed in 12h (Figure 2d). As for molecule v.1.1, we can figure out it was completely hydrolysed in 12h at 20 °C (Figure 2a)., if the hydrolysis temperature of molecule v.1.3. Since the hydrolysis rate of molecule v.1.1 is fast at 37°C, when monitoring the hydrolysis process of molecule v.1.1 with UV-Vis spectroscopy, fluorescence spectroscopy and optical images, the CES-catalysed process was selected at 20 °C to deliver a more accurately reflection of the kinetic process. For molecule v.1.2, the kinetic process monitoring was selected at 37 °C. The kinetic process results were shown in Figure 3. In the case of normal light kinetic images, it was hard to find any difference for both molecule v.1.1 and v.1.2; however, when turned to UV light (365 nm) images, we can observe the color transition from yellow to blue when they were completely hydrolysed. UV-Vis absorption spectra revealed a blue shift for both molecule v.1.1 (19 nm) and molecule v.1.2 (19 nm) and fluorescence spectra also showed a blue shift for both molecules, which was consistent with the UV light kinetic images.

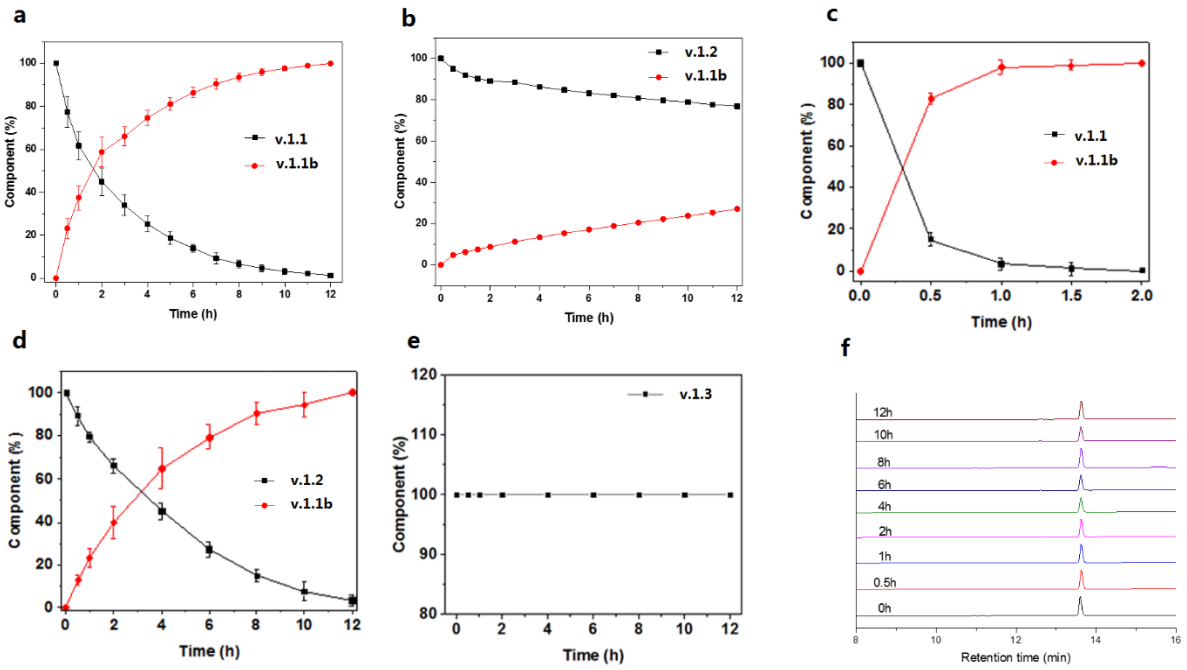

Figure 2. CES-catalysed hydrolysis kinetic profile of molecule v.1.1 and v.1.2 at 20 °C (a, b), and molecule v.1.1, v.1.2, v.1.3 at 37 °C (c, d, e). The HPLC spectra of hydrolysis process of molecule v.1.3 at 37 °C.

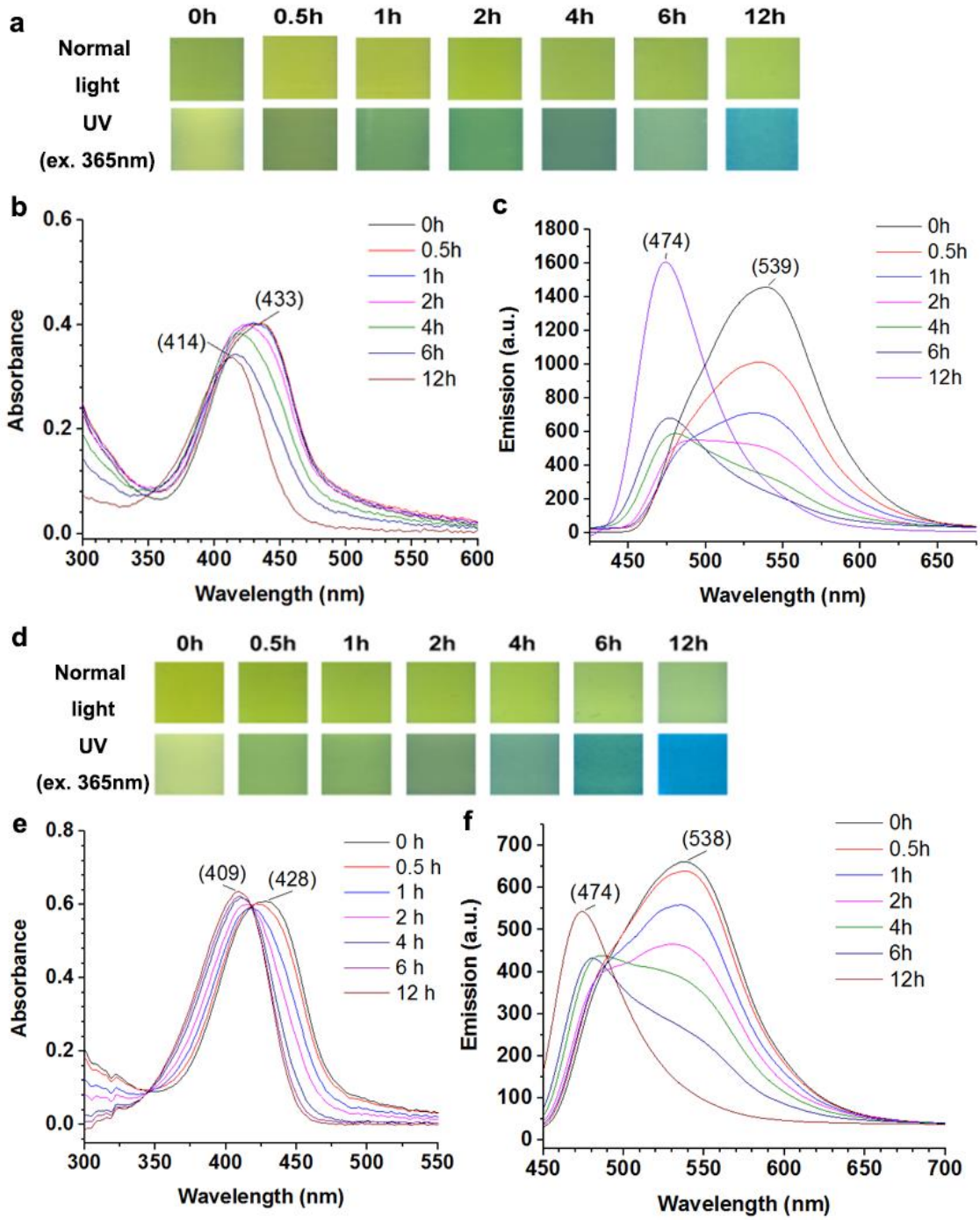

Figure 3. (a) Time-dependent optical images under normal light (upper row) and UV light (bottom row) of v.1.2 (50 μM with 1u of CES) in borate buffer. Time-dependent UV-Vis absorbance (b) and emission spectra (ex. 405nm) (c) of v.1.2 (50 μM with 1u of CES) in borate buffer; Time-dependent optical images under the normal light (upper row) and UV light (bottom row) of v.1.1 (50 μM with 1u of CES) in borate buffer (d). Time-dependent UV-Vis absorbance (e) and emission spectra (ex. 405nm) (f) of v.1.1 (50 μM with 1u of CES) in borate buffer.

V. 1. 3. 2. Intra cellular hydrolysis

CES-catalysed hydrolysis happened when molecule v.1.1/v.1.2 entered into the cell was confirmed by treating molecule v.1.1/v.1.2 with cell lysate. In the meantime, we also used the extracellular medium to treat molecule v.1.1/v.1.2, from HPLC monitoring in 12h, we cannot

observe any change in molecule v.1.1/v.1.2. Thus, confirmed that CES-catalysed hydrolysis will not happen before the molecule enter into the cell. Results were shown in Figure 4.

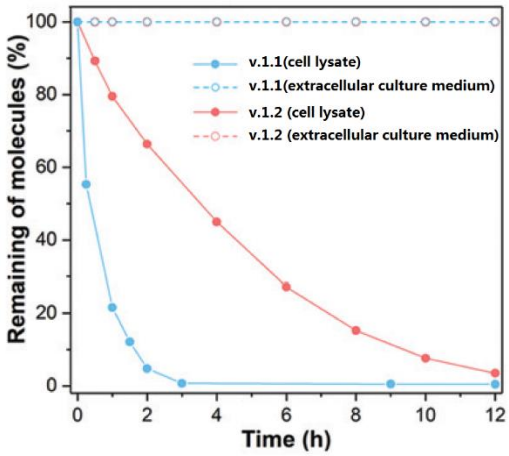

Figure 4. Kinetic profiles of CES-catalyzed hydrolysis of v.1.1 or v.1.2 in HeLa cell lysate or extracellular culture medium (isolated from cultured cells) at 37 ºC.

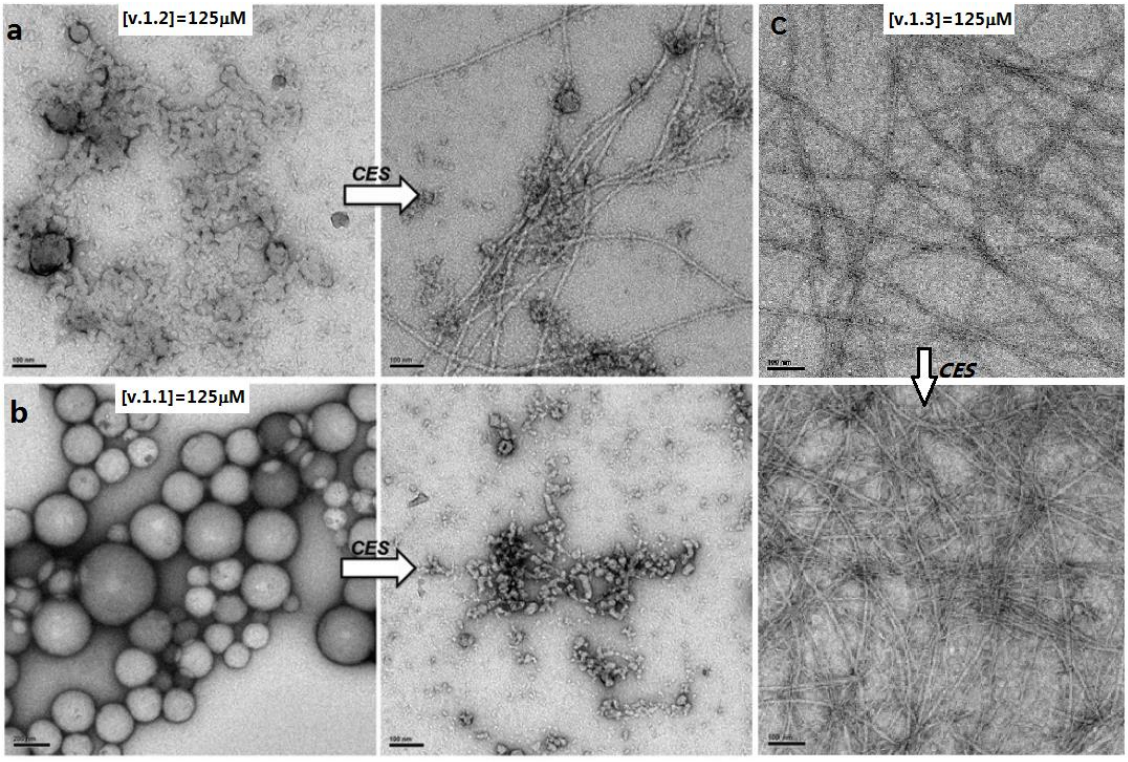

Figure 5. TEM images of molecule v.1.2 (a), v.1.1 (b) and v.1.3 (c) in borate buffer at a concentration of 125 μM before and after CES-catalysed hydrolysis.

When TEM was applied to check the nanostructures, we can observe that in borate buffer solution of v.1.2 (125 μM) only formed some irregular aggregates, after adding of CES, the enzyme catalysed reaction would induce the formation of uniform nanofibers (Figure 5a). In the case of molecule v.1.1, CES-catalysed reaction would disassemble the nanovesicles into some nanoaggregates (Figure 5b). For molecule v.1.3, since the addition of CES would not bring any change in the molecule, the self-assemble nanofiber kept intact (Figure 5c).

V. 1. 3. 3. 1- Octanol/water partition coefficient study

Lipid-water partition coefficient describes the ratio of concentrations of a compound in a mixture of immiscible solvents at equilibrium state. Log P value is used to provide the indications of a substance whether it will be absorbed by animals, humans or other living tissue, or to be easily carried away or disseminated by water.

$$Log\ P = Log_{10} \frac{[organic]}{[aqueous]}$$

Where the [] indicates the concentration of the solute in organic and aqueous partition.

In pharmaceutical industry, partition coefficient is applied to understand the distribution of drug molecules in the body. Log P value could be used as a criterion to screen drug candidates and for the further structure optimization of molecule candidate. According to the "Lipinski's Rule of 5" developed by Pfizer, if a drug is targeting central nervous system (CNS), an ideal Log P value is around 2; if it is administered through oral and intestinal absorption, the ideal Log P value is 1.35 – 1.8; if the drug is designed for sub-lingual absorption, the Log P value should > 5.[11]

The working standard curve were obtained by preparing a series of concentrations solution of molecule v.1.1, v.1.2 and v.1.3 dissolved in 1-octanol and checked their absorbance at 420nm. The Log P value of molecule v.1.1, v.1.2 and v.1.3 are determined through the above mention method and the results was shown in Figure 6.

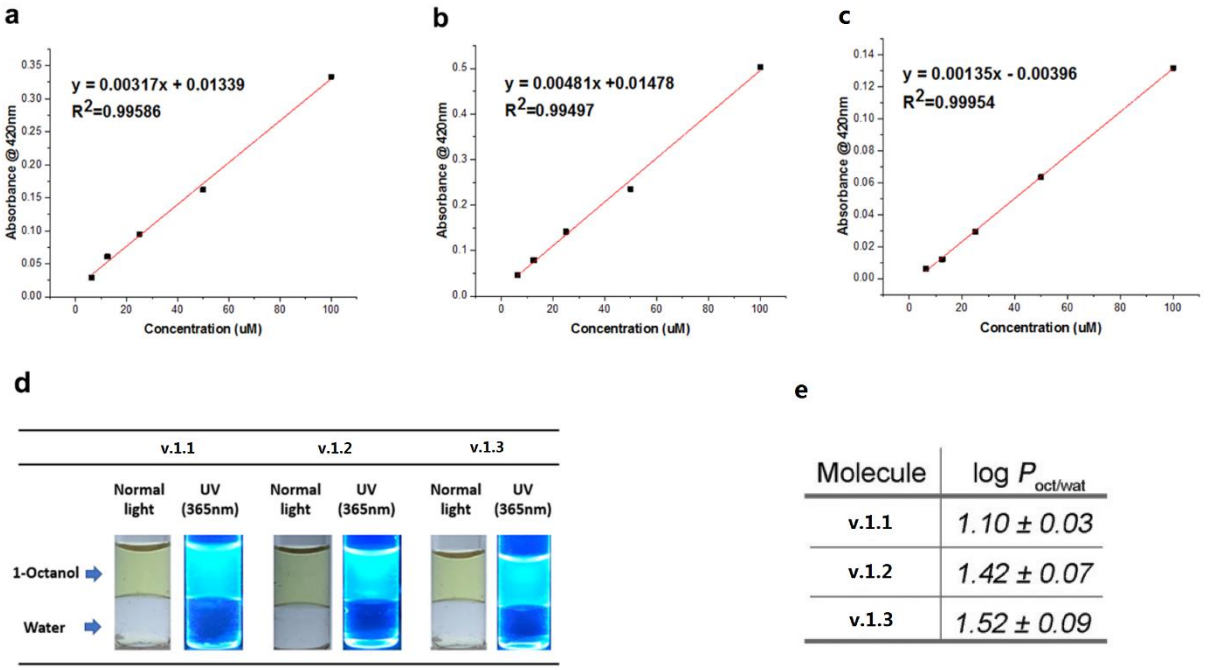

Molecule	log $P_{oct/wat}$
v.1.1	1.10 ± 0.03
v.1.2	1.42 ± 0.07
v.1.3	1.52 ± 0.09

Figure 6. Working standard curve of v.1.1(a), v.1.2(b), and v.1.3(c) obtained from UV-Vis absorption spectra; (d) Normal light and UV images of v.1.1, v.1.2, and v.1.3 after complete separation of the two phases; (e) Log P value of molecule v.1.1, v.1.2, and v.1.3.

V. 1. 3. 4. Co-assembly Study by Circular Dichroism (CD)

Circular dichroism (CD) is a spectroscopic method which depends on the chirality of the molecule, it absorbs differently on the right and left circularly polarized light and delivered a specific signal for the molecule. In life science, a vast majority of the biological molecules are chiral, for example, the basic unit of protein – amino acids are chiral. CD spectroscopy has been widely used to determine the secondary structure of proteins. In the case of peptides, the application of CD spectroscopy could be used to monitoring the conformational changes. In our current study, we applied CD spectroscopy to investigate the conformational change of the peptides before and after enzymatic catalysis. According to Prof. Itaru Hamachi's previous work using CD spectroscopy to determine whether two components will interact with each other.[12] Briefly, if the CD spectrum of simple sum of two components is equal to the results obtained from the two components in CD measurements, it indicates these two components didn't interact with each and they prefer the self-sorting behaviour in the mixture solution. In the contrast, if the CD spectrum of simple sum of the two components is different from the results from the measurements in the mixture solution, it indicates the two components prefer co-assembly in the mixture solution.

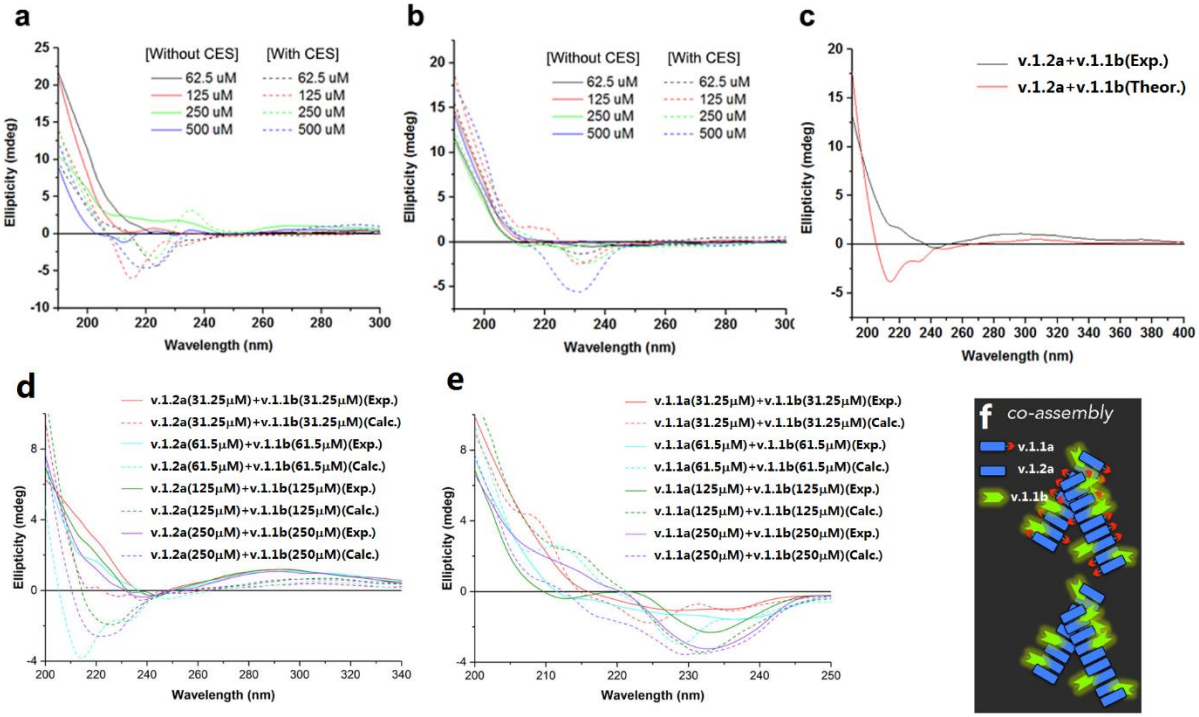

Figure 7. (a-b) CD spectra of v.1.1 and v.1.2 at different concentrations (solid line) and after CES hydrolysis (dash line); (c) CD spectrum of (v.1.2a + v.1.2b) at 125 μM in H_2O/DMSO (v/v = 95:5), theoretical spectrum is the simple sum of the spectra obtained from 1a and b in H_2O/DMSO (v/v = 95:5). (d, e) CD spectra of v.1.2a / v.1.1b (1 : 1) mixtures and v.1.1a / v.1.1b (1 : 1) mixtures (right) at various concentrations. Exp. and Calc. represent experimental and theoretically calculated CD spectra, respectively. (f) Schematic illustration of a molecular co-assembly between v.1.1a and v.1.1b or between v.1.2a and v.1.1b.

The results are shown in figure 7, at all the measured concentrations (62.5μM – 500 μM), the CD spectra of the molecule v.1.1 and v.1.2 before and after enzyme treatment is different (Figure 7a/b), it indicated conformational change after enzymatic hydrolysis. It was consistent with the nanostructure change before and after enzyme treatment (by TEM). When comparing

the simple sums of individual (v.1.1a/v.1.1b, v.1.2a/v.1.1b) CD spectra with the results from the enzymatic catalysis (Figure 7d/e), they are different, suggesting v.1.1a/v.1.1b and v.1.2a/v.1.1b assumed co-assembly behaviour after hydrolysis.[13] Thus, the fluorescence from v.1.1b could be used to indicate the location of the nanostructure. The co-assemble behaviour can be simply defined by the model shown in Figure 7f.

V. 1. 3. 4. Intracellular Study

V. 1. 3. 4. 1. Cellular Uptake Study

To realize the biological function of the molecule, it should have a relative amount of molecule enter into the cell and thus interact with the sub-organelle to realize its function. In our study, we first used confocal microscope to evaluate the cellular uptake of molecule v.1.1/v.1.2/ v.1.3. Combining with the commercial plasma membrane staining reagent (CellMask green), we can observe the fluorescence from molecule v.1.1/v.1.2 mainly stayed inside the cell (Figure 8a/b). However, little fluorescence was observed when treating with molecule v.1.3 (Figure 8c), it suggested v.1.3 was hardly absorbed by the cell.

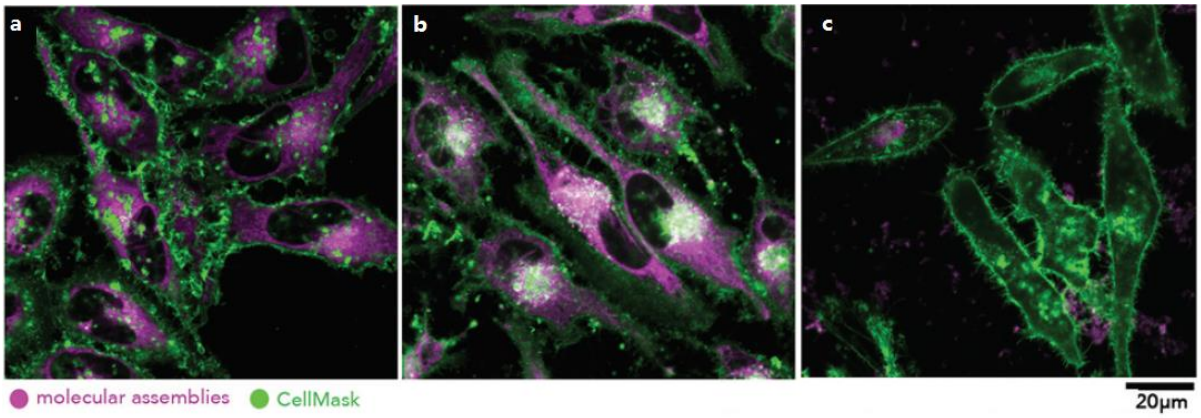

Figure 8. Fluorescent images of HeLa cells incubated with v.1.1 (a), v.1.2 (b), or v.1.3 (c) at a concentration of 10 μM for 4 hours and stained with CellMask Green (plasma membrane), violet represents the emissions of coumarin derivatives.

In the subsequent experiment, we use flow cytometry method to give a relative quantify of cellular uptake of molecule v.1.1/v.1.2. For a more precise quantification, we use HPLC to monitor the remaining amount of molecule v.1.1/v.1.2 in 6h incubation period. In the meantime, we carried out the control study on comparison of the cellular uptake of v.1.1a/v.1.2a. Results were shown in Figure 9.

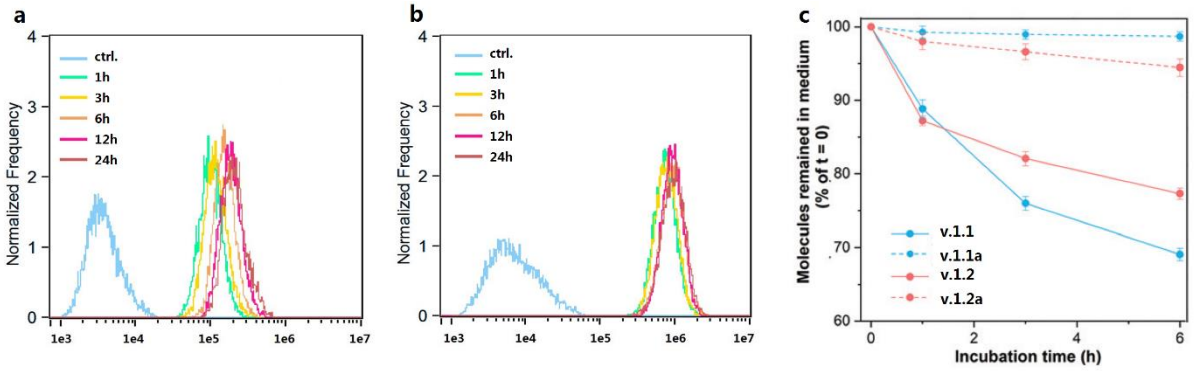

Figure 9. Internalized relative quantification of compound v.1.1 (a) and compound v.1.2 (b) by flow cytometer, (c) relative percentage of v.1.1, v.1.1a, v.1.2, or v.1.2a remaining in the extracellular culture medium during the first 6 hour HeLa cell incubation under treatment with those molecules at a concentration of 10 μM.

Time-dependent flow cytometry experiment showed an increase of fluorescence intensity, it indicated that molecule v.1.1/v.1.2 was steadily enriched inside the cell (Figure 9a/b). Further precisely quantification by monitoring the remaining amount of molecules in the extracellular culture medium by HPLC in 6 hour incubation period. Figure 9c showed that v.1.1 and v.1.2 is more easily to be absorbed by the cell compared to v.1.1a and v.1.2a, implying our prodrug design strongly enhance molecular cellular uptake.

V. 1. 3. 4. 2. Cell viability assay

Cellular toxicity evaluation was first evaluated on HeLa cell. Results were shown in Figure 10. Cell viability results showed that v.1.2a was toxic toward HeLa cells (Figure 10a), while v.1.1a was biocompatible (Figure 10b). It suggested the introduction of ethanolamine group into v.1.1a will bring molecular toxicity toward HeLa cells. The fluorescent motif v.1.1b is slightly toxic towards HeLa cells (Figure 10c). When treating the HeLa cells with a combination of v.1.2a/v.1.1b, we could discover a slight enhanced toxicity; in the case of v.1.1a/v.1.1b, we could observe slightly decrease of toxicity due to the diluted effect of v.1.1a. The combination treatment indicated the co-assembly behaviour didn't bring obvious effect on the toxicity of v.1.1a /v.1.2a. Compared to v.1.2a, v.1.2 was much more toxic towards HeLa cells (Figure 10d), implying the successfully of design on v.1.2a. In the control study of v.1.1, the enhanced molecular uptake didn't bring any more toxic effect towards HeLa cells (Figure 10e).

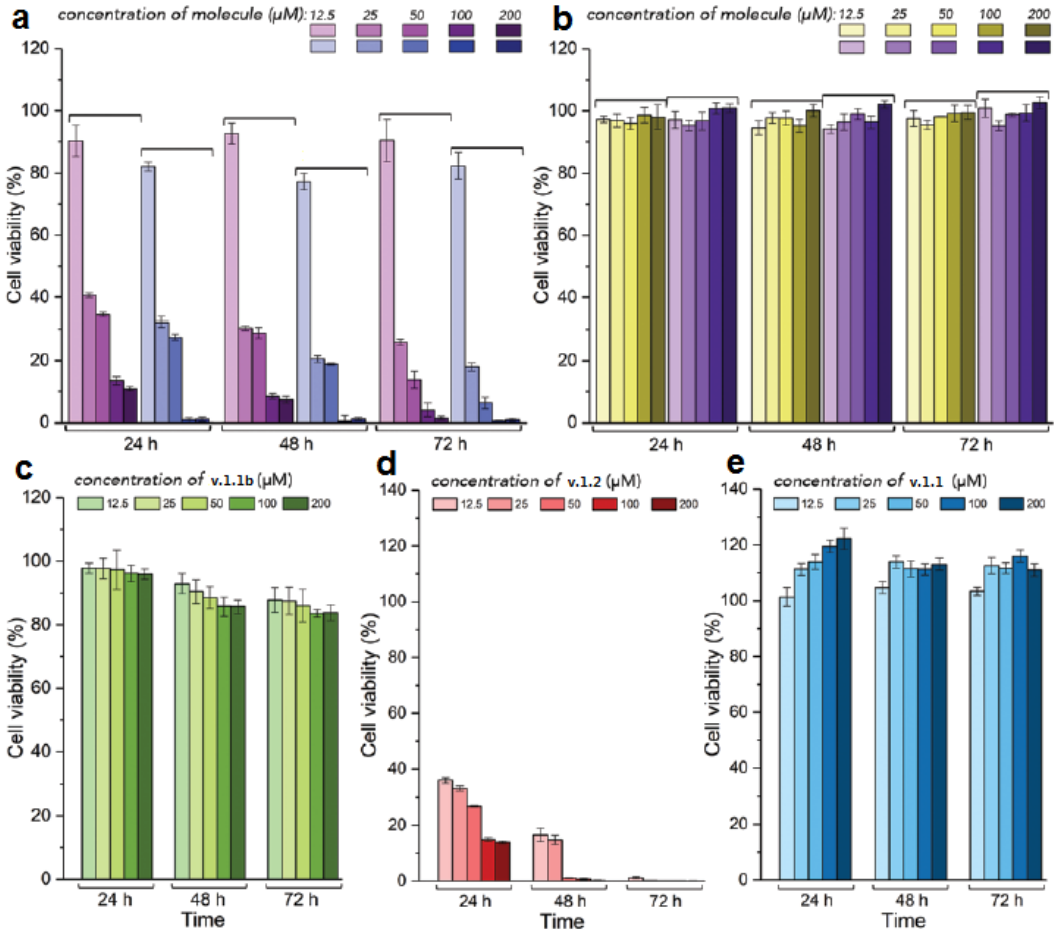

Figure 10. HeLa cell viability under treatment with a mixture of v.1.2a (violet) and v.1.2a/v.1.1b (1 : 1) (blue) (a), v.1.1a (yellow) or v.1.1a/v.1.1b (violet) mixture (1 : 1) (b), v.1.1b (c), v.1.2 (d), and v.1.1(e) at various concentrations.

Further evaluation of molecule v.1.2 on other cancer cell lines was carried out on ovarian cancer (SKOV3 and drug resistant OVCAR-3), liver cancer (HepG2), and metastatic pancreatic cancer (PANC-1). The viability results (Figure 11) showed that molecule v.1.2 also effectively inhibited growth of other cancer cell lines. Even 1-day treatment of v.1.2 will lead to more than 40% of cancer cell inhibition. Suggesting molecule v.1.2 was a successfully prodrug design and enhanced cellular uptake amplified its toxicity toward cancer cells.

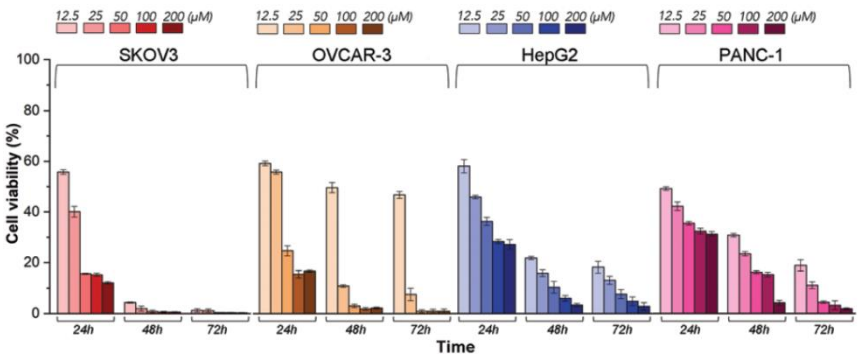

Figure 11. SKOV-3, OVCAR-3, HepG2 and PANC-1 cell viability under treatment with v.1.2 at various concentrations.

V. 1. 3. 4. 3. Location of the molecule after absorption by the cell

To figure out the potential interaction of molecule with sub-organelle, confocal microscopy was applied to investigate the location of molecule after treatment with HeLa cell. Commercial sub-organelle staining reagents were used to ensure the precisely location of the molecular self-assembly nanostructure. In our experiment, high-resolution confocal imaging experiment was carried out with presence of ER and mitochondria staining reagents. As is shown in Figure 12, the enzymatic hydrolysis components are more likely to have a close contact with ER.

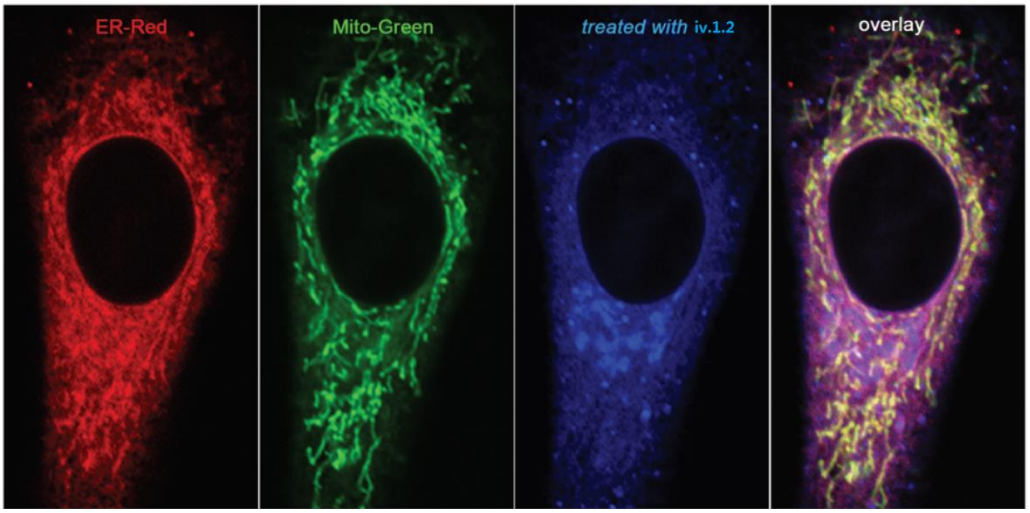

Figure 12. Fluorescence HeLa cell images after incubation with v.1.2 (10 μM) for 4 hours and co-staining with ER-Red, and Mito-Green. Blue represents the emissions of molecule v.1.2's derivatives.

To further figure out whether molecule v.1.2 would have an effect on the ER and mitochondria, we carried out cell section (above mentioned method) and observed the microstructure by TEM. As is shown in Figure 13, pink arrow indicated mitochondria, and yellow arrow stands for ER. Compared to control (Figure 13a), we cannot observe any obvious change in mitochondria

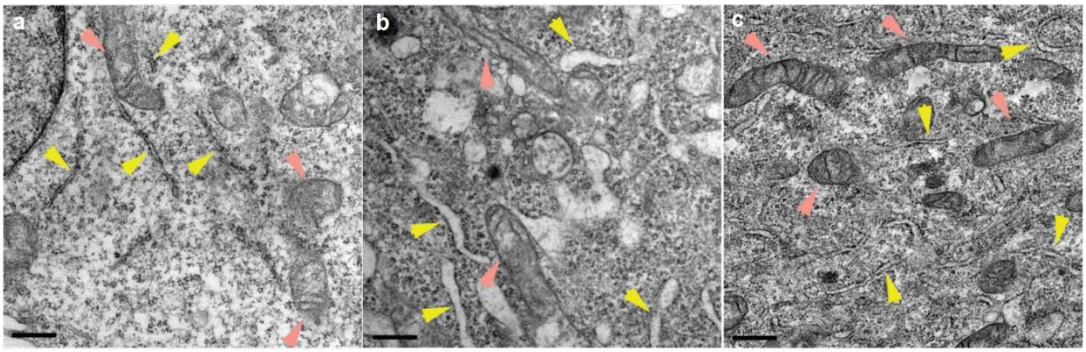

Figure 13. TEM images of HeLa cells without treatment (a), under treatment with v.1.2 (b) or under treatment with v.1.1 (c). The ER is shown by a yellow arrowhead. The mitochondria are shown by pink arrowheads.

either treated by molecule v.1.2 (Figure 13b) or molecule v.1.1 (Figure 13c). However, it is obviously that ER was dilated when treated by molecule v.1.2 (Figure 13b) compared with the

control group.[14] In the group of treated by molecule v.1.1 (Figure 13c), the ER structure did not show dilation.

Through the high-resolution confocal microscopy and cell section imaging, we assumed that the toxicity of molecule v.1.2 would be a consequence of its ER dilation.

V. 1. 3. 4. 4. Cell Apoptosis Mechanism Study

Currently, there are three well-accepted pathways to illustration the cell apoptosis (Figure 14).

1. Extrinsic pathway (initiated by death receptor);
2. Intrinsic pathway (mitochondria mediated);
3. Endoplasmic reticulum (ER) stress pathway.

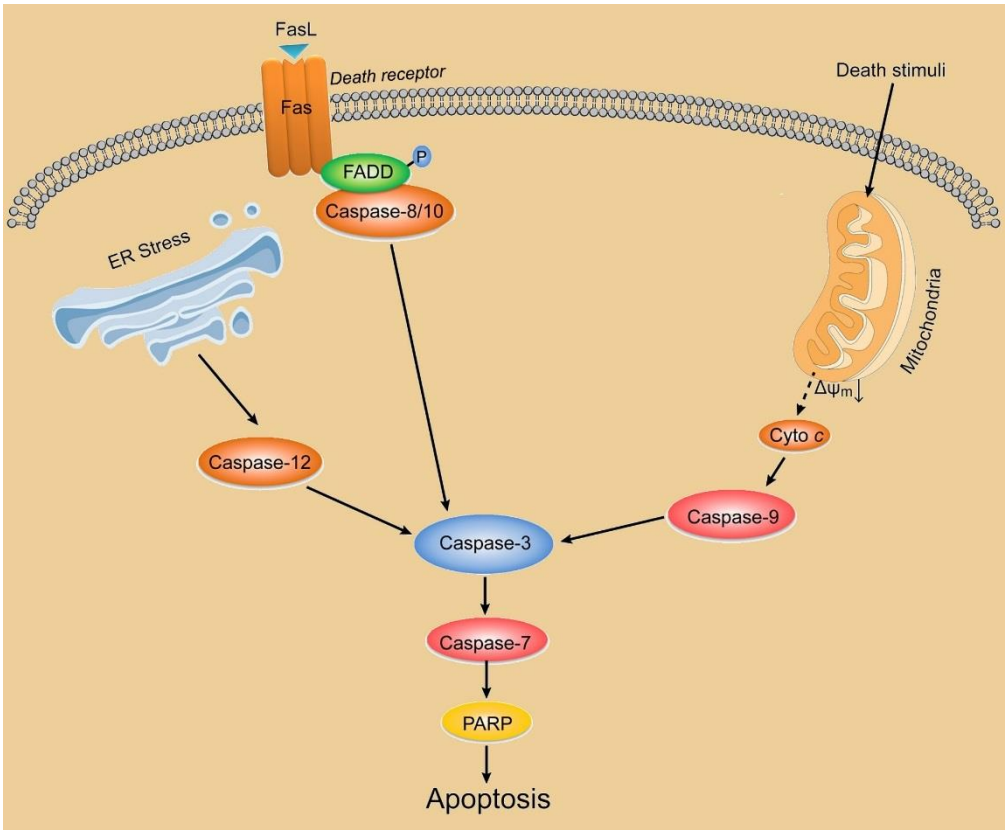

Figure 14. Illustration of cell apoptosis pathway.

To get a clear image of apoptosis activation, we carried out time-dependent western-blot experiment to monitor the content of DR5, caspase 8 (extrinsic pathway), caspase 9 (intrinsic pathway) and caspase 12 (ER stress pathway) in 24 hours. We chose β-actin as internal standard; the detail of the experiment was shown in the method part.

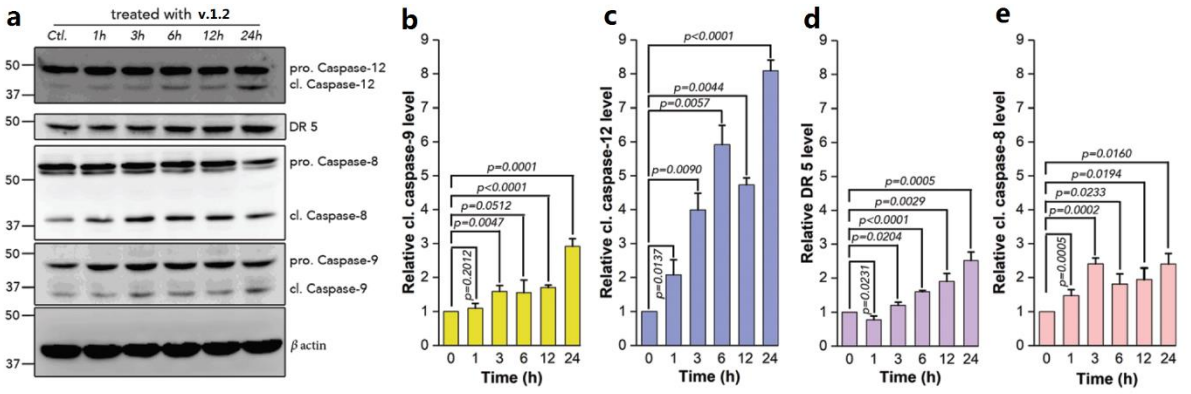

Figure 15. (a) Western blotting for caspase-12, DR 5, caspase-8, and caspase-9 expressed in HeLa cells under treatment with v.1.2 (20 μM). β-actin is the loading control. Time-dependent relative expression profiles of cl. caspase-9 (b), cl. caspase-12 (c), DR 5 (d), and cl. caspase-8 (e). Results are means ± S.D. of three independent experiments.

As is shown in Figure 15, the expression of cleaved caspase-9 did not show obvious in the first 12h, only showed 3-fold increase after 24h, which may be caused by the low viability of HeLa cells (Figure 15b). It suggested the apoptosis was not initiated by caspase-9 which is consistent with intact the morphology of mitochondria (Figure 13b);[15] in the contrary, we can observe a dramatic increase of cleaved caspase-12 from 3 hours and it steadily increased in the 24 hours experiment, it indicated the cell apoptosis was initiated by ER stress.[16] And the dilation of ER supported the western blot results (Figure 15c).[17] In the case of DR5 and cleaved caspase-8, both of them did not show obvious change during the 24 hours incubation.[18] Thus, we can draw a conclusion that when cancer cells were treated by molecule v.1.2, ER-specific apoptosis was activated *via* elevated ER stress, which was caused by ER structure disruption.

V. 1. 4. Conclusion

Inspired by the clinical study on alcoholic patients, we designed and synthesized molecule v.1.2a which was consisted by self-assembly building block and alcohol derivative. Self-assembly of molecular v.1.2a would enrich alcohol derivative on ER, thus showing "acute alcohol abuse" – like conditions and leading to subcellular organelle disruption. To reach more efficiently delivering of molecule v.1.2a, we adopted prodrug design by coupling coumarin derivative. The coumarin fragment would be catalyse-cleaved after entering into cancer cells by intracellular CES. Additionally, coumarin could also work as an indicator for the assemblies in the subcellular organelle. Elevated ER stress was found in the study, and it initiated cancer cell apoptosis process. Our study showed ER as a promising target subcellular organelle for anticancer research.

V. 2. Promote Dual-subcellular-targeting Anticancer Efficacy by Regulating the Intracellular Self-assembly Dynamics

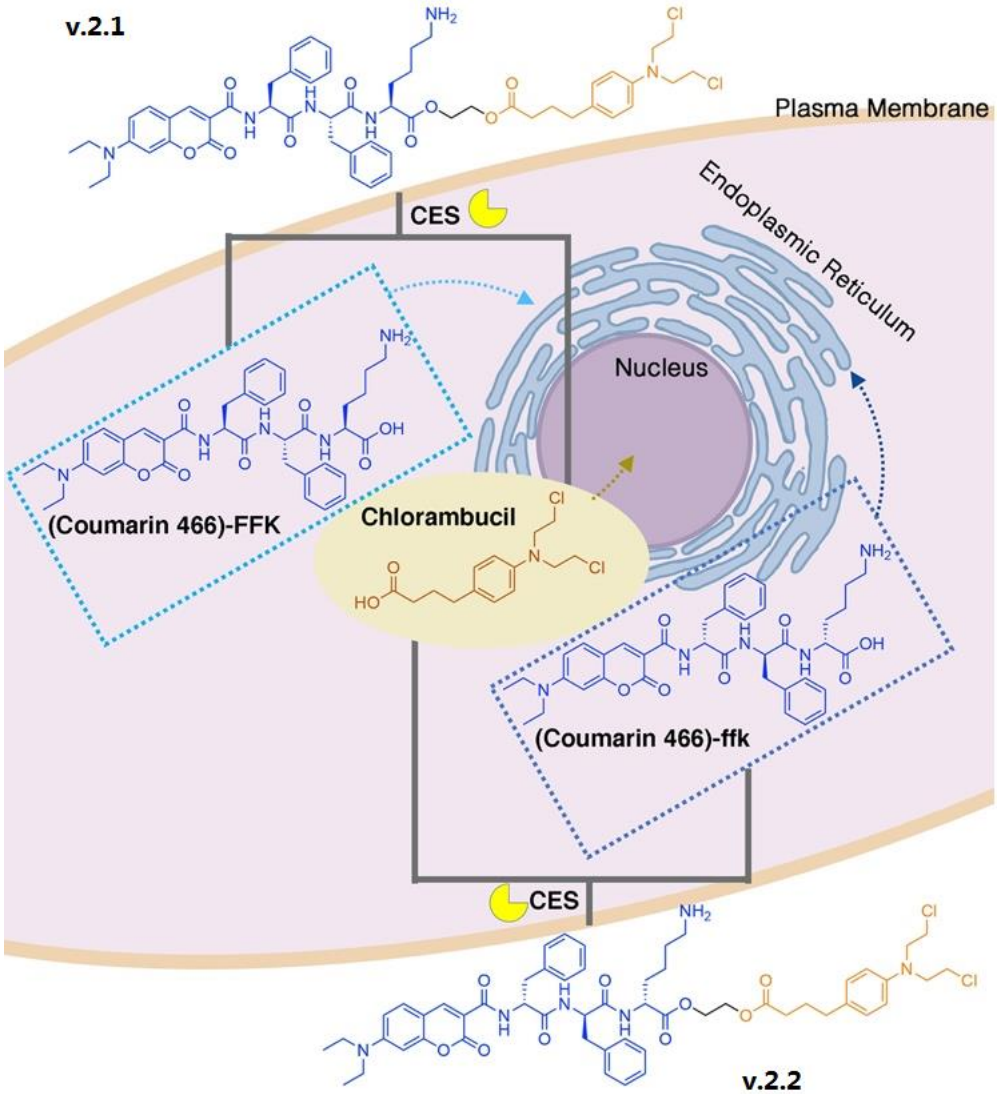

This chapter corresponding to the following manuscript:

Shijin Zhang and Ye Zhang*. "Promote Dual-subcellular-targeting Anticancer Efficacy by Regulating the Intracellular Self-assembly Dynamic" *ACS Appl. Mater. Inter.*, **2020**, 12, 41105-41112.

V. 2. 1. Introduction

Nanotechnology-based drug development has made important contributions in cancer treatment during the past decades,[1] while, most drug research still concentrated on small molecules since they have long been associated with biological discoveries.[2] Over 50% of the FDA-approved cancer drugs are protein targeted small molecules,[3] even though the poor bioavailability and the target-based resistance limit their applications. To improve the biocompatibility of small molecules, a nanoscale drug delivery system called small-molecule nanomedicine[4] assembled by small pharmaceutical molecules with minimum non-toxic excipients is constructed to enhance drug loading efficiency. Applying drug combinations to target multiple components of biological regulatory circuits produces stronger treatment combating drug resistance.[5] Meanwhile, molecular self-assembly in cell milieu is emerging as another practical strategy for multi-component targeting nanomedicine[6] without developing drug resistance,[6b] although the dynamics of self-assembly *in vitro* is still obscure.[7] Unfortunately, further investment beyond traditional R&D for drug development hindered the progress of such nanomedicine.

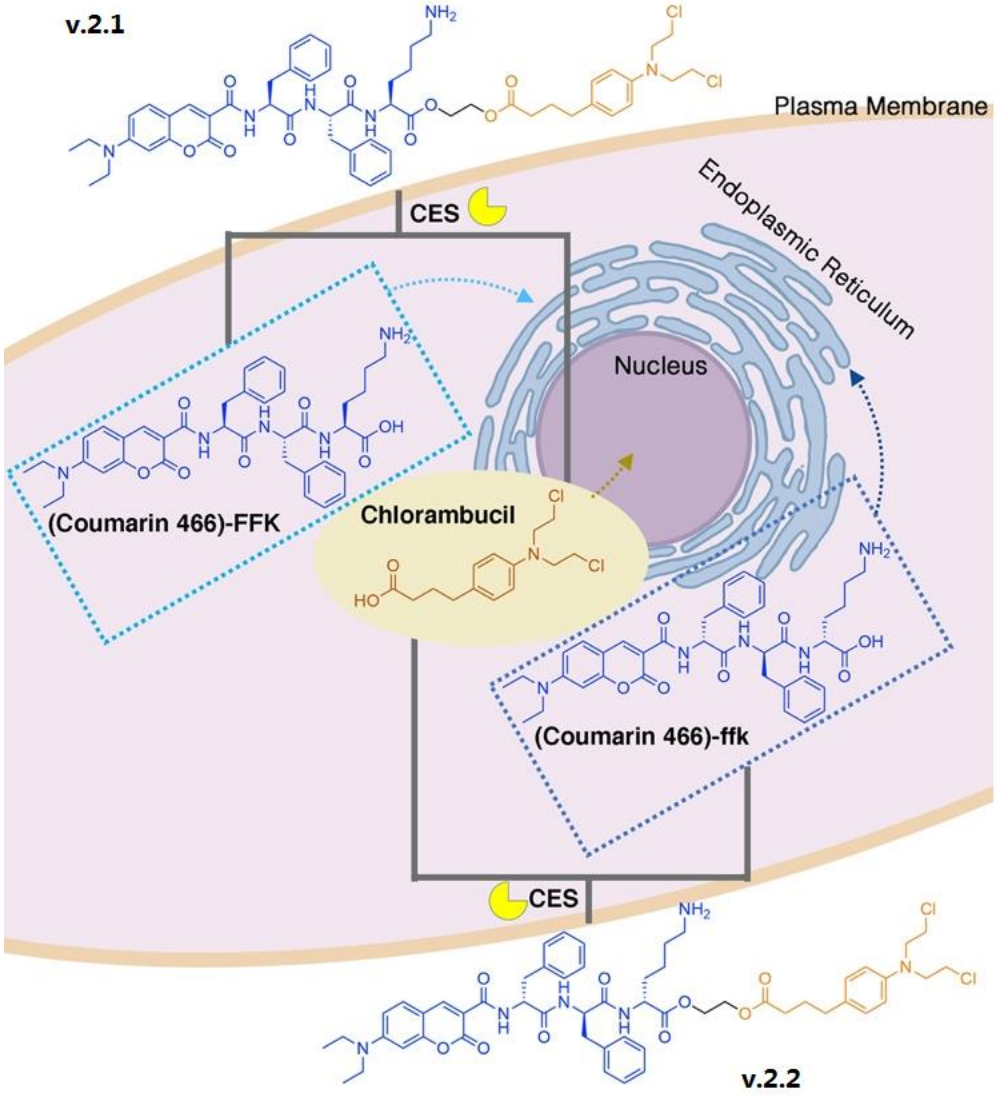

Scheme 1. Illustration of dual targeting molecular design for ER and nucleus.

Following the statement of James Black that 'the best way to discover a new drug is to start with an old one",[8] we came out the strategy of producing advanced version of small-molecule

nanomedicine for multi-targeting combination therapy.[5] As demonstrated in scheme 1, Chlorambucil, the small molecule chemotherapy medication that alkylates and crosslinks DNA[9] with poor water solubility was selected as the 'old drug' to couple with endoplasmic reticulum (ER)-targeting self-assembling molecule[10] (Coumarin 466)-FFK covalently via diester bond.[11] The obtained 'new drug' v.2.1 is a nanoscale delivery system for high chlorambucil loading. Upon the hydrolysis by carboxylesterase (CES) that is commonly expressed in tumor tissue,[12] chlorambucil is released to damage DNA, and (Coumarin 466)-FFK is released to self-assemble on ER inducing ER stress. The combination of small pharmaceutical molecule and subcellular-targeted self-assembly achieves synergistic therapeutic effect against cancer without developing target-based resistance.[13] To explore the intracellular self-assembly dynamics and the impact on cellular response, a D-version[14] ER-targeting 'excipient' (Coumarin 466)-ffk is applied to couple with Chlorambucil obtaining v.2.2 for comparison.

V. 2. 2. Experimental Section

V. 2. 2. 1. Materials

Chemical reagents	Grade	Manufacturer
Fmoc-Amino acid	98.0%	GL Biochem (Shanghai, China)
2-(1*H*-benzotriazol-1-yl)-1,1,3,3-tetramethyluronium hexafluorophosphate (HBTU)	98.0%	Sigma Aldrich
Trifluoroacetic acid (TFA)	99.0%	Sigma Aldrich
N-(3-dimethylaminopropyl)-*N*'-ethylcarbodiimide hydrochloride (EDCI)	98.0%	Sigma Aldrich
4-dimethylaminopyridine (DMAP)	99.0%	Sigma Aldrich
2,2,2-Trifluoroethanol	99.0%	Nacalai Tesque
N, N-Diisopropylethylamine (DIEA)	99.0%	Sigma Aldrich
Piperidine	99.0%	Nacalai Tesque
Meldrum's acid	98.0%	Sigma Aldrich
Ethylene glycol anhydrous	99.8%	Sigma Aldrich
Piperidinum acetate	98.0%	TCI (Japan)
4-(Diethylamino)salicylaldehyde	98.0%	TCI (Japan)
Pyridine	99.0%	Sigma Aldrich
Chlorambucil	98.0%	LKT laboratories, Inc.
Ethanol (EtOH)	99.5%	Nacalai Tesque
Methanol (MeOH)	99.0%	Nacalai Tesque
Hexane	96.0%	Nacalai Tesque
Tetrahydrofuran (THF)	99.5%	Nacalai Tesque
Acetic anhydride	95.0%	Nacalai Tesque
N, N-Dimethylformamide (DMF)	99.5%	Nacalai Tesque
Dichloromethane (DCM)	98.0%	Nacalai Tesque
Acetonitrile	HPLC grade	Nacalai Tesque

All organic solvents were dehydrated by a solvent purification system before experiment.

Biological reagents: LysoTracker Red DND-99 (ThermoFisher), ER-Tracker™ Red (BODIPY™ TR Glibenclamide), Protease Inhibitor (87785, ThermoFisher), CelLytic M

solution (Sigma-Aldrich), Blocking one-P (Nacalai tesque, Kyoto, Japan), Bip, Calnexin, IRE1α and PDI (Cell signalling, #9956), beta-actin (Abcam, ab8227) antibody, goat anti-mouse IgG (Bio-Rad, Hercules, CA, USA), peroxidase-conjugated goat anti-rabbit IgG (Bio-Rad, Hercules, CA, USA), ECLTM prime Western blotting detection reagent (GE Healthcare, Little Chalfont, UK).

V. 2. 2. 2. Instruments

Agilent 1260 Infinity Preparation HPLC (Column: 19 mm×150 mm XBridge® Peptide BEH C18 column), Agilent 1260 Infinity Analysis HPLC (Column: 2.1 mm×150 mm XBridge® Peptide BEH C18 column), Thermo LTQ-ETD mass spectrometer (ESI-MS), NMR equipment: Bruker AVANCE 400N spectrometer, Thermo Nanodrop 2000C spectrophotometer, Hamamatsu fluorescence spectrometer, Transmission Electron Microscope (JEM-1230R), Scanning Electron Microscope (FEI Quanta 250 FEG), Nivo3 microplate reader (PerkinElmer), flow cytometer (Merck Millipore ImageStream X Mark II), Circular dichroism spectropolarimeter JASCO J-820, Confocal microscope (Nikon A1).

V. 2. 2. 3. Synthesis

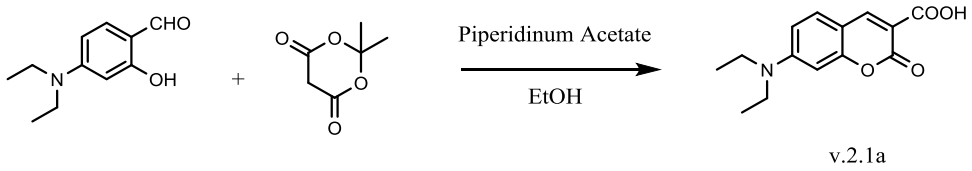

v.2.1a

Scheme 2. Synthesis of compound v.2.1a.

Compound v.2.1a: Meldrum's acid (3.60 g, 25 mmol), 4-(diethylamino) salicylaldehyde (4.83 g, 25 mmol), and piperidinum acetate (73 mg, 0.5 mmol) were transferred into a 100 mL round-bottom flask, 30 mL ethanol was added into the mixture and refluxed overnight. After cooling down, precipitate was filtered and washed with cooled down ethanol. The obtained orange target compound was dried in 50 ^{o}C oven for 3 hours, yield: 83.2%.

^{1}HNMR (400 MHz, $CDCl_3$) δ = 8.63 (d, *J*=0.6 Hz, 1H), 7.44 (d, *J*=9.1 Hz, 1H), 6.71 (dd, *J*=9.1, 2.5 Hz, 1H), 6.53 (dd, *J*=2.4, 0.4 Hz, 1H), 3.48 (q, *J*=7.2 Hz, 4H), 1.25 (t, *J*=7.2 Hz, 6H) ppm.

MS: calculated for $C_{14}H_{25}NO_4$ is 261.1001, found 284.0886, $[M + Na]^+$.

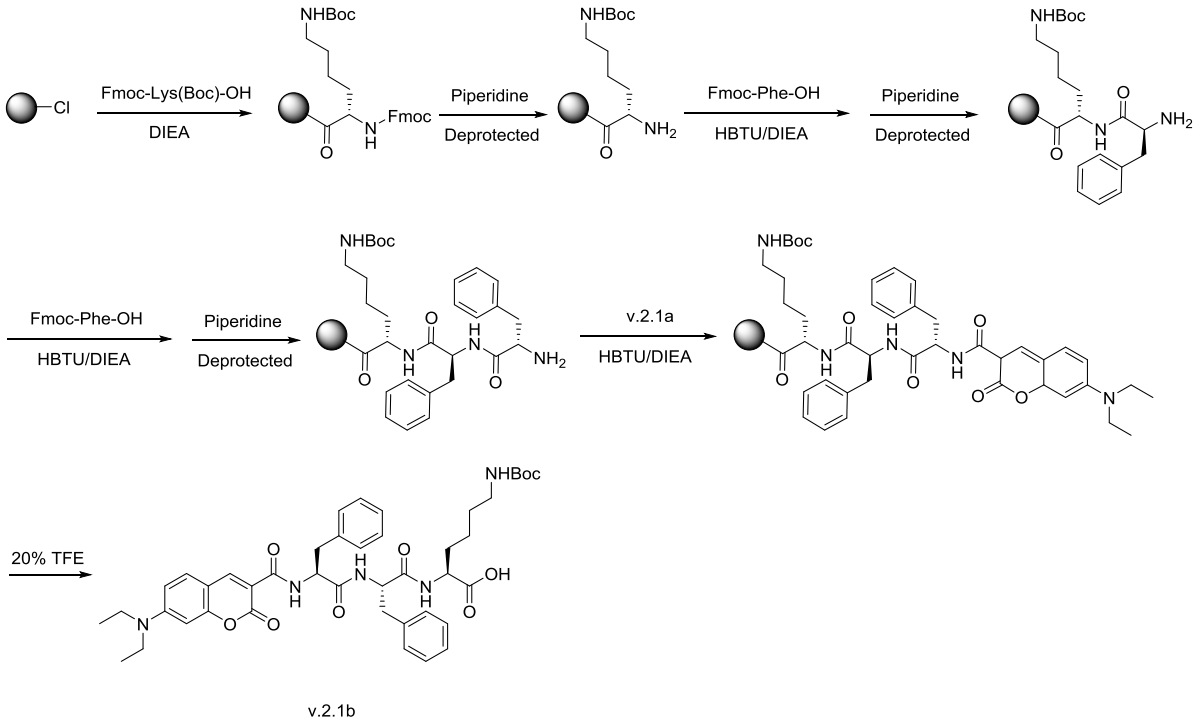

Scheme 3. Synthesis of compound v.2.1b.

Compound **v.2.1b**: Compound v.2.1b was obtained via solid phase peptide synthesis (SPPS). 2-Chlorotrityl chloride resin (2.0 g, 2 mmol) was swelled in anhydrous DCM for 20 min, further washed by anhydrous DMF for 5 times. L-Fmoc-Lys(Boc)-OH (2.34 g, 5 mmol) dissolved in anhydrous DMF was conjugated to resin with DIEA in 30 min. Then washed with anhydrous DMF for 3 times, unreacted sites in the resin were blocked with DCM/MeOH/DIEA (80:15:5) for 10 min and repeated once more, the resin was washed by anhydrous DMF for 5 times. Then piperidine solution (20% in DMF) was added into reaction for 30 min to remove the Fmoc protecting group on the amino acid. We carried out the peptide elongation according to standard SPPS protocol to get the desired compound. Target compound was cleaved off the resin using 20% TFE for 2h. After removing the solvent, anhydrous ether was added into the concentrated product and yellow precipitation of v.2.1b was obtained, yield: 88.3%.

^{1}H NMR (400 MHz, DMSO-*d6*) δ = 8.86 (d, *J*=7.7, 1H), 8.59 (s, 1H), 8.38 (d, *J*=8.4, 1H), 8.25 (d, *J*=7.4, 1H), 7.66 (d, *J*=9.0, 1H), 7.34 – 7.06 (m, 10H), 6.79 (d, *J*=7.4, 2H), 6.61 (s, 1H), 4.82 – 4.54 (m, 2H), 4.19 (d, *J*=5.4, 1H), 3.48 (d, *J*=6.9, 4H), 3.33 (s, 2H), 2.96 – 2.78(m, 4H), 1.79 – 1.59 (m, 2H), 1.45 – 1.27 (m, 13H), 1.14 (t, *J*=6.9, 6H).

MS: calculated for $C_{43}H_{53}N_5O_9$ is 783.3843, found 782.4097, $[M - H]^-$.

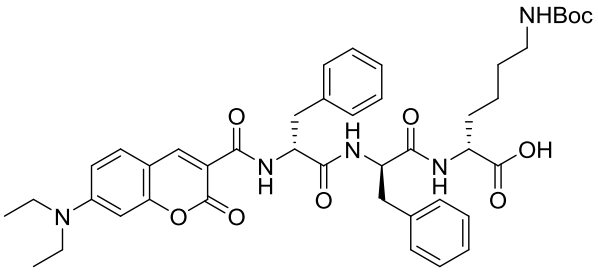

v.2.2b

Compound **v.2.2b**: compound v.2.2b was synthesized using the same protocol as compound v.2.1b, just changed the L-Fmoc-Amino acids to D-Fmoc-Amino acids. The yield was 83.6%.

^{1}H NMR (400 MHz, DMSO-*d6*) δ = 8.86 (d, *J*=7.7, 1H), 8.59 (s, 1H), 8.37 (d, *J*=8.4, 1H), 8.26 (d, *J*=7.5, 1H), 7.66 (d, *J*=9.0, 1H), 7.37 – 7.01 (m, 10H), 6.79 (d, *J*=7.5, 2H), 6.60 (s, 1H), 4.68 (dd, *J*=47.2, 4.2, 2H), 4.19 (d, *J*=5.5, 1H), 3.48 (dd, *J*=13.4, 6.5, 4H), 3.33 (s, 2H), 2.94 – 2.75 (m, 4H), 1.74 – 1.57 (m, 2H), 1.45 – 1.28 (m, 13H), 1.13 (t, *J*=6.8, 6H).

MS: calculated for $C_{43}H_{53}N_5O_9$ is 783.3843, found 782.4092, $[M - H]^-$.

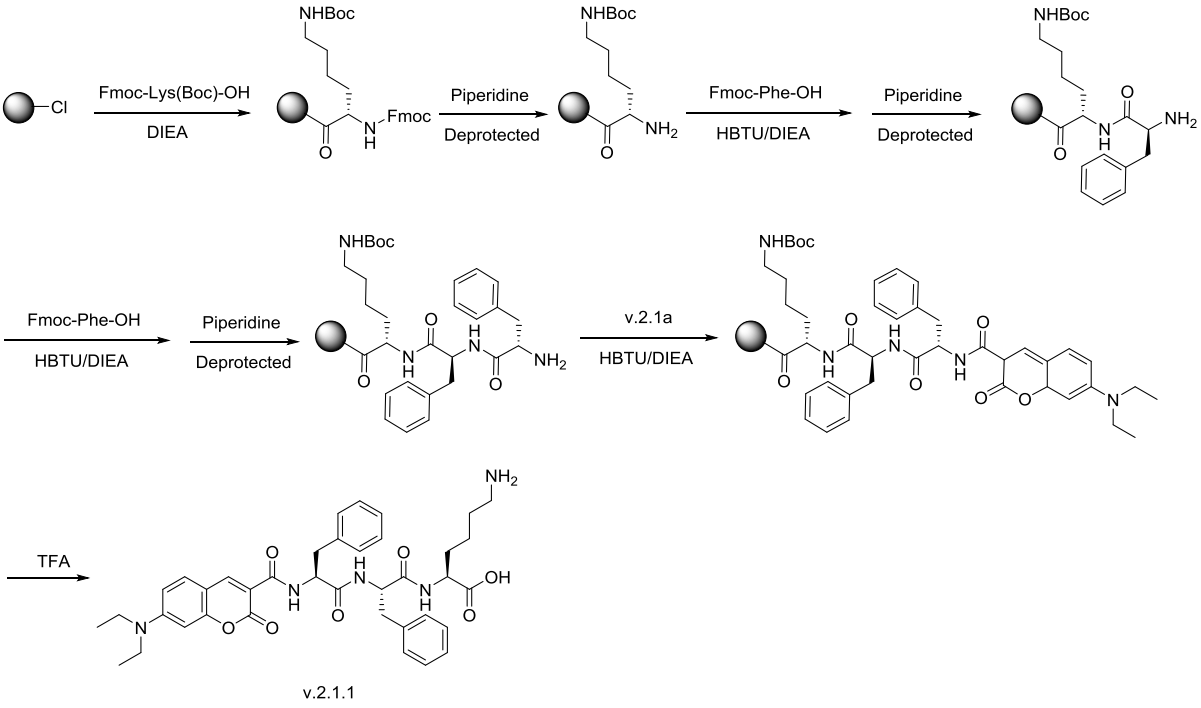

v.2.1.1

Scheme 4. Synthesis of compound v.2.1.1.

Compound **v.2.1.1**: Compound v.2.1.1 was obtained via solid phase peptide synthesis (SPPS). 2-Chlorotrityl chloride resin (2.0 g, 2 mmol) was swelled in anhydrous DCM for 20 min, L-Fmoc-Lys(Boc)-OH (2.34 g, 5 mmol) dissolved in anhydrous DMF was conjugated to resin with DIEA in 30 min. Then washed with anhydrous DMF for 3 times, unreacted sites in the resin were blocked with DCM/MeOH/DIEA (80:15:5) for 20 min and washed by anhydrous DMF for 5 times. Then piperidine solution (20% in DMF) was added into reaction for 30 min to remove the Fmoc protecting group on the amino acid. We carried out the peptide elongation according to standard SPPS protocol to get the desired compound. v.2.1.1 was cleaved off the

resin using TFA for 2h. After removing the solvent, anhydrous ether was added into the concentrated product and yellow precipitation of v.2.1.1 was obtained, yield: 90.2%.

^{1}H NMR (400 MHz, DMSO-*d6*) δ = 8.81 (d, *J*=7.8, 1H), 8.51 (s, 1H), 8.32 (dd, *J*=32.7, 7.9, 2H), 7.58 (d, *J*=9.0, 1H), 7.33 – 7.01 (m, 10H), 6.71 (d, *J*=9.1, 1H), 6.52 (s, 1H), 4.77 – 4.48 (m, 2H), 4.17 (dd, *J*=13.0, 8.1, 1H), 3.40 (d, *J*=6.9, 4H), 3.01 (dd, *J*=8.9, 5.2, 2H), 2.76 (ddd, *J*=17.4, 10.3, 4.8, 4H), 1.75 – 1.48 (m, 4H), 1.33 (dd, *J*=14.6, 7.2, 2H), 1.06 (t, *J*=6.9, 6H).

^{13}C NMR (101 MHz, DMSO-*d6*) δ = 173.81, 171.62, 170.76, 162.13, 157.72, 153.02, 148.33, 138.15, 137.53, 132.12, 129.84, 129.70, 128.47, 126.79, 126.70, 118.80, 115.85, 110.66, 109.14, 108.02, 96.27, 54.15, 54.10, 52.22, 44.81, 39.09, 38.45, 37.90, 30.95, 27.05, 22.85, 12.75.

MS: calculated for $C_{38}H_{45}N_5O_7$ is 683.3319, found 684.3408, $[M + H]^+$.

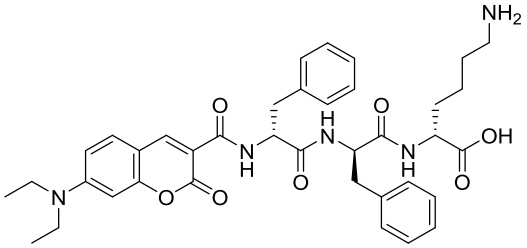

v.2.2.1

Compound **v.2.2.1**: compound v.2.2.1 was synthesized using the same protocol as compound v.2.1.1, just changed the L-Fmoc-Amino acids to D-Fmoc-Amino acids. The yield was 81.6%.

^{1}H NMR (400 MHz, DMSO-*d6*) δ = 8.80 (d, *J*=7.9, 1H), 8.51 (s, 1H), 8.35 (d, *J*=8.3, 1H), 8.27 (d, *J*=7.8, 1H), 7.59 (d, *J*=9.1, 1H), 7.29 – 7.00 (m, 10H), 6.73 (dd, *J*=9.1, 2.2, 1H), 6.52 (d, *J*=1.9, 1H), 4.73 – 4.47 (m, 2H), 4.22 – 4.11 (m, 1H), 3.46 – 3.39 (m, 4H), 3.09 – 2.93 (m, 2H), 2.81 – 2.66 (m, 4H), 1.79 – 1.46 (m, 4H), 1.37 – 1.26 (m, 2H), 1.06 (t, *J*=7.0, 6H).

^{13}C NMR (101 MHz, DMSO-*d6*) δ = 173.81, 171.62, 170.76, 162.12, 161.99, 157.73, 153.04, 148.34, 138.15, 137.52, 132.14, 129.84, 129.69, 128.48, 128.46, 126.79, 126.71, 110.68, 109.14, 108.03, 96.28, 54.13, 54.08, 52.19, 44.81, 39.10, 38.45, 37.89, 30.95, 27.04, 22.84, 12.76.

MS: calculated for $C_{38}H_{45}N_5O_7$ is 683.3319, found 684.3372, $[M + H]^+$.

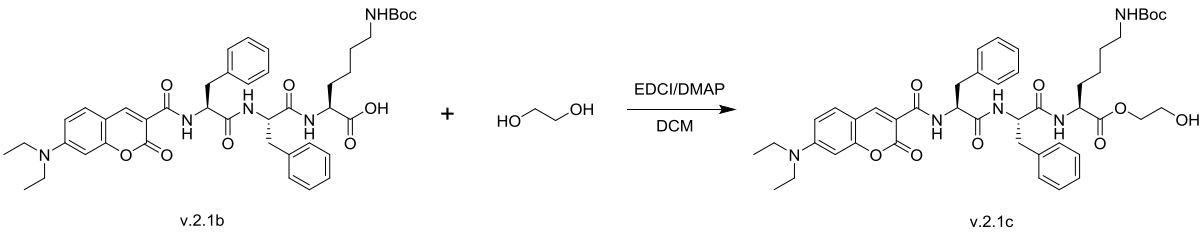

v.2.1b v.2.1c

Scheme 5. Synthesis of compound v.2.1c.

Compound **v.2.1c**: Compound v.2.1b (100.0 mg, 0.13 mmol), EDCI (26.8 mg, 0.14 mmol) and DMAP (1.2 mg, 0.01 mmol) were added into a 25 mL round-bottom flask and dissolved by 5

mL dry DCM, then added ethylene glycol (79.3 mg, 1.3 mmol) which was dissolved in 2 mL dry DCM. Stirring at room temperature for 12 h. The target compound was purified by silica column chromatography (Hex : EtOAc = 1:1). The yield was 73.8%.

^{1}H NMR (400 MHz, $CDCl_3$) δ = 9.25 (dd, J=66.6, 4.4, 1H), 8.18 (d, J=91.4, 1H), 7.41 – 6.73 (m, 10H), 6.63 (dd, J=11.2, 7.7, 2H), 6.49 – 6.34 (m, 1H), 4.60 – 4.30 (m, 3H), 4.11 (dd, J=21.5, 8.5, 2H), 3.78 – 3.60 (m, 2H), 3.41 (dd, J=6.8, 3.7, 4H), 3.19 – 2.85 (m, 6H), 1.72 (ddd, J=23.1, 13.9, 7.1, 2H), 1.37 (d, J=29.9, 11H), 1.28 – 1.06 (m, 8H).

MS: calculated for $C_{45}H_{57}N_5O_{10}$ is 827.4105, found 850.3902, $[M + Na]^+$.

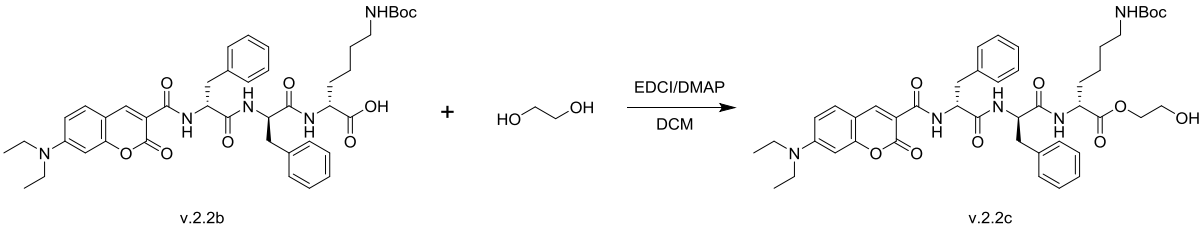

Scheme 6. Synthesis of compound v.2.2c.

Compound **v.2.2c**: Compound v.2.2c was synthesized using the same method as compound v.2.1c. The yield was 78.6%.

^{1}H NMR (400 MHz, $CDCl_3$) δ = 9.37 – 9.09 (m, 1H), 8.33 – 8.02 (m, 1H), 7.39 – 6.88 (m, 10H), 6.69 – 6.53 (m, 2H), 6.43 (dt, *J*=14.3, 7.2, 1H), 4.60 – 4.34 (m, 3H), 4.22 – 4.04 (m, 2H), 3.72 (t, *J*=4.5, 2H), 3.50 – 3.35 (m, 4H), 3.16 – 2.91 (m, 6H), 1.80 – 1.61 (m, 2H), 1.40 – 1.28 (m, 11H), 1.24 – 1.11 (m, 8H).

MS: calculated for $C_{45}H_{57}N_5O_{10}$ is 827.4105, found 850.3948, $[M + Na]^+$.

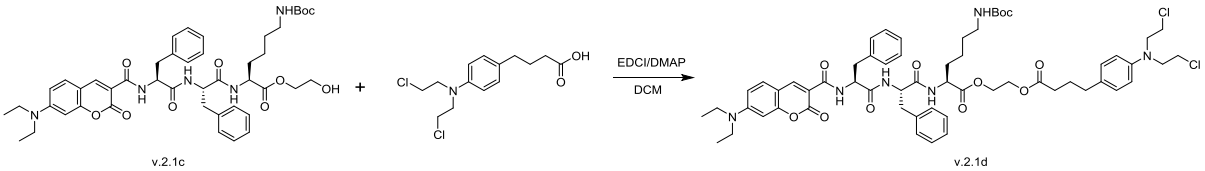

Scheme 7. Synthesis of compound v.2.1d.

Compound **v.2.1d**: Compound v.2.1c (70.0 mg, 0.088 mmol), EDCI (23.0 mg, 0.12 mmol) and DMAP (1.2 mg, 0.01mmol) were added into a 25 mL round-bottom flask and dissolved by 10 mL dry DCM, then added chlorambucil (32.9 mg, 0.11 mmol) which was dissolved in 2 mL dry DCM. Stirring at room temperature for 12h. The target compound was purified by silica column chromatography (Hex : EtOAc = 3:1). The yield was 78.8%.

^{1}H NMR (400 MHz, $CDCl_3$) δ = 9.13 (dd, J=11.0, 5.3, 1H), 8.28 (d, J=17.9, 1H), 7.37 – 6.92 (m, 10H), 6.84 (ddd, J=23.0, 15.9, 7.5, 3H), 6.68 (d, J=7.3, 1H), 6.63 – 6.51 (m, 3H), 6.43 (dd, J=9.0, 6.2, 1H), 4.61 – 4.40 (m, 3H), 4.30 – 4.15 (m, 4H), 3.64 – 3.48 (m, 8H), 3.46 – 3.33 (m, 4H), 3.18 – 2.88 (m, 6H), 2.48 (td, J=7.5, 4.6, 2H), 2.26 (dt, J=15.9, 5.4, 2H), 1.85 – 1.56 (m, 4H), 1.38 – 1.30 (m, 11H), 1.23 – 1.12 (m, 8H).

MS: calculated for $C_{59}H_{74}Cl_2N_6O_{11}$ is 1112.4793, found 1135.4666, $[M + Na]^+$.

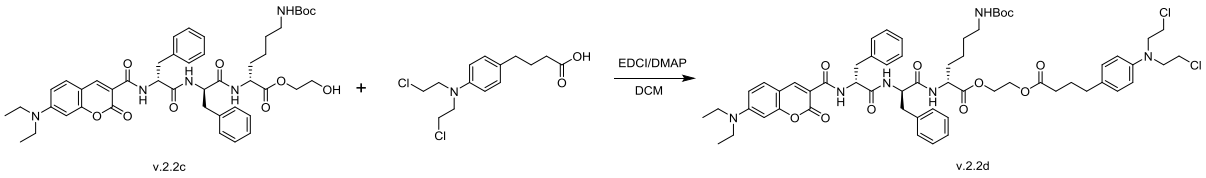

Scheme 8. Synthesis of compound v.2.2d.

Compound **v.2.2d**: Compound v.2.2d was synthesized using the same method as compound v.2.1d. The yield was 77.9%.

^{1}H NMR (400 MHz, $CDCl_3$) δ = 9.13 (dd, J=10.9, 5.2, 1H), 8.28 (d, J=17.5, 1H), 7.38 – 6.97 (m, 10H), 6.84 (ddd, J=20.4, 16.1, 7.6, 3H), 6.68 (d, J=7.3, 1H), 6.66 – 6.49 (m, 3H), 6.44 (t, J=2.8, 1H), 4.64 – 4.39 (m, 3H), 4.31 – 4.12 (m, 4H), 3.71 – 3.47 (m, 8H), 3.48 – 3.30 (m, 4H), 3.26 – 2.87 (m, 6H), 2.54 – 2.40 (m, 2H), 2.29 (t, J=7.5, 2H), 1.77 – 1.53 (m, 4H), 1.39 – 1.30 (m, 11H), 1.28 – 1.11 (m, 8H).

MS: calculated for $C_{59}H_{74}Cl_2N_6O_{11}$ is 1112.4793, found 1135.4665, $[M + Na]^+$.

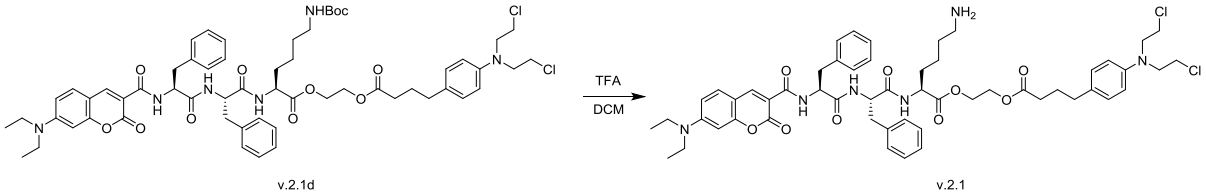

Scheme 9. Synthesis of compound v.2.1.

Compound **v.2.1**: Compound v.2.1d (50.0 mg, 0.045 mmol) was dissolved in 10 mL dried DCM and cooled down to 0 °C, then 2 mL TFA was slowly dropped into the solution. Stirring at 0 °C for 5h, and the target compound was purified by HPLC, the yield was 85.6%.

^{1}H NMR (400 MHz, DMSO-*d6*) δ = 8.88 (dd, *J*=10.5, 7.8, 1H), 8.58 (d, *J*=2.9, 1H), 8.47 – 8.39 (m, 1H), 7.68 – 7.61 (m, 1H), 7.31 – 7.09 (m, 10H), 7.00 (dt, *J*=8.3, 7.4, 2H), 6.80 (dd, *J*=9.1, 2.2, 1H), 6.69 – 6.57 (m, 3H), 4.77 – 4.50 (m, 2H), 4.32 – 4.16 (m, 5H), 3.68 (t, *J*=6.7, 8H), 3.48 (dd, *J*=14.0, 6.9, 4H), 3.07 – 2.68 (m, 6H), 2.47 – 2.38 (m, 2H), 2.32 – 2.22 (m, 2H), 1.80 – 1.25 (m, 10H), 1.14 (t, *J*=7.0, 6H).

^{13}C NMR (101 MHz, DMSO-*d6*) δ = 173.12, 172.21, 171.45, 170.67, 162.29, 161.99, 157.75, 153.05, 148.35, 144.95, 137.95, 137.40, 132.12, 129.90, 129.79, 129.76, 129.64, 128.52, 126.76, 112.37, 112.35, 110.68, 109.16, 108.02, 96.30, 63.02, 62.41, 62.27, 54.37, 54.24, 52.65, 52.09, 44.82, 41.61, 33.81, 33.68, 33.23, 30.74, 26.93, 25.78, 24.93, 22.49, 21.07, 12.76.

MS: calculated for $C_{54}H_{66}Cl_2N_6O_9$ is 1012.4268, found 1013.4240, $[M + H]^+$.

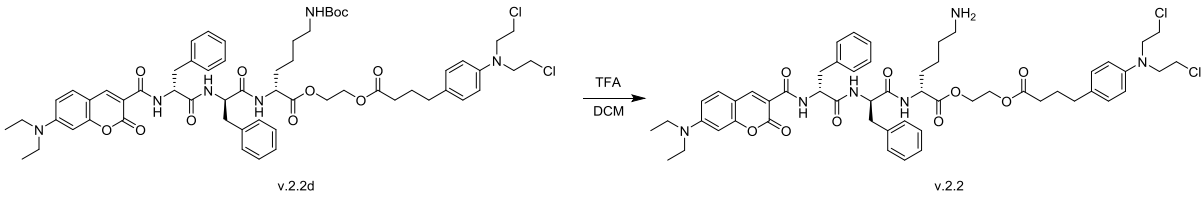

Scheme 10. Synthesis of compound v.2.2.

Compound **v.2.2**: Compound v.2.2d (50.0 mg, 0.045 mmol) was dissolved in 10 mL dried DCM and cooled down to 0 ^{o}C, then 2 mL TFA was slowly dropped into the solution. Stirring at 0 ^{o}C for 5h, and the target compound was purified by HPLC, the yield was 82.8%.

^{1}H NMR (400 MHz, DMSO-*d6*) δ = 8.91 – 8.88 (m, 1H), 8.61 – 8.53 (m, 1H), 8.44 (s, 1H), 7.79 – 7.61 (m, 3H), 7.39 – 6.91 (m, 10H), 6.81 (s, 1H), 6.71 – 6.49 (m, 2H), 4.80 – 4.59 (m, 2H), 4.40 – 4.15 (m, 5H), 3.80 – 3.65 (m, 8H), 3.15 – 2.93 (m, 4H), 2.89 – 2.66 (m, 6H), 2.46 – 2.38 (m, 2H), 2.31 – 2.20 (m, 2H), 1.84 – 1.35 (m, 10H), 1.12 (t, *J*=7.0, 6H).

^{13}C NMR (101 MHz, DMSO-*d6*) δ = 173.12, 172.36, 171.45, 170.50, 162.00, 157.70, 157.07, 152.88, 148.36, 144.95, 137.35, 132.13, 129.77, 129.64, 128.50, 126.81, 112.34, 110.69, 108.02, 63.03, 62.20, 54.19, 52.64, 52.15, 47.98, 44.82, 41.61, 33.81, 33.24, 26.93, 25.78, 24.93, 22.50, 12.77.

MS: calculated for $C_{54}H_{66}Cl_2N_6O_9$ is 1012.4268, found 1013.4248, $[M + H]^+$.

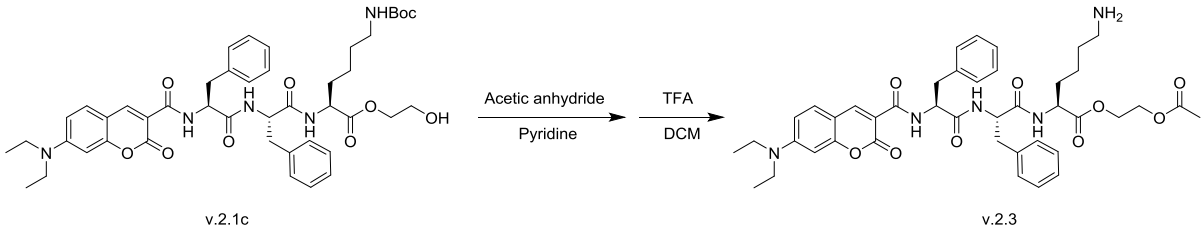

Scheme 10. Synthesis of compound v.2.3.

Compound **v.2.3**: compound v.2.1c (79.3 mg, 0.096 mmol) and acetic anhydride (14.7 mg, 0.144 mmol) were dissolved by 10 mL of pyridine at 25 mL round-bottom flask, the mixture was stirred at room temperature overnight. Pyridine was removed under reduced pressure rotor evaporator. The mixture was dissolved in 10 mL dried DCM, cooling down to 0 ^{o}C in ice bath. 3 mL of TFA was slowly dropped into the mixture and stirred at 0 ^{o}C for 5h. The target compound was purified by HPLC, the yield was 79.3%.

^{1}H NMR (400 MHz, DMSO-*d6*) δ 8.92 – 8.83 (m, 1H), 8.58 (d, *J* = 3.0 Hz, 1H), 8.52 – 8.40 (m, 2H), 7.65 (s, 1H), 7.32 – 7.12 (m, 10H), 6.80 (d, *J* = 9.1 Hz, 1H), 6.60 (dd, *J* = 4.3, 2.3 Hz, 1H), 4.85 – 4.51 (m, 3H), 4.32 – 4.20 (m, 4H), 3.51 – 3.46 (m, 4H), 3.09 – 2.99 (m, 2H), 2.87 – 2.71 (m, 4H), 2.00 (d, *J* = 6.5 Hz, 3H), 1.72 – 1.19 (m, 8H), 1.14 (t, *J* = 7.0 Hz, 6H).

^{13}C NMR (101 MHz, DMSO-*d6*) δ 172.23, 171.45, 170.70, 161.99, 157.75, 153.05, 148.36, 137.94, 137.41, 132.14, 129.84, 129.82, 129.65, 128.51, 128.46, 126.80, 126.76, 110.69, 109.15, 108.03, 96.31, 62.96, 62.35, 62.26, 54.20, 52.09, 44.81, 40.89, 38.46, 30.75, 26.90, 22.47, 21.05, 12.77.

MS: calculated for $C_{42}H_{51}N_5O_9$ is 769.3687, found 770.3703, $[M + H]^+$.

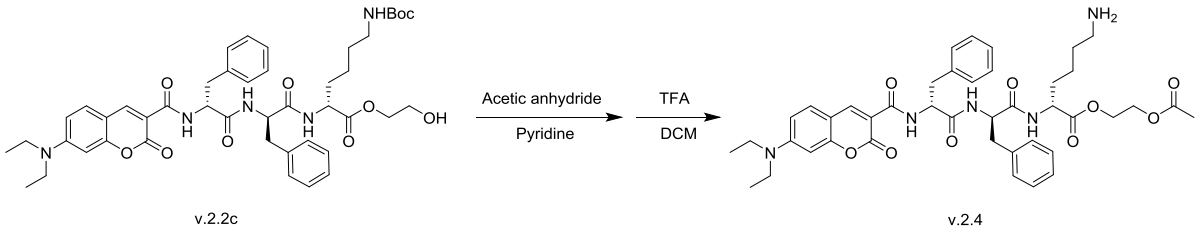

Scheme 12. Synthesis of compound v.2.4.

Compound **v.2.4**: compound v.2.4 was synthesized according to the same procedure of compound v.2.3, the yield was 82.3%.

^{1}H NMR (400 MHz, DMSO-*d6*) δ 8.90 – 8.83 (m, 1H), 8.58 (d, *J* = 2.8 Hz, 1H), 8.47 (dd, *J* = 30.1, 7.9 Hz, 2H), 7.67 (s, 1H), 7.30 – 7.11 (m, 10H), 6.81 (d, *J* = 9.1 Hz, 1H), 6.61 – 6.58 (m, 1H), 4.78 – 4.54 (m, 3H), 4.32 – 4.19 (m, 4H), 3.48 (q, *J* = 7.0 Hz, 1H), 3.10 – 3.01 (m, 2H), 2.87 – 2.70 (m, 4H), 1.99 (d, *J* = 7.4 Hz, 3H), 1.80 – 1.22 (m, 8H), 1.14 (t, *J* = 7.0 Hz, 6H).

^{13}C NMR (101 MHz, DMSO-*d6*) δ 172.17, 171.88, 170.80, 170.69, 162.11, 157.74, 153.05, 148.36, 138.13, 137.50, 132.15, 129.84, 129.65, 129.63, 128.52, 128.46, 126.79, 126.77, 110.69, 109.13, 108.03, 96.29, 62.97, 62.35, 54.07, 52.29, 46.70, 44.81, 39.08, 30.67, 26.98, 22.68, 21.04, 12.77.

MS: calculated for $C_{42}H_{51}N_5O_9$ is 769.3687, found 770.3701, $[M + H]^+$.

V. 2. 2. 4. CES catalyzed hydrolysis

In buffer

Esterase (CES) from rabbit liver lyophilized powder was purchased from Sigma-Aldrich (E0887-500UN). Following the protocol provided by Sigma-Aldrich, CES stock solution (0.2 u/μL) was prepared in borate buffer (pH 8.0). Desired concentration specimen solutions were prepared by diluting the stock solutions of compound v.2.1 or v.2.2 (40 mM in DMSO) with borate buffer. Proper volume of CES stock solution was added into 200 μL of specimen solution to a final concentration of 1u. HPLC and MS were applied to identify the reaction products and monitor the kinetic progress of hydrolysis at 37^{o}C.

Intracellular hydrolysis study

MCF-7 cell was cultured in 35 mm polystyrene culture dish. When cells reached approximately 80% confluence in the log phase growth period, aspirated media and gently washed by 1x PBS buffer. Removed the 1x PBS buffer, 2 mL of culture medium containing 30 μM compound v.2.1, v.2.2, v.2.3 and v.2.4 were added into the culture dish. Treated MCF-7 cells were incubated at 37 ℃ with a humidified atmosphere of 5% CO_2 for 6 hours. Media were aspirated and the gently washed by cooling down 1x PBS buffer for 3 times. 1 mL mixture of cold MeOH and 1x PBS solution (1:1) was added into the wells and scratched to harvest the MCF-7 cells. The obtaining cell suspensions were sonicated for 10 min, 20s pulse after every 10s interval at

0 °C to break the cell membrane, centrifuged at 20000 rpm for 5 min at 4 °C, and then collected the supernatant. The supernatants were analysed using HPLC-MS to study the intracellular CES catalysed hydrolysis.

V. 2. 2. 5. UV-Vis Absorption and emission spectroscopy

UV-Vis measurements were carried out on a Thermo Nanodrop 2000C spectrophotometer. The path length of the cuvette was 0.5 cm. The detection range was set to 250 - 700 nm with a spectral resolution of 1.0 nm. Emission spectra were collected by a home-made Hamamatsu fluorescence spectrometer. The excitation wavelength was set to 405 nm and emission collection wavelength was set between 415 and 750 nm.

V. 2. 2. 6. Transmission electron microscopy (TEM) imaging

TEM imaging was carried out on a JEM-1230R (JEOL, Japan) electron microscope. Specimen preparation was carried out as the following procedure: carbon-coated copper grids were firstly glow discharged to enhance hydrophilicity; then 5 μL of sample solution was placed on the grid, left the sample on the grid around 60s, the excess fluid was removed by a filter paper; washed the grid with 5 μL of distilled water for 3 times, the excess water was removed by a filter paper; 5 μL of 1% uranyl acetate was placed on the grid, after 20s staining, removed the excess staining solution by touching the edge of grid using a filter paper; washed by 5 μL of distilled water and dried the carbon-coated grid at room temperature before imaging.

V. 2. 2. 7. Circular dichroism (CD) analysis

CD spectra were recorded on a spectrometer (JASCO J-820) with bandwidth of 1.0 nm in the region (200-550 nm) under the nitrogen atmosphere. The specimen solution (200μM) was filled evenly into a 1 mm thick quartz cuvette.

V. 2. 2. 8. Cell culture

HeLa, SKOV3, OVCAR-3, MCF-7 cell lines were purchased from American-type Culture Collection (ATCC, USA) and cultured in ATCC recommended media. HeLa cell lines were cultured in DMEM containing 10% FBS, whereas SKOV3 cell line was cultured in McCoy's medium with 10% FBS, OVCAR3 was cultured in RPMI 1640 medium with 20% FBS and MCF-7 was cultured in EMEM with 0.01 mg/mL insulin and 10% FBS. Incubation was carried out at 37 ℃ with a humidified atmosphere of 5% CO_2. The cells were maintained at 80% confluency and used for the bioassays.

V. 2. 2. 9. Cell viability assay

Cells in exponential growth phase were seeded in a 96 well plate at a concentration of 1×10^4 cells/well for all cell lines. The cells were allowed to attach to the wells at 37 ℃, 5% CO_2. The culture media were removed following by addition of 100 μL culture media containing different concentrations (12.5, 25, 50 and 100μM) of compound v.2.1, v.2.2, v.2.3, v.2.4, v.2.1.1, v.2.2.1 and chlorambucil (immediately diluted from 80 mM stock solution in DMSO) and the mixture chlorambucil/v.2.1.1 (1:1) or chlorambucil/v.2.2.1 (1:1). After the desired time of incubation, 10 μL MTT solution (5 mg/mL) was added to each well and incubated at 37 ℃ for another 4 h, and then 100 μL of SDS solution (10% in Milli-Q water) was added to stop the

reduction reaction and dissolve the purple formazan. The absorbance at 570 nm was measured using Nivo3 microplate reader (PerkinElmer). All experiments were performed in triplicate and repeated three times.

V. 2. 2. 10. Western blotting

MCF-7 cells were seeded in 6-well plate at a density of 5.0×10^5 cells per well and allowed to attach for 24 hours. The cells were treated by at concentrations of 0, 5, 10 and 20 μM of v.2.1 and v.2.2; 0, 10, 25 and 50 μM of v.2.3 and v.2.4. After incubation for 12 hours, all cells were harvested and washed with ice cold 1 × PBS twice. 70μL CelLytic M solution (Sigma-Aldrich) containing protease inhibitors cocktail was added and incubated for 30 min on a shaker at 0 °C. Then centrifuge the lysed cells for 5 min at 20000 rpm (4 °C) to pellet the cellular debris. The protein concentrations of lysates were determined through the bicinchoninic acid (BCA) method. Proteins were dissolved in SDS sample buffer containing 2% β-mercaptoehtanol. Samples (10 μg of protein, ~ 10 μL) were loaded and separated by 10% Laemmli-SDS-PAGE. For Western blot analysis, the proteins were transferred onto a polyvinylidene difluoride (PVDF; Bio-Rad, Her-cules, CA, USA) membrane. After blocking with Blocking one-P (Nacalai tesque, Kyoto, Japan), the membrane was incubated with the antibody. Specifically, incubating with 1:1000 dilution for Bip, Calnexin, IRE1α and PDI (Cell signalling, #9956), and 1:2000 dilution for beta-actin (Abcam, ab8227) antibody for overnight at 4°C. After washing, the membrane was incubated with 1,000-fold diluted peroxidase-conjugated goat anti-rabbit IgG (Bio-Rad, Hercules, CA, USA) for 90 min, and then stained using ECLTM prime Western blotting detection reagent (GE Healthcare, Little Chalfont, UK).

V. 2. 2. 11. Cell confocal imaging

HeLa or MCF-7 cells were seeded in 35 mm glass bottom dish at a density of 1×10^5. The cells were allowed to attach for 24 h at 37 ℃ under 5% CO_2. Then, the culture media were removed and changed to fresh media containing v.2.1, v.2.2, v.2.3, v.2.4, v.2.1.1, and v.2.2.1 at a concentration of 20μM. After incubation for 2h, cells were washed using 1 × PBS buffer three times and stained with commercial fluorescent labels including ER-Tracker™ Red (BODIPY™ TR Glibenclamide) and LysoTracker™ Red DND-99 from ThermoFisher. After removing the staining solution, the cells were washed three times by 1 × PBS buffer. The cells were observed in Cell Imaging Solution by a Nikon A1 confocal microscope.

V. 2. 2. 12. Cell cycle assay

HeLa cells were seeded in 6-well plates at a density of 1×10^5 and allowed to attach the for 24 hours at 37 ℃ under 5% CO_2. The cells were treated with a concentration of 20 μM of compound v.2.1, v.2.2 at varied time incubations (6h, 12h, and 24h). HeLa cells without treatment were used as a control. Treated cells were harvested by trypsin and washed twice with ice-cold 1 × PBS buffer. The cells were further fixed with 70% ethanol at 4 °C overnight and treated with Rnase A for 30 min at 37°C, followed by PI staining for 30 min in the dark at room temperature. Cell cycle analysis was carried out by flow cytometer (Merck Millipore ImageStream X Mark II), and 2×10^4 events per sample were counted.

V.2.3 Results

In water, v.2.1 and v.2.2 both self-assemble into clusters of irregular nanovesicles with diameters around 100 nm (Figure 1a). The circular dichroism (CD) spectra of both molecules are specular images (Figure 1b) indicating that the chirality of the short peptide building blocks FFK/ffk is transferred supramolecularly to v.2.1 and v.2.2 assembled nanostructures.[9] Although they share the same chemical structures, the chirality difference leads to different dynamic profiles of CES-catalysed hydrolysis. As indicated in Figure 1c, under the same reaction condition, v.2.1 is hydrolysed at a slower speed than v.2.2. For example, the time required for complete hydrolysis reaction of v.2.1 is twice the time required for complete hydrolysis of v.2.2 (Figure 1c). And both hydrolysis reactions lead to self-assembling morphology transition into film like nanostructures (Figure 1d).

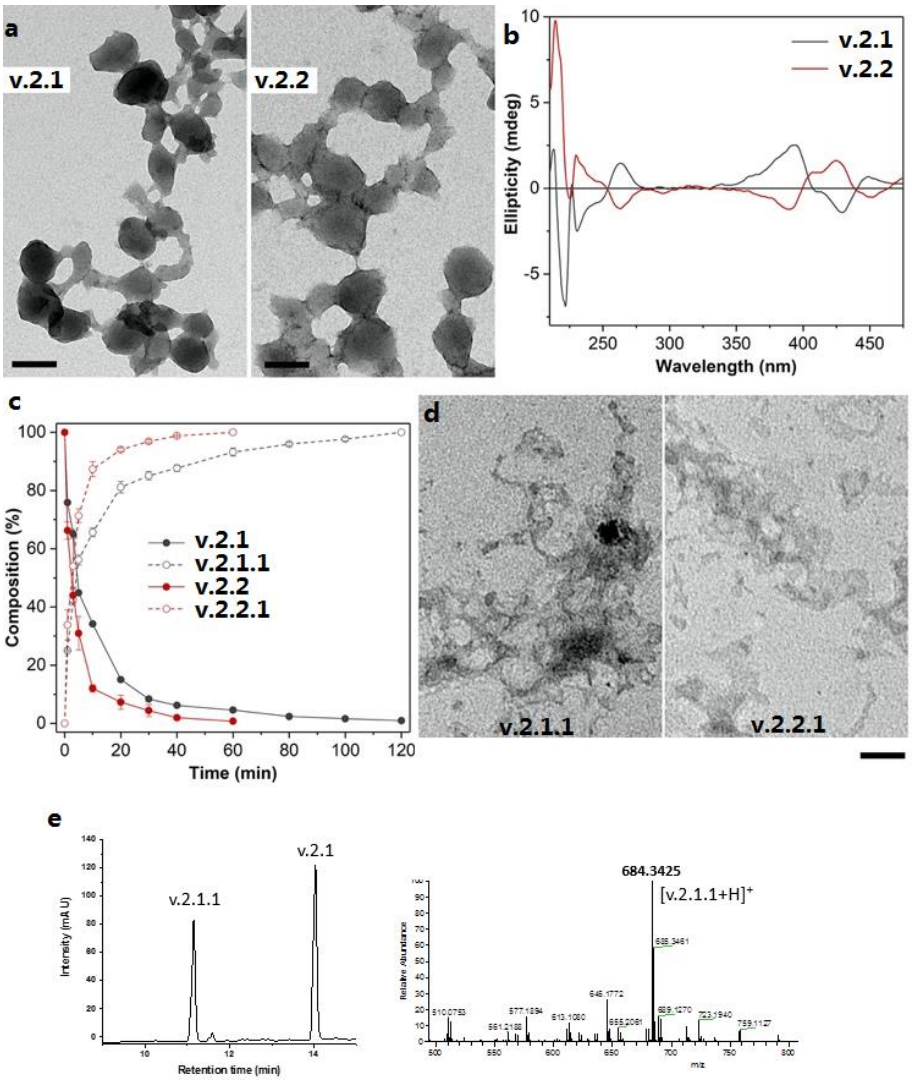

Figure 1. (a) TEM images of self-assembly of v.2.1 or v.2.2 in water at a concentration of 50 μM. Scale bars represent 100 nm. (b) CD spectra of v.2.1 or v.2.2 in water at a concentration of 200 μM. (c) Dynamic profiles of CES-catalysed hydrolysis of v.2.1 or v.2.2 at a concentration of 100 μM in borate buffer at 37 °C. (d) TEM images of self-assembly of v.2.1.1 or v.2.2.1 in water at a concentration of 50 μM. (e) HPLC spectrum of CES catalyzed-hydrolysis of v.2.1 at 3 min and MS spectrum of fraction of peak v.2.1.1 during the hydrolysis process of v.2.1, confirming it's molecule v.2.1.1.

The steady state absorption and emission spectra of v.2.1 (Figure 2a) and v.2.2 (Figure 2b) both exhibit absorption peak at 421 nm in water, whereas their hydrolysed analogue molecules exhibit absorption peak at 433 nm. The fluorescence emission peaks of v.2.1 and v.2.2 were both observed at 557 nm in water. After CES-catalysed hydrolysis, both analogue molecules

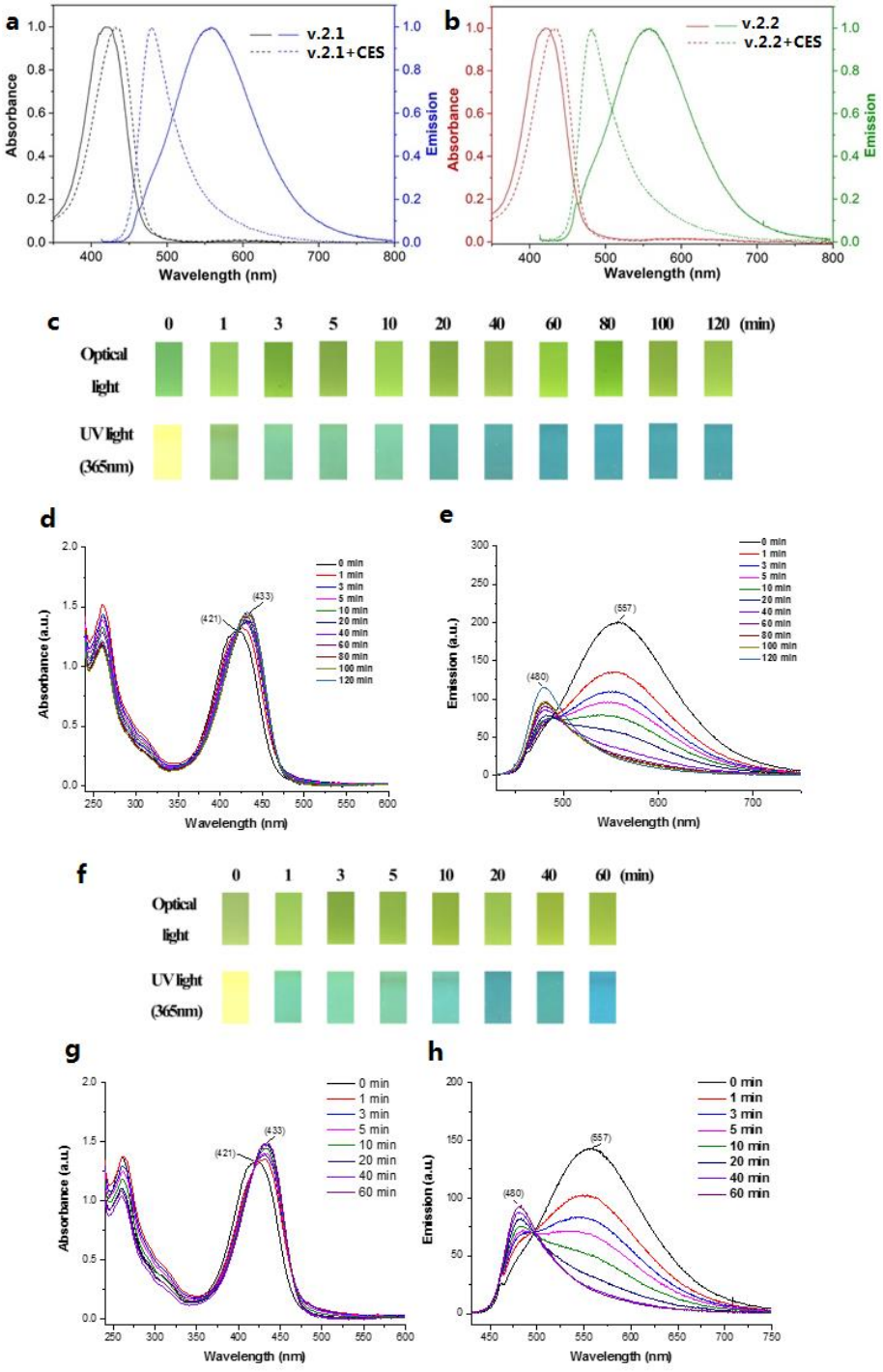

Figure 2. Normalized absorption and emission spectra of v.2.1 (a) or v.2.2 (b) before and after the hydrolysis by CES. (c) Time-dependent optical images under normal light (upper row) and UV light (bottom row) of v.2.1 (100 μM with 1u of CES) in borate buffer at 37 °C. Time-dependent UV-Vis absorbance (d) and emission spectra (ex. 405 nm) (e) of v.2.1 (100 μM with 1u of CES) in borate buffer; Time-dependent optical images under the normal light (upper row) and UV light (bottom row) of v.2.2 (100 μM with 1u of CES) in borate buffer (f). Time-dependent UV-Vis absorbance (g) and emission spectra (ex. 405 nm) (h) of v.2.2 (100 μM with 1u of CES) in borate buffer.

exhibit emission peak at 480 nm. The observed blue shift is highly possibly due to the H-type of aggregation of Coumarin 466 in hydrolysed analogues.[15] Such drastic fluorescence shift (91 nm) provides researcher the possibility of in situ observation of the dynamics of intracellular self-assembly triggered by CES-catalysed hydrolysis (Figure 2c-h).

The kinetic difference in hydrolysis of v.2.1, v.2.2, v.2.3 and v.2.4 are maintained the same tendency inside the cell (Figure 3).

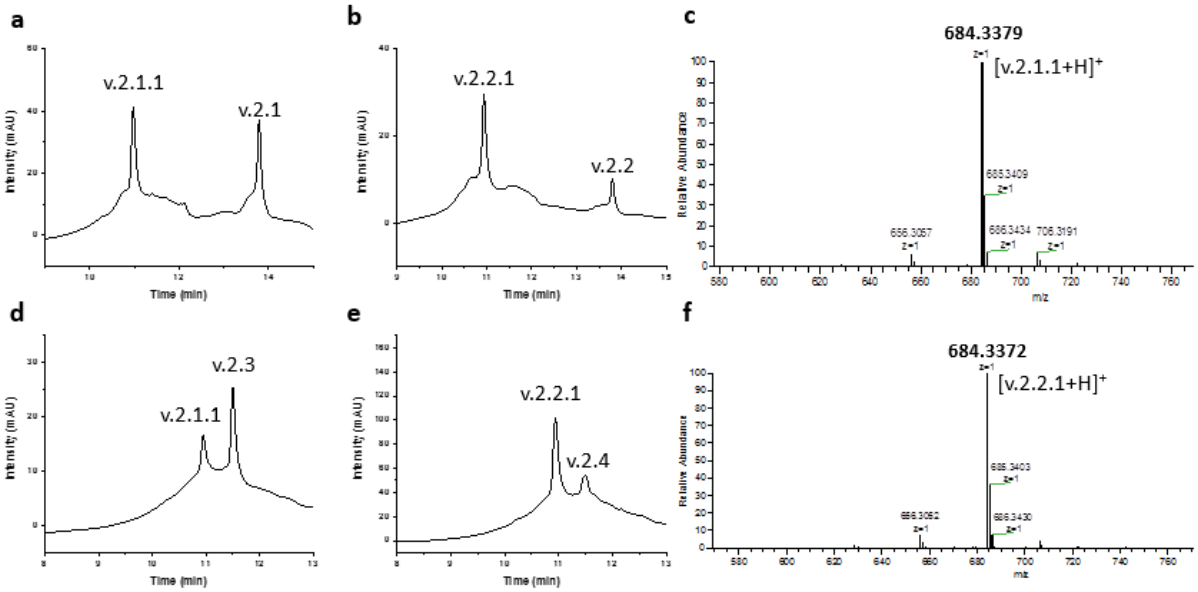

Figure 3. HPLC spectra of MCF-7 cell lysate supernatant treated by v.2.1 (a), v.2.2 (b), v.2.3 (d) and v.2.4 (e), MS spectra of fraction v.2.1.1 (c) and v.2.2.1 (f), confirming intracellular hydrolysis of v.2.1, v.2.2, v.2.3, and v.2.4 after cellular uptake**.**

Upon the treatment of v.2.1 or v.2.2 at relative low concentration (50 μM), DNA condensation was observed after short period of incubation (Figure 4).The flow cytometry analysis for cell cycle distribution confirmed the mitotic arrest induced by the treatment of v.2.1 or v.2.2 (Figure 5). The results suggest that efficient delivery of Chlorambucil is achieved by these two small-molecule nanomedicines.

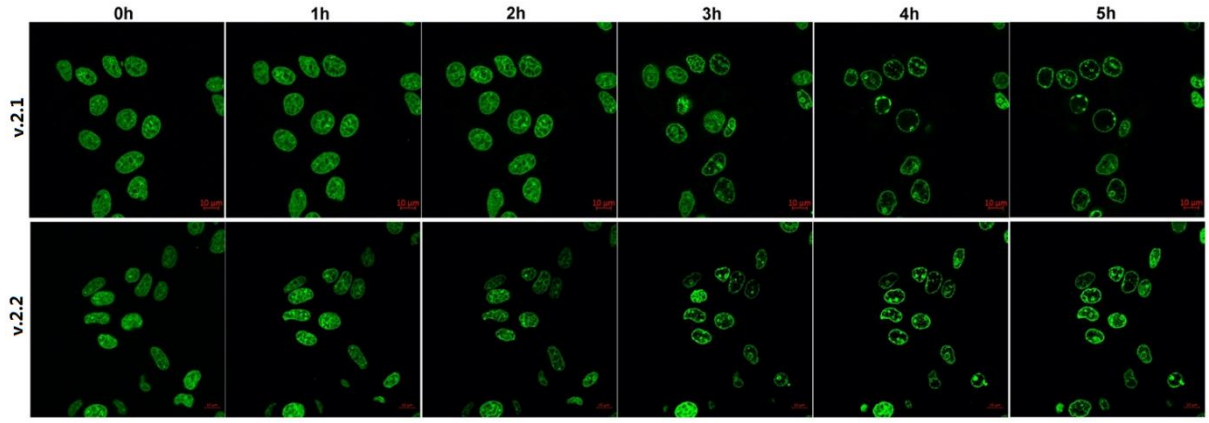

Figure 4. Time-lapse confocal imaging of HeLa-H2B(GFP) cells upon the treatment of v.2.1 and v.2.2 at concentration of 50 μM.

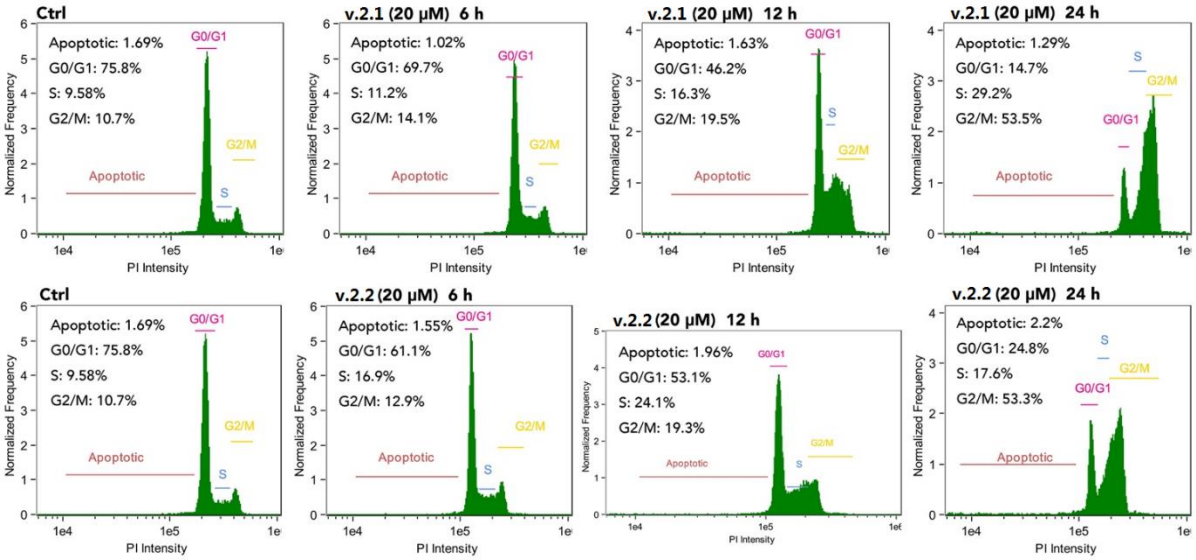

Figure 5. Time-dependent flow cytometry analysis for cell cycle distribution of HeLa cells without any treatment, and upon the treatment of v.2.1 and v.2.2 at concentration of 20 μM.

Confocal microscopy images confirmed that the hydrolysed analogue molecules v.2.1.1 and v.2.2.1 both accumulated on ER (Figure 6a and 6b), and the strong fluorescence signal also confirmed the high drug loading efficiency.

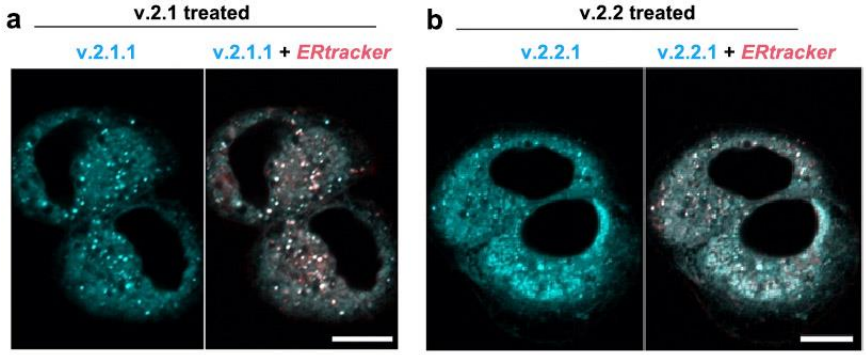

Figure 6. (a) Intracellular localization of v.2.1.1 in HeLa cells treated by v.2.1 (20 μM) for 2 hours and co-stained with ER-tracker (red). Scale bar represents 10 μm. (b) Intracellular localization of v.2.2.1 in HeLa cells treated by v.2.2 (20 μM) for 2 hours and co-stained with ER-tracker (red). Scale bar represents 10 μm.

In cell viability tests, the dual-targeting small-molecule nanomedicines are confirmed with high toxicity against different types of cancer cells including HeLa cells (cervical cancer) (Figure 7a), SKOV3 cells (ovarian cancer) (Figure 7b), OVCAR-3 cells (drug-resistant ovarian cancer) (Figure 7c), and MCF-7 cells (breast cancer) (Figure 7d). Even though MCF-7 cells are known for consistent resistance to alkylating agents by exhibiting close to 100% cell viability upon the treatment of Chlorambucil, v.2.1.1, v.2.2.1, and their combinations (Figure 7e),[16] v.2.1 and v.2.2 exhibited IC50 of 21.7 μM and 10.9 μM, respectively, much lower than the IC50 of prolidase-activated prodrug of Chlorambucil.[17] On all cancer cell lines, v.2.2 exhibits higher toxicity than v.2.1.

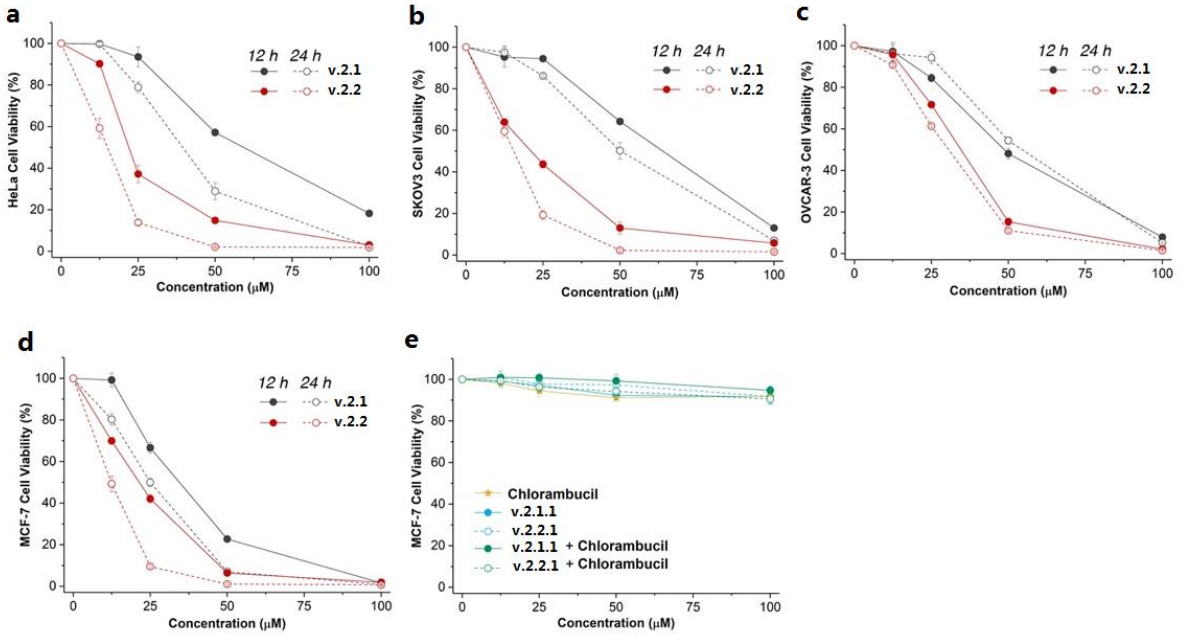

Figure 7. (a) 12-hour and 24-hour HeLa cell (a), SKOV3 cell (b), OVCAR-3 cell (c), and MCF-7 cell (d) viabilities upon the incubation with v.2.1 or v.2.2 at various concentrations. (e) 24-hour MCF-7 cell viability upon the incubation of Chlorambucil, v.2.1.1, v.2.2.1, and their mixtures at various concentrations.

Since direct treatment of v.2.2.1 in MCF-7 cell culture failed in accumulation on ER (Figure 8), to properly examine the influence induced by ER-targeted self-assembly, two small-molecule medicines v.2.3 and v.2.4 as CES-instructed nanoscale delivery systems are designed and synthesized (Figure 9a). Their absorptions at 436 nm and fluorescent emissions around 470 nm remained the same before or after CES treatment (Figure 9b).

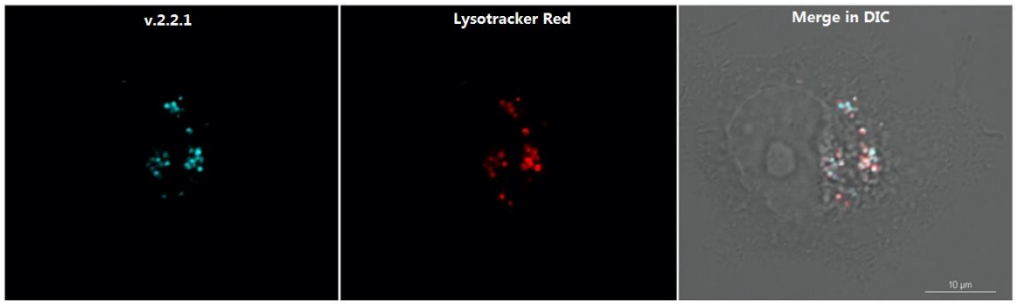

Figure 8. Intracellular localization of V.2.2.1 in MCF-7 cells upon the treatment of v.2.2.1 co-stained with Lysotracker Red.

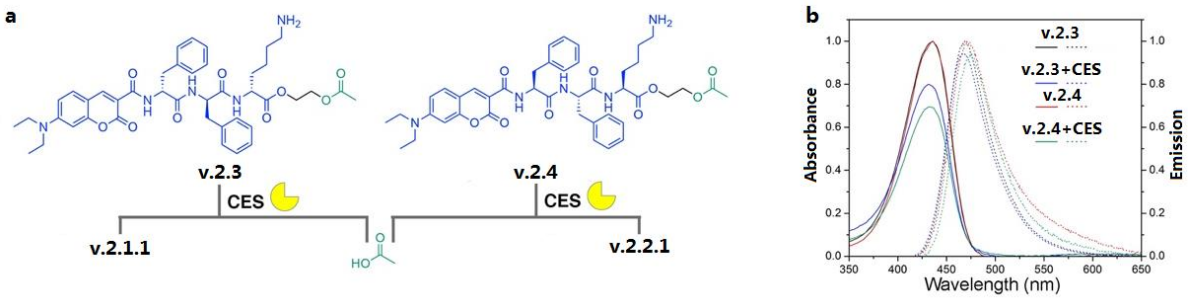

Figure 9. (a) Schematic illustration of CES-catalysed hydrolysis of v.2.3 or v.2.4. (b) Absorption and emission spectra of v.2.3 or v.2.4 before and after CES-catalysed hydrolysis.

The confocal microscopy imaging was conducted to examine intracellular localizations. Upon the treatment of these two molecules, v.2.1.1 and v.2.2.1 were successfully delivered to ER at high loading rate (Figure 10a and 10b) and exhibited similar concentration dependent toxicity against MCF-7 cells (Figure 10c).

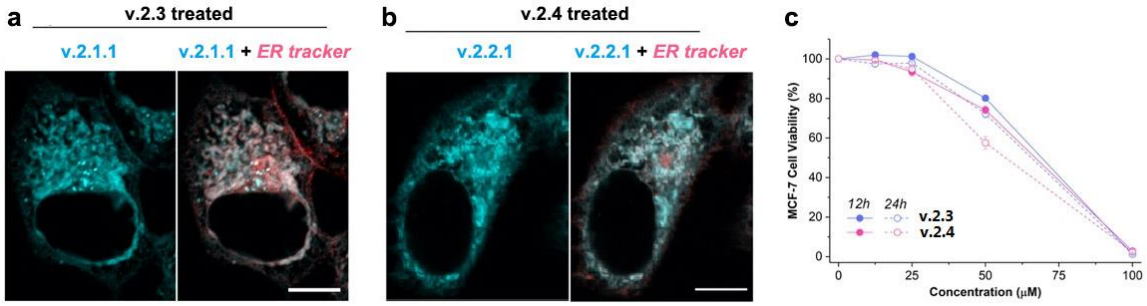

Figure 10. (a) Intracellular localization of v.2.1.1 in MCF-7 cells treated by v.2.3 (20 μM) for 2 hours and co-stained with ER-tracker (red). Scale bar represents 10 μm. (b) Intracellular localization of v.2.2.1 in MCF-7 cells treated by v.2.4 (20 μM) for 2 hours and co-stained with ER-tracker (red). Scale bar represents 10 μm. (c) 12-hour and 24-hour MCF-7 cell viability upon the incubation with v.2.3 or v.2.4 at various concentrations.

The quantitative protein expression analysis of ER transmembrane sensor protein IRE1α[19], ER stress regulators including ER chaperone proteins Bip[20] and Calnexin[21], and luminal ER oxidoreductase protein disulfide isomerase-A1 (PDI)[22] exhibited upregulation at different levels in MCF-7 cells upon the treatment of v.2.1, v.2.2, v.2.3, and v.2.4 at increased concentrations (Figure 11), which confirmed that ER-targeted self-assembly of v.2.1.1 and v.2.2.1 delivered by small-molecule nanomedicines inducing ER stress, thus triggering cell apoptosis.

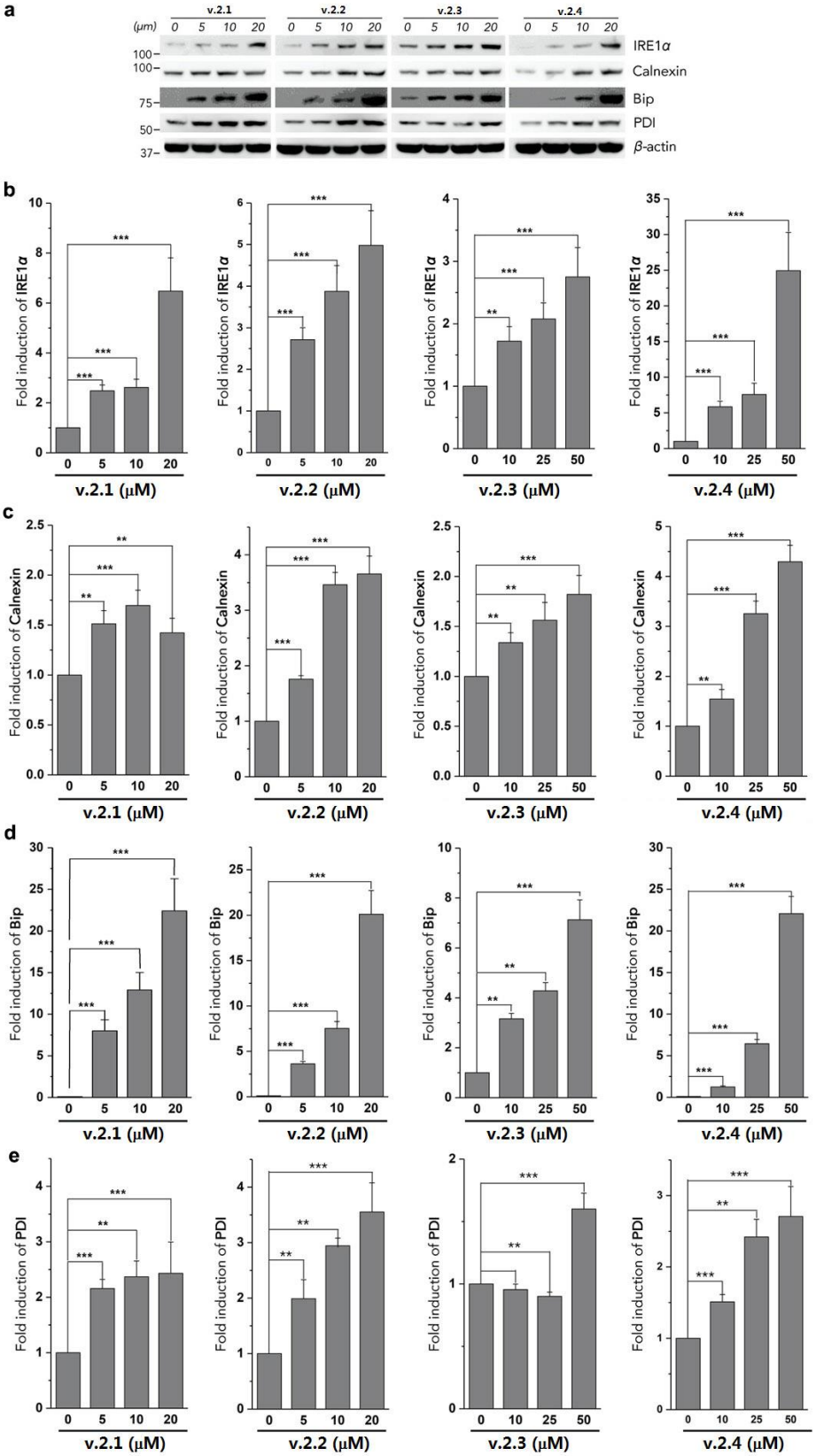

Figure 11. (a) Immunoblotting analysis of MCF-7 cells transiently expressing IRE1α, Calnexin, Bip, and PDI upon incubation with v.2.1, v.2.2, v.2.3, or v.2.4 at various concentrations for 12 hours. Quantitative analysis of IRE1α (b), Calnexin (c), Bip (d), and PDI (e) expression in MCF-7 cells upon the treatment of v.2.1, v.2.2, v.2.3, and v.2.4.

To understand the drug synergy for further optimization of beneficial drug interactions, we monitored the intracellular dynamics of CES-instructed self-assembly upon the treatment of v.2.1 and v.2.2 using time-lapse confocal microscopy imaging of MCF-7 cells (Figure 12a). Upon 1-hour treatment, both intracellular v.2.1 and v.2.2 are in reticular shape localized on ER with higher loading efficiency in v.2.2 treatment. At the same time, CES-catalysed hydrolysis efficiently proceeded exhibiting ER-targeted self-assembly of analogue molecules. Since 6-hour treatment, v.2.1 gradually transformed into punctuate shape aggregates colocalized with part of the v.2.1.1. Zoom-in image exhibited co-existence of punctuate and reticular shaped v.2.1.1, and the punctuates co-localized with v.2.1 (Figure 12b). Smaller amount of punctuate aggregation of v.2.2 was also observed after 6-hour treatment. After 12 hours, large amount of punctuate shaped v.2.1 were still remained, while most of the v.2.2 were hydrolysed except small amount in punctuate shape. Zoom-in image exhibited much higher accumulation rate of v.2.2.1 on ER than v.2.1.1.

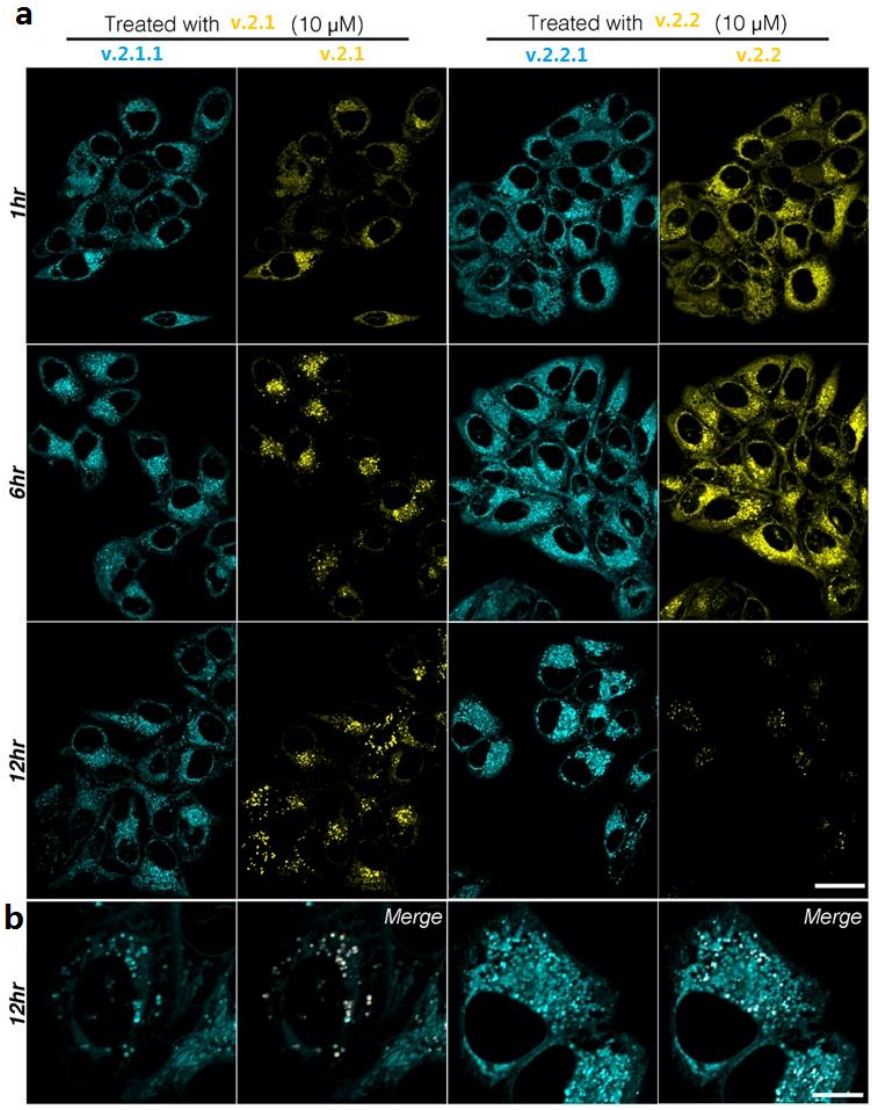

Figure 12. (a) Spatial distribution of v.2.1.1 and v.2.1 in MCF-7 cells upon the treatment of v.2.1 (10 μM) for 1, 6, and 12 hours. Spatial distribution of v.2.2.1 and v.2.2 in MCF-7 cells upon the treatment of v.2.2 (10 μM) for 1, 6 and 12 hours. Scale bar represents 30 μm. (b) Intracellular co-localization of v.2.1.1 with v.2.1 in MCF-7 cells upon the treatment of v.2.1 for 12 hours, or v.2.2.1 with v.2.2 in MCF-7 cells upon the treatment of v.2.2 for 12 hours. Scale bar represents 10 μm.

Regarding the intracellular morphology transition of self-assembled v.2.1/v.2.2, and their hydrolysis reaction rate, we tested the CES-catalysed hydrolysis in their aggregating state in solution (Figure 13). The results indicate that the hydrolysis is hindered when the reactants are tightly packed. And this may well explain why the unhydrolyzed intracellular v.2.1/v.2.2 are punctuate aggregates.

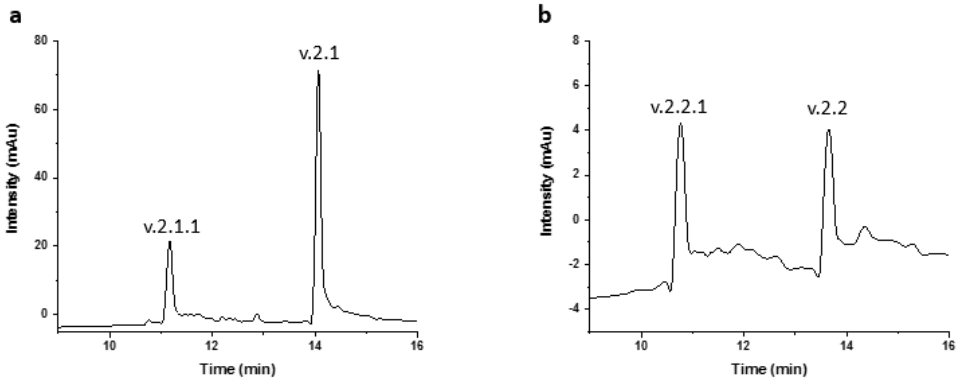

Figure 13. HPLC analysis of CES catalysed hydrolysis of v.2.1 (a) and v.2.2 (b) aggregates in borate buffer at 37 °C for 2 hours and 1 hour, respectively.

V.2.4 Conclusion

Since the CES-catalysed hydrolysis of v.2.2 is faster than v.2.1, higher production rate of v.2.2.1 than v.2.1.1 were achieved before v.2.2 and v.2.1 transform into punctuate aggregates. Therefore, less unhydrolyzed nanomedicines were remained in the v.2.2 treated MCF-7 cells, while more Chlorambucil was released for efficient DNA damaging. The higher stability of D-version peptide than the L-version also contribute to long-term higher accumulation rate of v.2.2.1 than v.2.1.1 raising ER stress for synergistic anticancer effect with Chlorambucil.

The higher anticancer toxicity of D-version peptide has been very well studied.[14] And it is generally agreed that the intracellular stability is the key for the efficacy. However, the observation and comparison of dynamic self-assembly and the correlated hydrolysis rate between L-version and D-version nanomedicines in cell milieu has not been reported yet.[23] The correlated dynamic profiles will offer important insights into the intracellular enzyme-instructed molecular self-assembly, which will provide valuable contribution to the development of nanomedicines.

VI. General Conclusion

- Self-assembly nanofiber from short aromatic peptide molecule can be further manipulated by conjugation with easily protonated functional group (e.g. taurine). By adjusting the pH value of the aqueous specimen, negatived charged nanofibers can be approached, and external mechanical force in the same direction can induce uniaxially arrangement of the nanofibers. Large scale well-orientated nanofiber fabrication can be achieved via slowly evaporation casting in capillary confinement. Negatived charged nanofibers in aqueous solution can be transferred into a highly ordered peptide film with varied interference colours at different domains.

- Unconventional nanostructures can be obtained through co-organizing components from degradation of pre-stabilized self-assembled nanostructures. By conjugation of the self-assembly peptide motif with light responsive functional groups (e.g. coumarin), it will endow the self-assembly molecule potential ability to generate new nanostructures via light irradiation. This strategy provides a new choice to fabricate metastable nanostructures that is hard to reach in the conventional way. In addition, light stimulus is a non-invasive, clean, good choice for spatial and temporal control.

- Constructing higher-order nanostructure can be reached via interaction between two components at the nanoscale. By carefully molecular design, two self-sorting molecules share some common molecular fragments, it provides the potential for the two self-sorting molecules to interact with each other. One component self-assembled into fibrous nanostructures, it works as the scaffold to facilitate the construction of the other components to reach a more sophisticated higher-order architecture.

- Precisely subcellular organelle delivery of self-assembly assemblies can be enhanced by conjugating with carboxyl esterase responsive functional groups. The self-assembly peptide molecule will be recovered when entering into the cancer cells due to the highly expressed of carboxyl esterase, and enrichment of the peptide assemblies on specific subcellular organelle (e.g. endothelial reticulum) will initiate cell apoptosis, leading to cancer cell death.

- Dual-subcellular-targeting is achieved by conjugating coumarin-functionalized peptide with DNA alkylating agent, synergistically targeting both ER and nucleus, thus enhancing anti-cancer effect.

Future Study

Above studies have proved the feasibility of using small peptidic molecules in fabricating advanced nanomaterials. In pursing biomedical applications of the peptidic molecular assemblies, sophisticate design of precursor molecule facilitates intracellular delivery and introduces intra-cellular molecular assembly, thus, leading to cancer cell dysfunction and apoptosis. However, there are still several points needed to be addressed in the future studies.

- Stability
  Peptidic molecules, especially natural amino acid sequence suffers degradation risks from various protein enzymes presented in cell cytoplasm. Non-natural amino acid sequence design in Chapter V.2 has proved a better anticancer effect *in vitro*. A combination of L-version and D-version amino acids will be applied in molecular design to enhance the biostability for elevated anti-cancer efficacy.

- Selectivity
  Side effects in clinical chemotherapy originate from non-differentiated effect on both tumor and normal tissues of anticancer agents. Enzyme-instructed peptide assembly has proved to be able to selectively target cancer cells rather than normal cells. Enzyme responsive motifs will be widely applied in the design of self-assembling peptidic molecules for high selectivity.

- Active agent encapsulation
  Previous study focuses on covalently conjugating self-assembling peptidic molecules with chlorambucil. Though it delivers high encapsulation efficiency for chlorambucil, it is not a convenient way to apply on other active agents due to potential challenges in chemical synthesis. Since the self-assembling peptidic molecules form vesicle structure, it is highly possible to encapsulate active agents through non-covalent interactions such as hydrophobic or ionic interactions. Combination of active agents and self-assembling peptides will be considered and evaluated.

- *In situ* monitoring
  The application of coumarin derivatives in molecular design has proved to be feasible in locating the assemblies *in vitro*. Switching UV-Vis emission to NIR fluorescent motifs such as cyanine derivatives will not only provide a deeper penetration depth to ensure accurately locating for *in vivo* evaluation, but also bring less photocytotoxicity to the cells or animals due to its long wavelength excitation property.

Overall, I would like to address all these aspects in molecular design in the future.

References

Chapter I

1. Moffat, A. S., *MOSAIC.* **1990**, *21* (30).
2. Whitesides, G. M.; Mathias, J. P.; Seto, C. T., Molecular Self-Assembly and Nanochemistry - a Chemical Strategy for the Synthesis of Nanostructures. *Science* **1991**, *254* (5036), 1312-1319.
3. Sridhar, R.; Lakshminarayanan, R.; Madhaiyan, K.; Barathi, V. A.; Limh, K. H. C.; Ramakrishna, S., Electrosprayed nanoparticles and electrospun nanofibers based on natural materials: applications in tissue regeneration, drug delivery and pharmaceuticals. *Chem Soc Rev* **2015**, *44* (3), 790-814.
4. Lewis, G. N., The atom and the molecule. *J Am Chem Soc* **1916**, *38*, 762-785.
5. Kim, D.; Kim, E.; Lee, J.; Hong, S.; Sung, W.; Lim, N.; Park, C. G.; Kim, K., Direct Synthesis of Polymer Nanocapsules: Self-Assembly of Polymer Hollow Spheres through Irreversible Covalent Bond Formation. *J Am Chem Soc* **2010**, *132* (28), 9908-9919.
6. Baek, K.; Yun, G.; Kim, Y.; Kim, D.; Hota, R.; Hwang, I.; Xu, D.; Ko, Y. H.; Gu, G. H.; Suh, J. H.; Park, C. G.; Sung, B. J.; Kim, K., Free-Standing, Single-Monomer-Thick Two-Dimensional Polymers through Covalent Self-Assembly in Solution. *J Am Chem Soc* **2013**, *135* (17), 6523-6528.
7. Lee, J.; Baek, K.; Kim, M.; Yun, G.; Ko, Y. H.; Lee, N. S.; Hwang, I.; Kim, J.; Natarajan, R.; Park, C. G.; Sung, W.; Kim, K., Hollow nanotubular toroidal polymer microrings. *Nature chemistry* **2014**, *6* (2), 97-103.
8. Shimizu, T.; Kameta, N.; Ding, W. X.; Masuda, M., Supramolecular Self-Assembly into Biofunctional Soft Nanotubes: From Bilayers to Monolayers. *Langmuir* **2016**, *32* (47), 12242-12264.
9. Tseng, W. C.; Fang, T. Y.; Lin, Y. C.; Huang, S. J.; Huang, Y. H., Reversible Self-Assembly Nanovesicle of UCST Response Prepared with Multi-L-arginyl-poly-L-aspartate Conjugated with Polyethylene Glycol. *Biomacromolecules* **2018**, *19* (12), 4585-4592.
10. Wang, H. M.; Feng, Z. Q. Q.; Xu, B., Intercellular Instructed-Assembly Mimics Protein Dynamics To Induce Cell Spheroids. *J Am Chem Soc* **2019**, *141* (18), 7271-7274.
11. Hu, K.; Liu, Y.; Xiong, W.; Gong, Y. J.; Che, Y. K.; Zhao, J. C., Fabrication of Single-Handed Nanocoils with Controlled Length via a Living Supramolecular Self-Assembly. *Chem Mater* **2019**, *31* (4), 1403-1407.
12. Diercks, C. S.; Yaghi, O. M., The atom, the molecule, and the covalent organic framework. *Science* **2017**, *355* (6328).
13. Hartgerink, J. D.; Beniash, E.; Stupp, S. I., Self-assembly and mineralization of peptide-amphiphile nanofibers. *Science* **2001**, *294* (5547), 1684-1688.
14. (a) Atkins, P. a. J. d. P., Physical Chemistry for the Life Sciences. *Oxford, UK: Oxford University Press* **2006**, *458*; (b) Sinnokrot, M. O.; Valeev, E. F.; Sherrill, C. D., Estimates of the ab initio limit for pi-pi interactions: The benzene dimer. *J Am Chem Soc* **2002**, *124* (36), 10887-10893.
15. Clark, D., General Chemistry. *Boston Medical Publishing Corporation* **1999**.
16. Matthews, R. P.; Welton, T.; Hunt, P. A., Competitive pi interactions and hydrogen bonding within imidazolium ionic liquids. *Phys Chem Chem Phys* **2014**, *16* (7), 3238-3253.
17. Bozzuto, G.; Molinari, A., Liposomes as nanomedical devices. *Int J Nanomed* **2015**, *10*, 975-999.
18. Xie, Y. Y.; Zhao, J.; Huang, R. L.; Qi, W.; Wang, Y. F.; Su, R. X.; He, Z. M., Calcium-

Ion-Triggered Co-assembly of Peptide and Polysaccharide into a Hybrid Hydrogel for Drug Delivery. *Nanoscale Res Lett* **2016**, *11*.
19. Li, Y.; Zhao, T.; Wang, C. S.; Lin, Z. Q.; Huang, G.; Sumer, B. D.; Gao, J. M., Molecular basis of cooperativity in pH-triggered supramolecular self-assembly. *Nat Commun* **2016**, *7*.
20. Wang, J.; Liu, K.; Yan, L. Y.; Wang, A. H.; Bai, S.; Yan, X. H., Trace Solvent as a Predominant Factor To Tune Dipeptide Self-Assembly. *ACS nano* **2016**, *10* (2), 2138-2143.
21. Moreira, I. P.; Piskorz, T. K.; van Esch, J. H.; Tuttle, T.; Ulijn, R. V., Biocatalytic Self-Assembly of Tripeptide Gels and Emulsions. *Langmuir* **2017**, *33* (20), 4986-4995.
22. Hong, Y.; Zhou, F. F.; Hua, Y. J.; Zhang, X. Z.; Ni, C. Y.; Pan, D. H.; Zhang, Y. Q.; Jiang, D. M.; Yang, L.; Lin, Q. N.; Zou, Y. W.; Yu, D. S.; Arnot, D. E.; Zou, X. H.; Zhu, L. Y.; Zhang, S. F.; Ouyang, H. W., A strongly adhesive hemostatic hydrogel for the repair of arterial and heart bleeds. *Nat Commun* **2019**, *10*.
23. Kuang, Y.; Shi, J. F.; Li, J.; Yuan, D.; Alberti, K. A.; Xu, Q. B.; Xu, B., Pericellular Hydrogel/Nanonets Inhibit Cancer Cells. *Angew Chem Int Edit* **2014**, *53* (31), 8104-8107.
24. Yang, Z. M.; Xu, K. M.; Guo, Z. F.; Guo, Z. H.; Xu, B., Intracellular enzymatic formation of nanofibers results in hydrogelation and regulated cell death. *Advanced materials* **2007**, *19* (20), 3152-+.
25. Araki, T.; Murayama, S.; Usui, K.; Shimada, T.; Aoki, I.; Karasawa, S., Self-Assembly Behavior of Emissive Urea Benzene Derivatives Enables Heat-Induced Accumulation in Tumor Tissue. *Nano Lett* **2017**, *17* (4), 2397-2403.
26. Holder, C. F.; Schaak, R. E., Tutorial on Powder X-ray Diffraction for Characterizing Nanoscale Materials. *ACS nano* **2019**, *13* (7), 7359-7365.
27. Greenfield, N. J., Using circular dichroism spectra to estimate protein secondary structure. *Nat Protoc* **2006**, *1* (6), 2876-2890.
28. Kong, J.; Yu, S., Fourier transform infrared spectroscopic analysis of protein secondary structures. *Acta Bioch Bioph Sin* **2007**, *39* (8), 549-559.
29. Danev, R.; Yanagisawa, H.; Kikkawa, M., Cryo-Electron Microscopy Methodology: Current Aspects and Future Directions. *Trends Biochem Sci* **2019**, *44* (10), 837-848.
30. Stylianou, A.; Kontomaris, S. V.; Grant, C.; Alexandratou, E., Atomic Force Microscopy on Biological Materials Related to Pathological Conditions. *Scanning* **2019**.
31. Kiss, G.; Lich, B.; Boughorbel, F.; Hekking, L.; Korkmaz, E., 3D isotropic volume imaging and reconstruction of biological samples using SEM. *Mol Biol Cell* **2014**, *25*.
32. Koike-Tani, M.; Tani, T.; Mehta, S. B.; Verma, A.; Oldenbourg, R., Polarized light microscopy in reproductive and developmental biology. *Mol Reprod Dev* **2015**, *82* (7-8), 548-562.
33. Rughani, R. V.; Schneider, J. P., Molecular Design of β-Hairpin Peptides for Material Construction. *MRS BULLETIN* **2008**, *33* (5), 530-535.
34. Yucel, T.; Micklitsch, C. M.; Schneider, J. P.; Pochan, D. J., Direct observation of early-time hydrogelation in beta-hairpin peptide self-assembly. *Macromolecules* **2008**, *41* (15), 5763-5772.
35. (a) Khoe, U.; Yang, Y. L.; Zhang, S. G., Synergistic Effect and Hierarchical Nanostructure Formation in Mixing Two Designer Lipid-Like Peptide Surfactants Ac-A(6)D-OH and Ac-A(6)K-NH2. *Macromol Biosci* **2008**, *8* (11), 1060-1067; (b) Qiu, F.; Chen, Y. Z.; Tang, C. K.; Zhao, X. J., Amphiphilic peptides as novel nanomaterials: design, self-assembly and application. *Int J Nanomed* **2018**, *13*, 5003-5022.
36. Zhang, S. G., Discovery and design of self-assembling peptides. *Interface Focus* **2017**, *7* (6).

37. Yokoi, H.; Kinoshita, T.; Zhang, S. G., Dynamic reassembly of peptide RADA16 nanofiber scaffold. *P Natl Acad Sci USA* **2005**, *102* (24), 8414-8419.
38. Webber, M. J.; Tongers, J.; Renault, M. A.; Roncalli, J. G.; Losordo, D. W.; Stupp, S. I., Development of bioactive peptide amphiphiles for therapeutic cell delivery. *Acta Biomater* **2010**, *6* (1), 3-11.
39. Lowik, D. W. P. M.; Garcia-Hartjes, J.; Meijer, J. T.; van Hest, J. C. M., Tuning secondary structure and self-assembly of amphiphilic peptides. *Langmuir* **2005**, *21* (2), 524-526.
40. Castelletto, V.; Hamley, I. W.; Adamcik, J.; Mezzenga, R.; Gummel, J., Modulating self-assembly of a nanotape-forming peptide amphiphile with an oppositely charged surfactant. *Soft Matter* **2012**, *8* (1), 217-226.
41. Hamley, I. W., Self-assembly of amphiphilic peptides. *Soft Matter* **2011**, *7* (9), 4122-4138.
42. Lock, L. L.; LaComb, M.; Schwarz, K.; Cheetham, A. G.; Lin, Y. A.; Zhang, P. C.; Cui, H. G., Self-assembly of natural and synthetic drug amphiphiles into discrete supramolecular nanostructures. *Faraday Discuss* **2013**, *166*, 285-301.
43. Jayawarna, V.; Ali, M.; Jowitt, T. A.; Miller, A. E.; Saiani, A.; Gough, J. E.; Ulijn, R. V., Nanostructured hydrogels for three-dimensional cell culture through self-assembly of fluorenylmethoxycarbonyl-dipeptides. *Advanced materials* **2006**, *18* (5), 611-+.
44. Wang, H. M.; Feng, Z. Q. Q.; Xu, B., Bioinspired assembly of small molecules in cell milieu. *Chem Soc Rev* **2017**, *46* (9), 2421-2436.
45. Gao, Y.; Shi, J. F.; Yuan, D.; Xu, B., Imaging enzyme-triggered self-assembly of small molecules inside live cells. *Nat Commun* **2012**, *3*.
46. Wang, H. M.; Feng, Z. Q. Q.; Del Signore, S. J.; Rodal, A. A.; Xu, B., Active Probes for Imaging Membrane Dynamics of Live Cells with High Spatial and Temporal Resolution over Extended Time Scales and Areas. *J Am Chem Soc* **2018**, *140* (10), 3505-3509.
47. Tanaka, A.; Fukuoka, Y.; Morimoto, Y.; Honjo, T.; Koda, D.; Goto, M.; Maruyama, T., Cancer Cell Death Induced by the Intracellular Self-Assembly of an Enzyme-Responsive Supramolecular Gelator. *J Am Chem Soc* **2015**, *137* (2), 770-775.
48. Smith, A. M.; Williams, R. J.; Tang, C.; Coppo, P.; Collins, R. F.; Turner, M. L.; Saiani, A.; Ulijn, R. V., Fmoc-Diphenylalanine self assembles to a hydrogel via a novel architecture based on pi-pi interlocked beta-sheets. *Advanced materials* **2008**, *20* (1), 37-+.
49. Moore, A. N.; Hartgerink, J. D., Self-Assembling Multidomain Peptide Nanofibers for Delivery of Bioactive Molecules and Tissue Regeneration. *Accounts Chem Res* **2017**, *50* (4), 714-722.
50. Zhan, H. N.; Lowik, D. W. P. M., A Hybrid Peptide Amphiphile Fiber PEG Hydrogel Matrix for 3D Cell Culture. *Adv Funct Mater* **2019**, *29* (16).
51. Hainline, K. M.; Gu, F. Q.; Handley, J. F.; Tian, Y. F.; Wu, Y. Y.; de Wet, L.; Vander Griend, D. J.; Collier, J. H., Self-Assembling Peptide Gels for 3D Prostate Cancer Spheroid Culture. *Macromol Biosci* **2019**, *19* (1).
52. Lam, S. J.; O'Brien-Simpson, N. M.; Pantarat, N.; Sulistio, A.; Wong, E. H. H.; Chen, Y. Y.; Lenzo, J. C.; Holden, J. A.; Blencowe, A.; Reynolds, E. C.; Qiao, G. G., Combating multidrug-resistant Gram-negative bacteria with structurally nanoengineered antimicrobial peptide polymers. *Nat Microbiol* **2016**, *1* (11).
53. Goto, C.; Hirano, M.; Hayashi, K.; Kikuchi, Y.; Hara-Kudo, Y.; Misawa, T.; Demizu, Y., Development of Amphipathic Antimicrobial Peptide Foldamers Based on Magainin 2 Sequence. *Chemmedchem* **2019**, *14* (22), 1911-1916.
54. Sahoo, J. K.; Roy, S.; Javid, N.; Duncan, K.; Aitken, L.; Ulijn, R. V., Pathway-dependent gold nanoparticle formation by biocatalytic self-assembly. *Nanoscale* **2017**, *9* (34),

12330-12334.
55. Mazza, M.; Hadjidemetriou, M.; de Lazaro, I.; Bussy, C.; Kostarelos, K., Peptide Nanofiber Complexes with siRNA for Deep Brain Gene Silencing by Stereotactic Neurosurgery. *ACS nano* **2015**, *9* (2), 1137-1149.
56. Luginbuhl, K. M.; Mozhdehi, D.; Dzuricky, M.; Yousefpour, P.; Huang, F. C.; Mayne, N. R.; Buehne, K. L.; Chilkoti, A., Recombinant Synthesis of Hybrid Lipid-Peptide Polymer Fusions that Self-Assemble and Encapsulate Hydrophobic Drugs. *Angew Chem Int Edit* **2017**, *56* (45), 13979-13984.
57. Pickart, L.; Vasquez-Soltero, J. M.; Margolina, A., GHK Peptide as a Natural Modulator of Multiple Cellular Pathways in Skin Regeneration. *Biomed Res Int* **2015**.
58. Robinson, L. R.; Fitzgerald, N. C.; Doughty, D. G.; Dawes, N. C.; Berge, C. A.; Bissett, D. L., Topical palmitoyl pentapeptide provides improvement in photoaged human facial skin. *International journal of cosmetic science* **2005**, *27* (3), 155-60.

Chapter III

1. Katoh, K.; Hammar, K.; Smith, P. J. S.; Oldenbourg, R., Birefringence imaging directly reveals architectural dynamics of filamentous actin in living growth cones. *Mol Biol Cell* **1999,** *10* (1), 197-210.
2. (a) Katta, P.; Alessandro, M.; Ramsier, R. D.; Chase, G. G., Continuous electrospinning of aligned polymer nanofibers onto a wire drum collector. *Nano Lett* **2004,** *4* (11), 2215-2218; (b) Pan, H.; Li, L. M.; Hu, L.; Cui, X. J., Continuous aligned polymer fibers produced by a modified electrospinning method. *Polymer* **2006,** *47* (14), 4901-4904.
3. (a) Cao, H.; Yuan, Q. Z.; Zhu, X. F.; Zhao, Y. P.; Liu, M. H., Hierarchical Self-Assembly of Achiral Amino Acid Derivatives into Dendritic Chiral Nanotwists. *Langmuir* **2012,** *28* (43), 15410-15417; (b) Zhang, S. M.; Greenfield, M. A.; Mata, A.; Palmer, L. C.; Bitton, R.; Mantei, J. R.; Aparicio, C.; de la Cruz, M. O.; Stupp, S. I., A self-assembly pathway to aligned monodomain gels. *Nat Mater* **2010,** *9* (7), 594-601.
4. Whitesides, G. M.; Mathias, J. P.; Seto, C. T., Molecular Self-Assembly and Nanochemistry - a Chemical Strategy for the Synthesis of Nanostructures. *Science* **1991,** *254* (5036), 1312-1319.
5. Fredy, J. W.; Mendez-Ardoy, A.; Kwangmettatam, S.; Bochicchio, D.; Matt, B.; Stuart, M. C. A.; Huskens, J.; Katsonis, N.; Pavan, G. M.; Kudernac, T., Molecular photoswitches mediating the strain-driven disassembly of supramolecular tubules. *P Natl Acad Sci USA* **2017,** *114* (45), 11850-11855.
6. (a) Ariga, K.; Ji, Q. M.; Nakanishi, W.; Hill, J. P.; Aono, M., Nanoarchitectonics: a new materials horizon for nanotechnology. *Mater Horiz* **2015,** *2* (4), 406-413; (b) Mendez-Ardoy, A. M.; Granja, J. R.; Montenegro, J., pH-Triggered self-assembly and hydrogelation of cyclic peptide nanotubes confined in water micro-droplets. *Nanoscale Horiz* **2018,** *3* (4), 391-396; (c) Fang, P. A.; Conway, J. F.; Margolis, H. C.; Simmer, J. P.; Beniash, E., Hierarchical self-assembly of amelogenin and the regulation of biomineralization at the nanoscale. *P Natl Acad Sci USA* **2011,** *108* (34), 14097-14102.
7. (a) Du, X. W.; Zhou, J.; Shi, J. F.; Xu, B., Supramolecular Hydrogelators and Hydrogels: From Soft Matter to Molecular Biomaterials. *Chem Rev* **2015,** *115* (24), 13165-13307; (b) Shang, Y. N.; Zhi, D. K.; Feng, G. W.; Wang, Z. Y.; Mao, D.; Guo, S.; Liu, R. H.; Liu, L. L.; Zhang, S. H.; Sun, S. H.; Wang, K.; Kong, D. L.; Gao, J.; Yang, Z. M., Supramolecular Nanofibers with Superior Bioactivity to Insulin-Like Growth Factor-I. *Nano Lett* **2019,** *19* (3), 1560-1569.
8. Zhang, Y.; Kuang, Y.; Gao, Y. A.; Xu, B., Versatile Small-Molecule Motifs for Self-Assembly in Water and the Formation of Biofunctional Supramolecular Hydrogels.

Langmuir **2011,** *27* (2), 529-537.
9. Tang, J. X.; Janmey, P. A., The polyelectrolyte nature of F-actin and the mechanism of actin bundle formation. *J Biol Chem* **1996,** *271* (15), 8556-8563.
10. Li, G. Y.; Sasaki, T.; Asahina, S.; Roy, M. C.; Mochizuki, T.; Koizumi, K.; Zhang, Y., Patching of Lipid Rafts by Molecular Self-Assembled Nanofibrils Suppresses Cancer Cell Migration. *Chem-Us* **2017,** *2* (2), 283-298.
11. De, S.; Groaz, E.; Margamuljana, L.; Abramov, M.; Marliere, P.; Herdewijn, P., Sulfonate derived phosphoramidates as active intermediates in the enzymatic primer-extension of DNA. *Org Biomol Chem* **2015,** *13* (13), 3950-3962.
12. Hansen, S. H.; Andersen, M. L.; Cornett, C.; Gradinaru, R.; Grunnet, N., A role for taurine in mitochondrial function. *J Biomed Sci* **2010,** *17*.
13. Fatayer, S.; Albrecht, F.; Zhang, Y. L.; Urbonas, D.; Pena, D.; Moll, N.; Gross, L., Molecular structure elucidation with charge-state control. *Science* **2019,** *365* (6449), 142-+.
14. Hall, M. S.; Alisafaei, F.; Ban, E.; Feng, X. Z.; Hui, C. Y.; Shenoy, V. B.; Wu, M. M., Fibrous nonlinear elasticity enables positive mechanical feedback between cells and ECMs. *P Natl Acad Sci USA* **2016,** *113* (49), 14043-14048.
15. Frederix, P. W. J. M.; Ide, J.; Altay, Y.; Schaeffer, G.; Surin, M.; Beljonne, D.; Bondarenko, A. S.; Jansen, T. L. C.; Otto, S.; Marrink, S. J., Structural and Spectroscopic Properties of Assemblies of Self-Replicating Peptide Macrocycles. *Acs Nano* **2017,** *11* (8), 7858-7868.
16. Huang, Z.; Lee, H.; Lee, E.; Kang, S. K.; Nam, J. M.; Lee, M., Responsive nematic gels from the self-assembly of aqueous nanofibres. *Nat Commun* **2011,** *2*.
17. (a) Zhou, J.; Du, X. W.; Gao, Y.; Shi, J. F.; Xu, B., Aromatic-Aromatic Interactions Enhance Interfiber Contacts for Enzymatic Formation of a Spontaneously Aligned Supramolecular Hydrogel. *J Am Chem Soc* **2014,** *136* (8), 2970-2973; (b) Zhao, F.; Gao, Y. A.; Shi, J. F.; Browdy, H. M.; Xu, B., Novel Anisotropic Supramolecular Hydrogel with High Stability over a Wide pH Range. *Langmuir* **2011,** *27* (4), 1510-1512.
18. Le Clainche, C.; Carlier, M. F., Regulation of actin assembly associated with protrusion and adhesion in cell migration. *Physiol Rev* **2008,** *88* (2), 489-513.
19. (a) Gu, Z. X.; Kothary, P.; Sun, C. H.; Gari, A.; Zhang, Y. F.; Taylor, C.; Jiang, P., Evaporation-Induced Hierarchical Assembly of Rigid Silicon Nanopillars Fabricated by a Scalable Two-Level Colloidal Lithography Approach. *Acs Appl Mater Inter* **2019,** *11* (43), 40461-40469; (b) Insua, I.; Montenegro, J., 1D to 2D Self Assembly of Cyclic Peptides. *J Am Chem Soc* **2020,** *142* (1), 300-307; (c) Paik, T.; Yun, H.; Fleury, B.; Hong, S. H.; Jo, P. S.; Wu, Y. T.; Oh, S. J.; Cargnello, M.; Yang, H.; Murray, C. B.; Kagan, C. R., Hierarchical Materials Design by Pattern Transfer Printing of Self-Assembled Binary Nanocrystal Superlattices. *Nano Lett* **2017,** *17* (3), 1387-1394; (d) Wang, Y. L.; Xia, Y. N., Bottom-up and top-down approaches to the synthesis of monodispersed spherical colloids of low melting-point metals. *Nano Lett* **2004,** *4* (10), 2047-2050.
20. Cherpak, V.; Korolovych, V. F.; Geryak, R.; Turiv, T.; Nepal, D.; Kelly, J.; Bunning, T. J.; Lavrentovich, O. D.; Heller, W. T.; Tsukruk, V. V., Robust Chiral Organization of Cellulose Nanocrystals in Capillary Confinement. *Nano Lett* **2018,** *18* (11), 6770-6777.
21. (a) Kato, T.; Hirai, Y.; Nakaso, S.; Moriyama, M., Liquid-crystalline physical gels. *Chem Soc Rev* **2007,** *36* (12), 1857-1867; (b) Kato, T.; Kutsuna, T.; Yabuuchi, K.; Mizoshita, N., Anisotropic self-aggregation of an anthracene derivative: Formation of liquid-crystalline physical gels in oriented states. *Langmuir* **2002,** *18* (18), 7086-7088; (c) Mizoshita, N.; Hanabusa, K.; Kato, T., Self-aggregation of an amino acid derivative as a route to liquid-crystalline physical gels - Faster response to electric fields. *Adv Mater* **1999,** *11* (5), 392-394; (d) Yabuuchi, K.; Rowan, A. E.; Nolte, R. J. M.; Kato, T., Liquid-

crystalline physical gels: Self-aggregation of a gluconamide derivative in mesogenic molecules for the formation of anisotropic functional composites. *Chem Mater* **2000,** *12* (2), 440-443.
22. Tadepalli, S.; Slocik, J. M.; Gupta, M. K.; Naik, R. R.; Singamaneni, S., Bio-Optics and Bio-Inspired Optical Materials. *Chem Rev* **2017,** *117* (20), 12705-12763.
23. Wang, Y. J.; Shang, S. H.; Li, C. Z., Aligned Biomimetic Scaffolds as a New Tendency in Tissue Engineering. *Curr Stem Cell Res T* **2016,** *11* (1), 3-18.

Chapter IV.1

1. Whitesides, G. M.; Mathias, J. P.; Seto, C. T., Molecular Self-Assembly and Nanochemistry - a Chemical Strategy for the Synthesis of Nanostructures. *Science* **1991,** *254* (5036), 1312-1319.
2. (a) Pappas, C. G.; Shafi, R.; Sasselli, I. R.; Siccardi, H.; Wang, T.; Narang, V.; Abzalimov, R.; Wijerathne, N.; Ulijn, R. V., Dynamic peptide libraries for the discovery of supramolecular nanomaterials. *Nat Nanotechnol* **2016,** *11* (11), 960-967; (b) Capito, R. M.; Azevedo, H. S.; Velichko, Y. S.; Mata, A.; Stupp, S. I., Self-assembly of large and small molecules into hierarchically ordered sacs and membranes. *Science* **2008,** *319* (5871), 1812-1816; (c) Du, X. W.; Zhou, J.; Shi, J. F.; Xu, B., Supramolecular Hydrogelators and Hydrogels: From Soft Matter to Molecular Biomaterials. *Chem Rev* **2015,** *115* (24), 13165-13307.
3. Murugan, A.; Zou, J.; Brenner, M. P., Undesired usage and the robust self-assembly of heterogeneous structures. *Nat Commun* **2015,** *6*.
4. (a) Ke, Y. G.; Ong, L. L.; Shih, W. M.; Yin, P., Three-Dimensional Structures Self-Assembled from DNA Bricks. *Science* **2012,** *338* (6111), 1177-1183; (b) Mirkin, C. A.; Letsinger, R. L.; Mucic, R. C.; Storhoff, J. J., A DNA-based method for rationally assembling nanoparticles into macroscopic materials. *Nature* **1996,** *382* (6592), 607-609; (c) Seeman, N. C., Nucleic-Acid Junctions and Lattices. *J Theor Biol* **1982,** *99* (2), 237-247; (d) Wei, B.; Dai, M. J.; Yin, P., Complex shapes self-assembled from single-stranded DNA tiles. *Nature* **2012,** *485* (7400), 623-+.
5. Groschel, A. H.; Muller, A. H. E., Self-assembly concepts for multicompartment nanostructures. *Nanoscale* **2015,** *7* (28), 11841-11876.
6. (a) Tantakitti, F.; Boekhoven, J.; Wang, X.; Kazantsev, R. V.; Yu, T.; Li, J. H.; Zhuang, E.; Zandi, R.; Ortony, J. H.; Newcomb, C. J.; Palmer, L. C.; Shekhawat, G. S.; de la Cruz, M. O.; Schatz, G. C.; Stupp, S. I., Energy landscapes and functions of supramolecular systems. *Nat Mater* **2016,** *15* (4), 469-+; (b) Williams, R. J.; Smith, A. M.; Collins, R.; Hodson, N.; Das, A. K.; Ulijn, R. V., Enzyme-assisted self-assembly under thermodynamic control. *Nat Nanotechnol* **2009,** *4* (1), 19-24.
7. (a) Tang, C.; Smith, A. M.; Collins, R. F.; Ulijn, R. V.; Saiani, A., Fmoc-diphenylalanine self-assembly mechanism induces apparent pKa shifts. *Langmuir : the ACS journal of surfaces and colloids* **2009,** *25* (16), 9447-53; (b) Smith, A. M.; Williams, R. J.; Tang, C.; Coppo, P.; Collins, R. F.; Turner, M. L.; Saiani, A.; Ulijn, R. V., Fmoc-Diphenylalanine self assembles to a hydrogel via a novel architecture based on pi-pi interlocked beta-sheets. *Adv Mater* **2008,** *20* (1), 37-+; (c) Raeburn, J.; McDonald, T. O.; Adams, D. J., Dipeptide hydrogelation triggered via ultraviolet light. *Chem Commun* **2012,** *48* (75), 9355-9357; (d) Tao, K.; Levin, A.; Adler-Abramovich, L.; Gazit, E., Fmoc-modified amino acids and short peptides: simple bio-inspired building blocks for the fabrication of functional materials. *Chem Soc Rev* **2016,** *45* (14), 3935-3953.
8. (a) Lin, Q. N.; Bao, C. Y.; Cheng, S. Y.; Yang, Y. L.; Ji, W.; Zhu, L. Y., Target-Activated Coumarin Phototriggers Specifically Switch on Fluorescence and Photocleavage upon

Bonding to Thiol-Bearing Protein. *J Am Chem Soc* **2012,** *134* (11), 5052-5055; (b) Yoshii, T.; Ikeda, M.; Hamachi, I., Two-Photon-Responsive Supramolecular Hydrogel for Controlling Materials Motion in Micrometer Space. *Angew Chem Int Edit* **2014,** *53* (28), 7264-7267; (c) Ji, X. F.; Shi, B. B.; Wang, H.; Xia, D. Y.; Jie, K. C.; Wu, Z. L.; Huang, F. H., Supramolecular Construction of Multifluorescent Gels: Interfacial Assembly of Discrete Fluorescent Gels through Multiple Hydrogen Bonding. *Adv Mater* **2015,** *27* (48), 8062-8066.

9. (a) Schmidt, R.; Geissler, D.; Hagen, V.; Bendig, J., Mechanism of photocleavage of (coumarin-4-yl)methyl esters. *J Phys Chem A* **2007,** *111* (26), 5768-5774; (b) Geissler, D.; Antonenko, Y. N.; Schmidt, R.; Keller, S.; Krylova, O. O.; Wiesner, B.; Bendig, J.; Pohl, P.; Hagen, V., (Coumarin-4-yl)methyl esters as highly efficient, ultrafast phototriggers for protons and their application to acidifying membrane surfaces. *Angew Chem Int Edit* **2005,** *44* (8), 1195-1198.
10. Raeburn, J.; Mendoza-Cuenca, C.; Cattoz, B. N.; Little, M. A.; Terry, A. E.; Cardoso, A. Z.; Griffiths, P. C.; Adams, D. J., The effect of solvent choice on the gelation and final hydrogel properties of Fmoc-diphenylalanine. *Soft Matter* **2015,** *11* (5), 927-935.
11. (a) Ji, W.; Liu, G. F.; Wang, F.; Zhub, Z.; Feng, C. L., Galactose-decorated light-responsive hydrogelator precursors for selectively killing cancer cells. *Chem Commun* **2016,** *52* (85), 12574-12577; (b) Ji, W.; Liu, G. F.; Li, Z. J.; Feng, C. L., Influence of C-H ⋯O Hydrogen Bonds on Macroscopic Properties of Supramolecular Assembly. *Acs Appl Mater Inter* **2016,** *8* (8), 5188-5195.
12. Onogi, S.; Shigemitsu, H.; Yoshii, T.; Tanida, T.; Ikeda, M.; Kubota, R.; Hamachi, I., In situ real-time imaging of self-sorted supramolecular nanofibres. *Nat Chem* **2016,** *8* (8), 743-752.
13. Ghosh, A.; Haverick, M.; Stump, K.; Yang, X. Y.; Tweedle, M. F.; Goldberger, J. E., Fine-Tuning the pH Trigger of Self-Assembly. *J Am Chem Soc* **2012,** *134* (8), 3647-3650.
14. Menzel, A. M., Tuned, driven, and active soft matter. *Phys Rep* **2015,** *554*, 1-45.
15. (a) Chen, H.; Yao, X. Y.; Ma, X.; Tian, H., Amorphous, Efficient, Room-Temperature Phosphorescent Metal-Free Polymers and Their Applications as Encryption Ink. *Adv Opt Mater* **2016,** *4* (9), 1397-1401; (b) Sun, H. L.; Chen, Y.; Zhao, J.; Liu, Y., Photocontrolled Reversible Conversion of Nanotube and Nanoparticle Mediated by -Cyclodextrin Dimers. *Angew Chem Int Edit* **2015,** *54* (32), 9376-9380; (c) Yamauchi, M.; Ohba, T.; Karatsu, T.; Yagai, S., Photoreactive helical nanoaggregates exhibiting morphology transition on thermal reconstruction. *Nat Commun* **2015,** *6*.

Chapter IV.2

1. (a) Cheng, J. Y.; Mayes, A. M.; Ross, C. A., Nanostructure engineering by templated self-assembly of block copolymers. *Nat Mater* **2004,** *3* (11), 823-828; (b) Gazit, E., Self-assembled peptide nanostructures: the design of molecular building blocks and their technological utilization. *Chem Soc Rev* **2007,** *36* (8), 1263-1269; (c) Whitesides, G. M.; Boncheva, M., Beyond molecules: Self-assembly of mesoscopic and macroscopic components. *P Natl Acad Sci USA* **2002,** *99* (8), 4769-4774; (d) Whitesides, G. M.; Mathias, J. P.; Seto, C. T., Molecular Self-Assembly and Nanochemistry - a Chemical Strategy for the Synthesis of Nanostructures. *Science* **1991,** *254* (5036), 1312-1319; (e) Yan, X. H.; Zhu, P. L.; Li, J. B., Self-assembly and application of diphenylalanine-based nanostructures. *Chem Soc Rev* **2010,** *39* (6), 1877-1890.
2. Groschel, A. H.; Muller, A. H. E., Self-assembly concepts for multicompartment nanostructures. *Nanoscale* **2015,** *7* (28), 11841-11876.

3. (a) Bowden, N.; Choi, I. S.; Grzybowski, B. A.; Whitesides, G. M., Mesoscale self-assembly of hexagonal plates using lateral capillary forces: Synthesis using the "capillary bond". *J Am Chem Soc* **1999,** *121* (23), 5373-5391; (b) Bowden, N.; Oliver, S. R. J.; Whitesides, G. M., Mesoscale self-assembly: Capillary bonds and negative menisci. *J Phys Chem B* **2000,** *104* (12), 2714-2724; (c) Bowden, N. B.; Weck, M.; Choi, I. S.; Whitesides, G. M., Molecule-mimetic chemistry and mesoscale self-assembly. *Accounts Chem Res* **2001,** *34* (3), 231-238; (d) Colfen, H.; Mann, S., Higher-order organization by mesoscale self-assembly and transformation of hybrid nanostructures. *Angew Chem Int Edit* **2003,** *42* (21), 2350-2365; (e) Choi, S. W.; Jo, S. M.; Lee, W. S.; Kim, Y. R., An electrospun poly(vinylidene fluoride) nanofibrous membrane and its battery applications. *Adv Mater* **2003,** *15* (23), 2027-2032; (f) Semerdzhiev, S. A.; Dekker, D. R.; Subramaniam, V.; Claessens, M. M. A. E., Self-Assembly of Protein Fibrils into Suprafibrillar Aggregates: Bridging the Nano- and Mesoscale. *Acs Nano* **2014,** *8* (6), 5543-5551.
4. Sear, R. P.; Pagonabarraga, I.; Flaus, A., Life at the mesoscale: the self-organised cytoplasm and nucleoplasm. *Bmc Biophys* **2015,** *8*.
5. (a) Gattazzo, F.; Urciuolo, A.; Bonaldo, P., Extracellular matrix: A dynamic microenvironment for stem cell niche. *Bba-Gen Subjects* **2014,** *1840* (8), 2506-2519; (b) Frantz, C.; Stewart, K. M.; Weaver, V. M., The extracellular matrix at a glance. *J Cell Sci* **2010,** *123* (24), 4195-4200; (c) Kim, S. H.; Turnbull, J.; Guimond, S., Extracellular matrix and cell signalling: the dynamic cooperation of integrin, proteoglycan and growth factor receptor. *J Endocrinol* **2011,** *209* (2), 139-151.
6. (a) Pandurangan, K.; Kitchen, J. A.; Blasco, S.; Boyle, E. M.; Fitzpatrick, B.; Feeney, M.; Kruger, P. E.; Gunnlaugsson, T., Unexpected Self-Sorting Self-Assembly Formation of a [4:4] Sulfate: Ligand Cage from a Preorganized Tripodal Urea Ligand. *Angew Chem Int Edit* **2015,** *54* (15), 4566-4570; (b) Morris, K. L.; Chen, L.; Raeburn, J.; Sellick, O. R.; Cotanda, P.; Paul, A.; Griffiths, P. C.; King, S. M.; O'Reilly, R. K.; Serpell, L. C.; Adams, D. J., Chemically programmed self-sorting of gelator networks. *Nat Commun* **2013,** *4*; (c) Draper, E. R.; Dietrich, B.; Adams, D. J., Self-assembly, self-sorting, and electronic properties of a diketopyrrolopyrrole hydrogelator. *Chem Commun* **2017,** *53* (11), 1868-1871; (d) Draper, E. R.; Adams, D. J., SUPRAMOLECULAR FIBRES Self-sorting shows its true colours. *Nat Chem* **2016,** *8* (8), 737-738; (e) Onogi, S.; Shigemitsu, H.; Yoshii, T.; Tanida, T.; Ikeda, M.; Kubota, R.; Hamachi, I., In situ real-time imaging of self-sorted supramolecular nanofibres. *Nat Chem* **2016,** *8* (8), 743-752; (f) Smith, M. M.; Smith, D. K., Self-sorting multi-gelator gels-mixing and ageing effects in thermally addressable supramolecular soft nanomaterials. *Soft Matter* **2011,** *7* (10), 4856-4860; (g) Cornwell, D. J.; Daubney, O. J.; Smith, D. K., Photopatterned Multidomain Gels: Multi-Component Self-Assembled Hydrogels Based on Partially Self-Sorting 1,3:2,4-Dibenzylidene-D-sorbitol Derivatives. *J Am Chem Soc* **2015,** *137* (49), 15486-15492; (h) Wang, F.; Han, C. Y.; He, C. L.; Zhou, Q. Z.; Zhang, J. Q.; Wang, C.; Li, N.; Huang, F. H., Self-sorting organization of two heteroditopic monomers to supramolecular alternating copolymers. *J Am Chem Soc* **2008,** *130* (34), 11254-+; (i) Safont-Sempere, M. M.; Fernandez, G.; Wurthner, F., Self-Sorting Phenomena in Complex Supramolecular Systems. *Chem Rev* **2011,** *111* (9), 5784-5814; (j) Jiang, W.; Schalley, C. A., Integrative self-sorting is a programming language for high level self-assembly. *P Natl Acad Sci USA* **2009,** *106* (26), 10425-10429; (k) He, Z. F.; Jiang, W.; Schalley, C. A., Integrative self-sorting: a versatile strategy for the construction of complex supramolecular architecture. *Chem Soc Rev* **2015,** *44* (3), 779-789; (l) Yan, L. L.; Tan, C. H.; Zhang, G. L.; Zhou, L. P.; Bunzli, J. C.; Sun, Q. F., Stereocontrolled Self-Assembly and Self-Sorting of Luminescent Europium Tetrahedral Cages. *J Am Chem Soc* **2015,** *137* (26), 8550-8555.

7. (a) Ji, W.; Liu, G. F.; Li, Z. J.; Feng, C. L., Influence of C-H center dot center dot center dot O Hydrogen Bonds on Macroscopic Properties of Supramolecular Assembly. *Acs Appl Mater Inter* **2016,** *8* (8), 5188-5195; (b) Ji, W.; Zhang, S. J.; Filonenko, G. A.; Li, G. Y.; Sasaki, T.; Feng, C. L.; Zhang, Y., Co-organizing synthesis of heterogeneous nanostructures through the photo-cleavage of pre-stabilized self-assemblies. *Chem Commun* **2017,** *53* (34), 4702-4705; (c) Ji, W.; Li, L. L.; Eniola-Adefeso, O.; Wang, Y. M.; Liu, C. T.; Feng, C. L., Non-invasively visualizing cell-matrix interactions in two-photon excited supramolecular hydrogels. *J Mater Chem B* **2017,** *5* (38), 7790-7795.
8. (a) Geissler, D.; Antonenko, Y. N.; Schmidt, R.; Keller, S.; Krylova, O. O.; Wiesner, B.; Bendig, J.; Pohl, P.; Hagen, V., (Coumarin-4-yl)methyl esters as highly efficient, ultrafast phototriggers for protons and their application to acidifying membrane surfaces. *Angew Chem Int Edit* **2005,** *44* (8), 1195-1198; (b) Schmidt, R.; Geissler, D.; Hagen, V.; Bendig, J., Mechanism of photocleavage of (coumarin-4-yl)methyl esters. *J Phys Chem A* **2007,** *111* (26), 5768-5774; (c) Lin, Q. N.; Bao, C. Y.; Cheng, S. Y.; Yang, Y. L.; Ji, W.; Zhu, L. Y., Target-Activated Coumarin Phototriggers Specifically Switch on Fluorescence and Photocleavage upon Bonding to Thiol-Bearing Protein. *J Am Chem Soc* **2012,** *134* (11), 5052-5055; (d) Lin, Q. N.; Huang, Q.; Li, C. Y.; Bao, C. Y.; Liu, Z. Z.; Li, F. Y.; Zhu, L. Y., Anticancer Drug Release from a Mesoporous Silica Based Nanophotocage Regulated by Either a One- or Two-Photon Process. *J Am Chem Soc* **2010,** *132* (31), 10645-10647; (e) Yoshii, T.; Ikeda, M.; Hamachi, I., Two-Photon-Responsive Supramolecular Hydrogel for Controlling Materials Motion in Micrometer Space. *Angew Chem Int Edit* **2014,** *53* (28), 7264-7267; (f) Ji, W.; Liu, G. F.; Wang, F.; Zhub, Z.; Feng, C. L., Galactose-decorated light-responsive hydrogelator precursors for selectively killing cancer cells. *Chem Commun* **2016,** *52* (85), 12574-12577.
9. (a) Smith, A. M.; Williams, R. J.; Tang, C.; Coppo, P.; Collins, R. F.; Turner, M. L.; Saiani, A.; Ulijn, R. V., Fmoc-Diphenylalanine self assembles to a hydrogel via a novel architecture based on pi-pi interlocked beta-sheets. *Adv Mater* **2008,** *20* (1), 37-+; (b) Raeburn, J.; McDonald, T. O.; Adams, D. J., Dipeptide hydrogelation triggered via ultraviolet light. *Chem Commun* **2012,** *48* (75), 9355-9357; (c) Tao, K.; Levin, A.; Adler-Abramovich, L.; Gazit, E., Fmoc-modified amino acids and short peptides: simple bio-inspired building blocks for the fabrication of functional materials. *Chem Soc Rev* **2016,** *45* (14), 3935-3953; (d) Tang, C.; Smith, A. M.; Collins, R. F.; Ulijn, R. V.; Saiani, A., Fmoc-diphenylalanine self-assembly mechanism induces apparent pKa shifts. *Langmuir : the ACS journal of surfaces and colloids* **2009,** *25* (16), 9447-53; (e) Fu, M. F.; Li, Q.; Sun, B. B.; Yang, Y.; Dai, L. R.; Nylander, T.; Li, J. B., Disassembly of Dipeptide Single Crystals Can Transform the Lipid Membrane into a Network. *Acs Nano* **2017,** *11* (7), 7349-7354; (f) Eisfeld, A.; Briggs, J. S., The J- and H-bands of organic dye aggregates. *Chem Phys* **2006,** *324* (2-3), 376-384.
10. Bairi, P.; Minami, K.; Hill, J. P.; Nakanishi, W.; Shrestha, L. K.; Liu, C.; Harano, K.; Nakamura, E.; Ariga, K., Supramolecular Differentiation for Construction of Anisotropic Fullerene Nanostructures by Time-Programmed Control of Interfacial Growth. *Acs Nano* **2016,** *10* (9), 8796-8802.
11. (a) Wang, H. M.; Feng, Z. Q. Q.; Lu, A.; Jiang, Y. J.; Wu, H.; Xu, B., Instant Hydrogelation Inspired by Inflammasomes. *Angew Chem Int Edit* **2017,** *56* (26), 7579-7583; (b) Zhou, J.; Du, X. W.; Berciu, C.; He, H. J.; Shi, J. F.; Nicastro, D.; Xu, B., Enzyme-Instructed Self-Assembly for Spatiotemporal Profiling of the Activities of Alkaline Phosphatases on Live Cells. *Chem-Us* **2016,** *1* (2); (c) Zhou, J.; Du, X. W.; Yamagata, N.; Xu, B., Enzyme-Instructed Self-Assembly of Small D-Peptides as a Multiple-Step Process for Selectively Killing Cancer Cells. *J Am Chem Soc* **2016,** *138* (11), 3813-3823; (d) Li, G. Y.; Sasaki, T.; Asahina, S.; Roy, M. C.; Mochizuki, T.; Koizumi, K.; Zhang, Y., Patching of Lipid Rafts

by Molecular Self-Assembled Nanofibrils Suppresses Cancer Cell Migration. *Chem-Us* **2017,** *2* (2), 283-298.
12.(a) Aono, M.; Ariga, K., The Way to Nanoarchitectonics and the Way of Nanoarchitectonics. *Adv Mater* **2016,** *28* (6), 989-992; (b) Komiyama, M.; Yoshimoto, K.; Sisido, M.; Ariga, K., Chemistry Can Make Strict and Fuzzy Controls for Bio-Systems: DNA Nanoarchitectonics and Cell-Macromolecular Nanoarchitectonics. *B Chem Soc Jpn* **2017,** *90* (9), 967-1004.

Chapter IV.3

1. Wolf, Y. I.; Katsnelson, M. I.; Koonin, E. V., Physical foundations of biological complexity. *P Natl Acad Sci USA* **2018,** *115* (37), E8678-E8687.
2. (a) Gerbelli, B. B.; Vassiliades, S. V.; Rojas, J. E. U.; Pelin, J. N. B. D.; Mancini, R. S. N.; Pereira, W. S. G.; Aguilar, A. M.; Venanzi, M.; Cavalieri, F.; Giuntini, F.; Alves, W. A., Hierarchical Self-Assembly of Peptides and its Applications in Bionanotechnology. *Macromol Chem Phys* **2019,** *220* (14); (b) Whitelam, S., Hierarchical assembly may be a way to make large information-rich structures. *Soft Matter* **2015,** *11* (42), 8225-8235.
3. Chen, L. J.; Yang, H. B., Construction of Stimuli-Responsive Functional Materials via Hierarchical Self-Assembly Involving Coordination Interactions. *Accounts Chem Res* **2018,** *51* (11), 2699-2710.
4. (a) Amabilino, D. B.; Ashton, P. R.; Boyd, S. E.; Lee, J. Y.; Menzer, S.; Stoddart, J. F.; Williams, D. J., The five-stage self-assembly of a branched heptacatenane. *Angew Chem Int Edit* **1997,** *36* (19), 2070-2072; (b) Huo, G. F.; Shi, X. L.; Tu, Q.; Hu, Y. X.; Wu, G. Y.; Yin, G. Q.; Li, X. P.; Xu, L.; Ding, H. M.; Yang, H. B., Radical-Induced Hierarchical Self-Assembly Involving Supramolecular Coordination Complexes in Both Solution and Solid States. *J Am Chem Soc* **2019,** *141* (40), 16014-16023.
5. (a) Peng, H. Q.; Liu, B.; Wei, P. F.; Zhang, P. F.; Zhang, H. K.; Zhang, J. F.; Li, K.; Li, Y.; Cheng, Y. H.; Lam, J. W. Y.; Zhang, W. J.; Lee, C. S.; Tang, B. Z., Visualizing the Initial Step of Self-Assembly and the Phase Transition by Stereogenic Amphiphiles with Aggregation-Induced Emission. *Acs Nano* **2019,** *13* (1), 839-846; (b) Qiu, H. B.; Hudson, Z. M.; Winnik, M. A.; Manners, I., Multidimensional hierarchical self-assembly of amphiphilic cylindrical block comicelles. *Science* **2015,** *347* (6228), 1329-1332; (c) Shao, L.; Sun, J. F.; Hua, B.; Huang, F. H., An AIEE fluorescent supramolecular cross-linked polymer network based on pillar[5]arene host-guest recognition: construction and application in explosive detection. *Chem Commun* **2018,** *54* (38), 4866-4869; (d) Yan, X. Z.; Li, S. J.; Cook, T. R.; Ji, X. F.; Yao, Y.; Pollock, J. B.; Shi, Y. H.; Yu, G. C.; Li, J. Y.; Huang, F. H.; Stang, P. J., Hierarchical Self-Assembly: Well-Defined Supramolecular Nanostructures and Metallohydrogels via Amphiphilic Discrete Organoplatinum(II) Metallacycles. *J Am Chem Soc* **2013,** *135* (38), 14036-14039; (e) Zhuo, M. P.; Wu, J. J.; Wang, X. D.; Tao, Y. C.; Yuan, Y.; Liao, L. S., Hierarchical self-assembly of organic heterostructure nanowires. *Nat Commun* **2019,** *10*.
6. Morphew, D.; Chakrabarti, D., Programming hierarchical self-assembly of colloids: matching stability and accessibility. *Nanoscale* **2018,** *10* (29), 13875-13882.
7. Menger, F. M., Supramolecular chemistry and self-assembly. *P Natl Acad Sci USA* **2002,** *99* (8), 4818-4822.
8. (a) Feng, Z. Q. Q.; Han, X. G.; Wang, H. M.; Tang, T. T.; Xu, B., Enzyme-Instructed Peptide Assemblies Selectively Inhibit Bone Tumors. *Chem-Us* **2019,** *5* (9), 2442-2449; (b) Li, G. Y.; Sasaki, T.; Asahina, S.; Roy, M. C.; Mochizuki, T.; Koizumi, K.; Zhang, Y., Patching of Lipid Rafts by Molecular Self-Assembled Nanofibrils Suppresses Cancer Cell Migration. *Chem-Us* **2017,** *2* (2), 283-298; (c) Feng, Z. Q. Q.; Wang, H. M.; Chen, X. Y.;

Xu, B., Self-Assembling Ability Determines the Activity of Enzyme-Instructed Self-Assembly for Inhibiting Cancer Cells. *J Am Chem Soc* **2017,** *139* (43), 15377-15384; (d) Wang, H. M.; Feng, Z. Q. Q.; Xu, B., Bioinspired assembly of small molecules in cell milieu. *Chem Soc Rev* **2017,** *46* (9), 2421-2436; (e) Zhou, J.; Du, X. W.; Berciu, C.; He, H. J.; Shi, J. F.; Nicastro, D.; Xu, B., Enzyme-Instructed Self-Assembly for Spatiotemporal Profiling of the Activities of Alkaline Phosphatases on Live Cells. *Chem-Us* **2016,** *1* (2); (f) Zhou, J.; Du, X. W.; Yamagata, N.; Xu, B., Enzyme-Instructed Self-Assembly of Small D-Peptides as a Multiple-Step Process for Selectively Killing Cancer Cells. *J Am Chem Soc* **2016,** *138* (11), 3813-3823.

9. Zhang, S. J.; Hu, X. W.; Mang, D. Z.; Sasaki, T.; Zhang, Y., Self-delivery of N-hydroxylethyl peptide assemblies to the cytosol inducing endoplasmic reticulum dilation in cancer cells. *Chem Commun* **2019,** *55* (52), 7474-7477.
10. Du, X. W.; Zhou, J.; Shi, J. F.; Xu, B., Supramolecular Hydrogelators and Hydrogels: From Soft Matter to Molecular Biomaterials. *Chem Rev* **2015,** *115* (24), 13165-13307.
11. (a) Rao, S. R.; Snaith, A. E.; Marino, D.; Cheng, X.; Lwin, S. T.; Orriss, I. R.; Hamdy, F. C.; Edwards, C. M., Tumour-derived alkaline phosphatase regulates tumour growth, epithelial plasticity and disease-free survival in metastatic prostate cancer. *Brit J Cancer* **2017,** *116* (2), 227-236; (b) Xu, G.; Zhang, W. H.; Ma, M. K.; McLeod, H. L., Human carboxylesterase 2 is commonly expressed in tumor tissue and is correlated with activation of irinotecan. *Clin Cancer Res* **2002,** *8* (8), 2605-2611.
12. Matson, J. B.; Stupp, S. I., Self-assembling peptide scaffolds for regenerative medicine. *Chem Commun* **2012,** *48* (1), 26-33.
13. (a) Lin, Q. N.; Bao, C. Y.; Fan, G. S.; Cheng, S. Y.; Liu, H.; Liu, Z. Z.; Zhu, L. Y., 7-Amino coumarin based fluorescent phototriggers coupled with nano/bio-conjugated bonds: Synthesis, labeling and photorelease. *J Mater Chem* **2012,** *22* (14), 6680-6688; (b) Liu, X. G.; Cole, J. M.; Chow, P. C. Y.; Zhang, L.; Tan, Y. Z.; Zhao, T., Dye Aggregation and Complex Formation Effects in 7-(Diethylamino)-coumarin-3-carboxylic Acid. *J Phys Chem C* **2014,** *118* (24), 13042-13051.
14. (a) Anamelechi, C. C.; Clermont, E. E.; Brown, M. A.; Truskey, G. A.; Reichert, W. M., Streptavidin binding and endothelial cell adhesion to biotinylated fibronectin. *Langmuir* **2007,** *23* (25), 12583-12588; (b) Dou, X. Q.; Zhang, J.; Feng, C. L., Biotin-Avidin Based Universal Cell-Matrix Interaction for Promoting Three-Dimensional Cell Adhesion. *Acs Appl Mater Inter* **2015,** *7* (37), 20786-20792.
15. Liang, X.; Xu, X. Y.; Qiao, D.; Yin, Z.; Shang, L. Q., Dual Mechanism of an Intramolecular Charge Transfer (ICT)-FRET-Based Fluorescent Probe for the Selective Detection of Hydrogen Peroxide. *Chem-Asian J* **2017,** *12* (24), 3187-3194.
16. Nishizawa, S.; Kato, Y.; Teramae, N., Fluorescence sensing of anions via intramolecular excimer formation in a pyrophosphate-induced self-assembly of a pyrene-functionalized guanidinium receptor. *J Am Chem Soc* **1999,** *121* (40), 9463-9464.

Chapter V.1

1. Wu, H. X.; Carvalho, P.; Voeltz, G. K., Here, there, and everywhere: The importance of ER membrane contact sites. *Science* **2018**, *361* (6401), Cp15-U70.
2. Farooqi, A. A.; Li, K. T.; Fayyaz, S.; Chang, Y. T.; Ismail, M.; Liaw, C. C.; Yuan, S. S. F.; Tang, J. Y.; Chang, H. W., Anticancer drugs for the modulation of endoplasmic reticulum stress and oxidative stress. *Tumor Biol* **2015**, *36* (8), 5743-5752.
3. (a) Lane, B. P.; Lieber, C. S., Ultrastructural Alterations in Human Hepatocytes Following Ingestion of Ethanol with Adequate Diets. *Am J Pathol* **1966**, *49* (4), 593-&; (b) Howarth,

D. L.; Vacaru, A. M.; Tsedensodnom, O.; Mormone, E.; Nieto, N.; Costantini, L. M.; Snapp, E. L.; Sadler, K. C., Alcohol Disrupts Endoplasmic Reticulum Function and Protein Secretion in Hepatocytes. *Alcohol Clin Exp Res* **2012**, *36* (1), 14-23.
4. Qin, S. Y.; Zhang, A. Q.; Cheng, S. X.; Rong, L.; Zhang, X. Z., Drug self-delivery systems for cancer therapy. *Biomaterials* **2017**, *112*, 234-247.
5. (a) Laizure, S. C.; Herring, V.; Hu, Z. Y.; Witbrodt, K.; Parker, R. B., The Role of Human Carboxylesterases in Drug Metabolism: Have We Overlooked Their Importance? *Pharmacotherapy* **2013**, *33* (2), 210-222; (b) Williams, F. M., Clinical-Significance of Esterases in Man. *Clin Pharmacokinet* **1985**, *10* (5), 392-403; (c) Feng, Z. Q. Q.; Wang, H. M.; Zhou, R.; Li, J.; Xu, B., Enzyme-Instructed Assembly and Disassembly Processes for Targeting Downregulation in Cancer Cells. *J Am Chem Soc* **2017**, *139* (11), 3950-3953; (d) Yu, B. C.; Zheng, Y. Q.; Yuan, Z. N.; Li, S. S.; Zhu, H.; De la Cruz, L. K.; Zhang, J.; Ji, K. L.; Wang, S. M.; Wang, B. H., Toward Direct Protein S-Persulfidation: A Prodrug Approach That Directly Delivers Hydrogen Persulfide. *J Am Chem Soc* **2018**, *140* (1), 30-33.
6. Zhang, Y.; Kuang, Y.; Gao, Y. A.; Xu, B., Versatile Small-Molecule Motifs for Self-Assembly in Water and the Formation of Biofunctional Supramolecular Hydrogels. *Langmuir* **2011**, *27* (2), 529-537.
7. Liang, X.; Xu, X. Y.; Qiao, D.; Yin, Z.; Shang, L. Q., Dual Mechanism of an Intramolecular Charge Transfer (ICT)-FRET-Based Fluorescent Probe for the Selective Detection of Hydrogen Peroxide. *Chem-Asian J* **2017**, *12* (24), 3187-3194.
8. Li, J.; Kuang, Y.; Shi, J. F.; Zhou, J.; Medina, J. E.; Zhou, R.; Yuan, D.; Yang, C. H.; Wang, H. M.; Yang, Z. M.; Liu, J. F.; Dinulescu, D. M.; Xu, B., Enzyme-Instructed Intracellular Molecular Self-Assembly to Boost Activity of Cisplatin against Drug-Resistant Ovarian Cancer Cells. *Angew Chem Int Edit* **2015**, *54* (45), 13307-13311.
9. Fors, B. P.; Poelma, J. E.; Menyo, M. S.; Robb, M. J.; Spokoyny, D. M.; Kramer, J. W.; Waite, J. H.; Hawker, C. J., Fabrication of Unique Chemical Patterns and Concentration Gradients with Visible Light. *J Am Chem Soc* **2013**, *135* (38), 14106-14109.
10. Belu, A.; Schnitker, J.; Bertazzo, S.; Neumann, E.; Mayer, D.; Offenhausser, A.; Santoro, F., Ultra-thin resin embedding method for scanning electron microscopy of individual cells on high and low aspect ratio 3D nanostructures. *J Microsc-Oxford* **2016**, *263* (1), 78-86.
11. (a) Moriguchi, I.; Hirono, S.; Nakagome, I.; Hirano, H., Comparison of Reliability of Log-P Values for Drugs Calculated by Several Methods. *Chem Pharm Bull* **1994**, *42* (4), 976-978; (b) Arnott, J. A.; Planey, S. L., The influence of lipophilicity in drug discovery and design. *Expert opinion on drug discovery* **2012**, *7* (10), 863-75.
12. Onogi, S.; Shigemitsu, H.; Yoshii, T.; Tanida, T.; Ikeda, M.; Kubota, R.; Hamachi, I., In situ real-time imaging of self-sorted supramolecular nanofibres. *Nature chemistry* **2016**, *8* (8), 743-52.
13. Ji, W.; Zhang, S. J.; Filonenko, G. A.; Li, G. Y.; Sasaki, T.; Feng, C. L.; Zhang, Y., Co-organizing synthesis of heterogeneous nanostructures through the photo-cleavage of pre-stabilized self-assemblies. *Chem Commun* **2017**, *53* (34), 4702-4705.
14. Akiyama, M.; Hatanaka, M.; Ohta, Y.; Ueda, K.; Yanai, A.; Uehara, Y.; Tanabe, K.; Tsuru, M.; Miyazaki, M.; Saeki, S.; Saito, T.; Shinoda, K.; Oka, Y.; Tanizawa, Y., Increased insulin demand promotes while pioglitazone prevents pancreatic beta cell apoptosis in Wfs1 knockout mice. *Diabetologia* **2009**, *52* (4), 653-663.
15. Guegn, C.; Vila, M.; Rosoklija, G.; Hays, A. P.; Przedborski, S., Recruitment of the mitochondrial-dependent apoptotic pathway in amyotrophic lateral sclerosis. *J Neurosci* **2001**, *21* (17), 6569-6576.
16. Hetz, C., The unfolded protein response: controlling cell fate decisions under ER stress and beyond. *Nat Rev Mol Cell Bio* **2012**, *13* (2), 89-102.

17. Nakagawa, T.; Zhu, H.; Morishima, N.; Li, E.; Xu, J.; Yankner, B. A.; Yuan, J. Y., Caspase-12 mediates endoplasmic-reticulum-specific apoptosis and cytotoxicity by amyloid-beta. *Nature* **2000**, *403* (6765), 98-103.
18. Lu, M.; Lawrence, D. A.; Marsters, S.; Acosta-Alvear, D.; Kimmig, P.; Mendez, A. S.; Paton, A. W.; Paton, J. C.; Walter, P.; Ashkenazi, A., Opposing unfolded-protein-response signals converge on death receptor 5 to control apoptosis. *Science* **2014**, *345* (6192), 98-101.

Chapter V.2

1. P. Grodzinski, M. Kircher, M. Goldberg, A. Gabizon, Integrating Nanotechnology into Cancer Care. *Acs Nano* **2019**, *13*, 7370-7376.
2. S. Hoelder, P. A. Clarke, P. Workman, Discovery of small molecule cancer drugs: successes, challenges and opportunities. *Mol Oncol* **2012**, *6*, 155-176.
3. R. Santos, O. Ursu, A. Gaulton, A. P. Bento, R. S. Donadi, C. G. Bologa, A. Karlsson, B. Al-Lazikani, A. Hersey, T. I. Oprea, J. P. Overington, A comprehensive map of molecular drug targets. *Nat Rev Drug Discov* **2017**, *16*, 19-34.
4. X. D. Xue, A. Lindstrom, H. J. Qu, Y. P. Li, Recent advances on small-molecule nanomedicines for cancer treatment . *Wires Nanomed Nanobi* 2020, *12*:e1607
5. Rationalizing combination therapies. *Nat Med* **2017**, *23*, 1113-1113.
6. (a)Z. Q. Q. Feng, H. M. Wang, S. Y. Wang, Q. Zhang, X. X. Zhang, A. A. Rodal, B. Xu, Enzymatic Assemblies Disrupt the Membrane and Target Endoplasmic Reticulum for Selective Cancer Cell Death. *J Am Chem Soc* **2018**, *140*, 9566-9573; (b)Y. Yuan, L. Wang, W. Du, Z. L. Ding, J. Zhang, T. Han, L. N. An, H. F. Zhang, G. L. Liang, Intracellular Self-Assembly of Taxol Nanoparticles for Overcoming Multidrug Resistance. *Angew Chem Int Edit* **2015**, *54*, 9700-9704; (c)H. M. Wang, Z. Q. Q. Feng, B. Xu, Bioinspired assembly of small molecules in cell milieu. *Chem Soc Rev* **2017**, *46*, 2421-2436.
7. (a)J. Zhan, Y. B. Cai, S. S. He, L. Wang, Z. M. Yang, Tandem Molecular Self-Assembly in Liver Cancer Cells. *Angew Chem Int Edit* **2018**, *57*, 1813-1816; (b)Z. Zheng, P. Y. Chen, M. L. Xie, C. F. Wu, Y. F. Luo, W. T. Wang, J. Jiang, G. L. Liang, Cell Environment-Differentiated Self-Assembly of Nanofibers. *J Am Chem Soc* **2016**, *138*, 11128-11131.
8. T. N. K. Raju, The Nobel Chronicles. *Lancet* **2000**, *356*, 81-81.
9. T. Robak, M. Kasznicki, Alkylating agents and nucleoside analogues in the treatment of B cell chronic lymphocytic leukemia. *Leukemia* **2002**, *16*, 1015-1027.
10. S. J. Zhang, X. W. Hu, D. Z. Mang, T. Sasaki, Y. Zhang, Self-delivery of N-hydroxylethyl peptide assemblies to the cytosol inducing endoplasmic reticulum dilation in cancer cells. *Chem Commun* **2019**, *55*, 7474-7477.
11. R. G. Fu, Y. Sun, W. B. Sheng, D. F. Liao, Designing multi-targeted agents: An emerging anticancer drug discovery paradigm. *Eur J Med Chem* **2017**, *136*, 195-211.
12. G. Xu, W. H. Zhang, M. K. Ma, H. L. McLeod, Human Carboxylesterase 2 Is Commonly Expressed in Tumor Tissue and Is Correlated with Activation of Irinotecan. *Clin Cancer Res* **2002**, *8*, 2605-2611.
13. L. Panasci, J. P. Paiement, G. Christodouplopoulos, A. Belenkov, A. Malapetsa, R. Aloyz, Chlorambucil Drug Resistance in Chronic Lymphocytic Leukemia: The Emerging Role of DNA Repair. *Clin Cancer Res* **2001**, *7*, 454-461.
14. (a)Z. Feng, B. Xu, Inspiration from the mirror: D-amino acid containing peptides in biomedical approaches. *Biomolecular concepts* **2016**, *7*, 179-187; (b)J. Zhou, X. W. Du, J. Li, N. Yamagata, B. Xu, Taurine Boosts Cellular Uptake of Small d-Peptides for Enzyme-Instructed Intracellular Molecular Self-Assembly. *J Am Chem Soc* **2015**, *137*, 10040-10043.

15. P. Verma, H. Pal, Intriguing H-Aggregate and H-Dimer Formation of Coumarin-481 Dye in Aqueous Solution As Evidenced from Photophysical Studies. *J Phys Chem A* **2012**, *116*, 4473-4484.
16. C. S. Morrow, P. K. Smitherman, S. K. Diah, E. Schneider, A. J. Townsend, Coordinated Action of Glutathione S-Transferases (GSTs) and Multidrug Resistance Protein 1 (MRP1) in Antineoplastic Drug Detoxification. *J Biol Chem* **1998**, *273*, 20114-20120.
17. A. Bielawska, K. Bielawski, K. Chrzanowski, S. Wolczynski, Prolidase-activated prodrug for cancer chemotherapy: Cytotoxic activity of proline analogue of chlorambucil in breast cancer MCF-7 cells. *Farmaco* **2000**, *55*, 736-741.
18. M. H. Abdelrahman, B. G. M. Youssif, M. A. Abdelgawad, A. H. Abdelazeem, H. M. Ibrahim, A. A. Moustafa, L. Treamblu, S. N. A. Bukhari, Synthesis, biological evaluation, docking study and ulcerogenicity profiling of some novel quinoline-2-carboxamides as dual COXs/LOX inhibitors endowed with anti-inflammatory activity. *Eur J Med Chem* **2017**, *127*, 972-985.
19. Y. Chen, F. Brandizzi, IRE1: ER stress sensor and cell fate executor. *Trends Cell Biol* **2013**, *23*, 547-555.
20. A. S. Lee, The ER chaperone and signaling regulator GRP78/BiP as a monitor of endoplasmic reticulum stress. *Methods* **2005**, *35*, 373-381.
21. R. Guerin, G. Arseneault, S. Dumont, L. A. Rokeach, Calnexin Is Involved in Apoptosis Induced by Endoplasmic Reticulum Stress in the Fission Yeast. *Mol Biol Cell* **2008**, *19*, 4404-4420.
22. P. Kranz, F. Neumann, A. Wolf, F. Classen, M. Pompsch, T. Ocklenburg, J. Baumann, K. Janke, M. Baumann, K. Goepelt, H. Riffkin, E. Metzen, U. Brockmeier, PDI is an essential redox-sensitive activator of PERK during the unfolded protein response (UPR). *Cell Death Dis* **2017**, *8:* e2986
23. Y. Gao, J. F. Shi, D. Yuan, B. Xu, Imaging enzyme-triggered self-assembly of small molecules inside live cells. *Nat Commun* **2012**, *3*, 1033